

NATIONAL AERONAUTICS AND SPACE ADMINISTRATION

Technical Report 32-1526

Volume XI

The Deep Space Network

Progress Report

For July and August 1972

JET PROPULSION LABORATORY
CALIFORNIA INSTITUTE OF TECHNOLOGY
PASADENA, CALIFORNIA

October 15, 1972

Preface

This report presents DSN progress in flight project support, TDA research and technology, network engineering, hardware and software implementation, and operations. Each issue presents material in some, but not all, of the following categories in the order indicated:

Description of the DSN

Mission Support

- Interplanetary Flight Projects
- Planetary Flight Projects
- Manned Space Flight Projects
- Advanced Flight Projects

Radio Science

Supporting Research and Technology

- Tracking and Ground-Based Navigation
- Communications, Spacecraft/Ground
- Station Control and Operations Technology
- Network Control and Data Processing

Network Engineering and Implementation

- Network Control System
- Ground Communications
- Deep Space Stations

Operations and Facilities

- Network Operations
- Network Control System Operations
- Ground Communications
- Deep Space Stations
- Facility Engineering

In each issue, the part entitled "Description of the DSN" describes the functions and facilities of the DSN and may report the current configuration of one of the five DSN systems (Tracking, Telemetry, Command, Monitor and Control, and Test and Training).

The work described in this report series is either performed or managed by the Tracking and Data Acquisition organization of JPL for NASA.

Contents

DESCRIPTION OF THE DSN

DSN Functions and Facilities	1
N. A. Renzetti	
Network Control System	5
J. R. Hall	

MISSION SUPPORT

Interplanetary Flight Projects

Pioneers 6-9 Mission Support	12
A. J. Siegmeth	
NASA Code 311-03-21-20	

Planetary Flight Projects

Pioneers 10 and G Mission Support	14
A. J. Siegmeth	
NASA Code 311-03-21-20	
Viking Mission Support	19
D. J. Mudgway	
NASA Code 311-03-21-70	

Advanced Flight Projects

Pioneer Venus Mission Support	23
A. J. Siegmeth	
NASA Code 311-03-21-20	

RADIO SCIENCE

Radio Science Support	26
K. W. Linnes	
NASA Code 311-03-21-90	

Contents (contd)

SUPPORTING RESEARCH AND TECHNOLOGY

Tracking and Ground-Based Navigation

A Comparison of Cowell's Method and a Variation-of-Parameters Method for the Computation of Precision Satellite Orbits: Phase Three Results	30
S. S. Dallas and E. A. Rinderle	
NASA Code 311-03-34-10	
Use of Doppler Determinations of Polar Motion Using Artificial Satellites to Support JPL Planetary Missions	36
H. F. Fliegel	
NASA Code 150-22-12-61	
An Evaluation of Charged Particle Calibration by a Two-Way Dual-Frequency Technique and Alternatives to This Technique	42
O. H. von Roos and B. D. Mulhall	
NASA Code 150-22-12-62	
Derivation of a General Expression for Ionospheric Range Corrections Valid for Arbitrary Solar Zenith Angles, Azimuths, Elevation Angles and Station Locations	53
O. H. von Roos and K. W. Yip	
NASA Code 310-10-60-52	
Topics in the Implementation and Application of Two-Station Tracking Data Types	62
K. H. Rourke and V. J. Ondrasik	
NASA Code 150-22-60-10	
Low Noise Receivers: Microwave Maser Development	71
R. Clauss, E. Wiebe, and R. Quinn	
NASA Code 310-20-66-01	

Communications, Spacecraft/Ground

Decoding the Golay Code	81
E. R. Berlekamp	
NASA Code 150-22-70-40	
Weights Modulo 8 in Binary Cyclic Codes	86
R. J. McEliece	
NASA Code 150-22-70-40	
Reducing the Complexity of Calculating Syndromes for Error-Correcting Codes	89
L. H. Harper and J. E. Savage	
NASA Code 150-22-70-40	

Contents (contd)

Efficient Generation of Statistically Good Pseudonoise by Linearly Interconnected Shift Registers	92
W. J. Hurd NASA Code 150-22-72-40	
NASTRAN Data Generation and Management Using Interactive Graphics	104
M. S. Katow and B. M. Cooper NASA Code 310-20-65-01	
Preliminary Analysis of the Microwave Weather Project Data for CY 1971	111
M. S. Reid and R. W. D. Booth NASA Code 150-22-66-20	

NETWORK ENGINEERING AND IMPLEMENTATION

Network Control System

High-Reliability Microcircuit Procurement in the DSN	121
E. F. Zundel NASA Code 312-03-14-21	

Ground Communications

Ground Communications Facility Functional Design for 1973-1974	124
J. P. McClure NASA Code 311-06-40-00	

Deep Space Stations

DSN Research and Technology Support	132
R. M. Gosline NASA Code 150-22-12-05	
Coaxial Switch Evaluation	135
H. G. Nishimura NASA Code 150-22-61-10	
Wideband Distribution Amplifier for Coherent Reference Generator	140
C. F. Foster NASA Code 311-03-42-48	
Dual Carrier Preparations for Viking	146
D. A. Bathker and D. W. Brown NASA Code 311-03-42-47	

Contents (contd)

Salvaging an Expensive Shaft by Brush Electroplating	150
---	------------

H. McGinness
NASA Code 311-03-42-45

Performance of the 64-meter-diameter Antenna Servo	153
---	------------

P. Lipsius
NASA Code 311-03-42-45

OPERATIONS AND FACILITIES

Network Operations

Network Operations Control	157
---	------------

R. J. Amorose
NASA Code 311-03-13-1111

Ground Communications

High-Speed Data Communication: A Description of Software Techniques	161
--	------------

R. W. Livermore
NASA Code 311-03

Deep Space Stations

Accuracy of the Signal-to-Noise Ratio Estimator: A Comment on the Derivation of the Estimator Mean	164
---	------------

J. R. Lesh
NASA Code 311-03-14-52

Bibliography	167
-------------------------------	------------

DSN Functions and Facilities

N. A. Renzetti
Mission Support Office

The objectives, functions, and organization of the Deep Space Network are summarized. The Deep Space Instrumentation Facility, the Ground Communications Facility, and the Network Control System are described.

The Deep Space Network (DSN), established by the National Aeronautics and Space Administration (NASA) Office of Tracking and Data Acquisition under the system management and technical direction of the Jet Propulsion Laboratory (JPL), is designed for two-way communications with unmanned spacecraft traveling approximately 16,000 km (10,000 mi) from Earth to planetary distances. It supports or has supported, the following NASA deep space exploration projects: Ranger, Surveyor, Mariner Venus 1962, Mariner Mars 1964, Mariner Venus 67, Mariner Mars 1969, Mariner Mars 1971 (JPL); Lunar Orbiter and Viking (Langley Research Center); Pioneer (Ames Research Center); Helios (West Germany); and Apollo (Manned Spacecraft Center), to supplement the Spaceflight Tracking and Data Network (STDN).

The Deep Space Network is one of two NASA networks. The other, STDN, is under the system management and technical direction of the Goddard Space Flight Center. Its function is to support manned and unmanned Earth-orbiting and lunar scientific and communications satellites. Although the DSN was concerned with unmanned lunar spacecraft in its early years, its primary objective now and into the future is to continue its support of planetary and interplanetary flight projects. A development objective has been to keep the network capability at the state of the art of telecommunications and data handling and to support as many flight projects as possible with a minimum of mission-dependent hardware and software. The DSN provides direct support of each flight project through that project's tracking and

data system. This management element is responsible for the design and operation of the hardware and software in the DSN which are required for the conduct of flight operations.

Beginning in FY 1973 a modified DSN interface has been established with the flight projects. In lieu of the SFOF, a multimission Mission Control and Computing Center (MCCC) has been activated as a separate functional and management element within JPL. This function, as negotiated with each flight project, will provide all computing and mission operations support for missions controlled from JPL. DSN computing support will be provided separately by the DSN. Radio metric, telemetry, and command data interfaces with the DSN are a joint DSN, MCCC, and flight project responsibility. The organization and procedures necessary to carry out these new activities will be reported in this document in the near future.

The DSN function, in supporting a flight project by tracking the spacecraft, is characterized by five network systems:

- (1) DSN Tracking System. Generates radio metric data; i.e., angles, one- and two-way doppler and range, and transmits raw data to mission control.
- (2) DSN Telemetry System. Receives, decodes, records, and retransmits engineering and scientific data generated in the spacecraft to Mission Control.
- (3) DSN Command System. Accepts coded signals from mission control via the GCF and transmits them to the spacecraft in order to initiate spacecraft functions in flight.
- (4) DSN Monitor and Control System. Instruments, transmits, records, and displays those parameters of the DSN necessary to verify configuration and validate the network. Provides operational direction and configuration control of the network and primary interface with flight project Mission Control personnel.
- (5) DSN Test and Training System. Generates and controls simulated data to support development, test, training and fault isolation within the DSN. Participates in mission simulation with flight projects.

The facilities needed to carry out these functions have evolved in three technical areas: (1) the Deep Space Stations (DSSs) and the telecommunications interface

through the RF link with the spacecraft is known as the Deep Space Instrumentation Facility (DSIF); (2) the Earth-based point-to-point voice and data communications from the stations to Mission Control is known as the Ground Communications Facility (GCF); (3) the network monitor and control function is known as the Network Control System (NCS).

I. Deep Space Instrumentation Facility

A. Tracking and Data Acquisition Facilities

A world-wide set of Deep Space Stations with large antennas, low-noise phase-lock receiving systems, and high-power transmitters provide radio communications with spacecraft. The DSSs and the deep space communications complexes (DSCCs) they comprise are given in Table 1.

Radio contact with a spacecraft usually begins when the spacecraft is on the launch vehicle at Cape Kennedy, and it is maintained throughout the mission. The early part of the trajectory is covered by selected network stations of the Air Force Eastern Test Range (AFETR) and the STDN of the Goddard Space Flight Center.¹ Normally, two-way communications are established between the spacecraft and the DSN within 30 min after the spacecraft has been injected into lunar, planetary, or interplanetary flight. A compatibility test station at Cape Kennedy (discussed later) tests and monitors the spacecraft continuously during the launch checkout phase. The deep space phase begins with acquisition by 26-m DSSs. These and the remaining DSSs listed in Table 1 provide radio communications until the end of the mission.

To enable continuous radio contact with spacecraft, the DSSs are located approximately 120 deg apart in longitude; thus a spacecraft in deep space flight is always within the field-of-view of at least one DSS, and for several hours each day may be seen by two DSSs. Furthermore, since most spacecraft on deep space missions travel within 30 deg of the equatorial plane, the DSSs are located within latitudes of 45 deg north and south of the equator. All DSSs operate at S-band frequencies: 2110-2120 MHz for Earth-to-spacecraft transmission and 2290-2300 MHz for spacecraft-to-Earth transmission. An X-band capability is being readied for future missions beginning in 1973.

¹The 9-m (30-ft) diam antenna station established by the DSN on Ascension Island during 1965 to act in conjunction with the STDN orbital support 9-m (30-ft) diam antenna station was transferred to the STDN in July 1968.

To provide sufficient tracking capability to enable returns of useful data from around the planets and from the edge of the solar system, a 64-m (210-ft) diam antenna subnet will be required. Two additional 64-m (210-ft) diam antenna DSSs are under construction at Madrid and Canberra and will operate in conjunction with DSS 14 to provide this capability. These stations are scheduled to be operational by the middle of 1973.

B. Compatibility Test Facilities

In 1959, a mobile L-band compatibility test station was established at Cape Kennedy to verify flight-spacecraft/DSN compatibility prior to the launch of the Ranger and Mariner Venus 1962 spacecraft. Experience revealed the need for a permanent facility at Cape Kennedy for this function. An S-band compatibility test station with a 1.2-m (4-ft) diameter antenna became operational in 1965. In addition to supporting the preflight compatibility tests, this station monitors the spacecraft continuously during the launch phase until it passes over the local horizon.

Spacecraft telecommunications compatibility in the design and prototype development phases was formerly verified by tests at the Goldstone DSCC. To provide a more economical means for conducting such work and because of the increasing use of multiple-mission telemetry and command equipment by the DSN, a Compatibility Test Area (CTA) was established at JPL in 1968. In all essential characteristics, the configuration of this facility is identical to that of the 26-m (85-ft) and 64-m (210-ft) diameter antenna stations.

The JPL CTA is used during spacecraft system tests to establish the compatibility with the DSN of the proof test model and development models of spacecraft, and the Cape Kennedy compatibility test station is used for final flight spacecraft compatibility validation testing prior to launch.

II. Ground Communications Facility

The GCF provides voice, high-speed data, wideband data, and teletype communications between the Mission Operations Center and the DSSs. In providing these capabilities, the GCF uses the facilities of the worldwide NASA Communications Network (NASCOM)² for all long

distance circuits, except those between the Mission Operations Center and the Goldstone DSCC. Communications between the Goldstone DSCC and the Mission Operations Center are provided by a microwave link directly leased by the DSN from a common carrier.

Early missions were supported by voice and teletype circuits only, but increased data rates necessitated the use of high-speed and wideband circuits for DSSs. Data are transmitted to flight projects via the GCF using standard GCF/NASCOM formats. The DSN also supports remote mission operations centers using the GCF/NASCOM interface.

III. Network Control System

The DSN Network Control System is comprised of hardware, software, and operations personnel to provide centralized, real-time control of the DSN and to monitor and validate the network performance. These functions are provided during all phases of DSN support to flight projects. The Network Operations Control Area is located in JPL Building 230, adjacent to the local Mission Operations Center. The NCS, in accomplishing the monitor and control function does not alter, delay, or serially process any inbound or outbound data between the flight project and tracking stations. Hence NCS outages do not have a direct impact on flight project support. Voice communications are maintained for operations control and coordination between the DSN and flight projects, and for minimization of the response time in locating and correcting system failures.

The NCS function will ultimately be performed in data processing equipment separate from flight project data processing and specifically dedicated to the NCS function. During FY 1973, however, DSN operations control and monitor data will be processed in the JPL 360/75 and in the 1108. In FY 1974 the NCS data processing function will be partly phased over to an interim NCS processor, and finally, in FY 1975, the dedicated NCS data processing capability will be operational. The final Network Data Processing Area will be located remote from the Network Operations Control Area so as to provide a contingency operating location to minimize single point of failure effects on the network control function. A preliminary description of the NCS appears elsewhere in this document.

²Managed and directed by the Goddard Space Flight Center.

Table 1. Tracking and data acquisition stations of the DSN

DSCC	Location	DSS	DSS serial designation	Antenna		Year of initial operation
				Diameter, m (ft)	Type of mounting	
Goldstone	California	Pioneer	11	26(85)	Polar	1958
		Echo	12	26(85)	Polar	1962
		(Venus) ^a	13	26(85)	Az-El	1962
		Mars	14	64(210)	Az-El	1966
—	Australia	Woomera	41	26(85)	Polar	1960
Tidbinbilla	Australia	Weemala (formerly Tidbinbilla)	42	26(85)	Polar	1965
		Ballima (formerly Booroomba)	43	64(210)	Az-El	Under construction
—	South Africa	Johannesburg	51	26(85)	Polar	1961
Madrid	Spain	Robledo	61	26(85)	Polar	1965
		Cebreros	62	26(85)	Polar	1967
		Robledo	63	64(210)	Az-El	Under construction

^aA research-and-development facility used to demonstrate the feasibility of new equipment and methods to be integrated into the operational network. Besides the 26-m (85-ft) diam Az-El mounted antenna, DSS 13 has a 9-m (30-ft) diam Az-El mounted antenna that is used for interstation time correlation using lunar reflection techniques, for testing the design of new equipment, and for support of ground-based radio science.

Network Control System

J. R. Hall
DSN Systems Office

This article provides: (1) background material describing philosophy leading to a Network Control System (NCS) function using data processing equipment separate from that equipment used by flight projects, (2) key characteristics of the NCS, (3) a listing of the functional requirements for each NCS subsystem, (4) a generic subsystem data flow description, and (5) an overall NCS data flow description.

In October of 1971 the Office of Space Sciences (OSS) and Office of Tracking and Data Acquisition (OTDA) reviewed the Planetary Mission Operations, Space Flight Operations Facility (SFOF), and network interface with the view to bringing the program control and budget functions more into line with management responsibilities. The intent is to develop an interface that would be reasonably clear in order to simplify technical management and to assure that budgeting requirements of the two offices are well understood.

The OTDA assumed responsibility for the tracking stations, NASA Communications Network (NASCOM)/Ground Communications Facility (GCF), and network control and monitoring. These responsibilities include (1) network scheduling, (2) network predicts, (3) network performance monitoring, (4) network validation tests,

(5) provision of real-time data streams to Mission Operations, (6) acceptance of commands from Mission Operations and transmission to stations and spacecraft, (7) provision of a clean record to Mission Operations of data streams for tracking, telemetry, and command, and as required, (8) participation with Mission Operations in mission simulations. The system is to be designed so that OTDA and OSS functions reside in separate hardware to provide for cleaner and more controllable interfaces.

Figure 1 depicts the flow between the DSN and the flight project and the manner in which the NCS is coupled into this flow. Inbound tracking and telemetry data and outbound command and mission simulation data are tapped off and sent to Network Control for validation and verification purposes. DSN monitor and control data are communicated between Network Control and

DSN elements. Mission information for operations control and DSN status data are exchanged via voice between Network Control and Mission Control. JPL central computers are utilized for non-operations-driven data processing.

One of the major objectives of the Mark III DSN design is to provide a multimission capability that presents a simple, fully standardized interface to using projects via standard GCF/NASCOM formats. The NCS plan maintains this objective in accomplishing the monitor and control function. It does not alter, delay, or serially process any inbound or outbound data between the flight project and tracking stations. Hence NCS outages should not have a direct impact on flight project support. Voice communications will be maintained for operations control and coordination between the DSN and flight projects and to minimize the response time in locating and directing system failures. The development schedule provides for a full-scale NCS capability by July 1, 1974.

An interim capability will be available by July 1, 1973. The interim capability will consist of flight project information on NCS displays for DSN tracking, telemetry, and command data validation and will incorporate a separate NCS processor for data validation and operations control purposes. This interim configuration requires that non-JPL flight projects maintain a tracking, telemetry, and command data processing capability in the JPL 360/75 if the network performance is to be suitably validated. The capability for July 1972 uses most of the current JPL 360/75 DSN capability.

The key functions of the DSN Control System provide the following:

- (1) Real-time validation of network configuration and performance.
- (2) No alteration or delay of inbound or outbound data by the validation technique. Outbound lines are shared with flight projects.
- (3) Near-real-time relaying of DSN status to Mission Control.
- (4) Close liaison with Mission Operations to minimize downtime and to locate and correct network failures.
- (5) Network control and Mission Operations functions performed in separate hardware.

- (6) A GCF Log which provides fill data, as requested by flight projects.
- (7) A capability for network test and training and for participation in mission simulations.
- (8) A DSN data base for network operations and performance analyses.
- (9) Support for remote as well as local mission control centers.

The NCS comprises seven subsystems as follows: Tracking, Telemetry, Command, Monitor and Control, Display, Support, and Test and Training. The NCS data processing requirements for these subsystems are as follows:

Tracking

- (1) Generate predictions from project-supplied state vector or from radio metric data.
- (2) Control and verify system configuration and data mode.
- (3) Generate tracking standards and limits.
- (4) Compare radio metric data with predictions.
- (5) Detect and report status of the DSN Tracking System.
- (6) Transmit alarms to Monitor and Control System and DSN Operations Control Area.
- (7) Generate System Performance Record for tracking.

Telemetry

- (1) Control and verify selected system configuration and data mode.
- (2) Generate telemetry standards and limits.
- (3) Decommunate data needed for system performance analysis.
- (4) Detect and report status of the DSN Telemetry System.
- (5) Transmit alarms to Monitor and Control System and DSN Operations Control Area.
- (6) Generate received signal level predictions.
- (7) Generate System Performance Record for telemetry.

Command

- (1) Control and verify selected system configuration and data mode.
- (2) Generate command standards and limits.
- (3) Detect and report status of DSN Command System.
- (4) Transmit alarms to Monitor and Control System and DSN Operations Control Area.
- (5) Generate System Performance Record for command.
- (6) Generate test commands.

Monitor and Control

- (1) Generate monitor standards and limits.
- (2) Receive Deep Space Information Facility (DSIF), NCS, and Ground Communications Facility (GCF) monitor data.
- (3) Receive Telemetry, Tracking, and Command System alarms and selected telemetry data.
- (4) Detect and report status of the DSN.
- (5) Transmit display data to DSN Operations Control Area.
- (6) Generate subsystem-common standards and limits parameter tables.
- (7) Monitor NCS configuration and performance.
- (8) Generate Network Performance Record.
- (9) Generate DSN operational schedules.
- (10) Generate DSN operational sequence of events and historic log.
- (11) Process discrepancy report data.
- (12) Process ODC traceability reporting system (TRS) data.

Display

- (1) Provide man/machine interface in DSN Operations Control Area for control of real-time monitors (RTMs).
- (2) Format and display received RTM data.
- (3) Provide remote terminal for Network Support Controller (NSC) support subsystem computer.

- (4) Format and display received NSC support subsystem data.
- (5) Provide consoles, displays, and working area for operations personnel.
- (6) Provide a computer-driven network status display board.

Support

- (1) Provide network support controller (NSC) processor, including operating system for all non-real-time programs.
- (2) Load and start programs in RTMs, NSC, and GCF; provide checkpoint recovery of NSC.
- (3) Provide utility print routines for demand dumps of any data being switched and routed or any data on NCS files, also non-real-time (NRT) de-log dumps of any tape.
- (4) Manage disk-to-disk transfers to/from RTMs.
- (5) Provide system-common standards and limits file extraction and high-speed data (HSD) output.
- (6) Provide NCS development support – RTM emulator, RTM compiler, NSC compiler.
- (7) Provide system-common GCF log replay data extractions (for project fill data only).
- (8) Provide test HSD block (for de-bug).
- (9) Receive NRT program input data in data driven mode.
- (10) Encode free-form text for HSD transmission.

Test and Training

- (1) Generate and control simulated data to support development, test, training, and fault isolation.
 - (a) DSIF data streams to exercise GCF and NCS subsystems.
 - (b) Spacecraft data patterns to exercise DSIF subsystems.
- (2) Participate in mission simulation with project.
 - (a) Control data flow within DSN to support mission test and training simulation.

- (b) Generate simulated DSN data to supplement project simulation data.

A generic subsystem data flow chart is shown in Fig. 2. The basic structures of the tracking, telemetry, command, and monitor and control subsystems comprise real-time and non-real-time functions. The real-time function will be accomplished through the use of minicomputer-based real-time monitors. System configuration verification and system performance validation will be accomplished by comparing incoming data with established standards and limits. System performance records will be accumulated in real-time for analysis, data recall, and historical purposes. Alarm diagnosis and system status and display data will be available for real-time operations control purposes. An initialization and recovery file is maintained for initial setup and for checkpoint recovery.

The non-real-time functions will be accommodated in a network support controller. This processor will be utilized to establish standards and limits, to generate predicts, to extract system performance data, to analyze data, to extract data for standards and limits transmission to the DSIF and GCF, and to extract project fill data.

Figure 3 depicts the Network Control System data and message flow configuration, which incorporates the following:

- (1) A DSN Operations Control Area located in the Mission Operations Center.
- (2) Network data system real-time monitors located in the Network Data Processing Area. Processed real-time monitor data are displayed in and controlled from the DSN Operations Control Area.
- (3) A network support controller in the Network Data Processing Area which is used for coordination of the real-time monitors and for network data processing. Data are output to the DSN Operations Control Area and to the Deep Space Stations.
- (4) A test and training processor and operations function located in the Network Data Processing Area.
- (5) A GCF terminal in Building 230 to interface with the DSN Operations Control Area and to provide the GCF log. A second GCF terminal is provided adjacent to the Network Data Processing Area.

A more detailed description of the Network Control System will be provided in a later issue of this document.

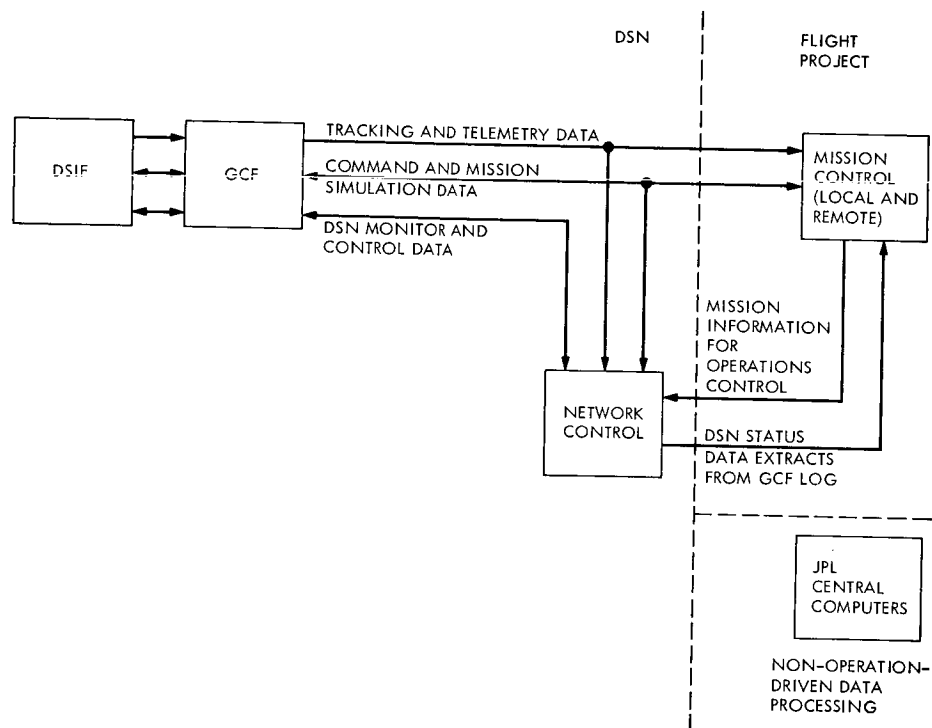


Fig. 1. DSN Control System key functional characteristics

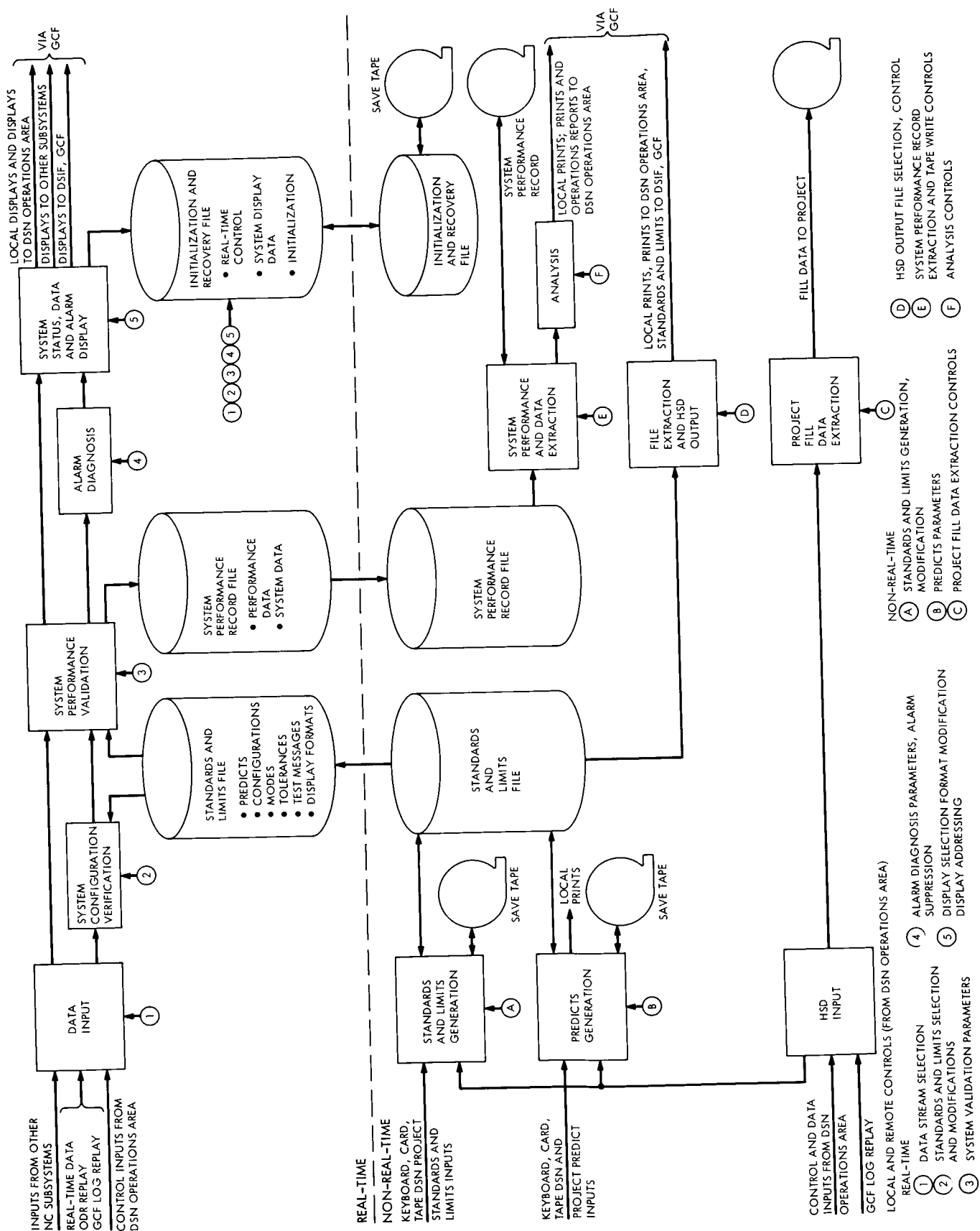


Fig. 2. Generic subsystem data flow chart

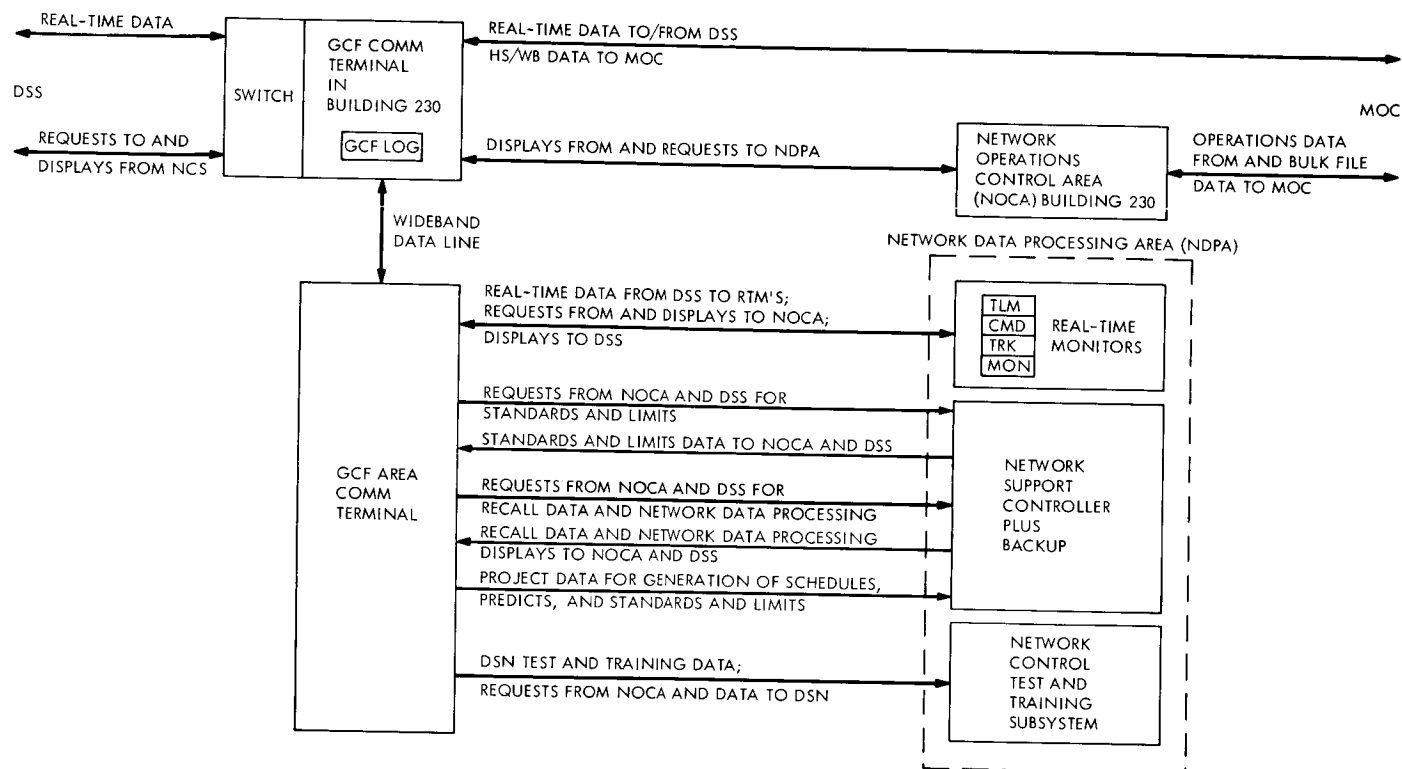


Fig. 3. Network Control System data and message flow requirements

Pioneers 6-9 Mission Support

A. J. Siegmeth
Mission Support Office

During July and August 1972, the DSN supported a radial experiment requiring signals of Pioneers 9 and 10 simultaneously. The Pioneer principal investigators plan to establish the distribution of fields and particle gradients. The DSN demonstrated a Mark III-system-type station software which can transmit Pioneers 6, 7, 8, and 9 telemetry data by high-speed data lines.

During this reporting period, the DSN supported a radial experiment of Pioneers 9 and 10. On August 6, 1972, the distance between the Sun and Pioneer 9 was approximately 120 million km, and Pioneer 10 was already speeding away from the Sun, having a 240-million-km Sun range. The DSN started to furnish Pioneer 9 support in mid-July 1972, and an average of seven tracking passes have been provided weekly. During the same time, Pioneer 10 support was continuous. The Pioneer 9 spacecraft was tracked most of the time by DSS 11 at Goldstone and DSS 51 in South Africa. Some tracking passes were provided by DSS 41 in Woomera, Australia.

The support of the Pioneer 9 and 10 radial experiment was a continuation of the DSN's effort to make possible simultaneous observations by two spacecraft separated by a large heliocentric radial distance. The Pioneer principal investigators plan to determine the parameters of

the solar wind and magnetic field in situations where the two spacecraft under surveillance are aligned on the same solar radial. The significance of this experiment was also magnified by the fact that the sun was quite active during the radial configuration, and therefore the interplanetary medium was more complex. More background information on the Pioneer radial and spiral opportunities was given in Ref. 1.

The Pioneer 6 spacecraft is still within the threshold range of the 26-m antenna stations. The DSN stations in Spain, South Africa, and Australia tracked an average of five passes per week for the Pioneer 6 mission. Pioneers 7 and 8 can be tracked only from the 64-m antenna station at Goldstone, California. Because of the heavy loading of this single advanced facility, Pioneers 7 and 8 were tracked for only a few passes.

The DSN continued to improve the network's effectiveness by attempting to support all unmanned missions in the DSN Mark III-type configuration. The engineers of DSS 62 in Madrid have recently developed a new station software which has already been demonstrated, making possible the support of Pioneer 6, 7, 8, and 9 missions in the same standard, multimission-type configuration as designed for the current and future unmanned planetary and interplanetary missions. This software has a capability to use the standard subcarrier demodulators, symbol synchronizers, and sequential decoders for the demodulation of the Pioneer signals. The on-site telemetry and command processor generates high-speed data blocks very similar to the ones used by Pioneer 10, records a digital magnetic tape called the Original Data Record, and also generates a teletype output which can transmit Pioneer 6, 7, 8, and 9 telemetry frames and a short status

monitoring frame. The DSN entered negotiations with the Pioneer Project to make possible operations on the second-generation Pioneers with this demonstrated software.

The JPL Mission Control and Computing Center started engineering planning for a proposed configuration making the demonstrated station software compatible with a flight project operational capability. After such a capability is implemented, the DSN plans to deactivate the Ground Operations Equipment (GOE). This equipment has been in service since the Pioneer 6 launch in December 1965. GOEs are still operational at DSSs 12 and 14 at Goldstone, California, and at DSS 51 in South Africa. The demonstrated on-site software subsystem will improve telemetry threshold support capabilities by approximately 1 dB using the latest state-of-the-art demodulation equipment.

Reference

1. Siegmeth, A. J., "Pioneer Mission Support," in *The Deep Space Network Progress Report*, Technical Report 32-1526, Vol. X, pp. 10-13. Jet Propulsion Laboratory, Pasadena, Calif., Aug. 15, 1972.

Pioneers 10 and G Mission Support

A. J. Siegmeth
Mission Support Office

The DSN has already completed 6 months of continuous telemetry data acquisition, command, and radio metric tracking support for Pioneer 10, which was launched on March 4, 1972. The Pioneer 10 spacecraft, on the way to the giant planet Jupiter, crossed the orbit of Mars during the first part of May and entered the asteroid belt in the middle of July 1972. A summary of extended mission support capabilities is presented.

The 250-kg Pioneer 10 spacecraft is the first man-made object to enter into the 210-million-km-wide asteroid belt region, where huge chunks of solid debris hurtle through space at tremendous speed orbiting the sun. Astronomers estimate that at least 50,000 of these asteroids measure 1.5 km or more in diameter. Ceres, the largest, is 900 km across. There is no way of knowing how many millions of small asteroids are circling the sun ranging in size from 1 km down to pebbles, sand, and meteorites. Even a relatively small asteroid could damage Pioneer 10 seriously. Such a disaster could become known on Earth only after the spacecraft downlink signals were lost.

The distribution of large asteroids in the asteroid belt is sparse enough to allow safe passage; it is the concentrations and sizes of asteroid fragments and dust particles

traveling approximately 15 km/s relative to the spacecraft which cause concern. (A bullet leaving the muzzle of a military rifle travels approximately 1 km/s.)

Since the asteroids are scattered far apart in the vastness of space, it is still a high probability that Pioneer 10 will conquer the hostile environment of the solar system and leave the asteroid belt safely in January 1973 to continue the voyage towards its next objective, Jupiter. Pioneer 10 will arrive at the largest planet of the solar system on December 4, 1973. The DSN has continuously collected the Pioneer 10 downlink telemetry signal, using almost all 26-m antenna stations of the network. Every operational measure was and is taken to monitor continuously the performance of the telecommunications downlink to assure the detection of any deviations from

nominal values affecting this link by any unforeseen collision processes. The DSN has also provided one tracking pass per week from the 64-m-antenna station at Goldstone to enhance telemetry performance and obtain precision two-way doppler-type radio metric information.

The telecommunications downlink operated during high elevation angles of the station antennas at 1024 bps. During the entrance and exit phases of the tracking passes the Project commanded the spacecraft telemetry rate to 512 bps to assure an errorless downlink telemetry stream obtained at the output of the sequential decoder from the on-site equipment. During the DSS 14 passes at Goldstone, the Project operated Pioneer 10 at a telemetry bit rate of 2048 bps.

To probe the hazards of space flight, Pioneer 10 is carrying a meteoroid detector. Dr. W. H. Kenard and four co-investigators at the Langley Research Center are concerned with encounters between the spacecraft and very small bits of matter. This experiment has panels of pressurized cells mounted from the back surface of the Pioneer 10 high-gain antenna, and penetrations of the cells are counted. The rate at which pressure is lost from a cell indicates the size of the hole made; and thus the mass and incident energy of the particle responsible will be learned. By combining such findings with trajectory data, the researchers will establish the statistical distribution modes of the spacial density of small meteoroids having masses of 10^{-9} g or more.

By August 9, the Pioneer 10 meteoroid detector registered a total of 63 hits. The first penetration was observed one day after Pioneer 10 launch, and one to seven hits were experienced during each 10 days of flight. As the spacecraft crossed the Mars orbit trace, no hits were observed for approximately eight days.

Telemetry information obtained from the asteroid meteoroid detector (also called Sisyphus) is under study. This instrument can detect particles ranging upward in mass from 10^{-6} g, and it can detect asteroids and meteoroids by the solar light that they reflect and scatter. Four independent telescopic subsystems provide four overlapping fields of view, and the light signatures are detected by photomultiplier tubes. The ranges and velocities of optically observed particles can be found by timing the entries and departures of the reflections in those four fields of view. The principal investigator of this detector is Dr. R. K. Soberman. Besides data obtained from the described asteroid and meteoroid detectors, the continuous collection of Pioneer 10 telemetry data by

the DSN also provided to the other nine experimenters new information on the environment of the solar system never before probed by any spacecraft.

Preceding the official change of the Pioneer Project/DSN interface in July 1972, the DSN delivered the 360/75 Model 6 software in June. This software included an automatic command transmission capability from the Remote Information Center of the Pioneer Project located at Ames Research Center (ARC), Moffett Field, California. Using this command input terminal, the Project started to send most of the automatic commands from ARC to the Pioneer 10 spacecraft via the Central Processing System located at the Mission Control and Computing Center (MCCC) at JPL to the Deep Space Stations. DSN has also delivered in June a capability to merge data records from the DSN-generated System Data Records and Original Data Record playback tapes. This merged Master Data Record capability is compatible with the Pioneer off-line system generating Experimenter Data Records.

Besides an automatic commanding capability provided to the flight project, the DSN has also tested emergency command transmission equipment and trained personnel. If for any reason the high speed data lines for interconnecting computers should fail, making the immediate transmission of commands to the spacecraft from the Pioneer Mission Control Area not possible, the DSN provides this emergency command capability. In this configuration the Mission Controller provides verbal instructions via voice line to the network Operation Control Chief and Station Controller. This voice command is entered at the stations by the telemetry and command processor (TCP) operator in the on-site computer via a keyboard device. Fail-safe voice command monitoring and verification techniques are also used to assure the timely transmission of commands necessary during possible urgent corrective actions. The DSN has also shortened the switchover time of telemetry bit rate and format changes at the stations to 1 min. This procedure makes possible speedy changes in the operational configuration with a minimum amount of loss of telemetry data.

The DSN has also completed the modification of numerous station voltage-controlled oscillators and doppler extractors necessary to make the stations compatible with Pioneer 10 doppler swings. The implementation of the 64-m antenna stations in Australia and Spain is on schedule. The DSN plans to make them available for Pioneer 10 support by July 1, 1973.

The performance of the real-time network support provided to the flight project was satisfactory. The Pioneer Mission Control Team used the DSN-furnished real-time data to monitor and analyze spacecraft and instrumentation health and to make spacecraft configuration adjustments to assure near optimum data return. The Project also calibrated the flight instruments at regular intervals and adapted their performance characteristics to the environment to be measured. Most of the time the Project controlled the mission from ARC using an XDS Sigma 5 real-time processor. Parallel with this capability, the Central Processing System of the MCCC was also operating and providing processed telemetry and command capability to a Pioneer team operating from the Pioneer MCCC area.

The production of continuous data records generated after the real-time operation was constrained by characteristics of the high-speed data lines interconnecting the on-site TCP computers with the Central Processing System located at JPL's Mission Control and Computer Center. The continuity of the System Data Records file established in real-time in the Central Processing System was constrained by a large number of data gaps. These gaps were caused mostly by the burst noises appearing in long high-speed data lines and by characteristics of the software of the computer systems connecting the station with the Mission Control and Computer Center. The DSN attempted to recover most of the larger gaps by recalling specific contents of the on-site Original Data Records. Because of resource, manpower, and budgetary constraints, it was not possible to fill all data gaps of the real-time System Data Records, thus causing a certain number of remaining gaps in the Master Data Records generated for the Pioneer Project by the Mission Control and Computing Center. The extent of small data gaps and the statistical distribution of the DSN-generated System Data Records is under study, and it is expected that the system performance can be improved to minimize the constraints affecting the full data return from some of the spacecraft instruments.

In August 1972, the Pioneer 10 medium-gain antenna reached threshold with the 64-m antenna station in Goldstone. Since that time, the Project has been using the spacecraft high-gain antenna exclusively as the transmission terminal of the downlink telecommunication link. The Project performed numerous DSN-supported automatic CONSCAN spin axis torqueing maneuvers and pointed the spacecraft high-gain antenna back toward Earth whenever the relative drift between the Earth and spacecraft location necessitated such a maneuver.

Figure 1 displays an estimate of the Pioneer 10 and G telecommunications link performance during the next 10 years. The Pioneer 10 geocentric range is shown from launch until the end of 1979. The geocentric range is displayed in astronomical units (1 au = 149.5 million km). The corresponding round-trip light time in minutes is also shown adjacent to the geocentric range scale.

The 26-m subnet will reach spacecraft telemetry threshold at a rate of 64 bps in 1974. In 1976, the spacecraft will fly at Saturn range, and a downlink operation of 256 bps can be provided using the 64-m subnet. Assuming that the radioisotope thermoelectric generators of the spacecraft are still delivering sufficient power to operate the spacecraft telecommunications equipment, Pioneer 10 can be supported with the 64-m antenna stations up to 1979, which is equivalent to a geocentric range of over 19 AU operating at 65 bps. It should be mentioned that if the same stations would use the latest state-of-the-art DSN block receivers with a 3-Hz carrier tracking bandwidth, the spacecraft could be supported by the ground facilities up to 1986, reaching a 30-AU range. The telemetry bit rate would be 16 bps at this time. Under similar circumstances the command threshold using the spacecraft medium-gain antenna and a 20-kW uplink power capability will be reached approximately in 1978 at a range of 16 AU. This range could be expanded to over 70 AU in 1997 if a 400-kW uplink was used. This capability would be somewhat academic in nature because the predicted half-life of the radioisotope fuel is 10 years.

If one assumes that the geocentric range of Pioneer G vs time is similar to the range given for Pioneer 10, the corresponding thresholds can also be obtained from Fig. 1 using the time scale provided for Pioneer G.

Planning for the testing and training necessary for the Pioneer G launch operations is on schedule. A maximum of 20 launch days appears feasible for this second Jupiter-bound mission. A launch window will open on April 4 and close on April 23, 1973. The daily launch windows will be targeted for a minimum of 30 min.

The Pioneer G will be a direct-ascent type. The desired direct trajectory will be accomplished by an Atlas/Centaur burn followed by a TE 364-4 solid-propellant third-stage engine. The launch azimuth will be kept constant throughout the launch opportunity at 108 deg. Beginning in the Atlas sustainer phase (147 s) the trajectories are yawed by guidance as required to obtain the necessary final target vector. The declination

angle of the target vector will range from -32.5 to -39.5 deg.

Because of the large negative declination angles, Pioneer G will fly farther to the south than Pioneer 10, and thus the Deep Space Stations located in the southern hemisphere will have long view periods, with a view disadvantage to the northern hemisphere stations. Because of this unfavorable low declination angle, there will be a direct view gap between the initial acquisition station in Johannesburg and Goldstone. To cover this

gap the STDN station at Ascension will be used, not only during launch day but for several days after launch until relative improvements of the declination angle will improve the length of view periods at the South African and Goldstone sites.

Documents covering the Pioneer G near-Earth-phase characteristics, station view periods, and the expected coverage capabilities have already been published. Additional information on Pioneer 10 and G is contained in Refs. 1-9.

References

1. Siegmeth, A. J., "Pioneer Mission Support," in *The Deep Space Network Progress Report*, Technical Report 32-1526, Vol. II, pp. 6-17. Jet Propulsion Laboratory, Pasadena, Calif., Apr. 15, 1971.
2. Siegmeth, A. J., "Pioneer Mission Support," in *The Deep Space Network Progress Report*, Technical Report 32-1526, Vol. III, pp. 7-19. Jet Propulsion Laboratory, Pasadena, Calif., June 15, 1971.
3. Siegmeth, A. J., "Pioneer Mission Support," in *The Deep Space Network Progress Report*, Technical Report 32-1526, Vol. IV, pp. 13-21. Jet Propulsion Laboratory, Pasadena, Calif., Aug. 15, 1971.
4. Siegmeth, A. J., "Pioneer Mission Support," in *The Deep Space Network Progress Report*, Technical Report 32-1526, Vol. V, pp. 4-16. Jet Propulsion Laboratory, Pasadena, Calif., Oct. 15, 1971.
5. Siegmeth, A. J., "Pioneer Mission Support," in *The Deep Space Network Progress Report*, Technical Report 32-1526, Vol. VI, pp. 13-24. Jet Propulsion Laboratory, Pasadena, Calif., Dec. 15, 1971.
6. Siegmeth, A. J., "Pioneer Mission Support," in *The Deep Space Network Progress Report*, Technical Report 32-1526, Vol. VII, pp. 5-16. Jet Propulsion Laboratory, Pasadena, Calif., Feb. 15, 1972.
7. Siegmeth, A. J., "Pioneer Mission Support," in *The Deep Space Network Progress Report*, Technical Report 32-1526, Vol. VIII, pp. 8-19. Jet Propulsion Laboratory, Pasadena, Calif., Apr. 15, 1972.
8. Siegmeth, A. J., "Pioneer Mission Support," in *The Deep Space Network Progress Report*, Technical Report 32-1526, Vol. IX, pp. 18-32. Jet Propulsion Laboratory, Pasadena, Calif., June 15, 1972.
9. Siegmeth, A. J., "Pioneer 6-9 Mission Support," in *The Deep Space Network Progress Report*, Technical Report 32-1526, Vol. X, pp. 10-13. Jet Propulsion Laboratory, Pasadena, Calif., Aug. 15, 1972.

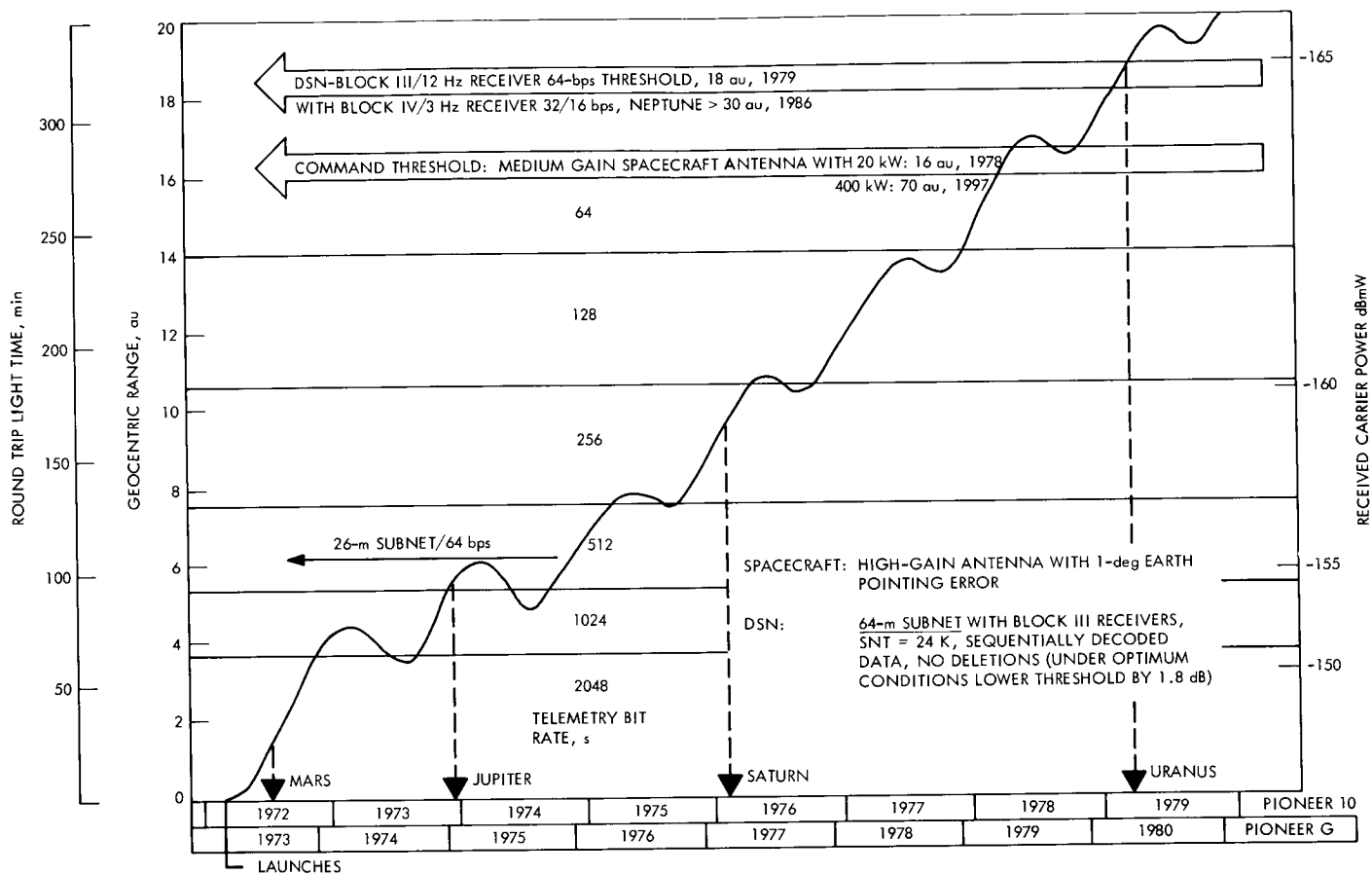


Fig. 1. Pioneers 10 and G telecommunications link performance estimate

Viking Mission Support

D. J. Mudgway
Mission Support Office

The DSN support for Viking continues to move from the completion of the planning and negotiating phase into the implementation phase in accordance with established schedules. Most documents reflecting this activity have been completed, and a major Project review of the ground data system design for Viking has been supported. A problem associated with the Viking requirement for simultaneous dual carrier operation is being investigated.

I. Introduction

The basic structure of DSN support for Viking was described in a previous article (Ref. 1). Over the past two months, activity has continued in all areas with the emphasis beginning to change from planning and negotiating towards design and implementation. At this stage, progress is best indicated by the completion and signoff of various documents reflecting agreements and decisions, and these are described below.

In one area, a significant technical problem has emerged and is being investigated at this time. Project-

sponsored reviews of activity have been supported, with major effect being given to the Launch and Flight Operations Preliminary Design Review.

II. Configuration

The DSN configuration for Viking has now been defined in functional terms in Ref. 2 for each of the DSN Systems. The configuration of the DSN Telemetry System for Viking is given in Fig. 1. Subsequent issues of this report will describe the remaining systems — Command, Tracking, and Test and Training.

III. Interfaces

The RF interfaces between the Orbiter and DSN and between the Lander and DSN have now been defined and passed through final review in preparation for approval and release. In addition to the customary RF interface parameters and telecommunications link performance curves, these interface documents contain all the telemetry and command data formats and associated material. This is to ensure that the DSN software residing in the telemetry and command processors is properly accounted for in defining the overall flight/ground compatibility criteria.

The remaining DSN interface — with the Viking Mission Control and Computing Center — is being developed to cover all data flow between the DSN and Viking Mission Control and Computing Center (VMCCC) and is in draft form at the present time.

IV. Schedules

Major milestones on the Tracking Data System (TDS)/Project schedules have been met with the release of the DSN Support Plan for Viking and the DSN support of the Flight Operations System Preliminary Design Review. As DSN support moves towards the implementation

phase, the Level 5 and Level 6 schedules contained in the DSN Support Plan and the Facilities Preparation Plan will be used to report progress in these areas.

V. Problem Areas

The Viking requirement for simultaneous dual carrier operation led to a configuration at the 64-m DSSs involving excitation of a single klystron power amplifier by two carriers. To keep the intermodulation products at an acceptable level, it was proposed to run each dual carrier at a level about 10 dB below the maximum single carrier rating for each klystron.

In the course of testing this configuration over recent months, other effects related to carrier mixing on the antenna surface with consequent interference in the downlink have been noted. A substantial effort to investigate these effects has been mounted using DSS 13 as a "test bed." The objective of these tests is to obtain an understanding of the processes by which these undesired signals are generated and to investigate means by which they may be eliminated. The background to this work and present status are described in another article in this issue (D. A. Bathker and D. W. Brown, *Dual Carrier Preparations for Viking*).

References

1. Mudgway, D. J., "Viking Mission Support," in *The Deep Space Network Progress Report*, Technical Report 32-1526, Vol. X, pp. 22-26. Jet Propulsion Laboratory, Pasadena, Calif., Aug. 15, 1972.
2. *DSN Support Plan for Viking*, Document 616-3. Jet Propulsion Laboratory, Pasadena, Calif. (a JPL internal document).

A. DATA FLOW PATHS

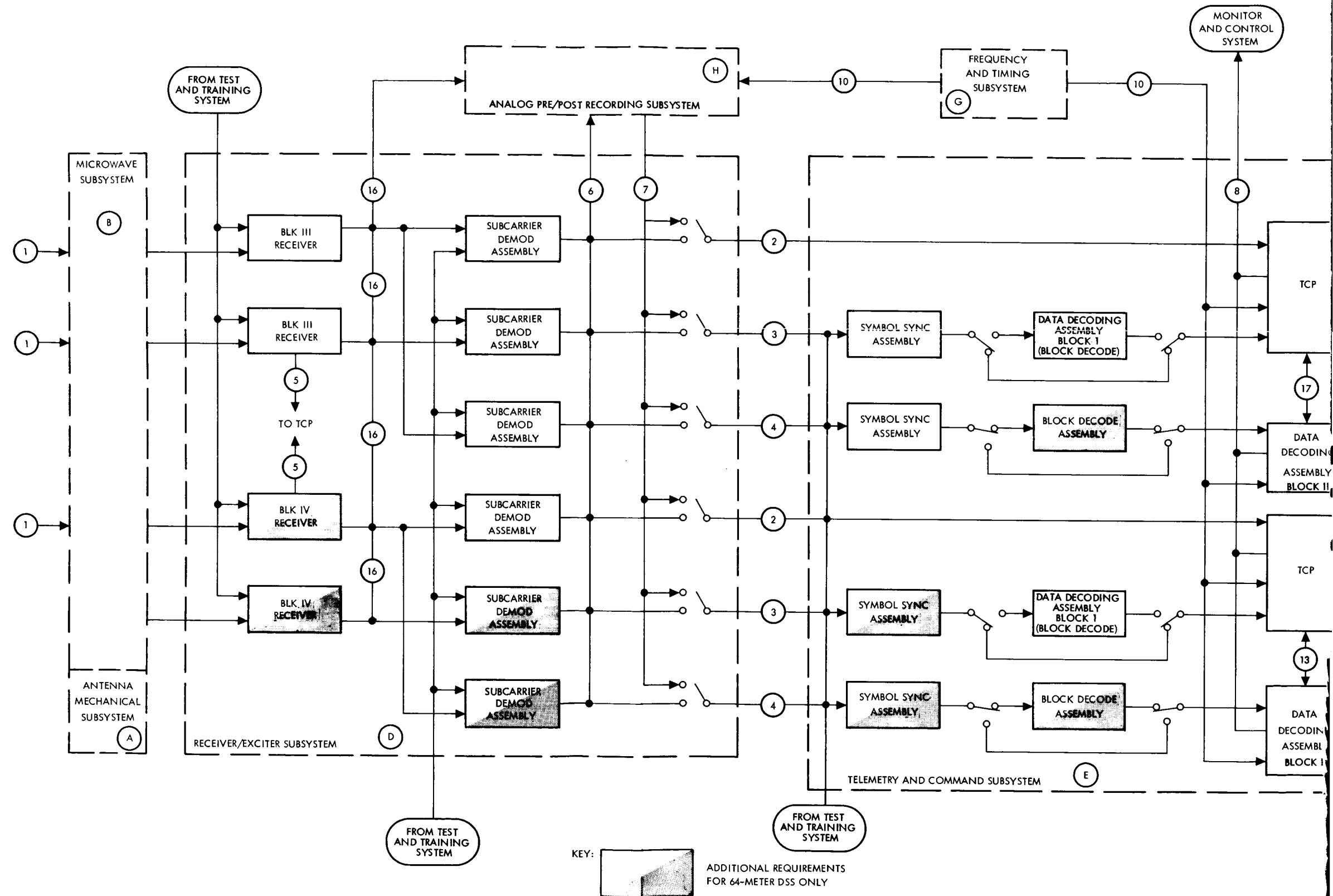
- ① SIMULTANEOUS S-BAND CARRIERS FROM UP TO TWO ORBITERS AND ONE LANDER, EACH CARRYING TWO SUBCARRIERS. THREE CARRIERS PER 64-m DSS; TWO CARRIERS PER 26-m DSS
- ② ORBITER LOW-RATE TELEMETRY DATA, UNCODED, 8-1/3 OR 7-3/4 OR 33-1/3 bps
- ③ LANDER MEDIUM-RATE TELEMETRY DATA, UNCODED 8-1/3 bps OR BLOCK CODED UP TO 1000 bps
- ④ ORBITER HIGH-RATE BLOCK-CODED DATA, UP TO 16.2 kbps OR 4 kbps UNCODED DATA
- ⑤ ILLUSTRATES GROUND AGC AVAILABLE FROM ANY RECEIVER TO 920 COMPUTER FOR TRANSMISSION TO VMCCC WITH TELEMETRY DATA STREAMS
NOTE: THIS INCLUDES X-BAND AGC WHEN EITHER OF BLOCK IV RECEIVERS IS IN X-BAND MODE
- ⑥ OUTPUT OF ALL SUBCARRIER DEMODULATOR ASSEMBLIES (SDA) IS RECORDED
- ⑦ PLAYBACK OF ANY OR ALL RECORDED SDA OUTPUT
- ⑧ PERIODIC STATUS, SIGNAL-TO-NOISE RATIO (SNR) CALCULATIONS, DATA/TAPE LOSS ALARMS
- ⑨ DIGITAL RECORDINGS OF 920 AND DATA DECODER ASSEMBLY (DDA) COMPUTER OUTPUT, PRIME ODR FOR TELEMETRY DATA, REPLAY OF TAPED DATA
- ⑩ UNIVERSAL TIME REFERENCE
- ⑪ REAL-TIME TELEMETRY DATA TRANSMISSION TO VMCCC AND NCS VIA HSS. ALL LOW-RATE AND MEDIUM-RATE DATA STREAMS, INCLUDING DSN TELEMETRY SYSTEM PARTIAL STATUS AND POSTPASS TAPE REPLAYS TO GCF LOG
- ⑫ REAL-TIME TELEMETRY DATA TRANSMISSION TO VMCCC AND NCS VIA WEB. ONE 8-kbps PLUS ONE 16-kbps DATA STREAM FOR DSSs 43 AND 63; TWO 16-kbps DATA STREAMS FROM DSS 14, INCLUDING POSTPASS TAPE REPLAYS TO GCF LOG
- ⑬ TDB
- ⑭ DSS INITIALIZATION CONDITIONS AND TELEMETRY STANDARDS AND LIMITS FROM NCS TO DSS VIA HIGH-SPEED DATA LINE (HSDL)
- ⑮ SPACECRAFT AGC, STATIC PHASE ERROR (SPE), AND COMMAND DETECTOR LOCK FROM TELEMETRY DATA TO STATION MONITOR CONSOLE FOR DSN COMMAND SYSTEM OPERATIONS
- ⑯ PREDETECTION RECORDINGS, OUTPUT OF ALL RECEIVERS, NO PLAYBACK CAPABILITY
- ⑰ PROVIDES FOR PROGRAM LOADING AND TRANSFER OF CONTROL INFORMATION FROM TCP COMPUTER TO DDA AND MONITOR INFORMATION FROM DDA TO TCP COMPUTER
- ⑱ TELEMETRY DATA, INCLUDING PARTIAL STATUS, FORMATTED FOR HSDL TRANSMISSION TO VMCCC AND NCS
- ⑲ TELEMETRY DATA, INCLUDING PARTIAL STATUS, FORMATTED FOR WBS TRANSMISSION TO VMCCC AND NCS IN 64-m SUBNET ONLY
- ⑳ TELEMETRY DATA FORMATTED FOR HSS TRANSMISSION
- ㉑ TO ㉔ NOT USED
- ㉕ ROUTING OF ALL REAL-TIME TELEMETRY DATA TO VMCCC VIA HSS FOR DECOMMUTATION, FORMATTING, AND PROCESSING FOR DISPLAY
- ㉖ TELEMETRY REQUESTS TO AND TELEMETRY DISPLAYS FROM NCS DATA PROCESSING FUNCTION
- ㉗ REAL-TIME TELEMETRY DIGITAL DATA FROM DSS TO REAL-TIME MONITORS (RTMs). REQUESTS FROM AND TELEMETRY DISPLAYS TO DSN OPERATIONS AREA
- ㉘ REQUESTS FROM DSN OPERATIONS FOR TELEMETRY STANDARDS AND LIMITS TRANSMISSION TO DSS
- ㉙ DISPLAYS OF TELEMETRY STANDARDS AND LIMITS DATA TO DSS/DSN OPERATIONS
- ㉚ DISPLAYS FROM DSN OPERATIONS FOR RECALL TELEMETRY DATA/NETWORK DATA PROCESSING
- ㉛ DISPLAYS TO DSN OPERATIONS/DSS OF RECALL TELEMETRY DATA/NETWORK DATA PROCESSING
- ㉜ TELEMETRY SIMULATION DATA
- ㉝ TELEMETRY FILL DATA TO PROJECT ON TAPE

B. EQUIPMENT/SUBSYSTEM CAPABILITIES

Ⓐ TBD

C. SOFTWARE CAPABILITIES

Ⓐ TBD



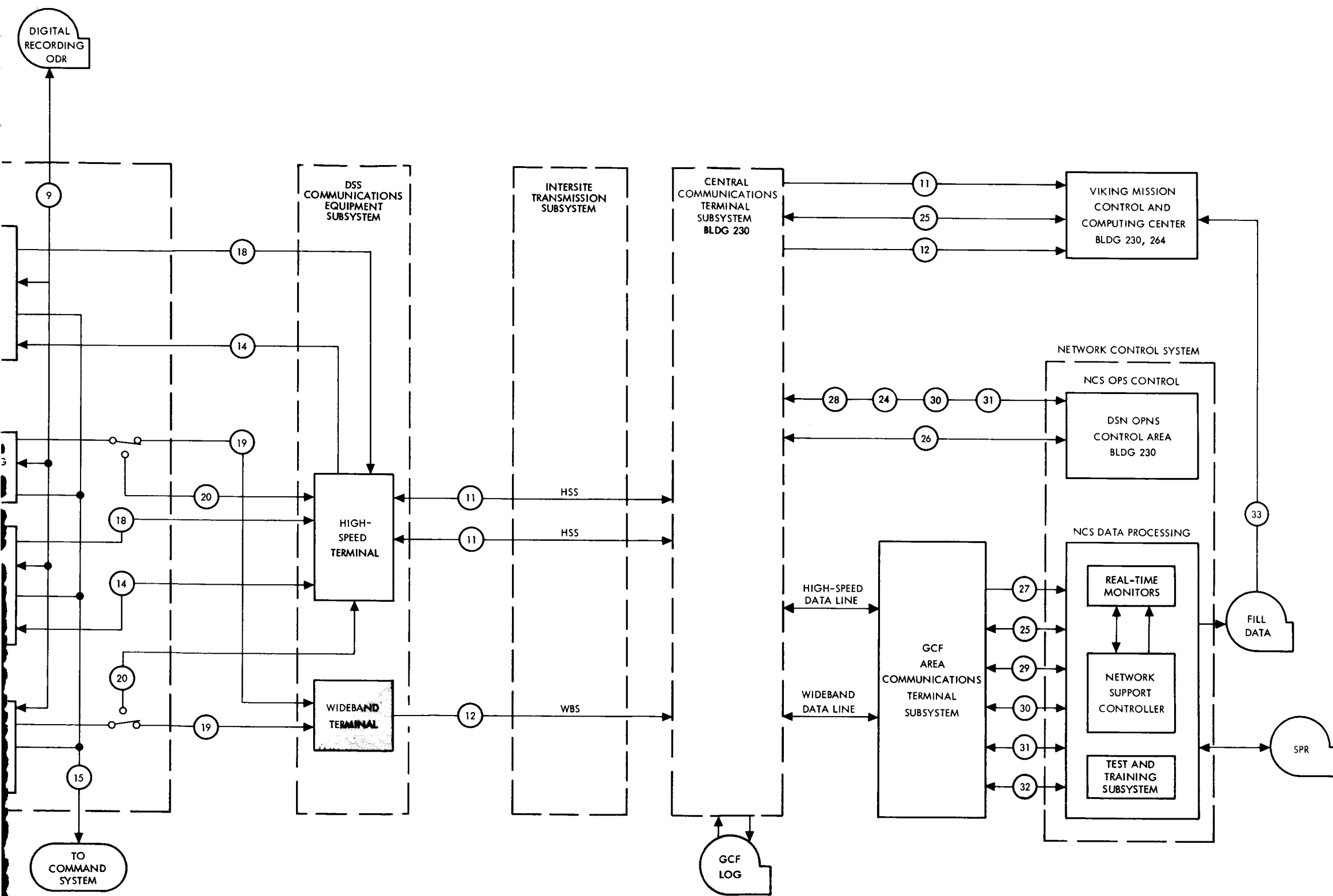


Fig 1. DSN/Viking telemetry system baseline functional requirements block diagram

2

Pioneer Venus Mission Support

A. J. Siegmeth
Mission Support Office

A summary of the history of the Pioneer Venus missions is presented. The characteristics of the 1976/77 probe missions are given. The Pioneer Project investigates a preliminary plan to develop a cooperative agreement on the Venus Orbiter mission with the European Space Research Organization.

A brief history of the Pioneer Venus project is given in Fig. 1. (See also Refs. 1-9). As reported previously, prior to 1972, Goddard Space Flight Center was involved in the study of missions, called Planetary Explorers, which would probe the Venusian atmosphere. The initial study began during the first quarter of 1968. The Phase A study was completed during the beginning of 1971. During the latter part of the same year the program was transferred to Ames Research Center and is now called Pioneer Venus. After the selection of contractors for a Phase B study for the duration of nine months, the execution phase of Pioneer Venus will start during the second quarter of 1973.

Four Pioneer Venus missions are on the planning board. Two probe missions will be launched, in December 1976 and January 1977. The universal bus of this mission will weigh 150 kg, the large landing probe 170 kg, and the

three small probes a total of 70 kg, thus comprising a total spacecraft weight of 390 kg. The flight time will be 325 days, and the probes will be separated 10 to 20 days before entering the Venusian atmosphere. The bus will also enter the Venusian atmosphere at a shallow entry angle and will transmit data until burn. The bus science package will weigh 10 kg, and the telemetry bit rate is estimated at 300 bps. The large probe will have a descent time of 90 min, the small probe a descent time of 60 min. The expected bit rate of the large probe will be 80 bps up to 52 km altitude. The 40-bps rate will be used from 52 km until at the surface of the planet. The small probes will have a bit rate of 1 bps.

The Pioneer orbiter mission will be flown during 1978 and a follow-on probe mission, which is the fourth of this series, will be flying towards Venus in 1980.

The European Space Research Organization (ESRO) is also involved in a study of a Venus orbiter mission. Recommendations were made for NASA/ESRO cooperation. ESRO is currently involved in a preliminary feasibility study of a 1978 Venus orbiter. A request for a proposal on this study was coordinated with Ames Re-

search Center. The study of a preliminary plan on the NASA/ESRO interface with the Pioneer Project has started. This plan assumes that ESRO would be responsible for integration of the experiments into a NASA-furnished bus. NASA would support the launch, mission operations, and tracking and data acquisition.

References

1. Siegmeth, A. J., "Pioneer Mission Support," in *The Deep Space Network Progress Report*, Technical Report 32-1526, Vol. II, pp. 6-17. Jet Propulsion Laboratory, Pasadena, Calif., Apr. 15, 1971.
2. Siegmeth, A. J., "Pioneer Mission Support," in *The Deep Space Network Progress Report*, Technical Report 32-1526, Vol. III, pp. 7-19. Jet Propulsion Laboratory, Pasadena, Calif., June 15, 1971.
3. Siegmeth, A. J., "Pioneer Mission Support," in *The Deep Space Network Progress Report*, Technical Report 32-1526, Vol. IV, pp. 13-21. Jet Propulsion Laboratory, Pasadena, Calif., Aug. 15, 1971.
4. Siegmeth, A. J., "Pioneer Mission Support," in *The Deep Space Network Progress Report*, Technical Report 32-1526, Vol. V, pp. 4-16. Jet Propulsion Laboratory, Pasadena, Calif., Oct. 15, 1971.
5. Siegmeth, A. J., "Pioneer Mission Support," in *The Deep Space Network Progress Report*, Technical Report 32-1526, Vol. VI, pp. 13-24. Jet Propulsion Laboratory, Pasadena, Calif., Dec. 15, 1971.
6. Siegmeth, A. J., "Pioneer Mission Support," in *The Deep Space Network Progress Report*, Technical Report 32-1526, Vol. VII, pp. 5-16. Jet Propulsion Laboratory, Pasadena, Calif., Feb. 15, 1972.
7. Siegmeth, A. J., "Pioneer Mission Support," in *The Deep Space Network Progress Report*, Technical Report 32-1526, Vol. VIII, pp. 8-19. Jet Propulsion Laboratory, Pasadena, Calif., Apr. 15, 1972.
8. Siegmeth, A. J., "Pioneer Mission Support," in *The Deep Space Network Progress Report*, Technical Report 32-1526, Vol. IX, pp. 18-32. Jet Propulsion Laboratory, Pasadena, Calif., June 15, 1972.
9. Siegmeth, A. J., "Pioneer 6-9 Mission Support," in *The Deep Space Network Progress Report*, Technical Report 32-1526, Vol. X, pp. 10-13. Jet Propulsion Laboratory, Pasadena, Calif., Aug. 15, 1972.

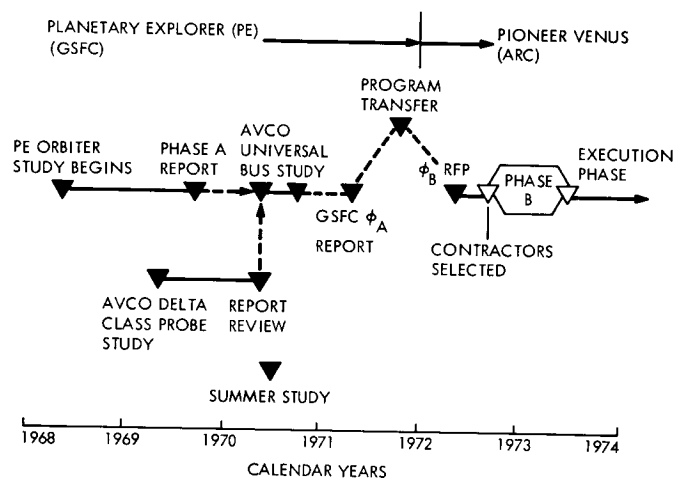


Fig. 1. History of Pioneer Venus

Radio Science Support

K. W. Linnes
Mission Support Office

Since 1967, radio scientists have used the Deep Space Network 26- and 64-m antenna stations to investigate pulsars, to study the effect of solar corona on radio signals, and to observe radio emissions from X-ray sources. More recently, very-long-baseline interferometry (VLBI) techniques have been used for high-resolution studies of quasars. During the reporting period, VLBI observations were made of quasars and pulsars. Support was also provided by the 64-m antenna for the measurement of cosmic background noise and weak radio sources to search for interstellar molecules and to observe radiation from Jupiter.

I. Introduction

The 26- and 64-m antenna stations of the DSN have been used for several years to support radio science experiments. NASA, JPL, and university scientists have used key DSN facilities whose particular and unique capabilities were required for the performance of the experiments. In order to formalize the method of selecting experiments and experimenters, a Radio Astronomy Experiment Selection (RAES) Panel was formed in 1969. Notice of availability of these facilities was placed in professional journals to inform the scientific community that they were available for limited use by qualified radio scientists (Ref. 1). No charge is made for use of the standard DSN facilities and equipment; special equipment, however, must be provided by the experimenters. A summary of all experiments conducted through June 1972 is reported in Refs. 2 through 7.

II. Radio Science Operations

In July and August, radio astronomy observations conducted under the auspices of the RAES Panel used approximately 97 hours on the 64-m-diameter antenna at Goldstone (DSS 14). The experiments supported are shown in Table 1. Most of the time was devoted to three 24-h observations of quasars and galaxies, under what is called, for convenience, the "quasar patrol." As described in Ref. 7, the purpose of this activity is to conduct a regularly scheduled set of observations for the purpose of detecting changes in structure and flux output of quasars and galaxies as well as searching for new sources. The proposal was formally approved by the RAES Panel during this reporting period. The various teams of investigators are shown in Table 2. It is the practice to schedule one such 24-h observation each month on a day that does not interfere with critical spacecraft activities and which

is also compatible with the schedule of the MIT Haystack 37-m antenna and/or the 42-m antenna of the National Radio Astronomy Observatory (NRAO). A second day was scheduled in late August in lieu of one in September. Mariner 9, orbiting Mars, will be at opposition in September, and the need is to track the spacecraft in support of a relativity experiment.

The other radio astronomy experiments in Table 1 were supported with several 8-h observations and are now completed.

As shown in Table 1, support was given to Radio Science programs sponsored by the Office of Space Science (OSS) as well as to radio science-related support of flight project requirements. The planetary radio astronomy observations of Jupiter and Uranus made use of the DSN-developed K-band (14 GHz) equipment. This equipment, consisting of antenna feed, microwave components, maser, and receiver, and also the noise-adding radiometer, is also used for searching for interstellar microwave lines.

The program on Earth dynamics sponsored by the Office of Applications (OA) was supported with a short baseline interferometry observation at Goldstone. A baseline between the 64-m antenna at the Mars site and the 26-m antenna at the Echo site was used to check out newly acquired NRAO Mark II very long baseline interferometry (VLBI) digital recording terminals.

Two observations were made that are radio science-related DSN developments. They were undertaken as part of the weak signal detection task. One was the attempt to detect the Jupiter satellite Callisto. The other was the attempt to detect the asteroid Toro. Data from these observations are being processed and analyzed.

III. Radio Astronomy Experiment Selection Panel Activities

The RAES Panel disapproved one proposal in the July-August period and approved the "quasar patrol" (see Table 2).

References

1. *Bulletin of the American Astronomical Society*, Vol. 2, No. 1, p. 177, 1970.
2. Linnes, K. W., Sato, T., and Spitzmesser, D., "Radio Science Support," in *The Deep Space Network Progress Report*, Technical Report 32-1526, Vol. III, pp. 46-51. Jet Propulsion Laboratory, Pasadena, Calif., June 15, 1971.
3. Linnes, K. W., "Radio Science Support," in *The Deep Space Network Progress Report*, Technical Report 32-1526, Vol. V, pp. 42-44. Jet Propulsion Laboratory, Pasadena, Calif., Oct. 15, 1971.
4. Linnes, K. W., "Radio Science Support," in *The Deep Space Network Progress Report*, Technical Report 32-1526, Vol. VI, pp. 43-45. Jet Propulsion Laboratory, Pasadena, Calif., Dec. 15, 1971.
5. Linnes, K. W., "Radio Science Support," in *The Deep Space Network Progress Report*, Technical Report 32-1526, Vol. VII, pp. 29-31. Jet Propulsion Laboratory, Pasadena, Calif., Feb. 15, 1972.
6. Linnes, K. W., "Radio Science Support," in *The Deep Space Network Progress Report*, Technical Report 32-1526, Vol. VIII, pp. 24-28. Jet Propulsion Laboratory, Pasadena, Calif., Apr. 15, 1972.
7. Linnes, K. W., "Radio Science Support," in *The Deep Space Network Progress Report*, Technical Report 32-1526, Vol. X, pp. 52-58. Jet Propulsion Laboratory, Pasadena, Calif., Aug. 15, 1972.

Table 1. Radio science experiments involving 64- and 26-m-diameter antenna facilities

Experiment	Purpose	Experimenter	DSN facility	Date
RAES Panel experiments				
Small-scale variations in cosmic background radiation	To search for small-scale spatial variations in the 2.7 K cosmic background radiation of 3.5 cm	R. Carpenter (Calif. State College of Los Angeles) S. Gulkis (JPL) T. Sato (JPL)	DSS 14	Jan. 10, 11, 1972 Feb. 11, 12, 22, 1972 Mar. 14, 25, 1972 May 8, 28, 1972 July 14, 1972
Weak radio source observations	To measure the "confusion distribution" of weak radio sources at 2.3 GHz	D. L. Jauncey (Cornell University) M. J. Yerbury (Cornell University) J. J. Condon (Cornell University) D. J. Spitzmesser (JPL)	DSS 14	June 5, 12, 1972 July 5, 13, 1972
Quasar structure by X-band VLBI "quasar patrol"	To monitor time variations and fine structure and apparent position of quasars	T. Clark (GSFC) R. Goldstein (JPL) H. Hinteregger (MIT) C. Knight (MIT) G. Marandino (University of Maryland) A. Rogers (MIT Haystack Observatory) I. Shapiro (MIT) D. J. Spitzmesser (JPL) A. Whitney (MIT)	DSS 14 (and MIT Haystack antenna)	June 9, 19, 1971 Sept. 19, 1971 Oct. 2-4, 10, 17, 1971 Jan. 4, 1972 Feb. 18, 1972 Mar. 10, 1972 May 9, 1972 July 3, 1972 Aug. 29, 1972
X-band VLBI "quasar patrol"	To study the structure of extra galactic sources with improved resolution	J. Broderick (NRAO) B. Clark (NRAO) K. Kellermann (NRAO) D. Jauncey (Cornell University) M. Cohen (Caltech) D. Shaffer (Caltech)	DSS 14 (64-m antenna at Goldstone) (and MIT Haystack antenna)	Feb. 1971 Nov. 2, 1971 Feb. 5, 1972 Mar. 4, 1972 Apr. 24, 1972 May 20, 1972 June 6, 1972 Aug. 8, 1972
OSS Experiments				
Interstellar microwave low-noise spectroscopy	To search for interstellar molecules at 14 GHz	S. Gulkis (JPL) T. Sato (JPL) B. Zuckerman (Univ. of Maryland) D. Cesarsky (Caltech) J. Greenstein (Caltech)	DSS 14	Apr. 2, 10, 18, 1972 May 2, 6, 14, 17, 1972 June 4, 19, 1972 Aug. 5, 1972
Planetary radio astronomy	To study radio emissions of Uranus and Jupiter at 14 GHz	S. Gulkis (JPL) B. Gary (JPL) M. Klein (JPL) M. Jansen (JPL Resident Research Associate) E. Olsen (JPL Resident Research Associate) P. Rosenkranz (JPL Resident Research Associate)	DSS 14	Apr. 29, 30, 1972 July 14, 1972 Aug. 3, 1972

Table 1 (contd)

Experiment	Purpose	Experimenter	DSN facility	Date
OA Experiment				
Earth dynamics VLBI	To demonstrate the NRAO Mark II digital recording terminal by measuring the baseline between DSS 14 and 12 at Goldstone	P. MacDoran (JPL) J. Fanelow (JPL) J. Thomas (JPL) J. Williams (JPL)	DSS 14 DSS 12	Aug. 15, 1972

Table 2. Recently approved radio astronomy experiments

Title	Purpose	Experimenters	Facilities required
"Quasar patrol"	To make detailed measurements on radio galaxies and quasars at 2.3, 7.8, and 15.6 GHz; to search for weak compact sources in the nuclei of extended radio galaxies and quasars; to monitor time variations in fine structure and apparent positions of quasars	<p>Group A</p> <p>D. S. Robertson, WRE A. J. Legg, WRE J. Gubbay, WRE A. T. Moffet, Caltech G. Nicholson, CSIR</p> <p>Group B</p> <p>J. J. Broderick, NAIC B. G. Clark, NRAO M. H. Cohen, Caltech D. L. Jauncey, Cornell K. I. Kellermann, NRAO G. H. Purcell, Caltech D. B. Shaffer, Caltech</p> <p>Group C</p> <p>T. A. Clark, GSFC R. M. Goldstein, JPL H. F. Hinteregger, MIT C. A. Knight, MIT G. E. Marandino, Univ. of Maryland G. Resch, Univ. of Maryland A. E. Rogers, Haystack Observatory I. I. Shapiro, MIT A. R. Whitney, MIT</p>	<p>64-m antenna at Goldstone (working with the MIT Haystack antenna and/or the NRAO 42-m antenna)</p> <p>26-m antenna in Australia</p>

A Comparison of Cowell's Method and a Variation-of-Parameters Method for the Computation of Precision Satellite Orbits: Phase Three Results

S. S. Dallas

Navigation and Mission Design Section

E. A. Rinderle

Flight Applications Programming Section

Additional test cases were run using a precision special perturbations program employing either Cowell's method or a variation-of-parameters method to compute a nearly circular, nearly equatorial orbit using two different perturbative accelerations. The results obtained again indicate that the variation-of-parameters method with a predict-only integrator and Cowell's method with a predict-partial-correct integrator are equally efficient, and both are significantly more efficient than Cowell's method with a predict-correct integrator.

I. Introduction

The primary objective of the second phase of this study was to determine an accurate measure of the improvement to be expected from using the variation-of-parameters method in place of Cowell's method when computing precision satellite orbits. Reference 1 shows that, in the case of the Mariner Mars 1971 Mission A orbit as described in Ref. 2,

- (1) The variation-of-parameters method integrating six parameters is not significantly more efficient than

Cowell's method with a predict-partial-correct integrator;

- (2) The variation-of-parameters method integrating six parameters and Cowell's method with a predict-partial-correct integrator are both significantly more efficient than Cowell's method with a predict-correct integrator. The Central Processing Unit (CPU) times are approximately 20% less, and the total costs are approximately 8% less. These percentages will be even larger for perturbative func-

tions which are more complex than the one used in this study.

The objective of this third and final phase of investigation is to compare the variation-of-parameters method with Cowell's method in the case of a nearly circular, equatorial orbit (an osculating eccentricity and inclination of 0 at t_0). The previous comparisons were made in the case of the eccentric Mariner Mars 1971 Mission A orbit (an osculating eccentricity and inclination at t_0 of approximately 0.633 and 80 deg, respectively). The initial state vector for this phase of study is

$$\begin{aligned} \mathbf{q}^T &= (a, e, i, \omega, \Omega, T) \\ &= (4643 \text{ km}, 0, 0 \text{ deg}, 328.3937 \text{ deg}, 38.3701 \text{ deg}, \\ &\quad 11/19/71 \text{ } 14^{\text{h}}42^{\text{m}} \text{ UTC}) \end{aligned} \quad (1)$$

In addition, two perturbative accelerations are used. The first perturbative acceleration $\dot{\mathbf{r}}_{J_2+NB+SP}$ is the same as the one used previously and includes the effects of the asphericity of the central body (J_2 only), N bodies other than the central body, and solar radiation pressure. The second perturbative acceleration $\dot{\mathbf{r}}_{J_2}$ contains only the effect of the asphericity of the central body (J_2 only).

II. Discussion

In this final phase of investigation, three of the four processes of orbit prediction compared in phase two of the study (Ref. 1) are compared for the case of a nearly circular orbit that lies nearly in the equatorial plane of Mars. The first process is the variation-of-parameters method with a predict-only, sixth-order, variable-step (ERMN/ERMN $\approx r_a/r$) integrator.¹ In this process the six parameters a_z , a_y , h_x , h_y , h_z , and L are integrated. The parameters a_z and n are determined from the integrated values of a_x , a_y , h_x , h_y , and h_z through the equations (see Ref. 3)

$$a_z = -\frac{1}{h_z} (a_x h_x + a_y h_y) \text{ and } n = \sqrt{\mu \left(\frac{1 - \mathbf{a} \cdot \mathbf{a}}{\mathbf{h} \cdot \mathbf{h}} \right)^{3/2}} \quad (2)$$

(Note that the parameter a_z is well determined since $h_z \gg 0$ in the case of $i \simeq 0$). The second process is Cowell's method with a predict-correct, tenth-order, variable-step (constant ERMN and ERMN) integrator.

The third process is Cowell's method with a predict-partial-correct, tenth-order, variable-step (constant ERMN and ERMN) integrator.

As in phase two, each of the three processes of orbit prediction was used to generate trajectory data in such a way that no calibration factors were necessary. In addition, the cost and accuracy criteria used are the same as those used in phase two (see Ref. 1).

Sixteen cases were run in this phase. Each case used the same initial state vector (Eq. 1) and one of the three processes of orbit prediction described above. Nine cases used the perturbative acceleration $\dot{\mathbf{r}}_{J_2+NB+SP}$ and seven cases used the perturbative acceleration $\dot{\mathbf{r}}_{J_2}$. The standard of comparison for each of the two sets was obtained using process two (Cowell predict-correct) with a very tight local error control (see Section 6.1 in Ref. 2). In the first set ($\dot{\mathbf{r}}_{J_2+NB+SP}$), three cases were run using each of the three processes (one case is the standard of comparison). The three cases differed only in the proportionality constants used in the local error control. In the second set ($\dot{\mathbf{r}}_{J_2}$), two cases were run using process one, three cases (one of which is the standard of comparison) were run using process two, and two cases were run using process three.

III. Results and Conclusions

These cases show that the two orbits differ significantly from each other and from the orbit integrated in phases one and two. The nearly circular, equatorial orbit using $\dot{\mathbf{r}}_{J_2}$ differs from the elliptical Mariner orbit primarily in size and shape (and therefore in size of integration step). The nearly circular equatorial orbit using $\dot{\mathbf{r}}_{J_2+NB+SP}$ differs from the elliptical Mariner orbit not only in size and shape but in the effect of solar radiation pressure. In the former, the solar radiation pressure plays a dominant role in the stepping procedure by requiring a restart each time the spacecraft passes in and out of the shadow of Mars (every revolution). In the latter, the spacecraft did not enter the shadow. The two nearly circular, equatorial orbits differ from each other in the complexity of the perturbative acceleration (and consequently in the cost of the derivative evaluations) as well as in the presence or absence of restarts due to solar radiation pressure.

Table 1 presents the cost and accuracy data for all three processes of orbit prediction using the perturbative

¹ERMN/ERMN = error maximum/error minimum.

acceleration $\dot{\mathbf{r}}_{J_2+NB+SP}$ in the nearly circular, equatorial orbit. Table 2 presents similar data for the perturbative acceleration $\dot{\mathbf{r}}_{J_2}$.

In comparing the accuracy of the variation-of-parameters cases and the Cowell cases, the single time-point comparisons used in phases 1 and 2 are inconsistent (a tighter ERMX does not necessarily yield more accuracy) and must be replaced by comparisons of the error propagation curves given in Figs. 1-4. This inconsistency appears to be due to the insensitivity of the local error control when the orbit is nearly circular. For example, the two cases run using Cowell's method with a predict-correct integrator yield the same accuracy for values of ERMX quite different (see Table 2).

The cases in Table 2 are essentially fixed-step integrations, since they begin with a step size of 30 seconds, immediately double until the local error approaches ERMX, and then continue at that step size. Unfortunately, the final step sizes in the Cowell cases do not appear to be optimally determined, since a tighter ERMX does not necessarily yield more accuracy.

Figures 1-4 exhibit the more systematic error growth in the case of the variation-of-parameters (consistent with phases 1 and 2). In addition, these figures show that the errors for all these cases are roughly the same during the first 20 revolutions. It appears that these cases need to be run for more than 20 revolutions or with a more sensitive local error control in order to show large error differences.

Based upon these tables and figures and the results of phases one and two (see Refs. 1 and 2), the following primary conclusions are made:

- (1) The variation-of-parameters method is not significantly more efficient than Cowell's method with a predict-partial-correct integrator regardless of the type of orbit or complexity of the perturbative acceleration.
- (2) The variation-of-parameters method with a predict-only integrator and Cowell's method with a predict-partial-correct integrator are both significantly more efficient than Cowell's method with a predict-correct integrator regardless of the type of orbit or complexity of the perturbative acceleration. The CPU times are approximately 20%, 17%, and 16% less, respectively, in the case of the elliptical orbit perturbed by $\dot{\mathbf{r}}_{J_2+NB+SP}$, and the nearly circular orbit

perturbed by $\dot{\mathbf{r}}_{J_2+NB+SP}$, and the nearly circular orbit perturbed by $\dot{\mathbf{r}}_{J_2}$. In addition, the total costs are approximately 8%, 12%, and 6% less, respectively. A comparison of these percentages for the cases of the nearly circular orbit shows that an increase in the complexity of the perturbative acceleration results in increases in these percentages. Consequently, these percentages will be even larger for perturbative accelerations that are more complex than the ones used in this study.

- (3) The variation-of-parameters method should not be incorporated into the standard production and mission operations versions of DPTRAJ, since the equally efficient Cowell's method with a predict-partial-correct integrator already exists as an option in these versions. However, the variation-of-parameters method should be maintained in the research version of DPTRAJ so that future studies can be conducted as new cost saving ideas arise and as funds and manpower become available.

In addition to these primary conclusions, the following secondary conclusions based on the data in phase three are made:

- (1) The present local error control based upon ERMX and ERMN is insensitive in the case of a nearly circular orbit. In this case, a fixed-step integrator should be used with a specialized algorithm for choosing the optimum step size.
- (2) Only the perturbative effects consistent with the desired accuracy should be used during an integration. For example, suppose an accuracy is desired of order J_2 in 20 revolutions of a nearly circular orbit. It would cost half as much and be four times as fast to integrate using $\dot{\mathbf{r}}_{J_2}$ instead of $\dot{\mathbf{r}}_{J_2+NB+SP}$ (see Tables 1 and 2).
- (3) The variation-of-parameters method as formulated in Ref. 3 can compute satellite orbits having eccentricities and inclinations near or equal to zero as efficiently as Cowell's method.

IV. Summary of Complete Study

Test cases run using a precision special perturbations program employing either Cowell's method or a variation-of-parameters method to compute an elliptical orbit for two widely different eccentricities and inclinations were analyzed to determine which method is more efficient.

The results obtained indicate that the variation-of-parameters method with a predict-only integrator and Cowell's method with a predict-partial-correct integrator are equally efficient, and both are significantly more efficient than Cowell's method with a predict-correct inte-

grator. Either of the former more efficient methods for computing precision satellite orbits offers the potential for reducing the total cost of computations during orbit design and computer execution time during real-time mission operations for future orbiter projects.

References

1. Dallas, S. S., and Rinderle, E. A., "A Comparison of Cowell's Method and a Variation-of-Parameters Method for the Computation of Precision Satellite Orbits: Addendum 1," in *The Deep Space Network Progress Report*, Technical Report 32-1526, Volume VII, pp. 32-36. Jet Propulsion Laboratory, Pasadena, Calif., Feb. 15, 1972.
2. Dallas, S. S., and Rinderle, E. A., "A Comparison of Cowell's Method and a Variation-of-Parameters Methods for the Computation of Precision Satellite Orbits," Section Technical Memorandum 392-66, Sept. 30, 1971 (JPL internal document).
3. Dallas, S. S., and Rinderle, E. A., "A Special Perturbations Theory Using the Variation-of-Parameters Formulation," Section Technical Memorandum 392-31, Apr. 1, 1970 (JPL internal document).

Table 1. Cost versus accuracy using $\hat{r}_{J_2+NB+SP}^\lambda$

Method	Local error control		Accuracy ^a		CPU time, s	Cost		Through-put time, s
	ERMx	ERMN	$ \Delta \mathbf{r} , \text{m}$	$ \Delta \dot{\mathbf{r}} , \text{m/s}$		Core time product, kiloword/h	Total cost, dollars	
1. Cowell predict-correct	10^{-11}	10^{-16}	0.149 0.082	0.00010 0.00005	247	7.50	81.43	514
2. Cowell predict-correct	10^{-9}	10^{-14}	0.465 0.379	0.00029 0.00026	187	6.24	67.47	445
3. Cowell predict-partial-correct	10^{-11}	10^{-16}	0.261 0.220	0.00018 0.00014	202	6.58	71.20	482
4. Cowell predict-partial-correct	10^{-10}	10^{-15}	1.67 1.75	0.00108 0.00116	176	6.00	64.81	451
5. Cowell predict-partial-correct	10^{-9}	10^{-14}	0.512 0.427	0.00032 0.00030	157	5.58	60.12	433
6. Variation-of-parameters, predict-only	$10^{-9} (r_a/r)$	$10^{-13} (r_a/r)$	2.203 2.276	0.00143 0.00151	188	6.29	68.15	465
7. Variation-of-parameters, predict-only	$5 \times 10^{-9} (r_a/r)$	$5 \times 10^{-13} (r_a/r)$	2.867 3.049	0.00187 0.00202	177	6.03	65.31	454
8. Variation-of-parameters, predict-only	$5/2 \times 10^{-8} (r_a/r)$	$5/2 \times 10^{-12} (r_a/r)$	0.766 0.802	0.00051 0.00052	155	5.42	59.00	437

^aThese errors occur in revolution 20 at $t - t_0 = 50 \text{ h } 40 \text{ min}$ and 52 h , respectively (period of orbit $\approx 2 \text{ h } 40 \text{ min}$)

Table 2. Cost versus accuracy using $\hat{r}_{J_2}^\lambda$

Method	Local error control		Accuracy ^a		CPU time, s	Cost		Through-put time, s
	ERMx	ERMN	$ \Delta \mathbf{r} , \text{mm}$	$ \Delta \dot{\mathbf{r}} , \text{mm/s}$		Core time product, kiloword/h	Total cost, dollars	
1. Cowell predict-correct	10^{-11}	10^{-16}	5.864 4.302	0.0036 0.0031	62	3.67	35.77	337
2. Cowell predict-correct	10^{-9}	10^{-14}	5.864 4.302	0.0036 0.0031	63	3.79	36.70	363
3. Cowell predict-partial-correct	10^{-11}	10^{-16}	5.983 4.569	0.0037 0.0032	52	3.47	33.47	304
4. Cowell predict-partial-correct	10^{-9}	10^{-14}	5.983 4.569	0.0037 0.0032	52	3.61	34.42	328
5. Variation-of-parameters, predict-only	$10^{-9} (r_a/r)$	$10^{-13} (r_a/r)$	0.874 0.328	0.0005 0.0002	60	3.19	32.21	316
6. Variation-of-parameters, predict-only	$5/2 \times 10^{-8} (r_a/r)$	$5/2 \times 10^{-12} (r_a/r)$	61.010 40.500	0.0651 0.0597	44	2.83	28.25	300

^aThese errors occur in revolution 20 at $t - t_0 = 50 \text{ h } 40 \text{ min}$ and 52 h , respectively (period of orbit $\approx 2 \text{ h } 40 \text{ min}$).

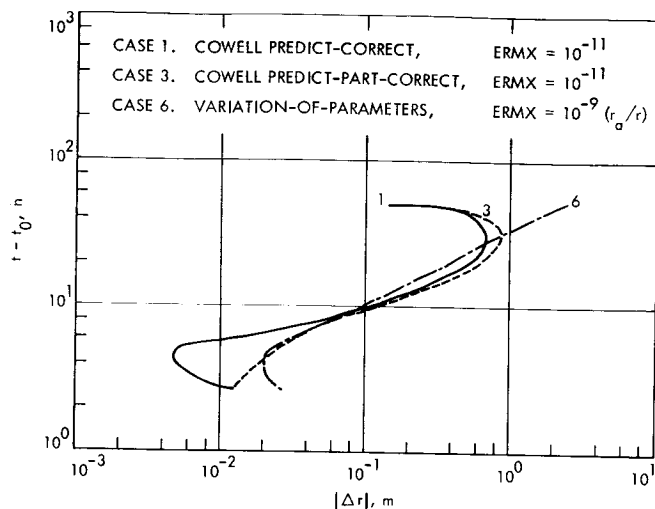


Fig. 1. Error propagation in the variation-of-parameters method and Cowell's method, cases 1, 3, and 6

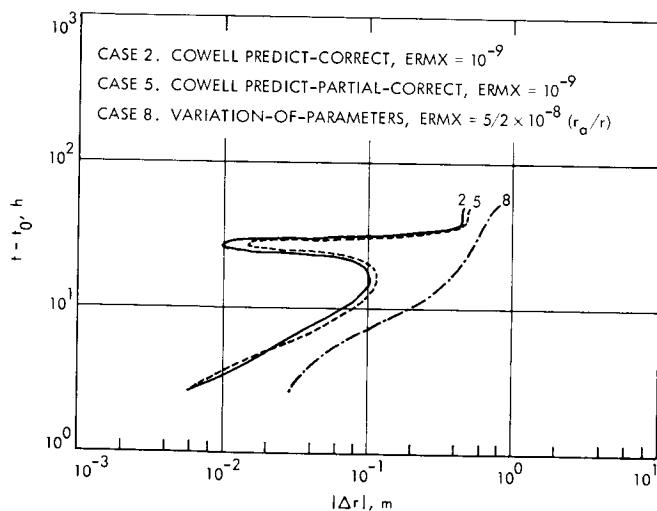


Fig. 2. Error propagation in the variation-of-parameters method and Cowell's method, cases 2, 5, and 8

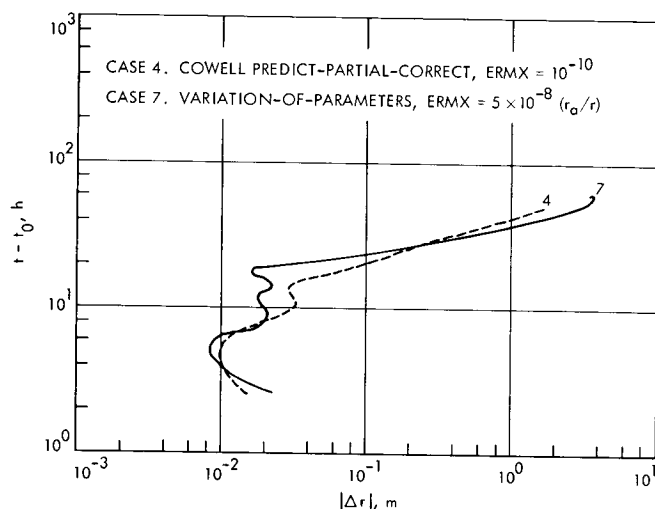


Fig. 3. Error propagation in the variation-of-parameters method and Cowell's method, cases 4 and 7

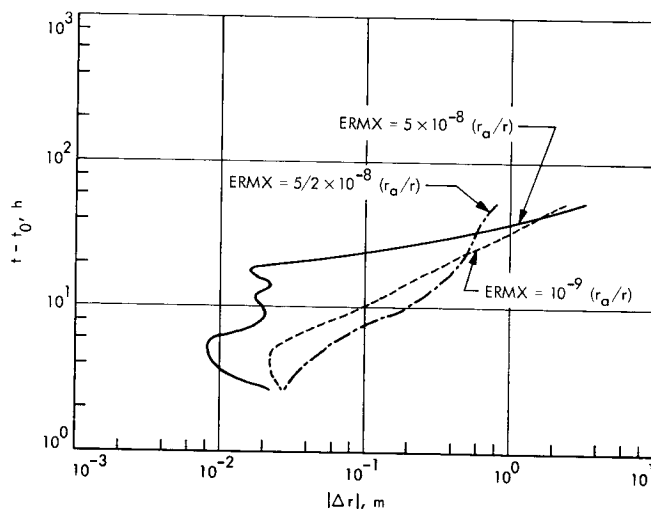


Fig. 4. Error propagation in the variation-of-parameters method

Use of Doppler Determinations of Polar Motion Using Artificial Satellites to Support JPL Planetary Missions

H. F. Fliegel

Tracking and Orbit Determination Section

Standard deviations and systematic differences are calculated between the U. S. Navy Weapons Laboratory (USNWL) determination of the X and Y coordinates of the pole, using artificial satellites, and the smoothed 5-day means published by the Bureau International de l'Heure (BIH). The results indicate slowly varying errors of about 1 meter in the conventionally obtained optical data of BIH, now used by JPL. Although current values of polar coordinates should be based upon the BIH Rapid Service, values for previous months might be improved with the help of USNWL doppler data.

An important factor in attaining the navigational accuracy realized in JPL deep space missions is precise knowledge of polar motion. To obtain such information during the Mariner Mars 1971 mission, JPL sponsored a contract with the Bureau International de l'Heure (BIH) to form a rapid time and polar motion service (Ref. 1). C. C. Chao and the author have considered the importance of using the U. S. Naval Weapons Laboratory (USNWL) polar motion values, obtained from doppler tracking data on navigational satellites, to check the results which are obtained by BIH using conventional astronomical means (Ref. 2). Here the biases and standard deviations of recent USNWL data are given with respect to BIH, thus updating the tables of Ref. 2.

The differences between the USNWL 5-day mean values of the X and Y coordinates of the pole and the BIH smoothed values interpolated to the same date are graphed in Figs. 1 and 2. The standard deviations and the mean values of these differences, calculated year by year from the inception of the USNWL service, are given in Tables 1 and 2. Notice that the values given here differ slightly from those given in Ref. 2. This is because in Ref. 2 we measured USNWL against unsmoothed BIH 5-day means and combined the results with other data to infer the standard deviations of USNWL and of BIH separately, whereas here are presented only the differences between USNWL and BIH smooth data. The BIH smoothed 5-day values are really

more than averages; they are values from a highly smoothed function read off and published by BIH at 5-day intervals. Calculations were made by interpolating normal points formed first from sets of 2, then in subsequent computer runs from sets of 3 and from sets of 4 BIH 5-day values. They never differed significantly from calculations made by interpolating the 5-day values directly. On the other hand, combining USNWL data into normal points reduces the noise level in the manner shown by Table 1 and Fig. 3. Table 1 indicates that the standard deviations in Y (the axis through the U.S.) are larger than those on X (through Europe) in 1970 and 1971, which may reflect the deployment and relative accuracy of the naval tracking stations. However, these differences are no doubt smaller than the uncertainties of the standard deviations.

Figure 3 illustrates how the random error of the doppler data decreases with the number of days of doppler data combined to form normal points. The curve is much flatter than that appropriate to a Gaussian distribution, indicating a fair amount of nonwhite, time-correlated noise.

The values of Table 2 represent the average biases between BIH and doppler results; and these biases, unlike the standard deviations, cannot be ascribed entirely to the doppler data. In Figs. 1 and 2 are shown both the International Polar Motion Service (IPMS) and the USNWL doppler values for X and Y, minus the BIH values. Thus, the X axes in Figs. 1 and 2 would indicate zero difference from BIH. There is evidently strong correlation of the IPMS data with the doppler data against BIH, especially in Y during 1970-1971. This correlation indicates that the slowly varying errors which produce the biases of Table 2 are produced largely by systematic effects in the BIH data or reduction procedure.

Nevertheless, BIH Rapid Service data are still the source of polar motion information best suited to JPL mission support, since BIH data are virtually free of the very large random residuals which occur in the doppler results. In real-time mission support, one typically encounters either of two situations:

- (1) A maneuver or some incident occurs only a few days before planetary encounter, as with Mariner 7. The orbit determination on which the success of

the mission depends is based upon the short arc of tracking data obtained after the maneuver or incident. The accuracy of this determination depends on the exactness with which polar motion is known during that short interval. Large random errors are more serious than slowly varying errors of 1 meter or less. In this crucial situation, the BIH Rapid Service supplies our need.

- (2) No maneuver or incident interrupts a long arc of tracking data, upon which the orbit determination may confidently be based, as with Mariner 9. Exact polar motion information is not so essential as in the former situation, because the characteristics of the orbit of the spacecraft around the Sun provide more information concerning its position than does the doppler signature produced by the rotation of the Earth. Nevertheless, determination of station locations are made more accurately if long-term errors in polar motion are minimized, and to this end the USNWL doppler data may be useful.

For future JPL missions such as MVM 73 and Viking, a mixed data set may be best, in which current values for polar position are based upon the BIH Rapid Service, and values for previous months are estimated with the help of USNWL doppler data. In future articles, we will discuss the best attainable models for polar motion, its physical characteristics, and optimal strategy for future missions.

The following conclusions have been drawn:

- (1) The standard deviations of USNWL doppler determinations of the X and Y coordinates of polar position have held more or less constant during 1969.0-1972.0, at about 1 meter.
- (2) The biases between USNWL and BIH are also at about the 1-meter level.
- (3) The strong correlation between USNWL and IPMS against BIH indicates a slowly varying error in BIH data.
- (4) Nevertheless, the BIH Rapid Service is still best suited to JPL needs. Both BIH and USNWL data should be used in support of future planetary missions.

References

1. Fliegel, H. F., "A Worldwide Organization to Secure Earth-Related Parameters for Deep Space Missions," in *The Deep Space Network Progress Report*, Technical Report 32-1526, Vol. V, pp. 66-73. Jet Propulsion Laboratory, Pasadena, Calif., Oct. 15, 1971.
2. Chao, C. C., and Fliegel, H. F., "Polar Motion: Doppler Determinations Using Satellites Compared to Optical Results," in *The Deep Space Network*, Space Programs Summary 37-66, Vol. II, pp. 23-28. Jet Propulsion Laboratory, Pasadena, Calif., Nov. 30, 1970.

Table 1. Standard deviations of USNWL data from smoothed 5-day means of BIH (meters)

Year	5-day means		10-day means		15-day means		20-day means	
	Coordinate							
	X	Y	X	Y	X	Y	X	Y
1968	1.575	1.390	1.448	1.045	1.409	0.974	1.369	0.882
1969	0.961	0.927	0.767	0.808	0.735	0.755	0.709	0.688
1970	0.960	1.006	0.871	0.934	0.844	0.881	0.823	0.823
1971	0.864	0.945	0.710	0.788	0.642	0.720	0.614	0.682

Table 2. Mean yearly differences (USNWL - BIH) (meters)

Year	Coordinate	
	X	Y
1968	+1.515	-1.911
1969	+1.037	-1.704
1970	-0.370	+0.000
1971	-0.290	-0.806

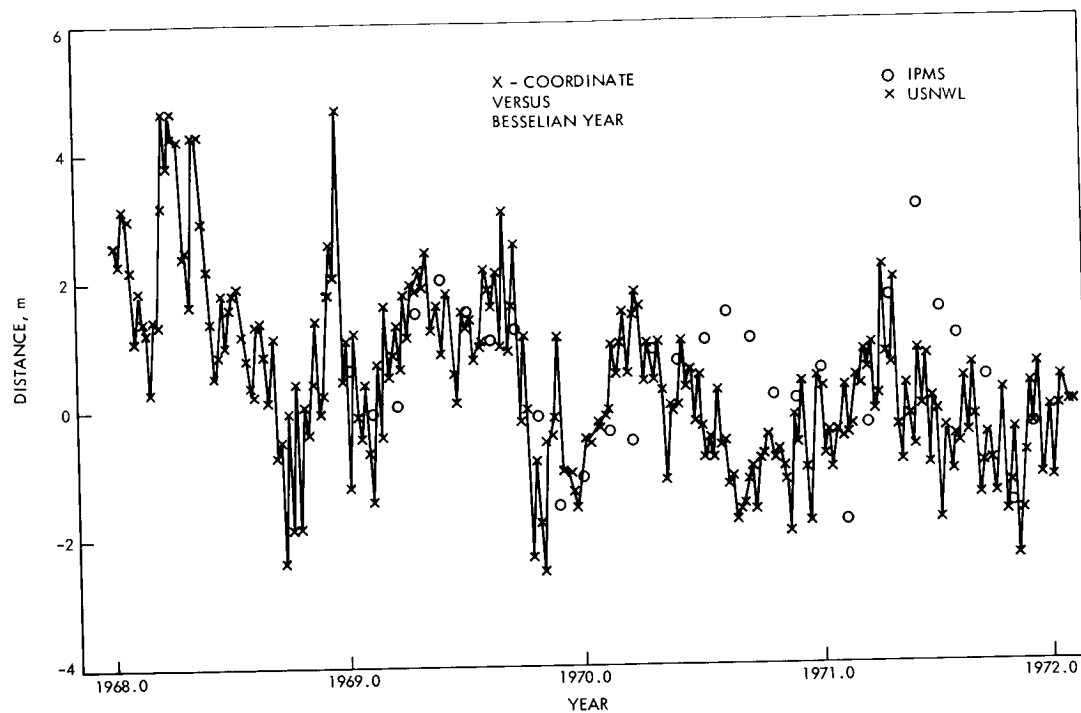


Fig. 1. Comparison between polar motion data types for X coordinate: USNWL/IPMS minus BIH values

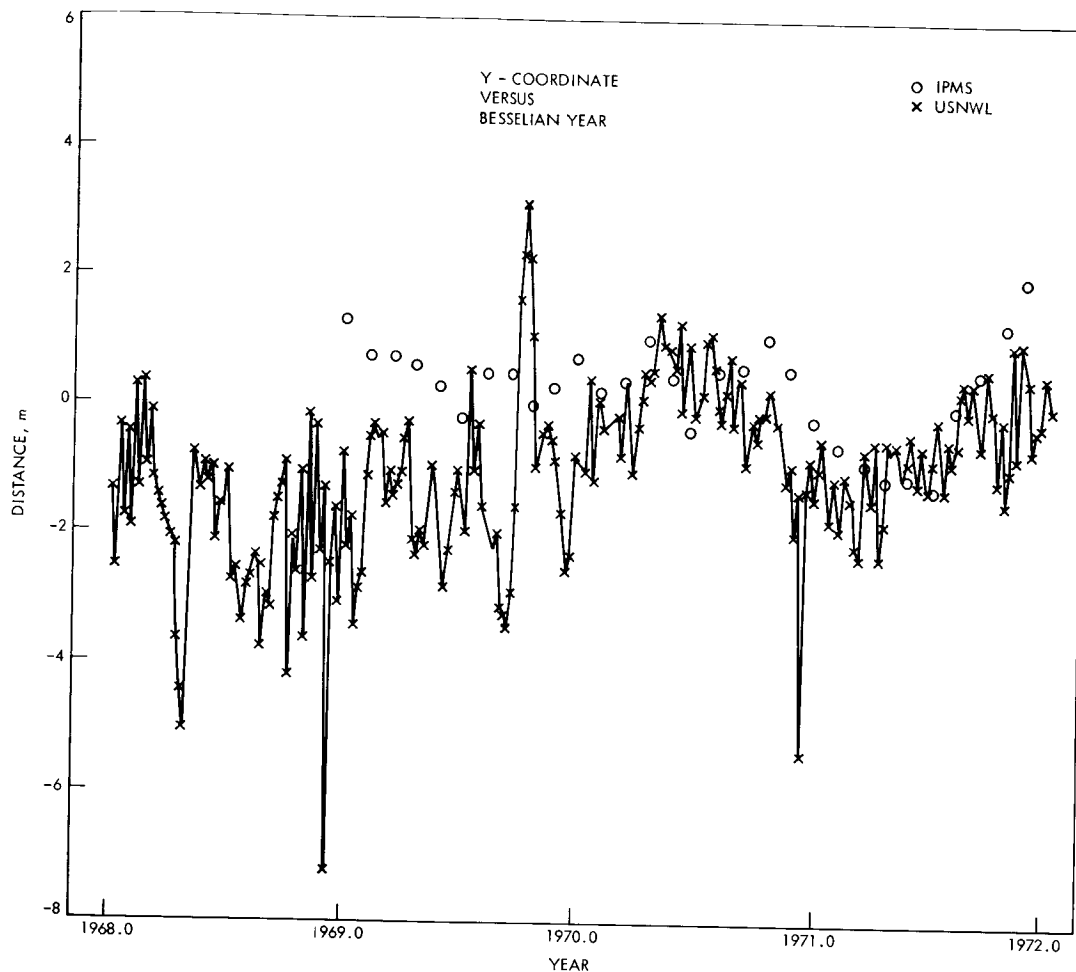


Fig. 2. Comparison between polar motion data types for Y coordinate: USNWL/IPMS minus BIH values

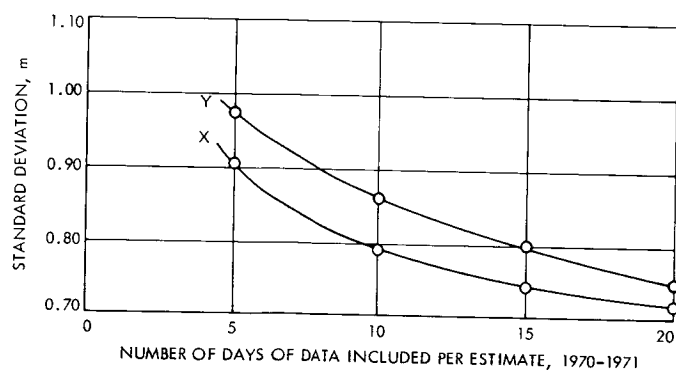


Fig. 3. Standard deviations of USNWL polar coordinates vs number of days of data included per estimate in 1970-1971

An Evaluation of Charged Particle Calibration by a Two-Way Dual-Frequency Technique and Alternatives to This Technique

O. H. von Roos and B. D. Mulhall
Tracking and Orbit Determination Section

This article relates to the accuracy of the three charged particle calibration methods — differenced range versus integrated doppler (DRVID), Faraday rotation, and dual frequency — as they apply to the various tracking modes, e.g., one-station tracking, two-station tracking, spacecraft very long baseline interferometry (VLBI). It is found that many calibration schemes are deficient at small Sun-Earth-probe angles (SEPs). Observations of the Sun during its active period between 1967 and 1969 have been used to obtain quantitative information on range degradation at small Sun-Earth-probe angles. Likewise, range errors at SEPs during a quiet Sun period (in this case the 1964-1965 solar minimum) have also been computed with the result that, even at times of a comparatively inactive Sun, range errors engendered by plasma clouds are still troublesome inasmuch as they prevent range measurement with an accuracy of less than 1 meter.

I. Introduction

In order to perform a systems analysis of the best possibilities for calibrating charged particles, the major tracking modes and the three major charged particle calibration methods are presented together with an error analysis.

II. Tracking Modes

The seven major tracking modes can be separated into two general categories: one-station tracking and two-station tracking.

A. One-Station Tracking Modes

- (1) *Two-way ranging.* This mode, very well established for years, consists of transmitting a range code toward the spacecraft that, when transmitted back, will be received at the transmitting station and referenced to the range code continuously generated. By this means the round-trip light time is measured and the range ascertained.
- (2) *Two-way doppler.* In this case the frequency shift of the RF carrier transmitted and received by a single station is determined and gives information

on the velocity of the spacecraft relative to the station.

B. Two-Station Tracking Modes

In two-station tracking, differences are measured, e.g., differences of range or range rates (doppler) as determined from two stations far apart. As shown in Ref. 1, these tracking modes are used because geocentric range and range rate are subject to a number of errors which, for convenience, are lumped together and termed "process noise" — erratic forces due to solar radiation pressure, pressure leaks in the spacecraft, etc., which are difficult to model. By differencing ranges or range rates as measured from two different stations, the geocentric range will drop out of the relevant equations and most of the process noise will be cancelled.¹ A number of new modes thus are made feasible.

- (3) *Two-way minus three-way doppler.* In this mode one station transmits a carrier frequency and two stations receive the returned signal simultaneously. By differencing the information, the range rate difference, $\rho_2 - \rho_3$, is determined.
- (4) *Two-way minus three-way ranging.* In this case a wideband signal modulated with a range code is transmitted to the spacecraft from one station, and two stations simultaneously receive the returned signal. By differencing the information, the range difference, $\rho_2 - \rho_3$, is obtained.
- (5) *Alternate ranging.* Here, ranging measurements are performed from two stations alternately because two different ranging machines transmit different range codes, and one transponder on the spacecraft cannot transpond the two signals if they are received simultaneously. This technique is operationally complicated, requiring approximately an hour of ranging by one station, then a transfer to the second station for an hour of ranging, then a transfer of the spacecraft to the first station, and so on until the overlap time expires.
- (6) *Simultaneous ranging.* This mode of ranging is quite similar to alternate ranging, the only difference being that the two stations range at the same time, which is possible if two frequencies and two transponders are employed. Two frequencies are under active consideration, for reasons to be discussed below.

¹The reason for this is that the angular motions are much less pronounced than the radial accelerations.

- (7) *Spacecraft VLBI.* In this mode of operation two stations are listening simultaneously to the spacecraft. No ground based transmission is involved. The received signals are cross-correlated and the differenced range determined directly.

III. Calibration Modes

Opposite the seven tracking modes are three basic charged particle calibration methods which can be used in any combination.

A. Faraday Rotation (FR)

This calibration method is based on the fact that the plane of a linearly polarized wave will be rotated in a magneto-active plasma. By measuring the rotation, conclusions can be drawn as to the electron content of the intervening plasma. Since the linearly polarized wave may be transmitted from the spacecraft or from an Earth satellite, there exist two different versions of the FR calibration method: satellite FR and spacecraft FR. The inherent accuracies of these two methods are somewhat different and will be discussed later.

B. Differenced Range Versus Integrated Doppler (DRVID)

This calibration is based on the fact that the group and phase velocities of an electromagnetic wave differ in a plasma. However, since the phase velocity is that of a very narrow bandwidth signal (doppler), DRVID is only capable of calibrating range *rates*.

C. Dual-Frequency Calibration

This is by far the most promising method for correcting the range and range rate errors caused by the ionosphere and the interplanetary plasma. It consists of transmitting and receiving the same signal at two different frequencies (S and X band). The difference in integrated doppler and also in range for the two frequencies is a direct measure of the total electron content. The differenced doppler provides a precise but ambiguous charged particle measurement, while the differenced range provides an unambiguous (though noisier) measurement.

IV. Error Analysis of the Major Calibrations

A. Faraday Rotation

The calibrations based on the FR are capable of removing only the range and range rate errors due to the

ionosphere (Ref. 2). This is even true, generally, for the spacecraft FR mode, since the space plasma's magnetic field is very small ($\approx 10^{-6}$ gauss) and the rotation of the plane of polarization amounts only to extremely small fractions of a degree at S-band (10^{-8} rad) while the ionosphere typically produces rotations of the order of 1 to 10 deg of S-band. An exception is the solar corona. When the Sun-Earth-probe angle (SEP) becomes less than 5 deg, the solar plasma activities may give rise to large excursions from the ionospheric background (Ref. 3). Very close to an active Sun, rapid changes of the plane of polarization of 40 deg/h are not uncommon.

An error analysis, (see Appendix A), has been performed on the degrading influence of the solar corona on FR measurements. There it has been shown to expect a range rate error of about 10 m/h due to the solar corona during a sunspot maximum at an SEP of 5 deg. Spacecraft FR calibration will be insensitive to the solar corona for SEPs larger than 5 deg because of the rapid decrease of the magnetic field strength in solar plasma clouds. However, the range uncertainty is still severe (> 1 m). It must be emphasized that the foregoing considerations presuppose an active Sun. During a quiet Sun period, however, the problem of range uncertainties still persists for very small SEPs (< 5 deg) simply because the solar corona is not known as accurately as required. The electron density quoted for instance in Ref. 3 may well be off by a factor of 2 (C. T. Stelzried, private communication). Therefore, for extremely small SEPs the spacecraft FR calibration mode will be uncertain regardless of the status of the Sun's activity.

We can deal with the satellite FR mode briefly, since it has been discussed at length elsewhere (Ref. 4). In short, the rotation of the plane of polarization of an electromagnetic wave in the line of sight between a satellite and an Earth-bound station is measured continuously. In this way the electron content of the ionosphere *in the line of sight between satellite and an Earth station* is determined. However, what is needed for calibration is a knowledge of the electron content in the line of sight between the spacecraft and this station. Therefore the electron content has to be mapped to the line of sight between spacecraft and station. This is done at JPL via the computer program Hyperion. A detailed description of Hyperion is given in Ref. 5. (Certain assumptions, e.g., a Chapman layer for the ionosphere, are inherent to the program.)

Although the above-mentioned assumptions have been proven to be generally correct, the actual deviations from

this model are such that a range error of 1.5 m accumulating during an 8-h pass can be expected in summer, and an error of 0.5 m can be expected in fall, winter, and spring. (Ref. 6).

To summarize, both FR modes have certain limitations. The satellite FR mode obviously can calibrate only the ionosphere and must therefore be complemented with other calibration schemes, but may then become quite useful. For the spacecraft FR mode the same holds generally true. Although there is the disadvantage of a lack of true ionospheric calibration at small SEPs (< 5 deg) during an active Sun period due to the solar corona, this is more than offset by the fact that the previously mentioned mapping with all its uncertainties is unnecessary. Later, when the dual-frequency method has been introduced we will see how the spacecraft FR mode can be used to advantage.

B. Differenced Range Versus Integrated Doppler

This method (see Ref. 7) is used to calibrate for charged particles. Its principle is based on the fact that phase and group velocities differ in a plasma. It can be used to calibrate range rates and range differences only, *never the absolute range*. As far as the accuracy is concerned it must be realized that the main problem in this type of calibration is the ranging channel. The signal-to-noise ratio for the ranging system slated for the outer planets mission is the same as for the Viking mission (G. E. Wood, private communication), and therefore the error analysis by MacDoran (Ref. 8) is applicable. According to this analysis $27 \cdot 10^{-9}$ s "ranging jitter" for a 15-min integration time provides a calibration accuracy to the 1-m level. The hardware requirements for this kind of accuracy do not seem to be insurmountable at all; as a matter of fact Madrid in his tracking system analytical calibration (TSAC) activities (Ref. 9) has already achieved a sigma of 1 m during the Mariner 9 mission. To summarize, DRVID is a useful tool for charged particle calibrations which can confidently be expected to be accurate to the 1-m level, but by its nature cannot calibrate absolute ranges and therefore does not apply to tracking methods 1, 4, 5, 6, or 7.

C. S/X Dual-Frequency Calibration

By far the most promising charged particle calibration mode is the utilization of a dual-frequency system. The question arises immediately whether a downlink only S/X-band system, which is presently planned, is sufficient for an accurate calibration or whether a combined up and down S/X system is needed. An analysis has been

made in Appendix B, showing that at SEPs smaller than 20 deg an uplink *and* downlink dual-frequency system is definitely needed if the Sun is active and the desired accuracy is to be below the 1-m level, the reason being of course that in a time-dependent medium the uplink total electron content cannot be inferred from the downlink content. The analysis has been applied to a numerical estimate of range errors at small SEPs if only a downlink S/X system is used; Fig. 1 gives the results. The solar plasma data used to evaluate Fig. 1 are extracted from Ref. 10 (see also Appendix B).

Summarizing, we emphasize that a dual-frequency calibration, if done on both the uplink and downlink, is by far the most accurate ranging calibration known. If only a downlink S/X band system is used, a range inaccuracy develops at small SEPs (< 20 deg). This is particularly true for an active Sun (see Fig. 1).²

V. Combination of Calibration Modes

After having delineated the main modes of calibration we will now briefly discuss combinations of them. It is clear that the FR methods can be used only in conjunction with the other two since the former only calibrates the ionosphere. On the other hand the two-way dual-frequency method is self sufficient. A promising combination of methods is combining either of the FR modes together with the downlink-only dual-frequency method. For, if the space plasma is quiet, because of a quiet Sun or because the SEP is large, the only long-term time variations are the diurnal variations of the ionosphere. The calibration for the uplink is then provided for by FR. If the space plasma is active, the downlink dual-frequency measurement will differ from the FR measurement and, though the exact calibration cannot be computed, the size of the error caused by neglecting the uplink space plasma effect can be bounded. It appears then that the most promising charged particle calibration techniques are:

- (1) Uplink and downlink dual-frequency.
- (2) Faraday rotation plus downlink dual-frequency.

Whereas the first method is foolproof, the second has some limitations. These limitations relate to the fact that for small SEPs and an active Sun, range uncertainties will occur as depicted in Fig. 1.

²For details see Appendix B.

One interesting combination, however, exists in which DRVID may help the downlink-only S/X-band *ranging* capability. Suppose the solar plasma is quiescent for some time prior to $t = t_0$. The downlink electron content is then the same as the uplink content, and the uplink content can therefore be determined. Suppose further that at t_0 and thereafter, solar plasma clouds and streamers enter the ray path and change the electron content rapidly (changes of $5 \cdot 10^{17} \text{m}^{-2}$ in the electron content within 30 min are not uncommon). DRVID will immediately become active and the uplink electron content may be determined. However, for SEPs less than 20 deg occasions of this type are rather rare.

VI. Comparison of Techniques

We can now compare the charged particle calibration modes and cross-correlate them with the various tracking modes mentioned at the beginning of this article. This is done in Table 1. The various ranging and tracking modes are listed according to the number assigned to them in Section I. It is to be noted from Table 1 that spacecraft VLBI is adequately calibrated with a downlink frequency system only. This is of course obvious, but it should be pointed out specifically. On the other hand, it would seem that the *differenced* tracking modes (3 to 6) are not beset by the range calibration uncertainties for small SEPs of the downlink-only S/X-band calibration method, since the two ray paths, separated by some 7000 km, experience generally the same plasma activities, and when the ranges are differenced, the uncertainties cancel to the 10-cm level. This happens indeed to be true for modes 3 and 4. Both of these modes have one common uplink, and therefore any range degradation caused by plasma clouds passing the ray path during the transit of the radio signal on its uncalibrated uplink will exactly cancel upon differencing the ranges. However, for modes 5 and 6 this is not true. In mode 5 the two stations track about an hour each alternately, and the uncalibrated uplink gives trouble at small SEPs since plasma clouds can come and go within an order of hours. Finally, mode 6 cannot be calibrated properly with a downlink-only S/X-band system simply because the two stations operate at two different frequencies and the space plasma affects them differently.

VII. Summary

We have described three methods by which the degrading influence of electromagnetic plasma interactions on range and range rate values can be eliminated, at least partially. Table 1 gives the results of this analysis.

We have found that the S/X-band dual-frequency calibration, if employed for both the uplink and downlink, is superior to all other methods, particularly for one-station tracking. However, downlink-only S/X is quite adequate for two-station tracking in modes 3, 4, and 7. We have also seen that a combination of Faraday rotation with

downlink-only dual-frequency is a viable candidate for charged particle calibration. Both methods work equally well during times of a quiet Sun; but at small Sun-Earth-probe angles and during periods of an active Sun, range calibration errors for downlink-only dual-frequency may become severe (see Fig. 1).

Table 1. Expected total range error over one pass due to charged particle calibration uncertainties

Ranging or tracking			Charged particle calibration mode				
			Satellite FR ^a	Spacecraft FR ^b	DRVID	S/X, downlink only	S/X, uplink and downlink ^c
ρ_2	(1)	(1)	1.5 m	1.5 m	Not applicable	0.5 m ^d	0.5 m
ρ_2	(2)	(2)	1.5 m	1.5 m	1 m	0.5 m ^d	0.5 m
$\rho_2 - \rho_3$	(3)	(3) ^e	2.0 m	2.0 m	1 m	0.5 m ^f	0.5 m
$\rho_2 - \rho_3$	(4)	(4) ^e	2.0 m	2.0 m	Not applicable	0.5 m ^f	0.5 m
Altitude ranging	(5) ^e		2.0 m	2.0 m	Not applicable	0.5 m ^e	0.5 m
Simultaneous ranging	(6) ^e		2.0 m	2.0 m	Not applicable	0.5 m ^e	0.5 m
Spacecraft VLBI	(7) ^e		2.0 m	2.0 m	Not applicable	0.5 m ^f	Not applicable

^aCalibrates the ionosphere only.

^bCalibrates the ionosphere only except for Sun-Earth-probe angles less than 5 deg, when the corona degrades calibration to an unacceptable level.

^cIn this ideal mode only instrumentation limitations are present. They are estimated to be at the half-meter level.

^dThe hardware limited value quoted is only applicable if the Sun-Earth-probe angle is larger than 20 deg and the Sun is not active (Fig. 1).

^eThe reason for the increase in inaccuracy for tracking modes (3) to (7), relating to the Faraday rotation, is the fact that the ionospheric environment differs between the two tracking sites and an rms average was taken.

^fThe only tracking modes for which downlink *only* S/X-band is totally adequate.

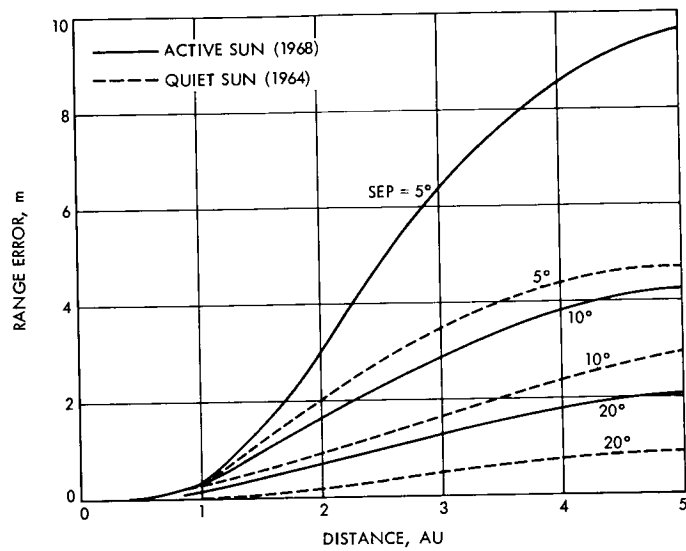


Fig. 1. Estimated range error for S/X-band downlink calibration only, due to time variation in the solar wind (valid for one-station two-way ranging ρ_2)

Appendix A

Range Degradation Due to the Solar Corona

The following analysis gives an estimate of the degrading influence of the solar corona on FR measurements. To be specific let the SEP be 5 deg, corresponding to a closest distance of the ray path from the Sun $R = 10$ (measured in Sun radii). Let us take the improved plasma electron density as given by Stelzried (Ref. 3):

$$N = 10^{14} \left(\frac{6000}{R^{10}} + \frac{0.002}{R^2} \right) (\text{in m}^{-3}) \quad (4 < R < 12) \quad (\text{A-1})$$

This is valid for the quiet Sun. If the closest distance of the straight ray path from the Sun is R_1 , then the total electron content within the sphere of the influence of the solar corona ($R < 12$) for a quiet Sun is given by

$$I = 10^{14} R' \int_{-(12^2 - R_1^2)^{1/2}}^{(12^2 - R_1^2)^{1/2}} \left(\frac{6000}{(R_1^2 + x^2)^5} + \frac{0.002}{R_1^2 + x^2} \right) dx \quad (\text{in m}^{-2}) \quad (\text{A-2})$$

where R' is the radius of the Sun in meters. Now, for $R_1 = 10$ this amounts to

$$I_{10} = 5.6 \cdot 10^{18} \text{m}^{-2}$$

corresponding to about 36 m of range error at S-band. Adopting a Parker magnetic field, the Faraday rotation turns out to be some 10 deg. When plasma bursts occur from an active Sun, similar polarization changes (10 deg/h) have been observed on Pioneer 6 (Ref. 3), which would indicate that range rate errors of some 30 m/h can occur under the assumption that the same magnetic fields prevail (this is for an SEP of 5 deg). However, the magnetic fields in plasma clouds close to the Sun are likely to be larger by a factor of 2 to 10, which cuts down the range error by the same factor. We therefore expect a range rate error of about 10 m/h due to the solar corona during a sunspot maximum at an SEP of 5 deg.

Appendix B

Analysis of a Time Changing Solar Plasma

The following analysis will show that at SEPs smaller than 20 deg, an uplink *and* downlink dual-frequency system is definitely needed if the Sun is active and the

accuracy derived is to be below the 1-m level³. The analysis goes as follows: Let R_s be the range as seen at the S-band frequency (Ref. 11)

$$R_s = R + \frac{\alpha}{\omega_s^2} \int_0^R N\left(x, \frac{x}{c} + t\right) dx + \frac{\alpha}{\omega_{st}^2} \int_0^R N\left(x, \frac{2R-x}{c} + t\right) dx \quad (B-1)$$

where

$$\alpha = \frac{\pi e^2}{m}$$

ω_s = S-band frequency

ω_{st} = S-band transponder frequency

R = true range

$N(x, t)$ = electron number density as a function of ray path x and time t

On the other hand the range as seen at the X-band frequency is, according to the foregoing, given by

$$R_x = R + \frac{\alpha}{\omega_x^2} \int_0^R N\left(x, \frac{x}{c} + t\right) dx + \frac{\alpha}{\omega_x^2} \int_0^R N\left(x, \frac{2R-x}{c} + t\right) dx \quad (B-2)$$

where

ω_x = X-band frequency.

Were it not for the explicit time dependence of the electron density, a time dependence which is particularly annoying and unpredictable when the ray path passes near the Sun, Eqs. (B-1) and (B-2) could easily be solved for the two unknown quantities R and the electron content. However in reality we have, in general, two equations and three unknown quantities.

To extract information on R proves to be generally impossible. Since the range is measured at many different times, the only possibility might be to shift the time by an amount Δ such that

$$\int_0^R N\left(x, \frac{x}{c} + t\right) dx = \int_0^R N\left(x, \frac{2R-x}{c} + t + \Delta\right) dx \quad (B-3)$$

The unknown integrals of Eqs. (B-1) and (B-2) are determined by differencing (B-1) and (B-2). In general, no such

Δ exists, and therefore a complete charged particle calibration is not possible. If, however, the time-dependent activity of the solar wind is localized in the path at x_0 , say, we may represent the electron density by

$$N = L\delta(x - x_0)F(t) \quad (B-4)$$

where L is the special extent, and have from Eq. (B-4),

$$F\left(\frac{x_0}{c} + t\right) = F\left(\frac{2R-x_0}{c} + t + \Delta\right) \quad (B-5)$$

so that $\Delta = 2(x_0 - R)/c$ indeed satisfies Eq. (B-4). However, we do not know x_0 .

As to the numerical estimates underlying Fig. 1, we notice first that the electron density behaves approximately as R^{-2} and the path length through a plasma cloud goes as R , where R is the distance from the Sun

³The considerations given here are applicable for tracking modes 1, 2, 5, and 6. In tracking modes 3 and 4 the space plasma is "differenced away" to well below the 1-m level.

(see in particular V. V. Vitkevich, Ref. 10), so that the total electron content of a plasma cloud is expected to behave as:

$$\int N ds \sim \frac{1}{R} \sim (\text{SEP})^{-1} \quad (\text{B-7})$$

Furthermore at an SEP of 20 deg the distance from the Sun is sufficiently large so that the electron content time variations as found by the Stanford group (R. L. Koehler,

T. A. Croft, Ref. 10) apply. The two integrals in Eqs. (B-1) and (B-2) are expected to differ by 2 m then in the limit of large R . For intermediate R the time delay between uplink and downlink becomes shorter and the difference between the two integrals in Eqs. (B-1) and (B-2) becomes progressively smaller. The references quoted so far pertain to an active Sun period. During a quiet Sun period there is still sufficient activity (plasma clouds, flares, etc.), however, to degrade the range determination by a few meters at small SEPs (Ref. 12).

References

1. Ondrasik, V. J., and Rourke, K. H., Paper AAS 71-399, presented at AAS/AIAA Astrodynamics Specialists Conference, Fort Lauderdale, Fla., Aug. 17, 1971.
2. Mulhall, B. D., "Charged Particle Calibration System Analysis," in *The Deep Space Network*, Space Programs Summary 37-64, Vol. II, pp. 13-21. Jet Propulsion Laboratory, Pasadena, Calif., Aug. 31, 1970.
3. Stelzried, C. T., *A Faraday Rotation Measurement of a 13-cm Signal in the Solar Corona*, Technical Report 32-1401. Jet Propulsion Laboratory, Pasadena, Calif., July 15, 1970.
4. Yip, K. W., and Mulhall, B. D., "Local and Transcontinental Mapping of Total Electron Content Measurements of the Earth's Ionosphere," in *The Deep Space Network Progress Report*, Technical Report 32-1526, Vol. VII, pp. 61-67. Jet Propulsion Laboratory, Pasadena, Calif., Feb. 15, 1972.
5. Mulhall, B. D., et al., *Tracking System Analytic Calibration Activities for the Mariner Mars 1969 Mission*, Technical Report 32-1499. Jet Propulsion Laboratory, Pasadena, Calif., Nov. 15, 1970.
6. Yip, K. W., and Mulhall, B. D., "Local and Transcontinental Mapping of Total Electron Content Measurements of the Earth's Ionosphere," in *The Deep Space Network Progress Report*, Vol. VII, pp. 61-67, Technical Report 32-1526. Jet Propulsion Laboratory, Pasadena, Calif., Feb. 15, 1972.
7. MacDoran, P. F., "A First-Principles Derivation of the Differenced Range Versus Integrated Doppler (DRVID) Charged-Particle Calibration Method," in *The Deep Space Network*, Space Programs Summary 37-62, Vol. II, pp. 28-34. Jet Propulsion Laboratory, Pasadena, Calif., Mar. 31, 1970.
8. MacDoran, P. F., IOM 391.13-385. Jet Propulsion Laboratory, Pasadena, Calif. (JPL internal document).
9. Madrid, G. A., "Tracking System Analytic Calibration Support for the Mariner Mars 1971 Mission," in *The Deep Space Network Progress Report*, Technical Report 32-1526, Vol. III, pp. 52-62. Jet Propulsion Laboratory, Pasadena, Calif., June 15, 1971.
10. Hewish, A., *Proc. Roy. Soc., Ser. A*, Vol. 200, p. 238; Jokipii, J. R., *Phys. Rev. Lett.*, Vol. 26, p. 666, 1971; Vitkevich, V. V., *Sov. Astron.-AJ*, Vol. 4, 1961; Dressler, A. J., *Rev. Geophys.*, Vol. 5, p. 1, 1967; Burlaga, L. F., *Solar Phys.*, Vol. 4, p. 67, 1968; Koehler, R. L., *J. Geophys. Res.*, Vol. 73, p. 4883, 1968; Landt, J. A., and Croft, T. A., *J. Geophys. Res.*, Vol. 75, p. 4623, 1970; Croft, T. A., *Rad. Sci.*, Vol. 6, p. 55, 1971; MacDoran, P. F., Callahan, P. S., and Zygielbaum, A. I., TR 32-1526, Vol. I. Jet Propulsion Laboratory, Pasadena, Calif., 1971; Eshleman, R., *Solar System Radio Astronomy*, Plenum Press, New York, 1955.
11. von Roos, O. H., "Analysis of the DRVID and Dual Frequency Tracking Methods in the Presence of a Time-Varying Interplanetary Plasma," in *The Deep Space Network Progress Report*, Technical Report 32-1526, Vol. III, pp. 71-76. Jet Propulsion Laboratory, Pasadena, Calif., June 15, 1971.
12. Hansen, R. T., et al., *Solar Physics*, Vol. 7, p. 417, 1969.

Derivation of a General Expression for Ionospheric Range Corrections Valid for Arbitrary Solar Zenith Angles, Azimuths, Elevation Angles and Station Locations

O. H. von Roos and K. W. Yip
Tracking and Orbit Determination Section

A general expression is derived for the electron density profile as a function of latitude and longitude for that part of the Earth which is in direct sunlight including dawn and dusk. This expression allows one to determine by standard means the range correction for arbitrary ray path directions. It is also shown that the naive application of the Chapman ionosphere entails range correction errors which for low elevation angles (<20 deg) and large solar zenith angles (>40 deg) cannot be tolerated. Numerical calculations are displayed showing the dependence of the range correction on the pertinent parameters.

I. Introduction

It is well known that for high frequencies ω of a radio wave, the susceptibility of a plasma $\epsilon - 1$ is given by

$$\epsilon - 1 = -\frac{\omega_p^2}{\omega^2} \quad (1)$$

where $\omega_p = 4\pi e^2 N/m$ is the plasma frequency proportional to the electron number density N (Ref. 1). A radio beam traversing the ionosphere for the purpose of tracking a satellite or a spacecraft will accordingly be affected by the plasma of the ionosphere.¹ It is also known (Refs. 3 and 4) that the quantity most important for the deter-

mination of the range correction is the total electron content:

$$I = \int N(s) ds \quad (2)$$

where the integral is taken over the ray path.

In order to successfully calibrate for range errors, I must therefore be known. Usually I is determined by means of Faraday rotation measurements (Ref. 5) along the ray path between a geostationary satellite and an observer on Earth. But, to calibrate the range to a spacecraft, the total electron content I in the ray path connecting the spacecraft with the observer must be known. In order to be able to determine this quantity, a mapping

¹If the cyclotron frequency $\omega_c \ll \omega$, magnetic effects are negligible (Ref. 2) and Eq. (1) is a very good approximation.

from one ray path to the other must be performed. This can be done only with a model of the ionosphere. In the next Section we will derive such a model based on principles laid down and explored by Chapman many years ago (Ref. 6).

This three-parameter model will be applied subsequently to the determination of the ionospheric range correction for any arbitrary ray path arbitrarily located on the sunlit face of the Earth.

II. The Ionospheric Electron Profile

For small zenith angles, the Chapman electron density profile is given by the expression

$$N_e(Z) = N_{e \max} \exp \left\{ \frac{1}{2} [1 - Z - \sec \chi \exp(-Z)] \right\} \quad (3)$$

where

$$Z = \frac{h - h_{\max}}{H}$$

$N_{e \max}$ = maximum electron concentration at altitude $h = h_{\max}$ and, for $\chi = 0$

χ = angle between the direction of the Sun's rays and the zenith

H = scale height of the ionosphere

From first principles it can be shown that the following expressions hold (see the derivation on pages 6 and 7);

$$\sigma_A N_0 H = \exp \left(\frac{h_{\max}}{H} \right) \quad (4a)$$

$$\left(\frac{\sigma_i N_0 S_\infty}{\alpha h \bar{\nu}} \right)^{1/2} = N_{e \max} \exp \left(\frac{1}{2} + \frac{1}{2} \frac{h_{\max}}{H} \right) \quad (4b)$$

relating the empirical quantities N_{\max} , h_{\max} to basic quantities as ionization cross sections, etc. These relations are needed for our derivation of the electron profile. The meaning of the various terms in Eqs. (4) is:

σ_A = absorption cross section for ultraviolet radiation in air, cm^2

N_0 = number density of air molecules on ground ($h = 0$), cm^{-3}

S_∞ = intensity of the Sun's ultraviolet radiation outside the Earth's atmosphere, $10^{-7} \text{ J cm}^{-2} \text{ s}^{-1}$

α = recombination coefficient of electrons with ions, $\text{cm}^3 \text{ s}^{-1}$

$h \bar{\nu}$ = average photon energy, 10^{-7} J

All quantities above are averages over the ionizing part of the solar spectrum. As is seen from Eq. (3), for $\chi = 90^\circ$ $N_e(z)$ becomes identically zero, which obviously means that Eq. (3) breaks down at large χ . We will now give a derivation of the electron profile applicable for all χ . To be sure, a derivation for this situation has been given by Chapman long ago. But since that derivation is somewhat pedantic and not generally well known, we felt a concise and short derivation at this place is not out of order, all the more so since the profile derived here encompasses *all* zenith angles of the Sun χ and is valid in three dimensions, unlike most derivations, which are essentially two-dimensional.

The reasons for formerly confining oneself to only two-dimensional considerations are certain symmetries which allow one to map the electron density profile into three dimensions only if it is known along the Sun's meridian. This will be explained later. For computational ease, a three-dimensional mapping is far superior. To proceed with the derivation, the coordinate system used in this study will be defined first (Fig. 1). It is a right-handed Cartesian coordinate system with the x -axis pointing toward the Sun and the y -axis lying in the equatorial plane of the Earth.

Note that if the declination of the Sun is $\delta \neq 0$, the z -axis of this coordinate system does not coincide with the spin axis of the Earth. Figures 2a and 2b give cross-sections through the x - y and the x - z planes, respectively, of Fig. 1 for clarification. A polar coordinate system associated with the Cartesian system just introduced shall be designated by r , θ_0 , ϕ_0 , where these symbols have their usual meaning. Later we shall link these coordinates to the usual geographical coordinates with the help of the declination δ of the Sun and the universal time (UT) (see Section III).

In order to find out the number of electrons at r , θ_0 , and ϕ_0 , we must first know how much radiation is absorbed at r , how much of this radiation ionizes, how much recombines, and finally use the stationarity condition $\dot{N}_e = 0$ to eventually obtain the electron profile. The intensity of radiation absorbed at the point r is:

$$dS = \sigma_A N S dl \quad (5)$$

where dl is a line element along a Sun's ray at position r , θ_0 , ϕ_0 ; S is the solar radiation flux; and N is the number

density of the neutral species assumed to obey an exponential law; viz.,

$$N = N_0 \exp\left(-\frac{r-R}{H}\right) \quad (6)$$

From Figs. 2a and 2b it is easy to deduce that the line element $d\ell$ can be expressed by

$$d\ell = dr \left(1 - \frac{y_0^2 + z_0^2}{r^2}\right)^{-1/2} \quad (7)$$

From Eqs. (5), (6), and (7) it follows that

$$\frac{dS}{S} = \sigma_A N_0 \exp\left(-\frac{r-R}{H}\right) \left(1 - \frac{y_0^2 + z_0^2}{r^2}\right)^{-1/2} dr \quad (8)$$

and since $S = S_\infty$ at $r = \infty$, we have

$S =$

$$S_\infty \exp \left\{ \sigma_A N_0 \int_\infty^r \exp\left(-\frac{x-R}{H}\right) \left(1 - \frac{y_0^2 + z_0^2}{x^2}\right)^{-1/2} dx \right\} \quad (9)$$

The number of ionized pairs created per second at r is now given by

$$\dot{n} = \sigma_i N \frac{S}{h\nu} \quad (10)$$

The rate of electron production \dot{n} and the rate of electron recombination $\alpha N_i N_e$, where N_i is the ion concentration, determines the net rate of change of the electron density:

$$\dot{N}_e = \dot{n} - \alpha N_i N_e \quad (11)$$

Assuming neutrality $N_i = N_e$ and stationarity $\dot{N}_e = 0$, we obtain

$$N_e = \sqrt{\frac{\dot{n}}{\alpha}} \quad (12)$$

the desired result.

From Eqs. (12), (10), and (9), there results

$$N_e = \left(\frac{\sigma_i S_\infty N_0}{\alpha h\nu}\right)^{1/2} \exp \left\{ \frac{1}{2} \left[-\frac{r-R}{H} + \sigma_A N_0 \int_\infty^r \exp\left(-\frac{x-R}{H}\right) \left(1 - \frac{y_0^2 + z_0^2}{x^2}\right)^{-1/2} dx \right] \right\} \quad (13)$$

We now wish to link the first-principle quantities σ_i , σ_A etc. to the three parameters which are universally adopted for a Chapman ionosphere, to wit, $N_{e \max}$, h_{\max} , and H . In Eq. (3), sec $\chi = 0$ corresponds to $y_0 = z_0 = 0$ in Eq. (13). Therefore, comparing Eq. (3) with Eq. (13), in this case, reveals that

$$\exp\left(\frac{h_{\max}}{H}\right) = \sigma_A N_0 H \quad (14a)$$

$$N_{e \max} \exp\left[\frac{1}{2} \left(1 + \frac{h_{\max}}{H}\right)\right] = \left(\frac{\sigma_i S_\infty N_0}{\alpha h\nu}\right)^{1/2} \quad (14b)$$

in order that Eqs. (3) and (13) agree. Using Eqs. (14), we finally obtain for the electron density profile in standard notation.

$$N_e = N_{e \max} \exp \left\{ \frac{1}{2} \left[1 - Z + \int_\infty^Z e^{-x} \left(1 - \frac{y_0^2 + z_0^2}{(Hx + R + h_{\max})^2}\right)^{-1/2} dx \right] \right\} \quad (15)$$

where

$$Z = \frac{r - R - h_{\max}}{H} \quad (16)$$

$$\begin{aligned} y_0 &= (HZ + R + h_{\max}) \sin \theta_0 \sin \phi_0 \\ z_0 &= (HZ + R + h_{\max}) \cos \theta_0 \end{aligned} \quad (17)$$

Finally, if we wish to determine the electron density profile radially above ground as a function of altitude Z at the arbitrary position θ_0 and ϕ_0 , we must put

and insert these expressions into Eq. (15). The range of Z extends from $Z = -h_{\max}/H$ at the surface of the Earth to infinity.

The great circle $\phi_0 = 0$, which intersects the x -axis and the z -axis as depicted in Fig. 1, is of course not unique in the sense that any great circle, provided it intersects the x -axis at $y = z = 0$, is equally good. The geometry of Fig. 1 is invariant with respect to rotations about the x -axis. If therefore the electron profile is known for all θ_0 and $\phi_0 = 0$, it is known throughout the lit hemisphere. In fact, the electron profile at $\phi_0 = 0$ and θ_0 is the same as that at $\theta_0 = \theta_1$ and $\phi_0 = \phi_1$ if

$$\sin \theta_0 = \sin \theta_1 \cos \phi_1 \quad (18)$$

Two-dimensional calculations as they have been done exclusively in the past ($r, \theta, \phi = \text{const.}$), would have been quite adequate. But since we are going to link the x, y, z system of Fig. 1 to an Earth-fixed geographical coordinate system to determine range corrections from arbitrary station locations into arbitrary directions, which are conveniently expressed in Earth-fixed coordinates, it was felt that a mapping of the electron density using one common coordinate system is advantageous.

Concluding this section, we note that no mention is made of the solar zenith angle χ in Eq. (15). For $\chi = 0$, Eq. (15) is identical with Eq. (3). But for all other zenith angles $\chi \neq 0$, Eq. (3) is only an approximation to the exact result of Eq. (15) (exact within the assumptions of this theory) and becomes progressively worse as χ increases. As a matter of fact, for $\chi = 90$ deg, Eq. (3) breaks down completely. However, Eq. (15) is still perfectly valid in this case. A glance at Fig. 1 shows that $\chi = 90$ deg corresponds to $\phi_0 = \pi/2$ or $\phi_0 = 3\pi/2$, in which case the integral of Eq. (15) is well defined and incidentally independent of θ_0 as it should be from symmetry.

$$\begin{aligned} \underline{e}_{\text{ray}} = & (\sin \gamma \sin \theta_0 \cos \phi_0 - \cos \gamma \cos \alpha \cos \theta_0 \cos \phi_0 - \cos \gamma \sin \alpha \sin \phi_0) \underline{e}_x \\ & + (\sin \gamma \sin \theta_0 \sin \phi_0 - \cos \gamma \cos \alpha \cos \theta_0 \sin \phi_0 + \cos \gamma \sin \alpha \cos \phi_0) \underline{e}_y \\ & + (\sin \gamma \cos \theta_0 + \cos \gamma \cos \alpha \sin \theta_0) \underline{e}_z \end{aligned} \quad (20)$$

In Eq. (18), θ_0 and ϕ_0 are the polar coordinates, as introduced earlier. On the other hand, γ is the elevation angle (the angle between the line of sight and the tangential plane at the surface of the Earth). The angle α is the azimuth of the line of sight. To be specific, α is the angle between the projection of the line of sight on the tangential plane and a meridian. We must emphasize that the coordinate system of Fig. 1 is geared to the Sun, in the sense that the x -axis points toward the Sun. Presently we shall give the coordinate transformation from the system of Fig. 1 to a geographical (Earth-fixed) sys-

The preceding derivation was made under the assumption that the three parameters $N_{e \text{ max}}$, h_{max} , and H are global in the sense that they are independent of location. This is, of course, most certainly not true. However, the geometrical considerations here and in the next section are not affected by this unfortunate circumstance. The three parameters just mentioned may then be considered functions of θ_0 and ϕ_0 .

In the next section we shall derive the range correction for an arbitrary ray path originating from an arbitrary location on Earth expressed in Earth-fixed coordinates as long as the station is located on the sunlit side of the Earth. We shall also dwell on the determination of the parameters determining the electron profile and show the errors made when using Eq. (3) instead of Eq. (15).

III. The Range Correction

It has been shown (Ref. 4) that the range correction due to a tenuous plasma is given by

$$\Delta \rho = \frac{2\pi e^2}{m \omega^2} \int_R^\infty dr \left(1 - \frac{R^2 \cos^2 \gamma}{r^2} \right)^{-1/2} N_e(s(r)) \quad (19)$$

The symbols in Eq. (19) have their usual meaning: $s(r)$ is the unperturbed (straight) ray path between the Earth-bound station and the distant space craft, expressed as a function of r , the distance from the center of the Earth. In the coordinate system displayed in Fig. 1, an arbitrary ray path or a line joining a station's antenna with the spacecraft may be obtained by the following expression:

tem. The quantities \underline{e} in Eq. (19) are unit vectors along their specified directions. Before effectuating the coordinate transformation just mentioned, we shall give the range correction Eq. (18) concisely in the coordinate system as explained by Fig. 1.

Defining:

$$s = -R \sin \gamma + \sqrt{r^2 - R^2 \cos^2 \gamma} \quad (21)$$

we merely have to insert the following expressions for y_0 and z_0 into Eq. (15) in conjunction with Eq. (19) to

obtain the range correction, to wit:

$$y_0 = s(\sin \gamma \sin \theta_0 \sin \phi_0 - \cos \gamma \cos \alpha \cos \theta_0 \sin \phi_0 + \cos \gamma \sin \alpha \cos \phi_0) + R \sin \theta_0 \sin \phi_0 \quad (22a)$$

and

$$z_0 = s(\sin \gamma \cos \theta_0 + \cos \gamma \cos \alpha \sin \theta_0) + R \cos \theta_0 \quad (22b)$$

If therefore the station location θ_0, ϕ_0 is known in this coordinate system and if the elevation angle γ as well as the azimuth α is also known, it is then an easy matter to determine the range correction using Eq. (19). However, coordinates are usually given in an Earth-fixed geographical coordinate system. We must therefore perform a transformation from the coordinate system of Fig. 1 to the conventional geographical system. Figure 3 will help to do this. There we show the old coordinate system x, y, z (x pointing toward the Sun and y lying in the equatorial plane) together with the new coordinate system X, Y, Z , where X and Y lie in the Earth's equatorial plane, and X defines the Greenwich meridian. The angle T between the Greenwich meridian and the direction x toward the Sun is called the universal time. The declination δ of the Sun is also known. From Fig. 3 it is clear that the connection between x, y, z and X, Y, Z is given by

$$\left. \begin{aligned} X &= x \cos T \cos \delta x - \sin T y - \cos T \sin \delta z \\ Y &= y \sin T \cos \delta x + \cos T y - \sin T \sin \delta z \\ Z &= z \sin \delta x + \cos \delta z \end{aligned} \right\} \quad (23)$$

Inverting Eqs. (22) yields

$$\left. \begin{aligned} x &= X \cos T \cos \delta X + \sin T \cos \delta Y + \sin \delta Z \\ y &= Y - \sin T X + \cos T Y \\ z &= Z - \cos T \sin \delta X - \sin T \sin \delta Y + \cos \delta Z \end{aligned} \right\} \quad (24)$$

Let us introduce polar coordinates θ_G and ϕ_G , where θ_G is the geographical colatitude ranging from 0 to π and ϕ_G is the geographical longitude ranging from 0 (at Greenwich) to 2π (again at Greenwich). The other angles of the ray path, γ and α in the old coordinate system, are also partially affected by the coordinate transformation. It is clear that γ is unaffected; however α goes over into α_G . Presently, with the aid of Eqs. (23) and (24), we will give the connections between the angles $\theta_G, \phi_G, \alpha_G$, and θ_0, ϕ_0 , and α . They are obtained by expressing x, y, z and XYZ in their respective polar coordinates, and read

$$\cos \theta_G = \sin \delta \sin \theta_0 \cos \phi_0 + \cos \delta \cos \theta_0 \quad (25a)$$

$$\begin{aligned} \sin \theta_G \cos \phi_G &= -\cos T \sin \delta \cos \theta_0 \\ &+ \cos T \cos \delta \sin \theta_0 \cos \phi_0 \\ &- \sin T \sin \theta_0 \sin \phi_0 \end{aligned} \quad (25b)$$

$$\begin{aligned} \sin \theta_G \sin \phi_G &= -\sin T \sin \delta \cos \theta_0 \\ &+ \sin T \cos \delta \sin \theta_0 \cos \phi_0 \\ &+ \cos T \sin \theta_0 \sin \phi_0 \end{aligned} \quad (25c)$$

These equations may be used to obtain θ_0 and ϕ_0 once T and δ as well as the station location θ_G and ϕ_G are known. The three equations (25) are of course not independent. Any two of these equations may be used for the determination of θ_0 and ϕ_0 . It is at the discretion of the programmer which equations to choose. Again, from Eqs. (20) and (24), it is easy to find expressions which determine the azimuth α once α_G , the azimuth given in an Earth-fixed system, is known. Here we display two equations which determine $\cos \alpha$ and $\sin \alpha$ as long as θ_0 and ϕ_0 have been computed from Eqs. (25):

$$\begin{aligned} \sin \gamma \cos \theta_G + \cos \gamma \cos \alpha_G \sin \theta_G &= \sin \delta (\sin \gamma \sin \theta_0 \cos \phi_0 - \cos \gamma \cos \alpha \cos \theta_0 \cos \phi_0 - \cos \gamma \sin \alpha \sin \theta_0) \\ &+ \cos \delta (\sin \gamma \cos \theta_0 + \cos \gamma \cos \alpha \sin \theta_0) \end{aligned} \quad (26a)$$

and

$$\begin{aligned} &\sin \gamma \sin \theta_G \cos \phi_G \\ &- \cos \gamma \cos \alpha_G \cos \theta_G \cos \phi_G \\ &- \cos \gamma \sin \alpha_G \sin \theta_G \sin \phi_G = \cos T \cos \delta (\sin \gamma \sin \theta_0 \cos \phi_0 - \cos \gamma \cos \alpha \cos \theta_0 \cos \phi_0 - \cos \gamma \sin \alpha \sin \theta_0) \\ &\quad - \sin T (\sin \gamma \sin \theta_0 \sin \phi_0 - \cos \gamma \cos \alpha \cos \theta_0 \sin \phi_0 + \cos \gamma \sin \alpha \cos \phi_0) \\ &\quad - \cos T \sin \delta (\sin \gamma \cos \theta_0 + \cos \gamma \cos \alpha \sin \theta_0) \end{aligned} \quad (26b)$$

It is now clear how to proceed in order to determine the range correction, Eq. (19). Once the parameters of the ray path are known it is not difficult to trace the analysis back with the help of the equations given above and actually compute the range correction for all contingencies. Suppose the colatitude θ_0 and the longitude ϕ_0 of a station are known, suppose also that the universal time T and the declination of the sun δ are known at a particular epoch.

It is then possible to determine the angles θ_0 and ϕ_0 with the help of Eqs. (25). Furthermore, the elevation angle γ and the azimuth α_0 of the ray path are also known. It is then possible to determine α from Eqs. (26). Once θ_0 , ϕ_0 , and α (γ is obviously invariant) are ascertained in the manner just described, Eqs. (22) must be used in conjunction with Eqs. (19) and (15) to obtain the range correction.

After having determined all geometrical quantities, the three parameters of the ionosphere profile (the scale height H , the altitude at which the maximum electron density occurs, h_{\max} , and the maximum electron density $N_{e \max}$) must be determined. Faraday rotation measurements determine the total electron content, in essence the integral of expression (15) over the ray path between the observing station and a satellite. Ionosonde measurements determine $N_{e \max}$ and h_{\max} (Ref. 8).

Once h_{\max} and $N_{e \max}$ are known, it is possible to determine the scale height H from the total electron content as found from Faraday rotation measurements in conjunction with Eq. (15). Concluding this section, we display a few plots based on the theory developed on the preceding pages. Displayed are comparisons between

the original Chapman equation (Eq. 3) and the more general expression, Eq. (15), as applied to the range correction, Eq. (19). The azimuth α is set equal to zero in all computations.

Figure 4 shows, for an elevation angle of $\gamma = 0$ deg, that for all solar zenith angles, except around 25 deg, the range equivalent difference between Eq. (15) and Eq. (3) is larger than 1 m. The Deep Space Network range accuracy is specified to be better than 1 m.

It is therefore clear that the Chapman ionosphere is inadequate. Figure 5 shows a similar comparison for an elevation angle of $\gamma = 15$ deg. The situation is somewhat better, however; at a solar zenith angle χ of 50 deg, the difference between the exact expression of Eq. (15) and the naive Chapman formulation is again an intolerable meter and becomes worse for larger χ .

Figure 6 displays the range correction as a function of the elevation angle γ rather than the solar zenith angle χ as in the preceding figures. Here it is seen that for large elevation angles (near zenith ranging) the discrepancy between the Chapman formulation (Eq. 3) and the exact Eq. (15)² is practically nonexistent. However, for elevation angles below 30 deg, the difference between the two formulations is again of the order of meters.

The conclusion is therefore inescapably that the Chapman electron density profile as given by Eq. (3) is inapplicable when solar zenith angles are large (>40 deg) and elevation angles are small (<30 deg).

²Within the context of the underlying model.

References

1. See, for instance, Ginzburg, V. L., *Propagation of Electromagnetic Waves in Plasma*, Gordon and Breach, New York, 1961.
2. von Roos, O. H., "Second Order Charged Particle Effects on Electromagnetic Waves in the Interplanetary Medium," in *The Deep Space Network Progress Report*, Technical Report 32-1526, Vol. II, pp. 42-48. Jet Propulsion Laboratory, Pasadena, Calif., Apr. 15, 1971.
3. Eshleman, R., "Radar Astronomy of Solar System Plasmas in Solar System Radio Astronomy," Lectures presented at the NATO Advanced Study Institute of the National Observatory of Athens, Cape Sounion, August 2-15, 1964.
4. von Roos, O. H., "Tropospheric and Ionospheric Range Corrections for an Arbitrary Inhomogeneous Atmosphere (First Order Theory)," in *The Deep Space Network Progress Report*, Technical Report 32-1526, Vol. II, pp. 42-48. Jet Propulsion Laboratory, Pasadena, Calif., Apr. 15, 1971.
5. Garriott, O. K., Smith, F. L., and Yuen, P. C., "Observations of Ionospheric Electron Content Using a Geostationary Satellite," *Planet. Space Sci.*, Vol. 13, pp. 829-838, Aug. 1965.
6. Chapman, S., *Proc. Roy. Soc.*, Vol. 43, p. 26, 1931.
7. Chapman, S., *Proc. Roy. Soc.*, Vol. 43, p. 483, 1931.
8. Rishbeth, H., and Garriott, O. K., *Introduction to Ionospheric Physics*, Academic Press, New York and London, 1969.

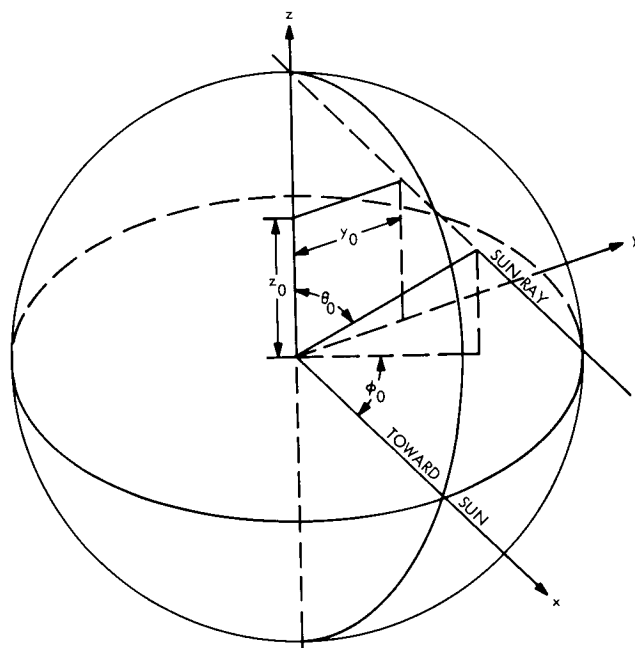


Fig. 1. Geometry of the system

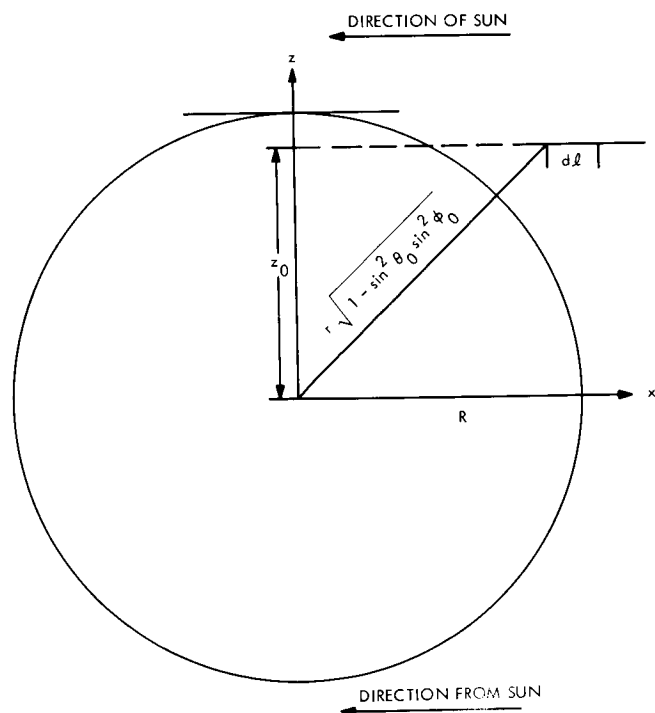


Fig. 2a. Cross section through the x - z plane of Fig. 1

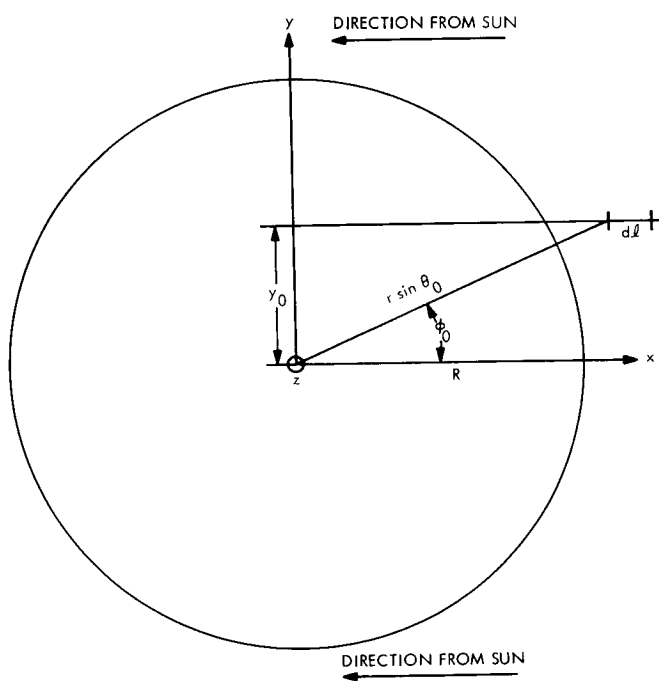


Fig. 2b. Cross section through the x - y plane of Fig. 1

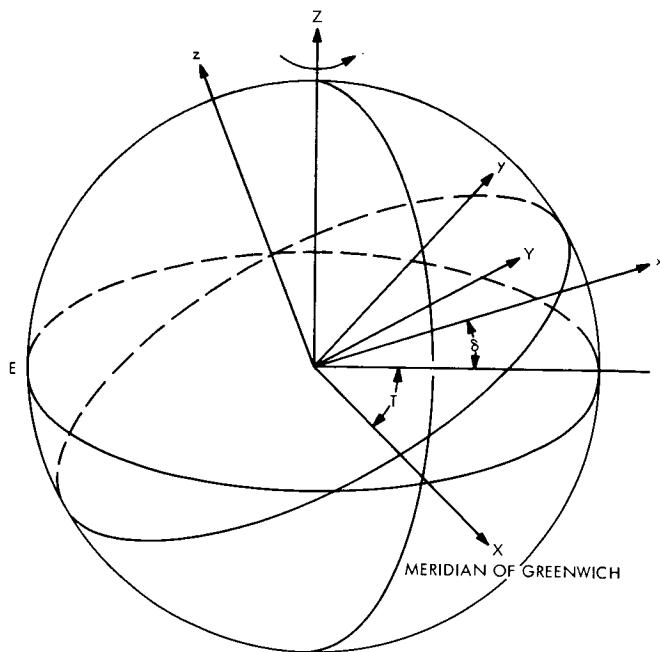


Fig. 3. Transformation from the Sun-oriented to the geographical coordinate system

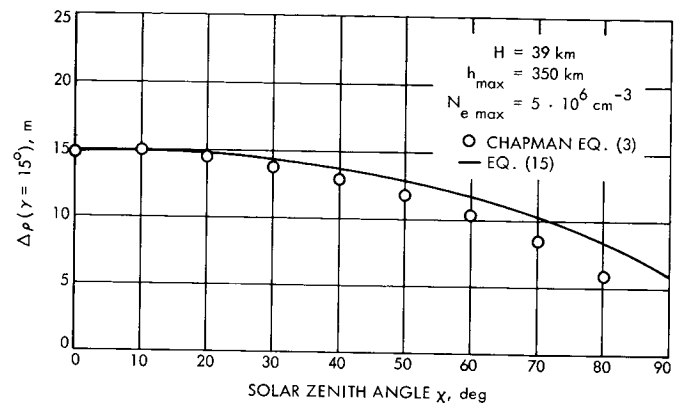


Fig. 5. Solar zenith angle vs range equivalent difference, for elevation angle of 15 deg

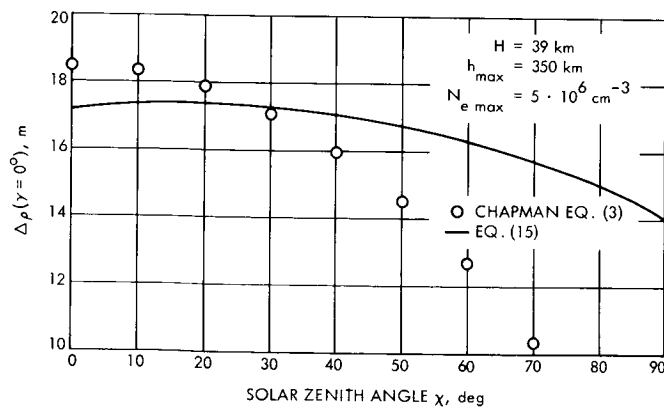


Fig. 4. Solar zenith angle vs range equivalent difference, for elevation angle of 0 deg

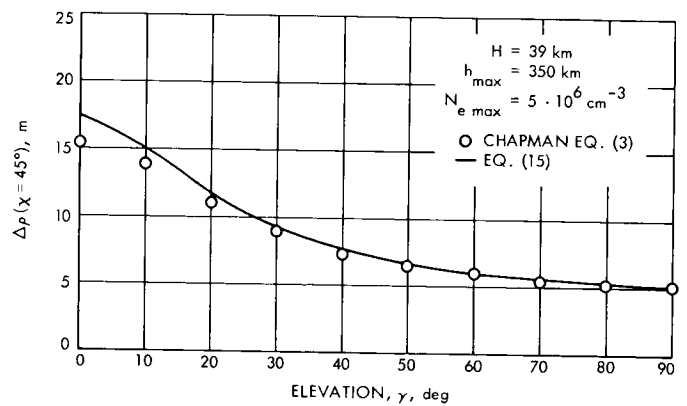


Fig. 6. Elevation angle vs range equivalent difference, for solar zenith angle of 45 deg

Topics in the Implementation and Application of Two-Station Tracking Data Types

K. H. Rourke and V. J. Ondrasik
Tracking and Orbit Determination Section

Two proposed two-station tracking data processing techniques, direct data filtering and differenced data filtering, are analyzed using advanced orbit determination filtering methods. Both techniques are shown to perform comparably, yet direct filtering methods prove to be more sensitive to error model assumptions. Two-station tracking data are shown to be potentially superior to conventional tracking data in determining Deep Space Network tracking station locations.

I. Introduction and Summary of Conclusions

The application of two-station tracking techniques to interplanetary navigation has been treated in several preceding *DSN Progress Report* articles (Refs. 1, 2, and 3). The articles present motivating analysis and orbit determination simulation results establishing two-station tracking techniques as an analytically practicable means for improving interplanetary navigation performance when conventional radio techniques are degraded by low declination geometry or poorly modeled spacecraft accelerations.

This article treats two topics: (1) the alternatives available in processing the simultaneous tracking data (the data can either be used directly or be explicitly differenced before it is processed to obtain orbit determination estimates), and (2) the use of two-station tracking to obtain more reliable station location determinations.

The general conclusions obtained from the analysis of these topics can be stated as follows:

- (1) Directly processing simultaneous tracking data and processing explicitly differenced simultaneous tracking data provide a feasible means for obtaining reliable orbit determination estimates.
- (2) The direct processing method, although potentially more powerful than explicitly differencing, places increased demands on the problem of orbit determination filter design. Errors due to spacecraft nongravitational accelerations are virtually eliminated by either technique. However, variations in the design of the filters used in implementing the directly processed data introduce significant variations in the effects due to other orbit determination error sources, e.g., station location errors.

- (3) The use of two-station tracking data eliminates station location determination errors resulting from spacecraft unmodeled acceleration, and therefore two-station techniques promise to be extremely useful in obtaining accurate station location solutions.

II. Directly Processing Simultaneous Tracking Data

The proper treatment of the simultaneous tracking data is discussed in Ref. 3, which points out that because available geocentric information is deleted from the differenced simultaneous data, better orbit determination performance may result by directly processing the simultaneous data with an orbit determination filter that properly accounts for the noisy spacecraft dynamics (sometimes referred to as process noise). The proper filtering is required to assure that the affected geocentric information is used without permitting the solution to become highly sensitive to acceleration uncertainties. The conventional batch orbit determination filters have only a limited acceleration error modeling capability; thus the proper treatment of the nondifferenced simultaneous data requires advanced filtering techniques, namely, the use of sequential filtering methods.

Although the advanced filtering methods can be expected to be less sensitive to process noise, their design requires an explicit specification of the expected process noise level. This introduces a possible sensitivity of the filter performance to the process noise assumptions used in the filter design. This possibility is investigated in this article by comparing the treatment of simulated tracking data—differenced and nondifferenced simultaneous range and range rate—by a selection of orbit determination filters, differing with respect to the process noise assumptions used in their design.

The results indicate that although the advanced filtering methods prove effective in reducing the sensitivity of the orbit determination errors to process noise, filter performance does vary considerably with respect to the process noise assumptions when the filter is operating on conventional and nondifferenced simultaneous tracking data. The differenced tracking data are virtually unaffected by process noise and, accordingly, the varying filter designs produce only insignificant variations in filter performance.

III. Filter Nomenclature

The following analysis consists of a comparison of several sequential filters as they are applied to a set of simulated tracking data. Before proceeding with the comparison, it is appropriate to introduce several basic concepts concerning sequential filters. The filtering algorithm used in this analysis is described in detail in Ref. 4. The algorithm is fundamentally equivalent to the Kalman sequential filter (see Ref. 5), although it is implemented in the numerically more stable "square root" form. The Kalman filter is predicated on the following linearized state dynamics and data models:

$$\left. \begin{aligned} x_{k+1} &= \Phi(k+1, k)x_k + \Gamma(k+1, k)u_k \\ z_k &= H_k x_k + v_k, \quad k = 1, \dots, N \end{aligned} \right\} \quad (1)$$

where x_k is the state vector at a particular stage k , representing the value of a "to be solved for" parameter vector evaluated at time t_k . For instance, one may have

$$x_k = \begin{bmatrix} \delta x(t_k) \\ \delta y(t_k) \\ \delta z(t_k) \\ \delta \dot{x}(t_k) \\ \delta \dot{y}(t_k) \\ \delta \dot{z}(t_k) \end{bmatrix}$$

where δx , δy , δz and $\delta \dot{x}$, $\delta \dot{y}$, $\delta \dot{z}$ are displacements in the components of spacecraft position and velocity relative to a nominal position and velocity, and

$$\Phi(t_{k+1}, t_k) = \frac{\partial(x(t_{k+1}), \dots, \dot{z}(t_{k+1}))}{\partial(x(t_k), \dots, \dot{z}(t_k))}$$

is the state transition matrix.

The vector x_k may also include other solve for parameters such as station locations and spacecraft accelerations. The u_k is the process noise vector, a sequentially uncorrelated stochastic variable with covariance function

$$Eu_k u_j^T = Q_k \delta_{kj} \quad (2)$$

Process noise allows the introduction of statistical uncertainty into the state dynamics, and as in the following application, can represent the effects of random accelerations on a spacecraft.

The data equation in Eq. (1) represents the navigation data in linearized form, i.e.,

$z_k = (\text{observed data} - \text{computed data}), \text{ available at the } k\text{th stage, and}$

$$H_k = \frac{\partial(\text{observable})}{\partial x_k}$$

The z_k is a vector representing data taken over times $t, t_k < t < t_{k+1}$. The v_k is assumed to be a sequentially uncorrelated data noise vector with covariance function

$$E v_k v_j^T = R_k \delta_{kj} \quad (3)$$

The statistical assumptions concerning Eq. (1) are fully determined upon the specification of an a priori covariance for the state vector; i.e.,

$$E x_1 x_1^T = P_1 \quad (4)$$

Given a model (Eq. 1) the specification of Eqs. (2), (3), and (4) determines a minimum variance sequential filter for estimating x_k given the data $z_j, j = 1, \dots, k$. A sequential formula (Ref. 5) for the estimate x_k is given by

$$\hat{x}_{k+1} = \Phi(t_{k+1}, t_k) (\hat{x}_k + K_k [z_k - H_k \hat{x}_k]), k = 1, \dots, N \quad (5)$$

where the filter "gain" K_k is given by

$$K_k = P_k H_k^T (H_k P_k H_k^T + R_k)^{-1} \quad (6)$$

with the filter covariance of estimate errors P_k determined by the following sequential relationship:

$$P_{k+1} = \Phi(t_{k+1}, t_k) (I - K_k H_k) P_k (I - K_k H_k)^T \Phi(t_{k+1}, t_k)^T + \Gamma(t_{k+1}, t_k) Q_k \Gamma(t_{k+1}, t_k)^T, \quad k = 1, \dots, N \quad (7)$$

These formulas are determined initially by assumed values for P_1 and \hat{x}_1 .

Under the assumption that $Q_k = 0$ for all k , the model is easily reformatted into the familiar batch or minimum variance parameter estimation form

$$z = Ax + \epsilon$$

where

$$z = \begin{pmatrix} z_1 \\ \vdots \\ \vdots \\ \vdots \\ z_n \end{pmatrix}$$

$$\epsilon = \begin{pmatrix} v_1 \\ \vdots \\ \vdots \\ \vdots \\ v_n \end{pmatrix}$$

and x may be any particular $x_k, k = 1, \dots, N$ since any one state vector value now uniquely determines all other values.

IV. Filter Performance and Q Magnitude

It is pointed out in Section III that the conventionally implemented batch filter can be considered as a sequential filter with $Q_k = 0, k = 1, \dots, N$. The restrictive error modeling capability of the batch filter may allow degradations in filter performance in certain applications. Specifically, in the case of a spacecraft affected by random accelerations, the conventional batch navigation filters have exhibited significant performance degradations (Ref. 6.)

With the application of sequential filters, with $Q_k \neq 0$, a new problem arises: the selection of the proper sequence of covariance matrices $Q_k, k = 1, \dots, N$. This problem is accompanied by the problem of selecting the proper sequence of data weights $R_k, k = 1, \dots, N$, a problem that can be handled somewhat arbitrarily for the batch filter. Often the general character of the R and Q matrices is reasonably well known with only their "magnitude" being uncertain. That is, assume matrices \bar{R}_k and \bar{Q}_k can be specified so that "proper" specification of R_k and Q_k entails only the selection of scalars r and q so that

$$R_k = r \bar{R}_k \text{ and } Q_k = q \bar{Q}_k, k = 1, \dots, N$$

A simple yet important fact concerning the relation between the values of r and q and filter performance can be stated as follows: Filter implementation as specified by the gain sequence $K_k, k = 1, \dots, N$, is unaffected by the absolute magnitudes of r and q , and depends only on their ratio q/r . Thus, given \bar{R} and \bar{Q} , the variations in filter performance (with respect to a fixed and not necessarily known error environment) can be ascertained by investigations of the effects of q (or r) variations alone. This result can be demonstrated inductively by noting that if

$$P_1 = q F_1 \left(\frac{q}{r} \right) + r G_1 \left(\frac{q}{r} \right)$$

for particular functions $F_1(\cdot)$ and $G_1(\cdot)$, then

$$K_1 = K_1 \left(\frac{q}{r} \right)$$

by Eq. (6), and if

$$P_k = qF_k \left(\frac{q}{r} \right) + rG_k \left(\frac{q}{r} \right)$$

then

$$K_k = K_k \left(\frac{q}{r} \right)$$

$$P_{k+1} = qF_{k+1} \left(\frac{q}{r} \right) + rG_{k+1} \left(\frac{q}{r} \right)$$

by Eq. (7).

V. Analysis of Simulated Tracking Data

The effect of varying filter Q levels is analyzed in the following through the evaluation of sequential filters in terms of their operation on simulated tracking data. The simulated data were generated from rigorous orbit determination analysis software and are contained in two sets. The first contains simulated data residuals that result from a spacecraft being perturbed by random accelerations with a standard deviation of 10^{-12} km/s² and an autocorrelation time of 5 days. The data are the same set used in Ref. 3: simultaneous and conventional tracking strategies applied to the encounter minus 30 days to encounter, data arc of Viking '75 Mission B.

Data set II is data set I with data residuals due to station location errors superimposed. The data-taking strategies and spacecraft trajectory used in generating the simulated data are detailed in Ref. 3.

The station location errors used to generate data set II are presented in Table 1. The errors are arbitrarily selected and are intended to be representative of the station location errors present for the Viking mission in 1975-1976. Note that the errors contain a bias and a random component, the random component chosen to represent apparent station location error effects such as timing, polar motion, and residual data transmission media calibration effects. The simulated differenced and nondifferenced range rate and range residuals for data sets I and II are shown in Figs. 1-4.

Four filters are applied to each of the data sets. Each filter solved for only the position and velocity of the spacecraft. The filters differ by their assumed Q levels. The Q matrices are determined by the assumption that the spacecraft experiences three-axis, spherically distributed piecewise constant accelerations, constant over 1 day and uncorrelated from day to day. The " Q level" is specified by the assumed single-axis acceleration standard deviations, with the four Q levels being 0, 10^{-12} , 10^{-11} and 10^{-10} km/s². The zero- Q level filter processes the tracking data as if it were a batch filter.

The results of the simulated data analysis are presented in Figs. 5-7. The results are presented in terms of estimates and standard deviations of the B -plane parameter $B \cdot R$, a position component particularly difficult to determine for the Viking mission B. The errors are presented for varying data arcs, from epoch to encounter minus 0.5, 5, 10, 15 and 20 days (encounter occurs at 30 days past epoch.) Since the simulated tracking data are due solely to modeled tracking data errors, the estimates ($\Delta B \cdot R$) are resulting navigation errors. The $\Delta B \cdot R$ (Deep Space Station (DSS)) are the estimate errors due to station location errors alone (data set II minus data set I) while the $\Delta B \cdot R$ (attitude control acceleration (ATA)) are the estimate errors due to acceleration errors alone (data set I.)

Figure 5 shows that, when using conventional data, the effects of the acceleration errors on the $B \cdot R$ estimates are significantly reduced with each increase in the Q level. Note, however, that the Q -level variations produce large differences in the responses to the station location errors, $\Delta B \cdot R$ (DSS). This is a disquieting characteristic in that the effects due to station location errors are usually expected to be perhaps large but stable with respect to various filter implementations.

Assessment of the general nature of these effects cannot be obtained through analysis of a few simulated data sets, as presented here; general results will require a detailed filter covariance analysis. The implication of these results are clear, however: that sequential filters when acting on conventional tracking data can reduce the effects of random spacecraft accelerations, at the expense of variations in the sensitivity to station location errors.

Figure 6 presents the filter performance results for simultaneous range and range rate data. Reference 3 points out that although the simultaneous data improve

station location error sensitivities (for near-zero declination spacecraft), the tight range specification greatly magnifies the random acceleration effects. This effect is well illustrated in Fig. 6. Note that the simultaneous data filter sigmas are more sensitive to the Q level assumptions than the conventional data filter sigmas. The batch filter is seen to be very sensitive to random acceleration, yet sufficiently large Q levels essentially eliminate the acceleration effects. The station location error effects, unfortunately, show even larger variations with changing Q level.

Figure 7 shows the differenced range and range rate $B \cdot R$ sigmas and errors for the batch filter only. The $Q \neq 0$ filters are not shown because their estimates are virtually unaffected by Q level. Similarly, the error responses due to random accelerations are not shown since they are all essentially zero.

One can conclude from these results that although the simultaneous range and range data may be, in principle, potentially superior to differenced data, initial applications using advanced filtering methods indicate that the results are particularly sensitive to filter model assumptions and not clearly superior to processing the differenced data with conventional filters.

VI. Station Location Determinations From Two-Station Tracking

In the analytical analysis of a single pass of radio tracking data performed in Ref. 1, it was shown how the effects of unmodeled spacecraft (S/C) accelerations can be expressed in terms of equivalent station location errors. Thus it should be expected that unmodeled S/C accelerations will degrade station location solutions obtained from radio metric tracking data. Since, as shown above, the effects of unmodeled S/C accelerations can be essentially eliminated by differencing simultaneous two-station data, such techniques may be useful in improving station location solutions.

The use of two-station simultaneous tracking data, in particular very long baseline interferometer (VLBI) measurements, is by no means a novel approach in determining station locations. The general effectiveness of such techniques is well established (see Ref. 7), and yet the fact that these methods offer special advantages in almost eliminating the station location solution sensitivities to S/C accelerations is not widely realized. The S/C

acceleration errors may include gravitational as well as nongravitational effects. For example, seemingly small S/C position errors or gravitational model errors can give rise to significant S/C acceleration discrepancies during planetary encounter and satellite phases of a mission.

To obtain some idea of the station location sensitivities to the unmodeled S/C accelerations, a brief "consider" covariance analysis was performed for the Saturn portion of a Jupiter-Saturn mission described in Ref. 8. This analysis was based upon a batch filter which estimated or considered the parameters shown in Table 2. For comparison, parallel analyses were carried out for long arc data sets which, as shown in Table 3, were identical except that in case 1 the simultaneous data are used directly and in case 2 the simultaneous data are explicitly differenced before processing.

The effects of the random data noise on the station locations solutions for cases 1 and 2 are expressed in terms of the formal standard deviations given in Fig. 8. The formal standard deviations associated with the differenced data are typically four times larger than the same quantities associated with the nondifferenced data. It is expected that the differenced data formal statistics will be larger, because, as mentioned previously, the differencing procedure deletes the acceleration information.

Figure 8 also contains the sensitivities of the station location solutions to errors in the planetary gravitational constant (GM) and to a constant S/C acceleration in the Sun-to-S/C direction. These sensitivities are represented in terms of errors in the station location solutions produced from errors in GM and S/C accelerations of magnitude $0.6 \times 10^2 \text{ km}^3/\text{s}^2$ and $0.5 \times 10^{-12} \text{ km/s}^2$, respectively. These sensitivity bars represent the effect of the particular error source only, and scale directly with the magnitude of the error. An examination of Fig. 8 clearly shows that if the unmodeled accelerations are present at the indicated levels, the long arc station location solutions will contain catastrophic errors unless the data are differenced.

Undoubtedly, it is possible to process conventional data so that the station location sensitivities to unmodeled S/C accelerations can be reduced from those shown in Fig. 8. However, Fig. 8 does show that the use of differenced data may be extremely useful in obtaining accurate station location solutions and that the concept certainly deserves a more detailed investigation.

References

1. Rourke, K. H., and Ondrasik, V. J., "Application of Differenced Tracking Data Types to the Zero Declination and Process Noise Problems," in *The Deep Space Network Progress Report*, Technical Report 32-1526, Vol. IV, pp. 49-60. Jet Propulsion Laboratory, Pasadena, Calif., Aug. 15, 1971.
2. Ondrasik, V. J., and Rourke, K. H., "An Analytical Study of the Advantages Which Differenced Tracking Data May Offer for Ameliorating the Effects of Unknown Spacecraft Accelerations," in *The Deep Space Network Progress Report*, Technical Report 32-1526, Vol. IV, pp. 61-70. Jet Propulsion Laboratory, Pasadena, Calif., Aug. 15, 1971.
3. Rourke, K. H., and Ondrasik, V. J., "Improved Navigation Capability Utilizing Two Station Tracking Techniques for a Low-Declination Distant Spacecraft," in *The Deep Space Network Progress Report*, Technical Report 32-1526, Vol. VII, pp. 51-60. Jet Propulsion Laboratory, Pasadena, Calif., Feb. 15, 1972.
4. Esposito, P. B., Thornton, C. L., Anderson, J. D., and Muhleman, D. O., "Classical Least Squares and Sequential Estimation Techniques as Applied to the Analysis of the Mariner VI and VII Tracking Data," AAS Paper No. 71-384, Presented at the AAS/AIAA Astrodynamics Specialists Conference, Aug. 17-19, 1971, Fort Lauderdale, Fla.
5. Kalman, R. E., "A New Approach to the Linear Filtering and Prediction Problems," *Trans. ASME, J. Basic Eng., Ser. D*, Vol. 82, pp. 35-40, Mar. 1960.
6. Rourke, K. H., "Viking Orbit Determination Analysis Bi-Monthly Report: A Preliminary Report on the Application of a Sequential Filter to the MM71 Approach Radio Tracking Data," IOM 391.2-280. Jet Propulsion Laboratory, Pasadena, Calif., Mar. 22, 1972 (JPL internal document).
7. Williams, J. G., "Very Long Baseline Interferometry and Its Sensitivity to Geophysical and Astronomical Effects," *Space Programs Summary* 37-62, Vol. II, pp. 49-54. Jet Propulsion Laboratory, Pasadena, Calif.
8. Ondrasik, V. J., et al., "Preliminary Evaluation of Radio Data Orbit Determination Capabilities for the Saturn Portion of a JSP 77 Mission" (in the present issue of *The Deep Space Network Progress Report*), Jet Propulsion Laboratory, Pasadena, Calif.

Table 1. Assumed station location errors

Error	Bias value, <i>m</i>			Random component standard deviation ^a
	California	Australia	Spain	
Spin axis	1.5	-1.5	1.5	1.0
Radius				
Longitude	3.0	3.0	3.0	1.0
Z height	10.0	10.0	10.0	1.0

^aThe random components are assumed to be due to gaussian first-order markov processes with autocorrelation times equal to 3 days.

Table 2. Estimated and considered parameters for station location solutions

Estimated parameters	A priori	"Consider" parameters	"Consider" σ
S/C position	10^7	Constant acceleration in Sun-S/C direction	$0.5 \times 10^{-12} \text{ km/s}^2$
S/C velocity	1 km/s		
Planetary ephemeris	1000 km		
DSS 14, 42, 61 locations		Planetary GM	$0.6 \times 10^2 \text{ km}^3/\text{s}^2$ ($2 \times 10^{-3} \%$)
Spin axis r_g	1 m		
Longitude λ	2 m		

Table 3. Case numbers and data sets

Case	Description	Data ^a ($E - 120 \rightarrow E + 30$)	Data weight ^b	Stations
1	3 stations	ρ	3 m	14, 42, 61
		$\dot{\rho}$	1 mm/s	14, 42, 61
2	Differenced	ρ	300 m	42
		$\dot{\rho}$	100 mm/s	42
		Diff ρ	3 m	14, 42, 61
		Diff $\dot{\rho}$	1 mm/s	14, 42, 61

^aFor exact tracking pattern, see Ref. 8. ρ = range, $\dot{\rho}$ = range-rate, diff = explicitly differenced data.

^bSee Ref. 8.

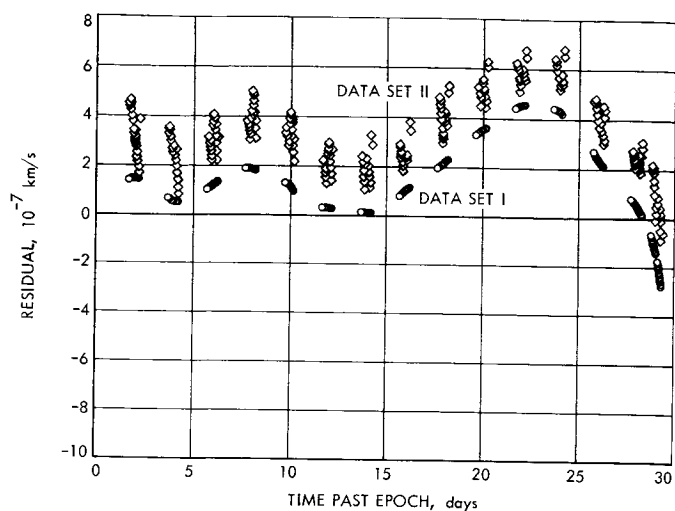


Fig. 1. Range rate residuals

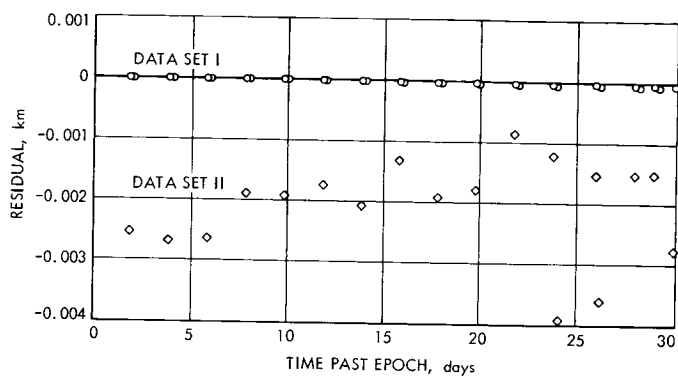


Fig. 4. Differenced range residuals

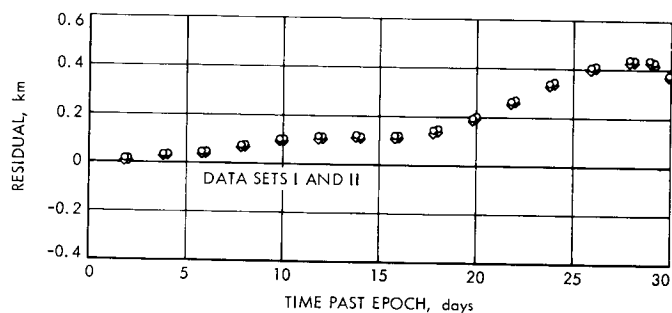


Fig. 2. Range residuals

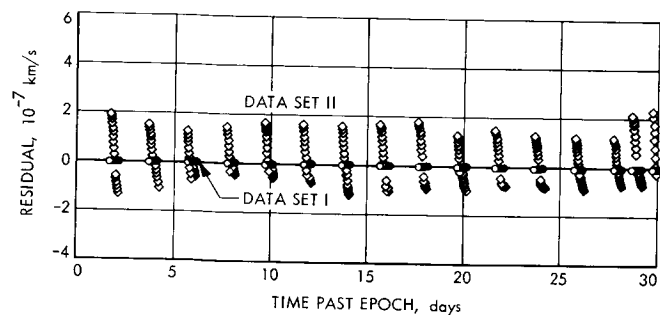


Fig. 3. Differenced range rate residuals

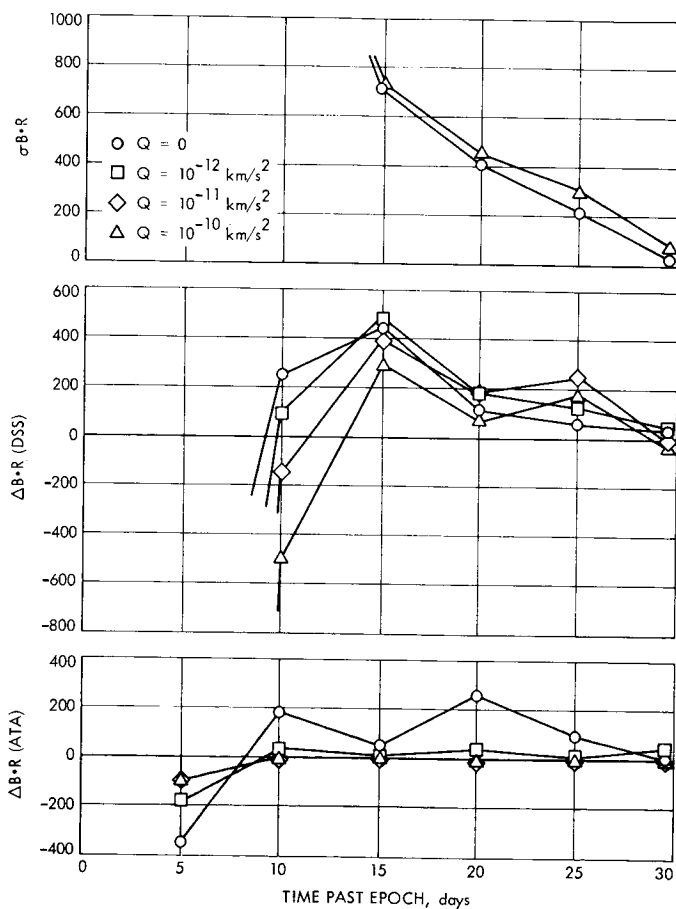


Fig. 5. Conventional range and range rate

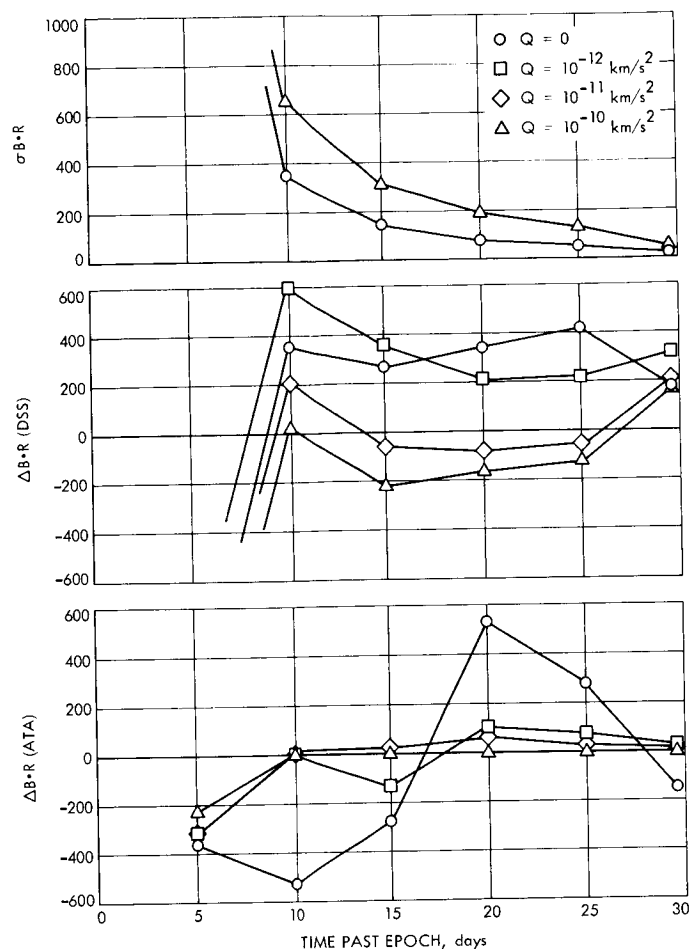


Fig. 6. Simultaneous range and range rate

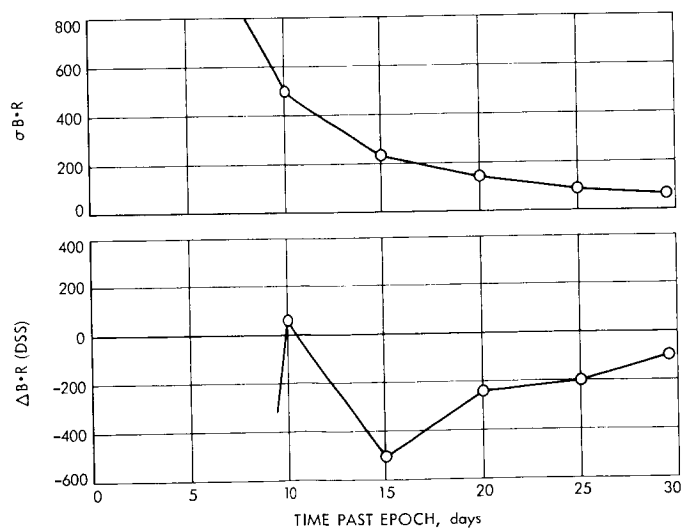


Fig. 7. Differenced range and range rate

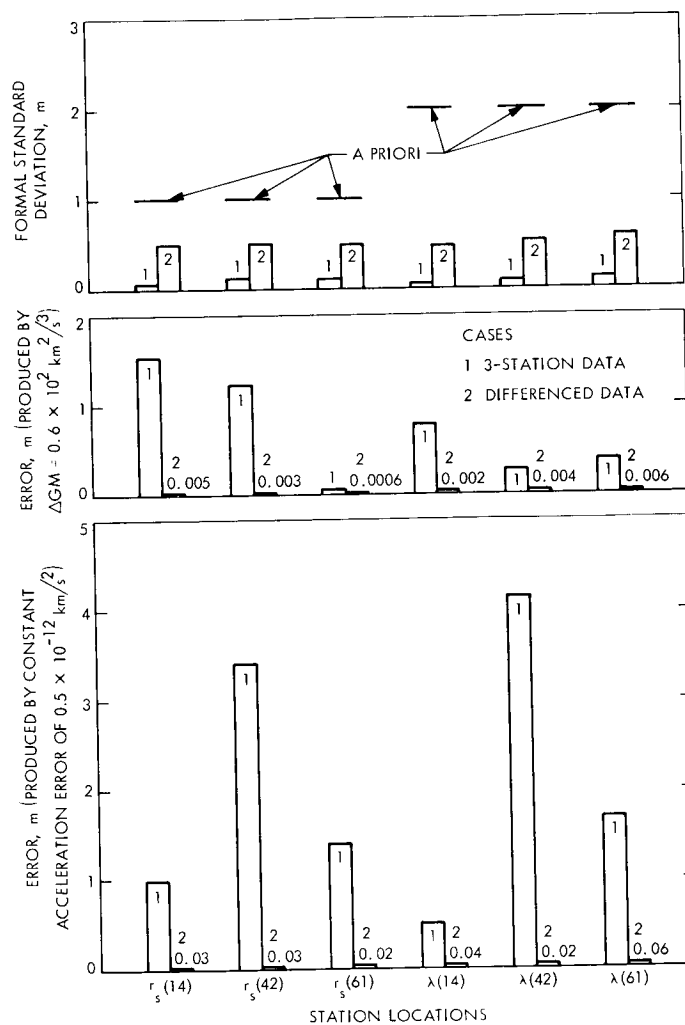


Fig. 8. Station location formal standard deviations and errors produced by GM and constant acceleration errors

Low Noise Receivers: Microwave Maser Development

R. Clauss, E. Wiebe, and R. Quinn
Communications Elements Research Section

A traveling wave maser, tunable from 7750 to 8750 MHz, has been completed and tested in the laboratory. The maser is ready for installation on the 64-m-diameter antenna at the Deep Space Communications Complex at Goldstone, Calif. Gain, phase, and group delay stability were measured as a function of magnetic field, refrigerator temperature, power supply voltages and large interfering signals. Several features have been included in this maser to improve the stability performance. A superconducting magnet provides a very stable magnetic field. Push-push pumping results in complete pump saturation and reduced pump frequency stability requirements. Low pass filters at a temperature of 4.5 K reduce pump power radiation in signal waveguides.

The maser has 45 dB net gain and 17-MHz, 3-dB bandwidth with an equivalent input noise temperature of $6\frac{1}{2}$ K at 8415 MHz and $8\frac{1}{2}$ K at 7850 MHz. Simultaneous operation at two frequencies, separated by up to 500 MHz, is available at reduced gain.

I. Introduction

A new X-band traveling wave maser, ready for installation on the 64-m-diameter antenna at the Goldstone Deep Space Communications Complex, is described in this article. Improved stability performance (as compared with previously used X-band masers; see Refs. 1, 2, and 3) has been measured in the laboratory. The results of gain, phase, and group delay stability tests are reported.

II. Maser Description

The maser is a ruby-loaded comb structure similar to one previously described (Ref. 2). The entire package is shown in Fig. 1. A superconducting magnet provides a magnetic field adjustable from 0 to 5500 gauss. A closed-cycle helium refrigerator (CCR) is used to provide a 4.5 K operating environment for the maser comb structure and magnet. The klystron pump package contains

two klystron oscillators and a power combiner for push-push operation. The pump package has been described previously (Ref. 4). The overall package weight (not including the feed horn shown in Fig. 1) is 70 kg. The maser may be operated in any position.

The maser and superconducting magnet are shown in Fig. 2; the CCR vacuum housing and radiation shields are not shown, and the magnet has been removed from the maser. The waveguide-to-coaxial-line transitions at the 4.5 K station (only the input side is shown) each contain 11 element coaxial low pass filters. The filter cutoff is 12 GHz. Rejection at the pump frequencies (18.4 to 19.6 GHz and 22.6 to 24.8 GHz) is more than 30 dB and the voltage standing wave ratio (VSWR) between 7700 and 8800 MHz is less than 1.2 to 1. The signal waveguides are of 0.064-cm-wall stainless steel with copper plating inside to reduce signal frequency loss. The waveguide low frequency cutoff is 6550 MHz.

Figure 3 shows the maser comb structure resting on the 4.5 K station of the CCR. Indium gaskets are used to provide intimate contact between the 4.5 K station, the maser flange, and the superconducting magnet assembly. Coils of wire, wound on the maser structure in a figure-eight pattern, are used to adjust the maser gain by changing the magnetic field shape. The field-shaping coil is controlled by a current-regulated power supply. The persistent mode (Cioffi-type) superconducting magnet and charging circuits were previously tested and reported by Berwin, Wiebe, and Dachel (Ref. 5).

III. Gain, Bandwidth, and Noise Temperature

Net gain of 45 dB is available at any frequency between 7750 and 8750 MHz. The measured equivalent input noise temperature is 10.5 K at 7750 MHz, 8.5 K at 7850 MHz, and 6.5 K from 8000 to 8650 MHz. Tuning across this range is accomplished from the maser control racks. The instantaneous 1-dB and 3-dB bandwidths (at 45-dB gain) are 10 and 17 MHz respectively. Gain vs frequency, with the maser tuned to 8415 MHz, is shown in Fig. 4. Current through the figure-eight field-shaping coil is used to adjust gain and bandwidth (measured values at a maser center frequency of 8415 MHz are shown in Table 1).

IV. Dual Frequency Operation

Current through the figure-eight field-shaping coil can be used to operate the maser at two frequencies separated by as much as 500 MHz. Additional pump sources must

be used to pump both signal frequencies. The maser net gain is between 17 and 22 dB during dual frequency operation. Figure 5 shows the curves for maser net gain vs frequency response during dual frequency operation.

V. Large Signals and Gain Compression

The maser was subjected to signal levels up to 1 mW to determine gain compression (saturation) sensitivity. Figure 6 shows the signal level (as a function of frequency) which causes a 3-dB reduction in maser gain. The maser was adjusted for a net gain of 45 dB at 8420 MHz prior to the test. Figure 7 shows maser gain compression as a function of signal power level at the maser center frequency. Power levels shown are at the maser input.

Two large signals at the maser center frequency, spaced 1 MHz apart, were used to saturate the maser. A level of -28 dBmW at the maser input reduced the net gain to unity. A spectrum analyzer was used to test for mixing products; the system could detect signals 60 dB below the level of the -28 dBmW test signals. No mixing products were observed.

VI. Stability Measurements

Gain, signal phase, and group delay stability measurements were made using a Hewlett-Packard network analyzer. Figure 8 shows the gain and signal phase shift vs frequency; a test signal was swept through the maser bandpass to produce the curve. The reference channel path contained a delay line of approximately 16 m equivalent free space length. The maser group delay at 8415 MHz (at 45 dB net gain) was measured to be 63.9×10^{-9} s (equivalent free space length of 19.17 m).

Changes in maser gain, group delay, and signal phase are caused by changes in the magnetic field, refrigerator operating temperature, and pump frequency and power. Figure 9 shows gain and group delay changes as the refrigerator temperature is changed from 4.32 to 4.76 K. Peak-to-peak signal phase changes were less than 5 deg. The total phase slope change was 0.6 deg/MHz. The measured data were recorded and are shown at two gain levels; the figure-eight field-shaping coil was used to set the specific gain values tested.

Large group delay changes are caused by magnetic field shape changes. Figure 10 shows group delay changes as the maser net gain is changed with the field-shaping

coil. Figure 11 shows changes in gain and group delay as a function of average magnetic field strength. A 1-gauss change in magnetic field produces a 2.5-MHz maser center frequency change. The magnetic field for 8415 MHz operation is 4940 gauss. A 1-gauss change results in a 0.25-dB gain reduction, a 0.40×10^{-9} -s group delay change (12 cm free space distance) and a 28-deg signal phase shift. These changes emphasize the need for a very stable magnetic field. Measurements in the laboratory and on a moving antenna show the superconducting magnet to be 30 times less sensitive to external magnetic fields than permanent magnets previously used with S- and X-band masers (Refs. 2, 3, and 6).

The effects of pump klystron changes are summarized in Table 2. Gain, signal phase, and group delay changes are shown as results of changes in klystron tuning, beam voltage and current, and reflector voltage. Complete pump transition saturation due to push-push pumping (Ref. 7) causes the maser performance to be relatively insensitive to pump frequency or power changes. Long-term phase and gain stability records with the maser operating in the laboratory (fixed position and constant ambient temperature) showed no detectable gain change (resolution 0.1 dB), 4 deg peak-to-peak signal phase

change, and 1.9×10^{-11} -s group delay change (0.57 cm free space distance) during a period of 12 h.

A summary of parameters affecting maser stability is shown in Table 3. The listed variations in pump frequency, power supply voltages, refrigerator temperature, and magnetic field are based on data from maser systems operating on the 64-m-diameter antenna at the present time. The predicted instability combines laboratory test data in this article with the previously measured maser system data. The various instabilities are expected to add in a random manner. The total expected gain, phase, and group delay changes include the effects of antenna motion during a 12-h time period. The total rms changes are as follows: ± 0.12 dB gain, ± 1.1 deg phase, and $\pm 0.08 \times 10^{-9}$ s group delay.

VII. Conclusion

Laboratory test data show the new X-band maser performance to be superior to previously used X-band masers in gain, bandwidth, noise temperature, and stability. The use of push-push pumping, pump frequency filters in the signal waveguides, and a superconducting magnet is responsible for the improved performance.

References

1. Petty, S. M., and Clauss, R. C., "Low Noise Receivers: Microwave Maser Development," in *The Deep Space Network*, Space Programs Summary 37-42, Vol. III, pp. 42-46. Jet Propulsion Laboratory, Pasadena, Calif., Nov. 1966.
2. Clauss, R. C., and Quinn, R. B., "Low Noise Receivers: Microwave Maser Development," in *The Deep Space Network*, Space Programs Summary 37-61, Vol. II, pp. 86-89. Jet Propulsion Laboratory, Pasadena, Calif., January 31, 1970.
3. Clauss, R., and Reilly, H., "Microwave Maser Development," in *The Deep Space Network Progress Report*, Technical Report 32-1526, Vol. VI, pp. 118-122. Jet Propulsion Laboratory, Pasadena, Calif., Dec. 15, 1971.
4. Clauss, R. C., and Quinn, R. B., "Low Noise Receivers: Microwave Maser Development," in *The Deep Space Network Progress Report*, Technical Report 32-1526, Vol. IX, pp. 128-136. Jet Propulsion Laboratory, Pasadena, Calif., June 15, 1972.
5. Berwin, R., Wiebe, E., and Dachel, P., "Superconducting Magnet for a Ku-Band Maser," in *The Deep Space Network Progress Report*, Technical Report 32-1526, Vol. V, pp. 109-114. Jet Propulsion Laboratory, Pasadena, Calif., Oct. 15, 1971.
6. Clauss, R. C., "Low Noise Receivers, Microwave Maser Development, Second Generation Maser," in *The Deep Space Network*, Space Programs Summary 37-51, Vol. II, pp. 73-77. Jet Propulsion Laboratory, Pasadena, Calif., May 31, 1968.
7. Clauss, R., "RF Techniques Research: System Studies for Frequencies above S-band for Space Communications," in *Supporting Research and Advanced Development*, SPS 37-61, Vol. III, pp. 90-93. Jet Propulsion Laboratory, Pasadena, Calif., Feb. 1970.

**Table 1. Maser gain and bandwidth at 8415 MHz
vs magnetic field shape**

Net gain, dB	Bandwidth, MHz		Field-shaping coil current, mA
	(1 dB)	(3 dB)	
57	8	13	180
45	10	17	270
35	14	26	300
30	23	35	315
25	42	53	330

**Table 2. Pump system stability effects with maser at 45 dB
net gain at 8415 MHz**

Pump system change	Gain change, dB	Signal phase change, deg	Group delay change, 10^{-9} s	Equivalent free space path length, cm
24-GHz klystron, retune ± 10 MHz	-0.1	± 1.7	± 0.11	± 3.3
19-GHz klystron, retune ± 10 MHz	-0.2	± 2.2	∓ 0.09	∓ 2.7
24-GHz klystron, beam voltage, ± 30 V	-0.3	∓ 0.2	± 0.06	± 1.8
19-GHz klystron, beam voltage, ± 30 V	-0.7	< 0.1	± 0.13	± 3.9
24-GHz klystron, reflector voltage, ± 20 V	-0.4	∓ 0.3	± 0.12	± 3.6
19-GHz klystron, reflector voltage, ± 20 V	-0.5	∓ 0.3	∓ 0.02	∓ 0.6

Table 3. Predicted maser system stability characteristics for 12 h on 64-m-diameter antenna at 8415 MHz

Variable parameter	Parameter change	Maser performance change			
		Gain, dB	Signal phase, deg	Group delay, 10^{-9} s	Equivalent free space distance, cm
Refrigerator temperature	± 0.005 K	∓ 0.08	< 0.1	∓ 0.04	∓ 1.2
Average magnetic field strength	± 0.03 gauss	-0.01	± 1.0	-0.01	-0.3
Field-shaping coil current	± 0.2 mA	∓ 0.06	< 0.1	∓ 0.06	∓ 1.8
24-GHz klystron pump frequency	± 2 MHz	-0.02	± 0.3	± 0.02	± 0.6
19-GHz klystron pump frequency	± 2 MHz	-0.04	± 0.4	± 0.02	± 0.6
Klystron power supply voltages	± 1 V	-0.04	< 0.1	± 0.01	± 0.3
Random combination of variable parameters	As above	± 0.12 rms	± 1.1 rms	± 0.08 rms	± 2.4 rms

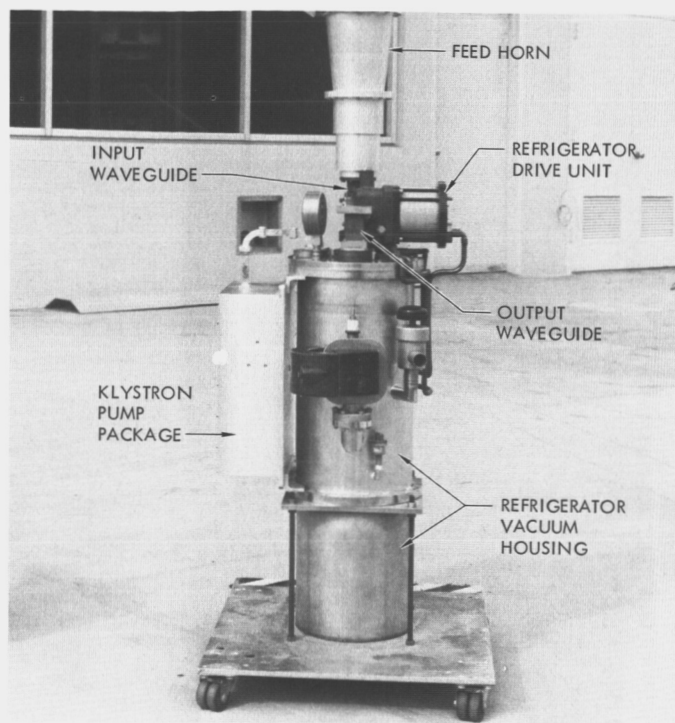


Fig. 1. X-band traveling wave maser assembly

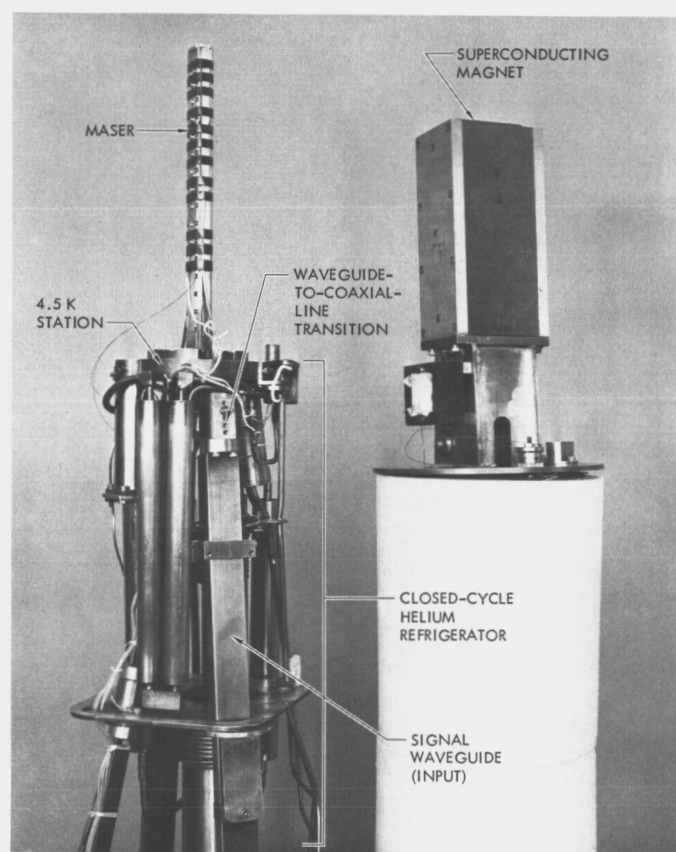


Fig. 2. Maser, superconducting magnet, and closed-cycle helium refrigerator

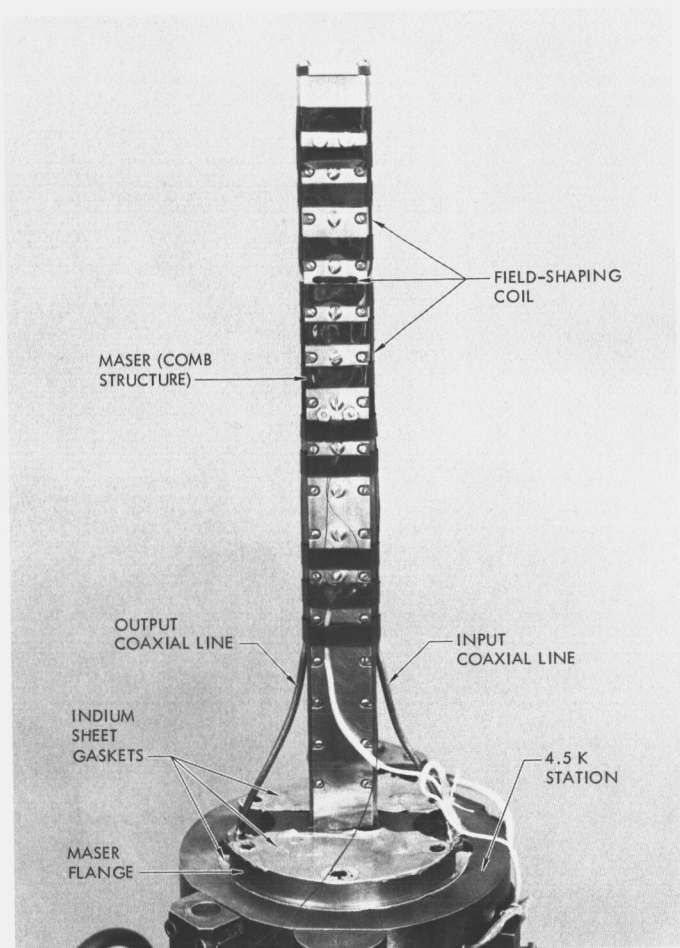


Fig. 3. Maser structure on 4.5-K heat station

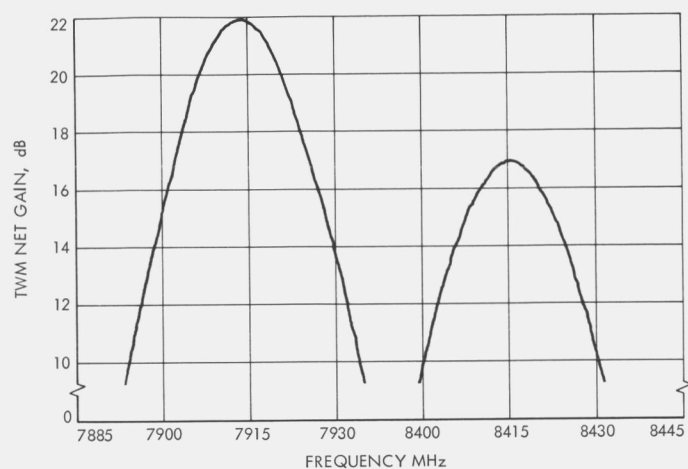


Fig. 4. Gain vs frequency for maser at 8415 MHz

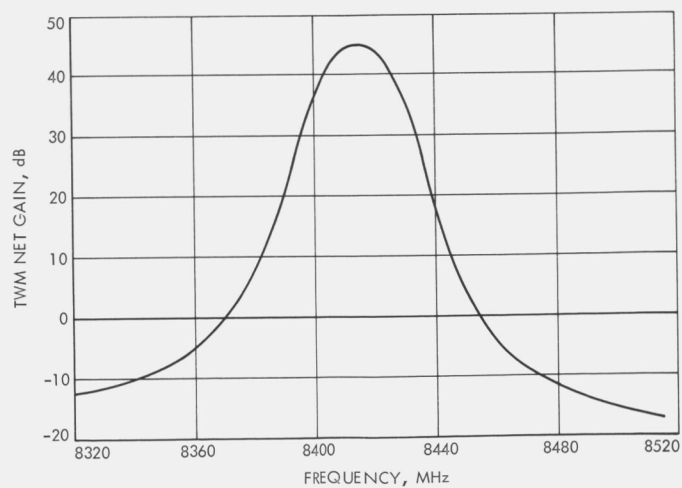


Fig. 5. Gain vs frequency for simultaneous operation at two frequencies

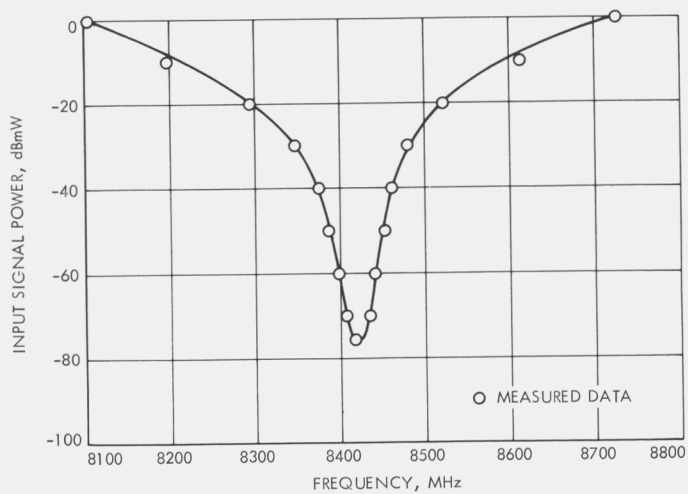


Fig. 6. Signal input power vs frequency for 3-dB maser gain compression

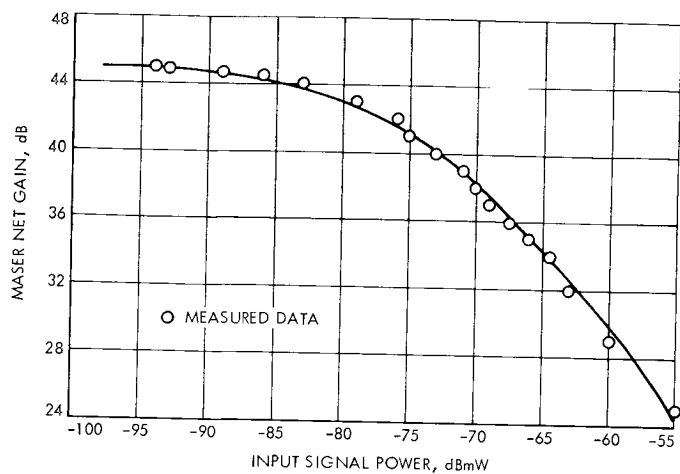


Fig. 7. Signal power vs gain at the maser center frequency

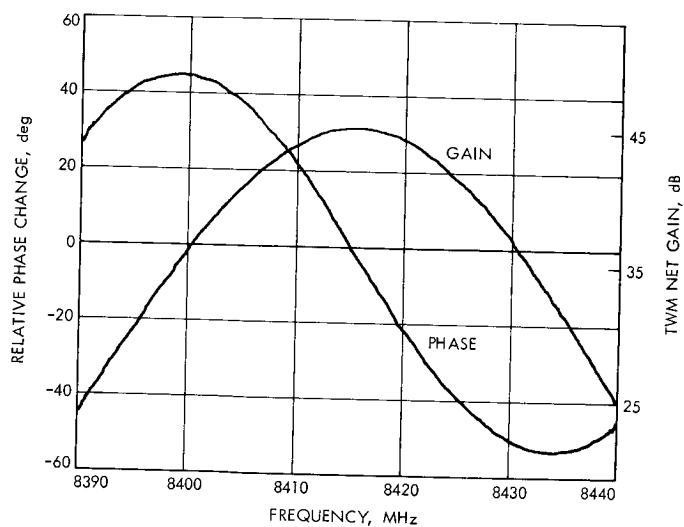


Fig. 8. Maser gain and phase shift vs frequency

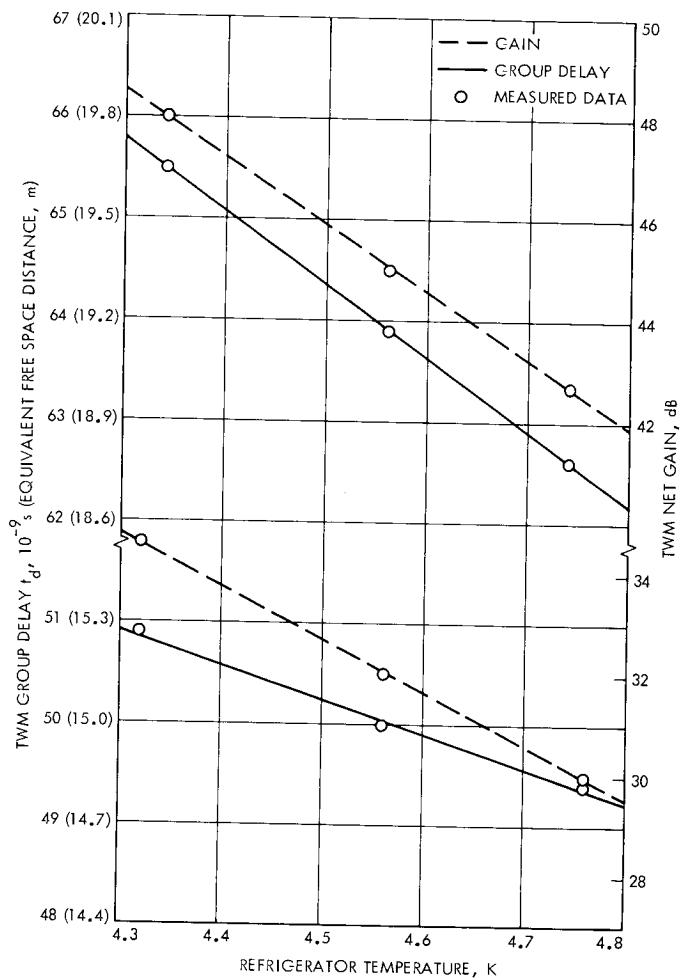


Fig. 9. Gain and group delay vs refrigerator temperature at two field-shaping coil current settings

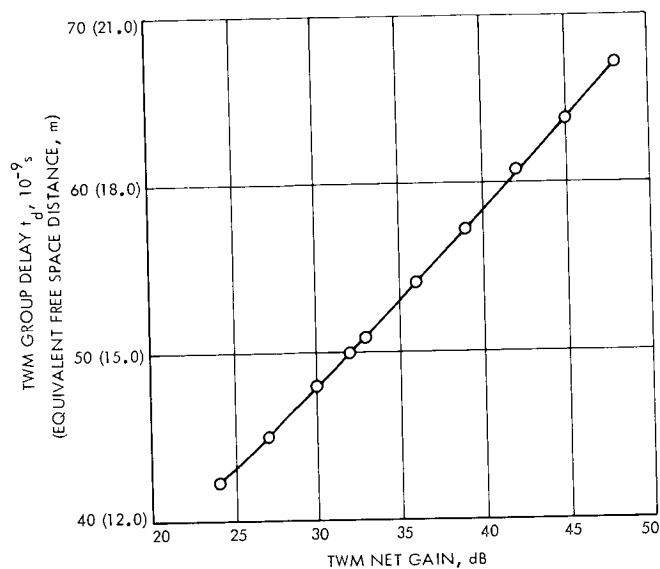


Fig. 10. Group delay vs net gain caused by field-shaping coil current changes

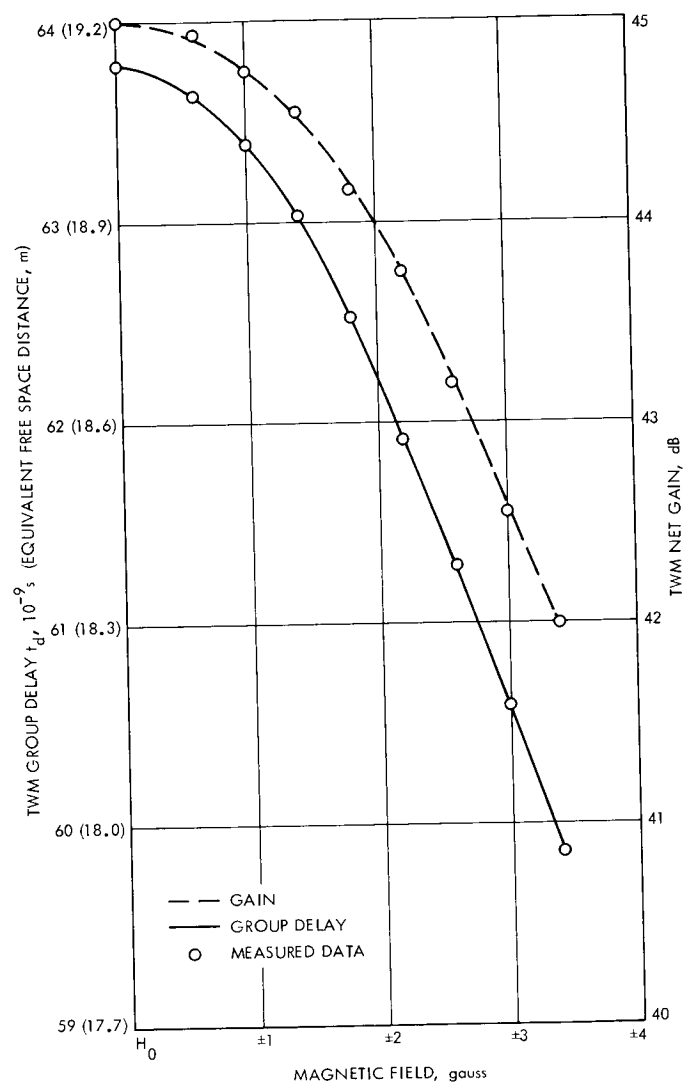


Fig. 11. Gain and group delay vs average magnetic field strength

Decoding the Golay Code

E. R. Berlekamp¹

Communications Systems Research Section

A procedure is described for correcting all patterns of three or fewer errors with the (23, 12) or (24, 12) Golay code. The procedure decodes any 24-bit word in about 26 "steps," each of which consists of only a few simple operations such as counting the number of ones in a 12-bit word. The procedure is based on the circulant viewpoint introduced by Karlin (1969). In addition it is shown how the (24, 12) Golay code can be used to correct certain patterns of more than three errors.

I. Introduction

Recently there has been a revival of interest in the use of binary block codes for deep space telemetry, since such codes can be used as the "outer" codes in concatenation schemes. These concatenation schemes are an attractive method of providing the very low bit error probabilities which will be required for the nonvideo science experiments on future deep space missions.

One of the most powerful known block codes is the Golay (24, 12) code, which is known to be capable of correcting all patterns of three or fewer bit errors. In Section II we describe a simple method of actually correcting these errors; this makes the Golay code (perhaps interleaved enough to deal with the bursts caused by the "inner" channel) a very attractive candidate for the "outer" code in certain concatenation schemes. In Section III we show how the Golay code can be used to correct certain patterns of more than three errors.

II. The Algorithm

It is known that the parity-check matrix of the (24, 12) Golay code may be written as

$$H = \begin{bmatrix} I & A \end{bmatrix}$$

where I is the 12×12 identity matrix and

$$A = \begin{bmatrix} 11011100010 & 1 \\ 01101110001 & 1 \\ 10110111000 & 1 \\ 01011011100 & 1 \\ 00101101110 & 1 \\ 00010110111 & 1 \\ 10001011011 & 1 \\ 11000101101 & 1 \\ 11100010110 & 1 \\ 01110001011 & 1 \\ 10111000101 & 1 \\ 11111111111 & 0 \end{bmatrix}$$

¹Consultant, Department of Mathematics and Electrical Engineering, University of California, Berkeley.

Let \hat{A} denote the 11×11 upper left submatrix of A . \hat{A} is a circulant matrix, each row of which is obtained by a cyclic right shift of the previous row. If the rows and columns of \hat{A} are labeled from 0 to 10, then

$$\hat{A}_{i,j} = \begin{cases} 1 & \text{if } j-i \text{ is 0 or a quadratic residue modulo 11} \\ 0 & \text{if } j-i \text{ is a quadratic nonresidue modulo 11} \end{cases}$$

From this, it is easily seen that $A^{-1} = A^t$.

Each codeword of the (24,12) code may be written as a row vector C , which satisfies the equation $HC^t = 0$. If C is transmitted and R is received, then the channel error pattern is $E = R - C$. The syndrome of R is the 12-dimensional column vector s^t defined by

$$s^t = HR^t$$

Since $HE^t = HR^t - HC^t = HR^t$, the syndrome of the received word is the same as the syndrome of the error word, and this is the sum of the columns of the H matrix corresponding to the error locations.

Let u_1, u_2, \dots, u_{12} denote the 12 unit row vectors in 12 dimensions (e.g., $u_3 = [001000000000]$); let A_1, A_2, \dots, A_{12} denote the rows of A , so that

$$A = \begin{bmatrix} A_1 \\ A_2 \\ \vdots \\ A_{12} \end{bmatrix}$$

and let $A_{13}^t, A_{14}^t, \dots, A_{24}^t$ denote the columns of A , so that

$$A = [A_{13}^t | A_{14}^t | \dots | A_{24}^t]$$

The syndrome $s^t = HE^t$ may now be represented as

$$s = \sum_{i=1}^{12} E_i u_i + \sum_{i=13}^{24} E_i A_i$$

Similarly,

$$A^t s = A^t H E = [A^t | I] \cdot E$$

whence

$$A^t s = \sum_{i=1}^{12} E_i A_i + \sum_{i=13}^{24} E_i u_{i-12}$$

If we now assume that $|E| \leq 3$, then at least one of the following must be true:

Case I:

$$|[E_{13}, E_{14}, \dots, E_{24}]| = 0, \quad |s| \leq 3, \quad \sum_{i=1}^{12} E_i u_i = s$$

Case II:

$|[E_{13}, E_{14}, \dots, E_{24}]| = 1$, there exists a_j , $13 \leq j \leq 24$ for which

$$|s + A_j| \leq 2, \quad \sum_{i=1}^{12} E_i u_i = s + A_j$$

Case III:

$$|[E_1, E_2, \dots, E_{12}]| = 0, \quad |sA| = |A^t s^t| \leq 3,$$

$$\sum_{i=13}^{24} E_i u_{i-12} = sA$$

Case IV:

$|[E_1, E_2, \dots, E_{12}]| = 1$, there exists a_j , $1 \leq j \leq 12$ for which

$$|sA + A_j| \leq 2, \quad \sum_{i=13}^{24} E_i u_{i-12} = sA + A_j$$

Hence, the decoding can be accomplished simply by weighing each of these 26 vectors:

$$s, s + A_1, s + A_2, \dots, s + A_{12}, \\ sA, sA + A_1, sA + A_2, \dots, sA + A_{12}$$

For example, suppose $s = 100011010010$. Since $|s| > 3$, we compute $s + A_1 = s + 110111000101 = 010100010111$. Since $|s + A_1| > 2$, we compute $|s + A_2| = 6 > 2$, $|s + A_3| = 6 > 2$, $|s + A_4| = 8 > 2$, $|s + A_5| = 6 > 2$, $|s + A_6| = 8 > 2$, $|s + A_7| = 4 > 2$, $|s + A_8| = 4 > 2$, $|s + A_9| = 10 > 2$, $|s + A_{10}| = 8 > 2$, $|s + A_{11}| = 6 > 2$, $|s + A_{12}| = 6 > 2$. It is now clear that if $|E| \leq 3$, then $|[E_1, E_2, \dots, E_{12}]| > 1$ and hence $|[E_{13}, E_{14}, \dots, E_{24}]| \leq 1$. So we continue by computing $A^t s^t = sA = 100110100111$, $|sA| = 7 > 3$, $sA + A_1 = 010001100010$, $|sA + A_1| = 4 > 2$, $|sA + A_2| = 6 > 2$, $|sA + A_3| = 6 > 2$, $|sA + A_4| = 6 > 2$, $|sA + A_5| = 8 > 2$, $|sA + A_6| = 4 > 2$, $sA + A_7 = 000100010000$. Since $|sA + A_7| = 2$, $E_7 = 1$ and $E = 0000001000000000100010000$.

Most of the decoding effort is counting the weights of the 26 relevant 12-bit vectors. For this reason, this decoding algorithm is particularly well-suited to computers

which have this instruction built in, such as the CDC 6400, 6500, 6600, and 7600. If programmed on a machine which is unable to count the weight of a 12-bit word in a single instruction, the easiest way to obtain this quantity is usually to break up the 12-bit word into pieces (say 2 pieces of 6 bits each or 3 pieces of 4 bits each) and obtain the weight of each piece by looking it up in a table.

III. Decoding More Than Three Errors

The Golay code has 2^{12} codewords of length 23, and since $\binom{23}{0} + \binom{23}{1} + \binom{23}{2} + \binom{23}{3} = 2^{23-12}$, every coset contains one word of weight ≤ 3 . However, the extended Golay code, which has 2^{12} codewords of length 24 has $\binom{24}{1} + \binom{24}{3} = 2^{11}$ cosets of odd weight and another $2^{11} = \binom{24}{0} + \binom{24}{2} + \frac{1}{6}\binom{24}{4}$ cosets of even weight. It is thus possible to correct $\frac{1}{6}$ of the $\binom{24}{4}$ possible error patterns of weight 4. Some of these words of weight 4 correspond to short bursts. Even though the space channel itself is memoryless, the convolutional code will occasionally make mistakes which the Golay code will see as error bursts. For this reason, short bursts of weight 4 are more probable error patterns than long bursts of weight 4.

The sum of any two words of weight 4 from the same coset is a codeword of weight 8. Hence we may gain a considerable amount of information about which words of weight 4 are correctable and which are not by studying the codewords of weight 8.

Since there is exactly one codeword of weight 8 which has 1s in any given five positions, the total number of codewords of weight 8 is $24 \times 23 \times 22 \times 21 \times 20 / 8 \times 7 \times 6 \times 5 \times 4 = 3 \times 11 \times 23$. Each codeword of weight 8 has 23 distinct cyclic shifts. The codewords of weight 8 lie in 33 sets of 23 codewords each. Furthermore, each codeword of weight 8 can be mapped into 11 different codewords by the permutation $C(x) \rightarrow C(x^{2^i}) \bmod (x^{23} + 1)$, for $i = 0, 1, \dots, 10$. Under this permutation, there are only 3 equivalence classes of codewords. The 11 members of each class are listed in Table 1.

The most probable error patterns of weight 4 are those which are due to the sum of one or more short bursts. The solid burst of length 5 occurs in codeword number 23 of Table 1. By inspecting this word, we see that the solid burst of length 5 in positions 0, 1, 2, 3, 4 lies in the same coset as the pattern of three isolated errors in positions 7, 10, and 12. Hence, if all error patterns of weight ≤ 3 are corrected, then a solid burst of length 5 cannot be corrected.

There are five codewords which contain solid bursts in positions 0, 1, 2, 3. These words may be found as cyclic shifts of lines numbered 1, 22, 23, 23, and 26 of Table 1. Since no codeword of weight 8 contains two disjoint solid bursts of length 4, *all solid bursts of length 4 may be corrected by the extended Golay code of length 24.*

A burst of length 5 and weight 4 must be of one of the following three types: 11101, 11011, 10111. Type 11101 is contained in Table 1 codewords numbered 2, 6, 22, 23, 24, Type 11011 in codewords numbered 1, 6, 11, 14, 23, and Type 10111 in codewords numbered 1, 2, 5, 12, 23.

The most probable error patterns of weight four are those which are due to the sum of one or two short bursts. These types of error patterns and the codewords of Table 1 which contain them are as follows:

Error type	Reference numbers of Table 1 codewords
111 plus 1	1, 3, 4, 5, 6, 11, 12, 17 21, 22, 23, 24, 26, 28, 33
11 plus 11	1, 3, 4, 6, 8, 9, 10, 11, 12, 14 17, 21, 25, 26, 27, 29, 30, 31, 32, 33

An examination of the conflicts between the goal of correcting 111 plus 1 and 11 plus 11 reveals the following dangerous codewords through positions 0, 1, 2:

	Codeword	Reference number
0, 1, 2	7, 8, 9, (13), (17)	4
0, 1, 2	(6), (10), 16, 17, 18	4
0, 1, 2	4, 5, (9), 18, 19	6
0, 1, 2	10, 11, 13, 14, (19)	11
0, 1, 2	5, 6, 12, 13, (15)	33

This shows that any pair of two sets of double adjacent errors can be corrected and that one can also correct any error pattern of the type 111 plus 1 (i.e., a solid burst of length 3 and an additional isolated error) unless the isolated error follows the burst by 6, 9, 10, 13, 17, 15, or 19 digits. If the isolated error follows the burst of length 3 by 9, 19, or 15, the syndrome is the same as for a pair of bursts of length 2; if the isolated error follows the burst of 3 by 13, 17, 6, or 10, then there is ambiguity with another error pattern of the same type.

Bibliography

- Berlekamp, E. R., *Algebraic Coding Theory*, McGraw-Hill Book Co., New York, 1968 (see Sec. 15.2, pp. 352–361, particularly Eq. 15.242, p. 357).
- Karlin, M., "New Binary Coding Results by Circulants," *IEEE Trans. Inform. Th.*, Vol. 15, pp. 81–92 (see Fig. 1, p. 82).

Table 1. One codeword of weight 8 from each of the 33 cyclic equivalence classes

Reference number	Positions of 1s in the codeword	Lengths (origins) of solid bursts
1	0 8 12 13 7 5 10 11	<u>4(10)</u> 2(7)
2	0 16 1 3 14 10 20 22	3(22)
3	0 9 2 6 5 20 17 21	2(5) 2(20)
4	0 18 4 12 10 17 11 19	3(10) 3(17)
5	0 13 8 1 20 11 22 15	3(22)
6	0 3 16 2 17 22 21 7	<u>3(21)</u> 2(2) 2(16)
7	0 6 9 4 11 21 19 14	
8	0 12 18 8 22 19 15 5	2(18) 2(22)
9	0 1 13 16 21 15 7 10	2(0) 2(15)
10	0 2 3 9 19 7 14 20	2(2) 2(19)
11	0 4 6 18 15 14 5 17	3(4) 2(14) 2(17)
12	0 2 4 6 5 10 11 ∞	3(4) 2(10)
13	0 4 8 12 10 20 22 ∞	2(22)
14	0 8 16 1 20 17 21 ∞	2(16) 2(20) 2(0)
15	0 16 9 2 17 11 19 ∞	2(16)
16	0 9 18 4 11 22 15 ∞	2(22)
17	0 18 13 8 22 21 7 ∞	3(21) 2(7)
18	0 13 3 16 21 19 14 ∞	2(13)
19	0 3 6 9 19 15 5 ∞	2(5)
20	0 6 12 18 15 7 10 ∞	2(6)
21	0 12 1 13 7 14 20 ∞	3(12) 2(0)
22	0 1 2 3 14 5 17 ∞	<u>4(0)</u>
23	0 1 2 4 3 12 7 10	<u>5(0)</u>
24	0 2 4 8 6 1 14 20	3(0)
25	0 4 8 16 12 2 5 17	2(4) 2(16)
26	0 8 16 9 1 4 10 11	<u>4(8)</u> 2(0)
27	0 16 9 18 2 8 20 22	2(8) 2(22)
28	0 9 18 13 4 16 17 21	3(16)
29	0 18 13 3 8 9 11 19	2(8) 2(18)
30	0 13 3 6 16 18 22 15	2(15) 2(22)
31	0 3 6 12 9 13 21 7	2(6) 2(12)
32	0 6 12 1 18 3 19 14	2(0) 2(18)
33	0 12 1 2 13 6 15 5	3(0) 2(5) 2(12)

Weights Modulo 8 in Binary Cyclic Codes

R. J. McEliece

Communications Systems Research Section

A new technique is provided for computing the weights modulo 8 in binary cyclic codes. These codes have proved to be the most important for GCF error detection/correction, and the method described will frequently aid in the detailed analysis of such codes.

I. Introduction

In this article we will obtain an improved method of calculating the value of the weights modulo 8 in a binary cyclic code. Such codes are the most important class of block codes known. For example, the (32, 6) block code used in the high-rate telemetry system, the (1200, 1167) BCH error detection code used on the GCF/NASCOM lines, and the (23, 12) Golay code currently being studied for use on a concatenation scheme for MJS77 are all essentially binary cyclic codes. Weight information is a first step toward analyzing the error correction properties of a code.

If C is an (n, k) binary cyclic code, denote its weight enumerator by

$$A(Z) = \sum_{i=0}^n A_i Z^i$$

A_i being the number of words of weight i in C . Knowledge of $A(Z)$ is vital for evaluating the performance of the

code C , but often C contains so many codewords that a direct enumeration is not possible. Thus indirect methods must be adopted. In Section II we present a technique which can usually be used to evaluate $A(Z)$ modulo $Z^8 - 1$. This information can then be added to other known information about $A(Z)$ in the attempt to calculate $A(Z)$. An example of the technique is given in Section III.

II. The New Technique

Let $c = (c_0, c_1, \dots, c_{n-1})$ be a codeword from C . We assume n is odd. Then the Mattson-Solomon polynomial of c ,

$$s(x) = \sum_{i=0}^{n-1} s_i x^i$$

has the property that $c_j = s(\theta^j)$, where θ is a primitive n th root of unity in some extension of $GF(2)$. The n coefficients s_i also lie in an extension of $GF(2)$, and $s_i^2 = s_{2i}$

(subscripts mod n). Let us write the weight of c in its binary expansion

$$w(c) = \Gamma_1(c) + 2\Gamma_2(c) + 4\Gamma_4(c) + \dots$$

where $\Gamma_{2^r}(c) = 0$ or 1 .

Let us first show that $\Gamma_1(c) \equiv s_0 \pmod{2}$. $\Gamma_1(c) \equiv w(c) \equiv c_0 + c_1 + \dots + c_{n-1} \pmod{2}$. Thus

$$\Gamma_1(c) \equiv \sum_{j=0}^{n-1} \sum_{i=0}^{n-1} s_i \theta^{ji} \equiv \sum_{i=0}^{n-1} s_i \sum_{j=0}^{n-1} \theta^{ij} \pmod{2}. \quad (1)$$

Now since for $i = 1, 2, \dots, n-1$ θ^i is a zero of

$$\frac{x^n - 1}{x - 1} = \sum_{j=0}^{n-1} x^j$$

the inner sum in (1) is zero unless $i = 0$. Thus $\Gamma_1(c) \equiv ns_0 \equiv s_0 \pmod{2}$.

The simple argument above was extended by Solomon and McEliece (Ref. 1) to Γ_2 and to Γ_4 . They assumed that $\Gamma_1(c) = 0$. This assumption involves no essential loss of generality, since in a binary (n, k) cyclic code with n odd, either all words have even weight, or else exactly half have odd weight, the words of odd weight being the mod-2 complements of the words of even weight. Under this assumption, Solomon and McEliece proved

$$\Gamma_2(c) \equiv \sum \{s_i s_j : i < j, i + j \equiv 0 \pmod{n}\} \pmod{2} \quad (2)$$

To give their expression for Γ_4 , we must first introduce some notation. Let P_r represent the set of unordered selections, with repetitions permitted, of r elements from the set $\{0, 1, 2, \dots, n-1\}$. Let P_r^0 be the subset of P_r of those selections whose entries sum to $0 \pmod{n}$. Thus if $n = 3$, P_4 contains 15 selections but P_4^0 contains only 0000, 0012, 0111, 0222, and 1122. If $\alpha = (\alpha_1 \alpha_2 \alpha_3 \alpha_4) \in P_4$, define $s_\alpha = s_{\alpha_1} s_{\alpha_2} s_{\alpha_3} s_{\alpha_4}$. Then Solomon and McEliece proved that

$$\Gamma_4(c) \equiv \sum_{\alpha \in P_4^0} A_\alpha s_\alpha \pmod{2} \quad (3a)$$

where the coefficients A_α are all zero, except that $A_\alpha = 1$ in the four mutually exclusive cases

$$\alpha = (i, i, j, k) \quad i, j, k \text{ distinct} \quad (3b)$$

$$\alpha = (i, i, i, j) \quad i, j \text{ distinct} \quad (3c)$$

$$\alpha = (i, j, n-i, n-j) \quad i, j \text{ distinct} \quad (3d)$$

$$\alpha = (i, i, n-i, n-i) \text{ and } n \equiv 1 \pmod{4}. \quad (3e)$$

Our object here is to show that (3a) can be greatly simplified. First, the sum in (3a) over the terms (3e) is, when $n \equiv 1 \pmod{4}$,

$$\sum s_i^2 s_{n-1}^2 \equiv \sum s_i s_{n-1} \equiv \Gamma_2(c) \pmod{2}$$

from (2). Next the sum over the terms (3d) is

$$\sum_{i < j} s_i s_{n-1} s_j s_{n-j}.$$

But this is just the second elementary symmetric function of the terms $s_\alpha, \alpha \in P_2^0$.

We now come to the terms (3b) and (3c). If α is a term in (3b), $s_\alpha = s_i^2 s_j s_k = s_{2i} s_j s_k$, since as mentioned above $s_i^2 = s_{2i}$. Similarly in case (3c) $s_\alpha = s_i^3 s_j = s_{2i} s_i s_j$. Of course these terms could "collapse" further if, for example, $2i \equiv j \pmod{n}$. Thus every term s_α from (3b) and (3c) "collapses" to a term of one of the forms $s_a s_b s_c$ with $a < b < c$ and $a + b + c \equiv 0 \pmod{n}$ or $s_a s_b$ with $a < b$ and $a + b \equiv 0 \pmod{n}$.

Thus we are led to define Q_r as the set of unordered selections, *without* repetition, of r objects from $\{0, 1, \dots, n-1\}$, and Q_r^0 as the subset of Q_r of those selections whose entries sum to $0 \pmod{n}$. We have seen that every term $\alpha \in P_4^0$ from (3b) or (3c) collapses to a term in either Q_3^0 or Q_2^0 . Let us now see how many elements in P_4^0 can collapse to a particular element in Q_3^0 or Q_2^0 .

First consider Q_2^0 . A typical term is (i, j) with $i < j$ and $i + j \equiv 0 \pmod{n}$. We easily see that the only terms in P_4^0 which collapse to (i, j) are:

$$\left(\frac{i}{4}, \frac{i}{4}, \frac{j}{2}, j\right) = \alpha_1$$

$$\left(\frac{j}{4}, \frac{j}{4}, \frac{i}{2}, i\right) = \alpha_2$$

$$\left(\frac{i}{2}, \frac{i}{2}, \frac{j}{2}, \frac{j}{2}\right) = \alpha_3$$

The last of these terms is not of form (3b) or (3c) and so does enter into the sum (3). The other two terms are distinct elements of P_4^0 , either of class (3b) or (3c), and since $s_{\alpha_1} + s_{\alpha_2} \equiv 0 \pmod{2}$, we see that the terms of P_4^0 which collapse to terms in Q_2^0 do not contribute to the sum (3).

Finally we consider those terms (3b) and (3c) of P_4^0 which collapse to a term in Q_3^0 . A typical term in Q_3^0 is

(i, j, k) with $i < j < k$ and $i + j + k \equiv 0 \pmod{n}$. The terms in P_4^0 which collapse to (i, j, k) are then

$$\left(\frac{i}{2}, \frac{i}{2}, j, k\right) = \alpha_1$$

$$\left(i, \frac{j}{2}, \frac{j}{2}, k\right) = \alpha_2$$

$$\left(i, j, \frac{k}{2}, \frac{k}{2}\right) = \alpha_3$$

Now α_1, α_2 and α_3 are all distinct elements of P_4^0 belonging to either (3b) or (3c). And since $s_{\alpha_1} + s_{\alpha_2} + s_{\alpha_3} = s_i s_j s_k$, we see that the sum in (3) over the α 's in classes (3b) and (3c) is $\sum \{s_{\alpha} : \alpha \in Q_3^0\}$.

Finally let us define $\sigma_j^{(n)}(c)$ as the j th elementary symmetric function of the terms $s_{\alpha}, \alpha \in Q_r^0$. We have then proved that the formula of Solomon-McEliece (3a) can be rewritten as:

$$\Gamma_4(c) \equiv \sigma_1^{(3)}(c) + \sigma_2^{(2)}(c) + (1 + n_1) \sigma_1^{(2)}(c) \pmod{2} \quad (4)$$

where $n = n_m \cdots n_2 n_1 1$ is the binary expansion of n . This is our main result. In Section III we give an example of the use of (4).

III. An Example

We will illustrate our result on the (17, 8) cyclic code whose check polynomial $x^8 + x^5 + x^4 + x^3 + 1$ is irreducible mod 2. It follows from the Mattson-Solomon results that every codeword $c \in C$ has $s_j = 0$ except possibly for $j \in \{1, 2, 4, 8, 16, 15, 13, 9\} = K$; i.e., $j \equiv 2^m \pmod{17}$ for $m = 0, 1, \dots, 7$. Furthermore for each such codeword there will exist a unique $x \in GF(2^8)$ such that $s_{2^m} = x^{2^m}$.

Now we are ready to apply our formula for Γ_4 . The first term, $\sigma_1^{(3)}(c)$, will involve only those selections (i, j, k) from Q_4^0 , all of whose elements lie in the set K . But it is easily verified that no such tuples (i, j, k) exist. Thus $\sigma_1^{(3)}(c) = 0$ for all $c \in C$. The next two terms are the first two elementary symmetric functions of the nonzero terms $\{s_{\alpha} : \alpha \in Q_2^0\}$;

i.e., $\{s_1 s_{16}, s_2 s_{15}, s_4 s_{13}, s_8 s_9\}$ but since $s_{2^m} = x^{2^m}$ for some $x \in GF(2^8)$ this set is $\{x^{17}, x^{17 \cdot 2}, x^{17 \cdot 4}, x^{17 \cdot 8}\}$. If $x \neq 0$, $x^{2^8-1} = x^{17 \cdot 15} = 1$ in $GF(2^8)$, and so x^{17} in fact lies in the smaller field $GF(2^4)$. In fact for every $y \in GF(2^4) - \{0\}$, there are exactly 17 values of $x \in GF(2^8) - \{0\}$ such that $x^{17} = y$. For every codeword c corresponding to such an x , then

$$\Gamma_4(c) = \sigma_2(y) + \sigma_1(y),$$

where $Z^4 + \sigma_1(y) Z^3 + \sigma_2(y) Z^2 + \sigma_3(y) Z + \sigma_4(y) = (Z - y)(Z - y^2)(Z - y^4)(Z - y^8)$ is the field polynomial for y .

Similarly, but more easily,

$$\Gamma_2(c) = \sigma_1(y).$$

Finally all that is needed is a list of the field polynomials of the 15 nonzero elements of $GF(2^4)$:

Polynomial	Number of distinct roots	Γ_4	Γ_2
$Z^4 + Z + 1$	4	0	0
$Z^4 + Z^3 + 1$	4	1	1
$Z^4 + Z^3 + Z^2 + Z + 1$	4	0	1
$Z^4 + Z^2 + 1$	2	1	0
$Z^4 + 1$	1	0	0

Thus we see that in the code C there are, apart from the all-zero word,

$$85 = 17 \cdot 5 \text{ words with weight } \equiv 0 \pmod{8}$$

$$68 = 17 \cdot 4 \text{ words with weight } \equiv 2 \pmod{8}$$

$$34 = 17 \cdot 2 \text{ words with weight } \equiv 4 \pmod{8}$$

$$68 = 17 \cdot 4 \text{ words with weight } \equiv 6 \pmod{8}$$

Since the BCH bound assures us that there are no words of weight less than 5 or greater than 12, the complete weight enumerator for C is

$$A(Z) = 1 + 68Z^6 + 85Z^8 + 68Z^{10} + 34Z^{14}$$

Reference

1. Solomon, G., and McEliece, R., "Weights of Cyclic Codes," *J. Comb. Th.* Vol 1, pp. 459-475, 1966.

Reducing the Complexity of Calculating Syndromes for Error-Correcting Codes

L. H. Harper and J. E. Savage¹
Communications Systems Research Section

The calculation of the syndrome—the first step performed by all decoders of linear codes—can require a number of logical operations which grows faster than the square of block length. It is shown that the complexity of syndrome calculation can be reduced for many linear codes by a factor of log of the code block length and that Hamming codes can be decoded with combinational machines having a number of logic elements which is linear in block length.

I. Introduction

It has been suggested that error-correcting coding be used to improve the reliability of Ground Communications Facility (GCF) data transfer. However, if such coding is to be used, the problem of real-time decoding must first be dealt with; this problem will be especially acute in the 50-kbits/s wideband mode. This note shows how decoding complexity can be decreased for many important coding schemes.

Every linear (parity-check) code has a parity check matrix H associated with it. If the code words $\mathbf{x}_1, \dots, \mathbf{x}_M$ are N -tuples over $GF(q)$, then H is an $N \times (N - K)$ matrix over $GF(q)$ where K is the number of information digits needed to represent the code word and $N - K$ is the number of dependent digits in a code word. Also,

$M = q^K$ and every code word satisfies the equation

$$\mathbf{x}_i H = \mathbf{0}$$

Let \mathbf{y} be the received sequence when \mathbf{x}_i is transmitted and let $\mathbf{e} = \mathbf{y} - \mathbf{x}_i$ be the error sequence associated with \mathbf{x}_i . The *syndrome* \mathbf{s} associated with \mathbf{y} and \mathbf{e} is

$$\mathbf{s} = \mathbf{y} H = \mathbf{e} H$$

and \mathbf{s} is a compact reflection of the channel errors.

In this note we show that the calculation of \mathbf{s} can be reduced for many codes by making use of the structure of H . We begin with an examination of Hamming codes.

II. Hamming Codes

The parity-check matrix H_m of the Hamming code (Ref. 1) is $N = 2^m - 1$ by m dimensional binary matrix which contains all binary m -tuples as rows except for the

¹Division of Engineering, Brown University, and consultant, Communications Systems Research Section.

zero m -tuple. It is easily shown that each column of H_m contains 2^{m-1} ones, so that the straightforward calculation of each digit of s would require $2^{m-1} - 1$ modulo-2 sums of pairs for a total of $m(2^{m-1} - 1)$ additions. This number grows as $N \log_2 N$. We shall show that this number can be reduced to linear in N .

Theorem 1

The calculation of syndromes for a Hamming code of length $N = 2^m - 1$ can be accomplished with $2[2^m - (m + 1)]$ mod-2 additions, and at least $2^m - 2$ additions are required.

Proof

There is no loss of generality in assuming that the rows of H_m (which are m -tuples) are listed in order of increasing integers which they represent in dyadic form. Form H_m^* from H_m by adding the zero m -tuple as the first row. For example,

$$H_3^* = \begin{bmatrix} 0 & 0 & 0 \\ 0 & 0 & 1 \\ 0 & 1 & 0 \\ 0 & 1 & 1 \\ 1 & 0 & 0 \\ 1 & 0 & 1 \\ 1 & 1 & 0 \\ 1 & 1 & 1 \end{bmatrix} \quad H_3 = \begin{bmatrix} 0 & 0 & 1 \\ 0 & 1 & 0 \\ 0 & 1 & 1 \\ 1 & 0 & 0 \\ 1 & 0 & 1 \\ 1 & 1 & 0 \\ 1 & 1 & 1 \end{bmatrix}$$

Note that H_{m+1}^* can be formed from H_m^* as indicated below:

$$H_{m+1}^* = \left[\begin{array}{c} 0 \\ 0 \\ \vdots \\ 0 \\ \dots\dots\dots \\ 1 \\ \vdots \\ 1 \end{array} \begin{array}{c} H_m^* \\ \\ \\ \\ \\ H_m^* \end{array} \right] \begin{array}{l} \left. \vphantom{\begin{matrix} 0 \\ 0 \\ \vdots \\ 0 \end{matrix}} \right\} 2^m \\ \left. \vphantom{\begin{matrix} \dots\dots\dots \\ 1 \\ \vdots \end{matrix}} \right\} 2^m \end{array}$$

The number of modulo-2 additions to multiply H_{m+1} on the left, P_{m+1} , is the number to multiply with H_{m+1}^* . But, this is twice P_m plus the number to add each half of columns 2 through $m + 1$ of H_{m+1}^* , namely, m plus the number to multiply by the first column. The recursive construction of H_{m+1}^* shows that the bottom quarter of

the second column of H_{m+1}^* , namely, the lower half of the first column of H_m^* , contains ones, so that the partial sum of the $2^m/2$ last components of y computed for the second column of H_{m+1}^* can be used to compute its first column. Using partial sums computed for the third and later columns, the first column can be computed with an additional m additions.

Then,

$$P_{m+1} = 2P_m + 2m$$

and it is easily shown that $P_2 = 2$. This is a linear difference equation with homogeneous solution $c2^m$ and particular solution $-2(m + 1)$. Therefore,

$$P_m = c2^m - 2(m + 1)$$

and $c = 2$ for $P_2 = 2$. Or

$$P_m = 2(2^m - (m + 1)).$$

To show that at least $2^m - 1$ additions are necessary to compute s , we observe that in computing $(y_1, y_2, \dots, y_{2^m})H_m^*$ the sums $y_2, y_{2+1} + y_{2^2}, y_{2^2+1} + \dots + y_{2^3}, \dots, y_{2^{m-1}+1} + \dots + y_{2^m}$ must be formed and that these are sums of overlapping variables. Also, each sum except the last is added to other partial sums. Therefore, the number of additions is at least

$$\sum_{j=1}^{m-1} 2^{j-1} + 2^{m-1} - 1 = 2^m - 2$$

This completes the proof of the theorem.

This reduction by a factor of $\log_2(N + 1)$ in the complexity of syndrome calculations can be carried over to some BCH codes, as shown next.

III. Binary BCH Codes

A t -error-correcting BCH code (Ref. 1) over $GF(2)$ has a parity check matrix

$$H = \begin{bmatrix} 1 & 1 & \dots & 1 \\ \alpha & \alpha^3 & & \alpha^{2^t-1} \\ \alpha^2 & (\alpha^3)^2 & & (\alpha^{2^t-1})^2 \\ \vdots & & & \vdots \\ \alpha^{N-1} & (\alpha^3)^{N-1} & & (\alpha^{2^t-1})^{N-1} \end{bmatrix}$$

where 1 and α are elements of $GF(2^m)$ and N is the multiplicative order of α .

Theorem 2

The syndrome \mathbf{s} of a binary, t -error-correcting BCH code can be computed using $2t(2^m - (m + 1)) \bmod 2$ additions when α is primitive and the multiplicative orders of $\alpha^3, \alpha^5, \dots, \alpha^{2t-1}$ are all relatively prime to $N = 2^m - 1$, the block length of the code.

Proof

Each element of $GF(2^m)$ can be represented by a binary m -tuple. Under the conditions of the theorem, each element $\alpha, \alpha^5, \dots, \alpha^{2t-1}$ is primitive in $GF(2^m)$ and each column contains all the nonzero m -tuples. Invoking Theorem 1, the result follows.

Under the conditions of the theorem the number of mod-2 additions to form H directly, without using partial sums for various columns, would be $mt(2^{m-1} - 1)$. Thus, a savings of a factor of about $m/4$ can be achieved.

When the conditions of Theorem 2 are not met, the bound of Theorem 2 may not apply. The interested reader can satisfy himself that 47 additions will be needed, using techniques of this note, for the (15,7) BCH code while the bound of Theorem 2 would predict 44. In this case, α^3 is not primitive in $GF(2^4)$.

IV. On Decoding Hamming Codes

Hamming codes can be decoded with a logic circuit containing a number of logic elements proportional to the block length N , as is now shown. The Hamming codes correct all single errors, and decoding is done by changing the i th received digit if \mathbf{s} is equal to the i th row of H .

The circuit which generates correction signals from a syndrome vector computes all but one of the terms of the form $s_1^{c_1} \cdot s_2^{c_2} \cdot \dots \cdot s_m^{c_m}$ where \cdot denotes AND, (c_1, c_2, \dots, c_m) is a binary m -tuple, and $s_i^1 = s_i$, $s_i^0 = \bar{s}_i$, the INVERSE of s_i . The only term not computed is $s_1 \cdot \dots \cdot s_m$. These terms are known as minterms, and it can be shown by induction that they can all be realized using $2(2^m - 1)$ logic elements of the type AND, OR, INVERSE (Ref. 2).

Thus, with a total number of logic elements proportional to N , syndromes can be computed and correction signals generated.

V. Conclusion

The reductions in decoder complexity demonstrated in this note might also be achieved for many other codes.

References

1. Peterson, W. W., *Error-Correcting Codes*. M.I.T. Press and Wiley and Sons, New York, 1961.
2. Savage, J. E., "The Effective Computing Power of Computer Memory," in *The Deep Space Network*, Space Programs Summary 37-64, Vol. II, pp. 30-32. Jet Propulsion Laboratory, Pasadena, Calif., Aug. 31, 1970.

Efficient Generation of Statistically Good Pseudonoise by Linearly Interconnected Shift Registers

W. J. Hurd

Communications Systems Research Section

Some new algorithms are presented for generating pseudorandom noise utilizing binary maximal length linear recursive sequences of high degree and with many nonzero terms. The ability to efficiently implement high degree recursions is important because the number of consecutive bits which can be guaranteed to be both linearly and statistically independent is equal to the degree of the recursion. The implementations are by interconnection of several short shift registers in a linear manner in such a way that different widely spaced phase shifts of the same pseudonoise sequence appear in the stages of the several registers. This is efficient both in hardware and in software. Several specific algorithms are subjected to extensive statistical evaluation, with no evidence found to distinguish the sequences from purely random binary sequences.

I. Introduction

Digitally generated pseudorandom noise and analog-generated random noise are extensively used in various research, development, simulation, testing and system evaluation and calibration activities. Digital pseudonoise has basic advantages over analog-generated noise, in its repeatability and inherent stability. Therefore, analog noise signals are frequently generated by converting digital noise to analog, and digital computer applications rarely use analog-generated noise.

This paper presents some efficient new algorithms for generating digital pseudonoise. The algorithms are efficient because a large number of new pseudorandom bits are generated at each iteration of a computer implementation, or at each clock pulse of a hardware implementation. The pseudonoise has good statistical

properties because the several simultaneously generated bits are the corresponding bits from different phase shifts of the same maximal length linear recursive sequence. These sequences, also called maximal length shift register sequences, *pn*-sequences, and *m*-sequences, are well known to have good randomness properties (Refs. 1 and 2).

Some of the key features of the new algorithms are:

- (1) The algorithms are efficient in both hardware and software implementations. Besides being independently useful in the two applications, this has the advantage that specific proposed hardware implementations can be efficiently simulated and evaluated before hardware is constructed.
- (2) In software applications, the new algorithms are more efficient than existing algorithms for *pn*-

sequences with comparable randomness properties. Some efficient algorithms are known for particularly simple recursions, but the resulting sequences have poor statistical properties which the new algorithms avoid.

- (3) Wideband pseudo-gaussian analog signals can be easily generated from hardware implementations. This is accomplished by the analog summation of voltage waveforms corresponding to the several new bits generated at each clock pulse. A noise generator has been constructed utilizing this principle, in similar manner to an earlier digital gaussian noise generator described elsewhere (Ref. 3).
- (4) The statistical properties of the sequences have been evaluated extensively, with no evidence found to distinguish the sequences from purely random sequences of independent, equally likely, binary numbers.

This paper is divided into three main sections. First, some of the properties of pn -sequences are reviewed, and standard implementations are discussed. This serves as a motivation for the development of the new algorithms. Second, the new algorithms are described in general, and specific implementations are discussed. Finally, the results of extensive statistical evaluation of the pseudo-noise are presented, and the sequences are shown to have favorable randomness characteristics.

II. Motivation for Use of pn -Sequences

A binary linear recursive sequence is a sequence $\{X_k\}$ of zeroes and ones satisfying a linear recursion of the form

$$X_k = \sum_{i=1}^n a_i D^i X_k \quad (1)$$

where D is the delay operator, i.e., $D^i X_k = X_{k-i}$, the a_i are zero or one, and addition is modulo-2. The degree of the recursion is the largest value of i for which $a_i = 1$, and the maximum possible period of a sequence from a linear recursion of degree n is $2^n - 1$. These maximal length linear recursive sequences, called pn -sequences, occur when the polynomial

$$P(D) = 1 + \sum_{i=1}^n a_i D^i$$

is primitive over $GF(2)$.

A. Randomness Properties

PN -sequences are known to have many favorable randomness properties (Refs. 1 and 2). Some important properties common to all pn -sequences are:

- (1) For degree n , all of the $2^n - 1$ possible nonzero n -tuples, or sets of n consecutive bits, occur equally often. This means that binary numbers formed from disjoint subsets of the same n -tuple are independent and jointly uniformly distributed.
- (2) All phase shifts are essentially uncorrelated, when correlation is defined as the number of places in which the phase shifts agree, less the number in which they disagree.
- (3) Under suitable conditions, sets of n -tuples from different phase shifts of a sequence are uncorrelated, when considered as binary numbers (Ref. 2).

These properties indicate not only that pn -sequences are good sources of random numbers, but that it may be possible to utilize different phase shifts of the same sequence as essentially independent noise sequences.

The properties we have discussed so far apply equally to all pn -sequences, but other properties cause some sequences to appear more random than others. In particular, consider m -tuples for m greater than the degree n . Since some of the bits of the m -tuples are linearly related, they are not statistically independent. Fortunately the statistical dependence is usually not observed unless the recursion is a particularly simple one. Lindholm (Ref. 4), however, has investigated the weights of m -tuples, i.e., the number of ones. In a purely random sequence, the weights would be binomially distributed symmetrically about $m/2$, but there is significant deviation from this when the recursion is a trinomial or divides some trinomials of low degree.

The above properties of pn -sequences indicate that the randomness properties tend to improve with the degree and complexity of the recursion. They also indicate that bits from several phase shifts of the same sequence might be as useful as the same total number of bits from one phase shift. As we shall see, this has implementation advantages.

B. Well-Known Implementation

PN -sequences are easily generated one bit at a time in binary shift registers, as shown in Fig. 1. The input to the first stage is labeled X_k , and the outputs of the

n -stages are $X_{k-1}, X_{k-2}, \dots, X_{k-n}$, the values of X_k at the n previous instants of time. As the time index advances from k to $k+1$, the state of each stage of the register assumes the value of its input. The register shown satisfies the trinomial recursion

$$X_k = X_{k-1} + X_{k-n} \pmod{2} \quad (2)$$

so that its characteristic polynomial in the delay operator is

$$P(D) = 1 + D + D^n \pmod{2} \quad (3)$$

The resulting sequence $\{X_k\}$ is a pn -sequence if $P(D)$ is primitive.

One can generate several phase shifts of the same sequence by several straightforward methods, using the cycle-and-add property. This property is that the mod-2 sum of any two phase shifts is another phase shift. Thus one method is to sum the outputs of any two stages to yield a new phase shift. Another method can be used if the input X_k depends on several, say N , of the previous n states. Then X_k is implemented in a series of $N-1$ two-input modulo-2 adders, and the output of each adder is a different phase shift. Both of these methods suffer the implementation deficiencies that the complexity increases with the number of terms in the recursion and the number of phase shifts generated, and that they are not amenable to software systems. They have the statistical deficiency that the various phase shifts are simply related, and therefore cannot be considered statistically independent, even though they must be uncorrelated.

In software, it is fairly easy to generate n successive bits of a degree n recursion in a few machine instructions, provided that the recursion is a trinomial, as was done by Kendall (Ref. 5) for $n = 47$. Unfortunately, the algorithm complexity increases with the number of terms in the recursion, and trinomial recursions result in statistical dependencies which sometimes lead to erroneous simulation results, as observed by Heller (Ref. 6). Furthermore, the method is efficient only when n is less than the number of bits in one or two computer words, because of the shifting operations which are required.

In summary, the considerations above indicate that there is a need both in hardware and software for algorithms for efficiently generating long period pn -sequences with complex recursions. The efficiency is to be gained by generating several new bits simultaneously,

either consecutive bits from a sequence, or bits from several different phase shifts of a sequence. It is the latter approach which we develop here.

III. Sequence Generation by Interconnection of Shift Registers

The algorithms presented here utilize the linear interconnection of several shift registers to simultaneously generate several phase shifts of the same pn -sequence. For a degree n recursion, the n bits in memory at any one time are not consecutive bits from one pn -sequence, but are bits from several phase shifts. Nevertheless, they are linearly independent, and they retain the important statistical property that all disjoint subsets, considered as binary numbers, are independent and jointly uniformly distributed. This follows because all of the $2^n - 1$ possible nonzero states of the n bits occur equally often.

The algorithms are efficient both for hardware and software. The theoretical minimum of n stages of shift register and still fewer gates are required in hardware for a polynomial of degree n , and one new word is generated at each clock pulse. In software, approximately 12 machine instructions are required to generate one new word of pseudorandom bits, even though the degree of the polynomial may be much higher than the word length. Since the degree determines the number of consecutive bits which are guaranteed to be statistically independent, a number of successive independent computer words can be generated without sacrificing efficiency.

Figure 2 shows a simple linear interconnection of three shift registers. The registers are labeled 0, 1, and 2, with inputs at time k of $X_k^{(0)}, X_k^{(1)},$ and $X_k^{(2)}$. At time k , the first (leftmost) stages of the registers store the input values at time $k-1$, i.e., $X_{k-1}^{(0)}, X_{k-1}^{(1)},$ and $X_{k-1}^{(2)}$. The shifting is from left to right, so, in general, stage j of register i stores the value $X_{k-j}^{(i)}$ at time k .

In the particular example of Fig. 2, register 0 has three stages, and registers 1 and 2 have four stages. The input to each register is the modulo-2 sum of the output of the last stage of the same register, and the output of one stage from the previous register. Thus we can define the recursion by

$$X_k^{(i)} = X_{k-q_i}^{(i)} + X_{k-d_{i-1}}^{(i-1)}, \quad i = 0, 1, 2 \pmod{3} \quad (4)$$

where q_i is the number of stages in register i , and d_{i-1} is the stage of register $i-1$ which forms an input to register i . We can also write

$$X_k^{(i)} = D^{q_i} X_k^{(i)} + D^{d_{i-1}} X_k^{(i-1)}, \quad i = 0, 1, 2 \pmod{3} \quad (5)$$

and this set of equations is easily solved in general for the characteristic polynomial in the delay operator as

$$P(D) = \prod_{i=0}^{N-1} (1 + D^{q_i}) + D^{\sum_{i=0}^{N-1} d_i} \quad (6)$$

where we have now generalized to N registers, labeled $0, 1, 2, \dots, N-1$.

For the particular case of Fig. 2,

$$P(D) = 1 + D^3 + D^5 + D^8 + D^{11} \quad (7)$$

which is a primitive polynomial, as can be verified by calculation or from tables (Ref. 7). Thus the sequence of states of the stages of each register is the pn -sequence defined by $P(D)$, or by the recursion

$$X_k = X_{k-3} + X_{k-5} + X_{k-8} + X_{k-11} \quad (8)$$

C. Final Configuration

To achieve simple implementations, it is necessary to restrict the register interconnections to some regular form. However, forms which have each input depend on only two register stages, as in Fig. 2, are probably not satisfactory, because they tend to suffer some of the statistical deficiencies of trinomial recursions, even though trinomial characteristic polynomials do not typically result.

The next alternative could be to have each input depend on three register stages. Most configurations in which each input depends on at least three register stages would probably be satisfactory statistically. However, for implementation considerations, we have chosen, instead, to have the first stage of each register depend on only two inputs and to modify the connections to the last stage of each register so that its input is the sum of its own output state and the state of the preceding stage. This operation is known as toggling, because the stage toggles, i.e., changes state, whenever its input is 1. This is the natural operation of a T flip-flop, or a J-K

flip-flop with the two inputs the same. In delay operator notation, this stage performs the operation

$$\frac{D}{1+D}$$

instead of the operation D .

The final configuration consists in general of N registers of the form shown in Fig. 3. Register i has q_i stages, the first $q_i - 1$ of which shift, and the last stage of which toggles. Thus the stage outputs of register i at times k are

$$DX_k^{(i)}, D^2 X_k^{(i)}, \dots, D^{q_i-1} X_k^{(i)} \text{ and } \frac{D^{q_i}}{1+D} X_k^{(i)}$$

The input $X_k^{(i)}$ to register i is the modulo-2 sum of the last stage of register $i-1 \pmod{N}$ and stage d_{i-2} of register $i-2 \pmod{N}$. Thus the system is defined by the equations

$$\left. \begin{aligned} X_k^{(i)} &= \frac{D^{q_{i-1}}}{1+D} X_k^{(i-1)} + D^{d_{i-2}} X_k^{(i-2)} \\ i &= 0, 1, \dots, N-1 \pmod{N} \end{aligned} \right\} \quad (9)$$

D. Specific Realizations

In order to find specific systems corresponding to primitive polynomials, it is necessary to calculate the polynomials for various values of the system parameters and to test for primitivity. This is best done with a computer, and programs have been written for this purpose. To test for primitivity, one computes $D^r \pmod{P(D)}$ for all integers r which divide $2^n - 1$. The polynomial $P(D)$ is primitive if $r = 2^n - 1$ is the smallest value of r such that $D^r \equiv 1 \pmod{P(D)}$. This test cannot be performed for all degrees n , because the factors of $2^n - 1$ are not known in general. Furthermore, the average number of computations required to find a primitive polynomial increases as n^4 . The highest degree for which a primitive polynomial system of the special form was found is 310.

Table 1 summarizes some of the realizations found which have primitive characteristic polynomials. This table is restricted to equal length shift registers of length q , with degree $n = Nq$. The d_i are also restricted. They are allowed to assume only two values, $d_i = d_0$ for $i = 0, 1, \dots, N_0 - 1$, and $d_i = d_{N-1}$ for $i = N_0, N_0 + 1, \dots, N-1$. In other words, the first N_0 of the d_i are equal to d_0 , and the rest are equal to d_{N-1} . Column T in Table 1 gives the number of nonzero coefficients in the resulting polynomial, i.e., it is a T-nomial.

Many more primitive configurations can be found by lifting the restrictions on the q_i and d_i .

E. Software Implementation

For computer implementation, realizations using equal length registers are most useful, especially when the number of registers is equal to the computer word length. If all registers are of length q , then a q word array of memory is used, as shown in Fig. 4. The last word of the array stores the first bit of each of the N shift registers, the next to last word stores the second bit of each register, etc. Thus word $q - j + 1$ stores

$$D^j X_k^{(0)}, D^j X_k^{(1)}, \dots, D^j X_k^{(N-1)}$$

for $j = 1, 2, \dots, q - 1$, and word 1 stores

$$\frac{D^q}{1+D} X_k^{(0)}, \frac{D^q}{1+D} X_k^{(1)}, \dots, \frac{D^q}{1+D} X_k^{(N-1)}$$

We can envision shifting words upwards through the array, with toggling of the first word.

The computer program must accomplish three things, in principle simultaneously. First, it must selectively merge the various words to form a word

$$D^{d_0} X_k^{(0)}, D^{d_0} X_k^{(1)}, \dots, D^{d_{N-1}} X_k^{(N-1)}$$

and modulo-2 add the proper shift of this word to the proper shift of word 1 to form the new word q . Second, it must form the new word 1 by modulo-2 adding words 1 and 2. Third, it must shift the old words $q, q - 1, \dots, 3$ into $q - 1, q - 2, \dots, 2$. In practice, it is more efficient to generate a new array of q words at one time, i.e., the N registers are each shifted q places, yielding n new pseudo-random bits.

Several specific algorithms have been programmed for the XDS Sigma 5 computer. The statistical properties of these sequences are evaluated in Section IV, and a FORTRAN program for degree 288 with $N = 32$, $q = 9$ is described in the Appendix. In this particular program, the registers have been permuted so that the input to register i depends on registers $i - 5$ and $i - 10$, instead of on registers $i - 1$ and $i - 2$. The program execution time is $37 \mu\text{s}$ per 32-bit number.

F. Hardware Applications

The realizations for small n and N are useful in hardware applications. A pseudo-gaussian noise generator has been constructed for $N = 12$, $n = 60$ using only 20

integrated circuits. For this implementation, the d_i for $i = 0, 1, \dots, N - 1$ are 3, 2, 1, 4, 2, 4, 3, 2, 1, 4, 4, 1, and the polynomial has 25 nonzero coefficients. To transform from a binary to a pseudo-gaussian sequence, voltage waveforms corresponding to the 12 new bits generated at each clock pulse are summed in a resistor network and then filtered, in a similar manner to the noise generator of Ref. 1. The advantage to the new method over the earlier noise generator is that less hardware is required so that the cost is substantially less. Furthermore, the pseudonoise properties of this noise generator are very good, as will be shown next.

IV. Evaluation of Statistical Properties

Extensive chi-squared tests were performed on the sequences generated by computer programs for algorithms of degrees 310, 288, 160, and 60. The program for degree 60 implemented the same system as the hardware noise generator described above. The other three cases are the polynomials with the largest numbers of nonzero coefficients given in Table 1. These were evaluated to determine their suitability for use as standard computer noise generator algorithms. The sequences were tested to see whether computer words treated as binary numbers were jointly uniformly distributed in several dimensions, and the weight distributions of m -tuples were tested for being binomial for various m . The results of these tests showed no evidence to distinguish any of these pseudonoise sequences from truly random binary sequences.

A. Tests for Jointly Uniform Distributions

The results of the tests for uniformity are summarized in Table 2. To illustrate the use of this table, we explain the entries in each column of the second row. The first column identifies the case as corresponding to the degree 60 polynomial, or the one implemented in hardware. The second and third columns indicate that this test was for joint uniformity in three dimensions, with 999 degrees of freedom. This means that the data were sorted into 1000 bins, and since all bins were of equal size, the bin dimensions are $0.1 \times 0.1 \times 0.1$ if the numbers are considered to be between 0 and 1. The next column indicates that 25,000 data samples were used to compute each value of χ^2 . In this case, 25,000 sets of three numbers were required. The last five columns indicate that 100 tests were run; the values of χ^2 which should be exceeded 99% and 95% of the time were exceeded in all but 0 and 10 tests, respectively; the values which should be exceeded 1% and 5% of the time were exceeded 0 and 8 times, respectively.

In order to search for any possible anomalies in the joint distributions of nonadjacent words on the sequences, the data samples used for the tests of Table 2 were not all adjacent words in the sequences. For a k -dimensional test, the first five sets of k words were adjacent on the sequence, the k words of the next five sets were spaced two words apart, the k words of the next five sets were spaced three words apart, etc., until the spacing between the words of last five sets of k -words was equal to the number of tests divided by five.

For all cases, the number of observances of large and small values of χ^2 are very close to the expected values of these events for independent and uniformly distributed random numbers. In particular, for the 2965 tests performed on the degree 288 polynomial, a total of 20 values of χ^2 were less than the 99% value, and 25 exceeded the 1% value. This is, in both cases, less than two standard deviations from the mean value of 29.65, since the standard deviation is 5.42. Considering the extensiveness of the tests performed, sequences whose statistics differed significantly from the statistics tested for would almost certainly result in many more large values of χ^2 than expected. Thus there is no evidence to distinguish the sequences from purely random sequences.

B. Test of Weight Distribution

For the same four algorithms, the distributions of the weights of m -tuples of consecutive bits were tested for being binomially distributed, as would be the case for a purely random sequence. This test was performed because pn -sequences generated by trinomials will fail this test.

Each m -tuple considered was made up of the bits of an integer number of words, where word length corresponds to the number of shift registers in the corresponding hardware implementation. Thus m is always a multiple of 12 for the degree 60 case, 31 for the degree 310 case, and 32 for the other two cases.

Table 3 summarizes the results of these tests. The columns in Table 3 are the same as in Table 2, except that the second column indicates the lengths of the m -tuples. Various m -tuple lengths up to more than 1200 were tested for each of the four algorithms. In all cases, the number of times χ^2 exceeded the 1% and 5% values was approximately as expected. Also, the numbers of values less than the 95% values were near the means.

The only unusual result was that only one value of χ^2 was less than the 99% value. We attribute this to the fact that the 99% threshold used was not the correct value for the actual observables, because the observables are only asymptotically chi-squared distributed. The deviation of the actual distribution from chi-squared is significant for small values. For example, a truly chi-squared variate can take on the value zero, whereas our observables had a minimum value greater than zero. This was because the observation space was divided into bins with non-integer expected numbers of occurrences. Since the numbers of observed values of χ^2 less than the 95% values were close to the mean, we do not consider the sparsity of extremely small values to be significant. The overall conclusion drawn from the weight distribution tests is that there is no evidence to distinguish the bit sequences from truly random sequences of independent, equally likely bits.

References

1. Golomb, S. W., *Shift Register Sequences*. Holden Day, San Francisco, 1967.
2. Tausworthe, R. C., "Random Numbers Generated by Linear Recurrence Modulo Two," *Math. Comp.*, Vol. 19, No. 90, April 1965, pp. 201-209. See also *Supporting Research and Advanced Development*, JPL Space Programs Summary 37-27, Vol. IV, pp. 185-189, Jet Propulsion Laboratory, Pasadena, Calif., June 30, 1964.
3. Hurd, W. J., "A Wideband Gaussian Noise Generator Utilizing Simultaneously Generated PN-Sequences," in *Proceedings of the Fifth Hawaii International Conference on System Sciences*, January 1972, pp. 168-170. See also *The Deep Space Network Progress Report*, Technical Report 32-1526, Vol. III, pp. 111-115, Jet Propulsion Laboratory, Pasadena, Calif., June 15, 1971.
4. Lindholm, J. H., "An Analysis of the Pseudo-Randomness Properties of Subsequences of Long m-Sequences," *IEEE Trans. Info. Theory*, Vol. IT-14, No. 4, July 1968, pp. 569-576.
5. Kendall, W. B., "A Generator of Uncorrelated Pseudo Random Numbers for Scientific Data Systems (SDS) Computers," *Supporting Research and Advanced Development*, JPL Space Programs Summary 37-34, Vol. IV, pp. 296-298, Jet Propulsion Laboratory, Pasadena, Calif., Aug. 31, 1965.
6. Heller, J. A., "Improved Performance of Short Constraint Length Convolutional Codes," *JPL Space Programs Summary 37-56*, Vol. II, p. 83, Jet Propulsion Laboratory, Pasadena, Calif., Apr. 30, 1969.
7. Peterson, W. W., *Error-Correcting Codes*. MIT Press and John Wiley, New York, 1961.

Table 1. Some primitive polynomial configurations

n	N	q	T	d_0	d_{N-1}	N_0
20	4	5	7	1	2	1
20	4	5	7	1	3	1
20	4	5	11	1	4	1
60	10	6	29	2	3	3
60	15	4	31	2	1	2
80	16	5	25	4	3	7
155	31	5	79	2	3	2
160	32	5	29	2	1	3
160	32	5	57	2	1	5
288	32	9	81	6	7	13
310	31	10	95	5	8	2
310	31	10	119	5	6	3
310	31	10	93	3	8	4
310	31	10	117	6	9	4
310	31	10	97	2	7	5
310	31	10	97	5	2	5

Table 2. Chi-squared tests for uniformity

Polynomial degree	Number of dimensions	Degrees of freedom	Samples per test	Number of tests	Values less than		Values exceeding	
					χ^2_{99}	χ^2_{95}	χ^2_{01}	χ^2_{05}
60	1	1023	25,000	100	1	7	1	6
60	3	999	25,000	160	0	10	0	8
60	Totals			260	1	17	1	14
160	3	999	25,000	225	2	9	1	11
288	1	999	25,000	250	2	20	3	7
288	2	960	25,000	750	8	46	11	37
288	3	999	25,000	750	5	30	4	24
288	4	1295	25,000	750	4	37	5	30
288	5	1023	25,000	465	1	19	2	19
288	Totals			2965	20	152	25	117
310	3	999	25,000	280	2	20	2	10

Table 3. Chi-squared tests on weight distributions

Polynomial degree	m-tuple length	Degrees of freedom	Samples per test	Number of tests	Values less than		Values exceeding	
					χ^2_{99}	χ^2_{95}	χ^2_{01}	χ^2_{05}
60	60	26	25,000	25	1	2	1	2
60	120	36	25,000	25	0	0	1	2
60	180	44	25,000	25	0	2	1	1
60	240	50	25,000	25	0	1	0	0
60	300	56	25,000	25	0	2	0	2
60	600	76	25,000	25	0	0	0	1
60	1200	106	25,000	25	0	0	1	2
60	1800	126	25,000	70	0	2	1	4
60	Totals			245	1	9	5	14
160	32	18	25,000	25	0	2	0	0
160	96	32	25,000	25	0	1	1	2
160	160	42	25,000	25	0	0	0	0
160	320	58	25,000	25	0	0	0	0
160	640	78	25,000	37	0	5	1	2
160	1280	108	25,000	25	0	1	2	3
160	Totals			162	0	9	4	7
288	32	18	25,000	25	0	1	0	0
288	96	32	25,000	25	0	0	1	1
288	160	42	25,000	25	0	1	0	4
288	320	58	25,000	25	0	1	0	1
288	640	78	25,000	25	0	0	0	1
288	640	88	100,000	25	0	2	0	2
288	1280	108	25,000	25	0	2	1	1
288	Totals			175	0	7	2	10
310	31	17	10,000	25	0	1	0	0
310	155	37	10,000	25	0	1	0	3
310	310	52	10,000	25	0	0	0	3
310	620	70	10,000	25	0	1	1	2
310	1240	96	10,000	10	0	0	0	0
310	1240	116	50,000	10	0	1	0	0
310	Totals			120	0	4	1	8

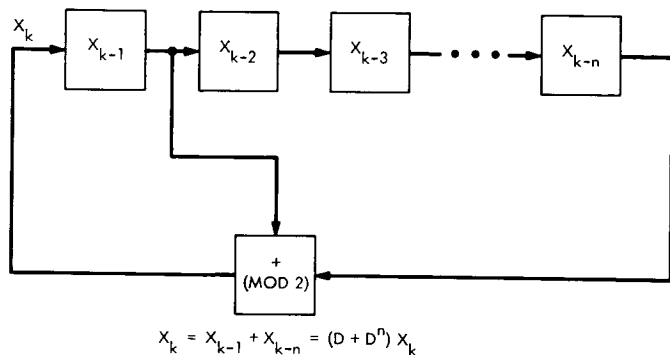


Fig. 1. Shift register of degree n with linear feedback

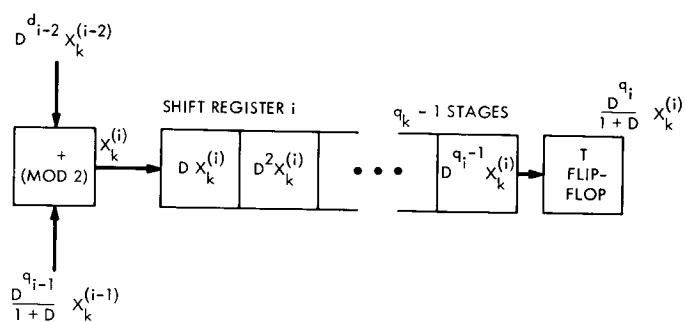


Fig. 3. General register of final configuration

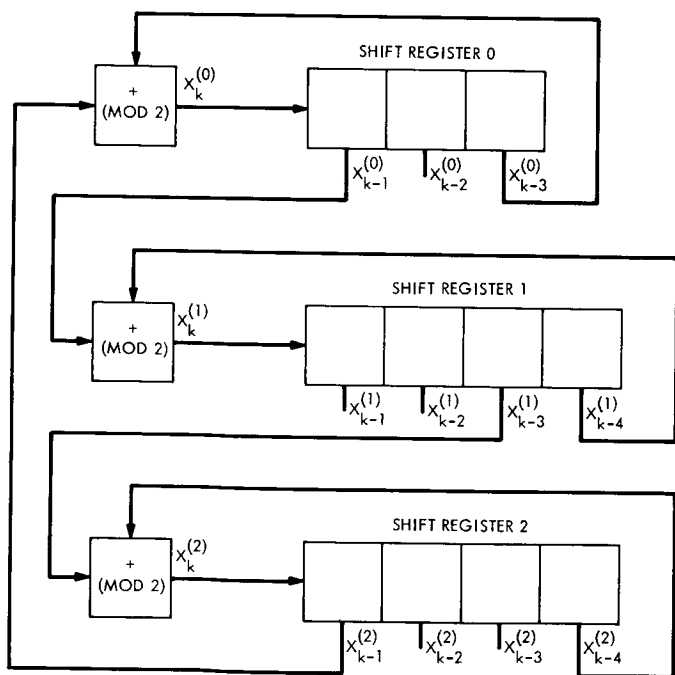


Fig. 2. A simple linear interconnection of three shift registers

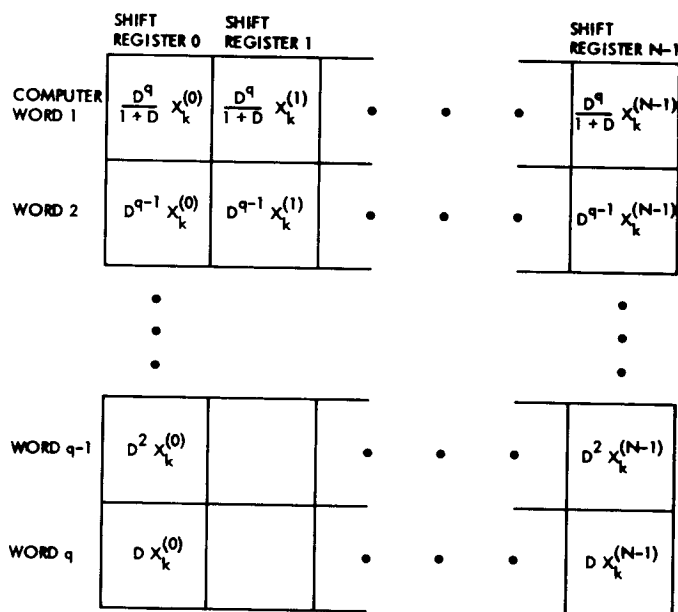


Fig. 4. Computer realization of shift registers

Appendix

XDS Sigma 5 FORTRAN Subroutine

The XDS Sigma 5 FORTRAN subroutine for the polynomial of degree 288 is listed in Fig. A-1. The program utilizes the machine dependent in-line code features of XDS Extended FORTRAN IV and is therefore not compatible with other machines. Usage is as follows:

- (1) CALL PN288(N): Nine pseudorandom integers are returned in array *N*. Their distribution is uniform from -2^{31} to $2^{31}-1$.
- (2) CALL PN1(M): One new number is returned in *M*.
- (3) CALL PIX(N): The state of the nine words of memory determining the next

output are returned in array *N*. These are not the same as returned by a CALL to PN-288.

- (4) CALL PAX(N): Packs the nine words of memory from array *N*.
- (5) CALL PIXJ(M): Returns the value of a pointer used by PN1.
- (6) CALL PAXJ(N): Sets the pointer.

A general random number package utilizing this basic algorithm has been written by R. Winkelstein and will be reported on in a future article.


```

1:      SUBROUTINE PN2R8(NOUT)
2:      DIMENSION N(18),NOUT(0:1)
3:      DATA J,NW/19,9/
4:      DATA (N(I),I=1,9)/2036521439,=1235874521,1985321452,1478598765,
5:      1=888521432,963598521,=1235741258,=2100352140,1865423518/
6:      S      BAL,2      2S
7:      S      LW,3      N+9
8:      S      LCI      9
9:      S      STM,3      *NOUT
10:     J=19
11:     RETURN
12:  S2      LI,3      =9
13:  S1      LW,4      N+11,3
14:  S      LW,5      =X194A5294A'
15:  S      LS,4      N+12,3
16:  S      SCS,4      =5
17:  S      EOR,4      N
18:  S      SCS,4      =5
19:  S      STW,4      N+18,3
20:  S      LW,5      N
21:  S      EOR,5      N+10,3
22:  S      STW,5      N
23:  S      BIR,3      1S
24:  S      LCI      8
25:  S      LM,4      N+10
26:  S      STM,4      N+1
27:  S      B      *2
28:     ENTRY PN1(N1)
29:     IF(J.LE.18)GOTO 20
30:     J=10
31:  S      BAL,2      2S
32:  20      N1=N(J)
33:     J=J+1
34:     RETURN
35:     ENTRY PAX(NOUT)
36:     D8 30 I=NW,1,=1
37:  30      N(I)=NOUT(I-1)
38:     J=19
39:     RETURN
40:     ENTRY PIX(NOUT)
41:     D8 40 I=NW,1,=1
42:  40      NOUT(I-1)=N(I)
43:     RETURN
44:     ENTRY PAXJ(JOUT)
45:     J=MAX0(JOUT,NW+1)
46:     RETURN
47:     ENTRY PIXJ(JOUT)
48:     JOUT=J
49:     RETURN
50:     END

```

D7 INTO R4

D6 INTO R4 6N MASK

ANS IN R4, NOT PROPERLY SHIFTED

ANS IN R4, PROPERLY SHIFTED

ANS IN N=ARRAY, LOWER PART

NEW D9 INTO N

Fig. A-1. XDS Sigma 5 FORTRAN subroutine for the polynomial of degree 288

NASTRAN Data Generation and Management Using Interactive Graphics

M. S. Katow
DSIF Engineering Section

B. M. Cooper
Science and Engineering Computing Section

For effective use of the NASA Structural Analysis (NASTRAN) computer system, the input bulk data must accurately model the structure to be analyzed and result from a minimum of time and money expended. A method of using an interactive graphics device to generate a large portion of the input bulk data with visual checks of the structure and the card images is described. The generation starts from GRID and PBAR cards. The visual checks result from a three-dimensional display of the model in any rotated position. By detailing the steps, the time saving and cost effectiveness of this method may be judged, and its potential as a useful tool for the structural analyst may be established.

I. Introduction

The generation of NASTRAN input bulk data to correctly simulate or model a large structure to be analyzed usually consumes much time. Sketches and/or drawings are necessary to define the GRID numbers connected by structural elements identified with Element Identification (EID) numbers and their property identification (PID)

numbers. After the constraints are organized, a list for keypunching must be prepared. After the cards are keypunched and input to the computer, more time is required to debug the input data for compliance with the NASTRAN formats before an answer is output. Debugging procedures usually employ plotting capabilities available in NASTRAN to provide visual checks of the structural model. Normally, further checking follows by

noting values in the load vectors generated by gravity loadings, the coordinates of the center of gravity, and symmetry or equating of the single-point constraint values to the input load vectors.

Besides the schedule time deadlines, the total cost of the analysis must be considered. Procedures or processes that can reduce the time of preparing input data invariably reduce costs. If during these processes the correctness of the model can be raised to a high level before input to a computer, the NASTRAN computing costs can be reduced.

At JPL, with the installation of the UNIVAC Advanced Graphics Display System to the UNIVAC 1108 — EXEC 8 time-sharing computer used for scientific computing purposes, the development of the use of interactive graphics to generate and check NASTRAN bulk data has proceeded.

II. Configuration Description

The UNIVAC Advanced Graphics Display System is composed of two major units: the display controller minicomputer (Type 1557) and the display console (Type 1558). The purpose of the minicomputer is to provide computing and control capabilities to handle, internally, display functions and programs that are tailor-made by the user to meet NASTRAN bulk data requirements. It also serves as an interactive device to the UNIVAC 1108 processor to provide additional large-scale processing capabilities.

The display console consists of a cathode ray tube (CRT) display, keyboard, display control, and light pen. The unit is designed for display of grid points, line vectors, alphanumeric characters, and special symbols necessary for the NASTRAN program. It features a high-speed, high-precision CRT to accommodate the wide variety of graphic displays.

The basic configuration of the system interfaces directly with an input/output channel of the UNIVAC 1108 processor. The basic storage for the minicomputer contains 8192 locations.

III. Graphics Programming Library

A primary purpose of the UNIVAC 1108 — EXEC 8 computer and Graphics Programming Library (GPL) is

to provide easily manipulated data structures that describe and define a displayable image for the 1557/1558 graphics minicomputer/display console.

The GPL permits both the graphics entities which constitute the images to be displayed and nongraphic associated or managerial data to be defined and stored in the data base. Entities of both types can be grouped to form single higher level or parent groups capable themselves of being grouped to form still higher-level groups, giving rise to a hierarchically organized data structure.

A large central data base is required to support the NASTRAN package; thus many automatic facilities are included in the system to make management of these data both convenient and efficient. In order to maintain the integrity of the data file, it is accessible only through the GPL subroutines. These subroutines permit total flexibility in defining, manipulating, and displaying images on the display screen.

Interaction control tables (ICTs) provide a unique approach to the problem of defining and accomplishing the processing to be performed in the minicomputer. These tables handle the function of basic attention handling, analyze and change both its data base and display file, and send and request information to and from the central computer as required. The ICTs are a hardware-independent, interpretively executed, interactively oriented language in which processing performed by the minicomputer is programmed by the user.

IV. The Use of Interactive Graphics

A. Structure Development Program

In the normal analysis, the preparation of the input bulk data cards starts with the GRID cards. The grid point numbers of these cards are defined on a sketch or drawing. Also, from these pictures the coordinate values are ascertained directly or by calculations on a desk machine. Normally, these coordinate values are described within the precision limits of the computer, although in the real structure there are larger errors. These errors can be evaluated as to their effects on the answers from the analysis as one more separate problem in structural analysis to be considered. Because of the symmetrical nature of many structures, precise coordinate values usually aid in debugging as well as enhancing the use of partial section analysis, thereby reducing the time and cost of analysis.

For this method of interactive graphic adaptation, the GRID cards are keypunched to suit NASTRAN format. For this discussion we will assume that only CBARs are used, so PBARs are keypunched next.

At this point, these NASTRAN cards are input to a catalog file in the 1108, and the 1557/1558 unit through GPL is activated so that the CBARs can be generated or completely listed and keypunched for observation and updating by interactive graphics. The NASTRAN graphics package consists of three subprograms: a structure development subprogram for the CBAR generation, a rotation subprogram for visual demographics, and a data edit subprogram for card image alterations. Each subprogram can be used in a stand-alone mode or can be subroutinized to operate interchangeably.

The graphics tube face layout has been designed from a human engineering standpoint, with speed and efficiency coordinated at each user/hardware operation. The tube face is divided and overlaid by windows, each representing a segment of the visual data structure. One window contains a "menu" which informs the user of his current status in the program. These window and menu concepts can be seen in Fig. 1.

In the left window, the grid point identification numbers from the catalog file are listed in columns. Above it are listed the PID numbers of the PBARs. To the right side of the grid ID, there is space for displaying the generated CBAR data.

The right window of the tube displays, as point vectors, the grid point locations initially as they appear normal to the XY plane. Then by pressing either X, Y, or Z on the keyboard, the views in XY, XZ, or YZ planes, respectively, can be displayed.

The light-sensitive pen is then pointed to the first GA of the desired CBAR. The screen responds by displaying a \pm "local indicator" next to the listed GA as well as the point vector on the right window. When in succession, the GB, PID, and GO are selected via light pen interaction; then a "C" in the keyboard enters the CBAR, which is shown by an entry in the CBAR connection list data in the left window and a directional vector between the point vectors of the GA and GB. The formats described are shown by a photograph of the screen after some CBARs have been developed (Fig. 1).

At any time during this development of the structural model the rotation subprogram may be called and the

model can be visually checked from any oblique angle. Figure 2 shows the model of Fig. 1 viewed by rotations around the X and Z axes of 30 deg each. Figure 3 shows the complete development at a -30-deg angle about the X axis.

B. Rotation Subprogram

This monitor (a 1557 software operating system) performs three-dimensional rotation on the two-dimensional screen, which gives the user complete control of visual structure demographics: rotation about any axis, at any incremental angle, at any speed. This combination of control leads to "animated" movement in three dimensions for visual analysis and to hard copy graphics of the structure.

If at this time the card images of a GRID or CBAR require changes, the GRID data may be edited by a call to the data edit subprogram. A typical display is shown in Fig. 4. By use of the keyboard, specific changes can be made in the card image inputs.

C. Data Set Edit Subprogram

The data set edit routine can be utilized as a stand-alone procedure to update an existing NASTRAN data package or as a subroutine in a structure development production.

The data set edit routine presents the "card image" run stream by paging data and control messages across the screen at the user's discretion. On each page, the user has control of editing options and can direct the program. The user can change a card image, delete a card image, and add a card image which represents a CBAR or PBAR, while maintaining all structure credibilities connected to the member unless entirely deleted.

The user can switch the rotation monitor on and visually check his structure, flag a member, and automatically have the program page to the card image representing the member for further analysis and editing.

To prevent loss of completed connections, a page of 25 CBARs is automatically stored in the user's FASTRAND file. In turn, the next 25 CBARs may be entered. This program has restart capabilities in case of computer failure or "current" analysis changes.

When the visual checks of the interactive graphics output signal a good set of GRID, CBAR, and PBAR

cards, the final exit can be made by requesting the 1108 to punch out the edited cards as presently programmed, or, in the 1108, it is possible to have data files read into a catalog file so that an immediate NASTRAN run can be made from the remote terminal used for the 1557/1558 unit.

V. Advantages of Interactive Graphics

The replacement of the normal listing of CBARs and subsequent keypunching with the use of interactive graphics will save time. However, the greatest values should result from the opportunity to make intermittent three-dimensional visual checks of the structural model. The analyst can ensure the accuracy of the model as well

as provide an opportunity for study to optimize the geometric arrangement.

As the system is now working, using many satellite ICT routines and self-contained monitors with the minicomputer, minimum demand time is required of the 1108. The current cost of working the system is approximately \$50/h. This includes "roll-in/roll-out" of the three monitors and full user utilization in a demand environment.

Acknowledgement

Appreciation is expressed to Larry Bauer of UNIVAC for advanced development of the GPL and to Robert Patton for research and development of the rotation subprogram.

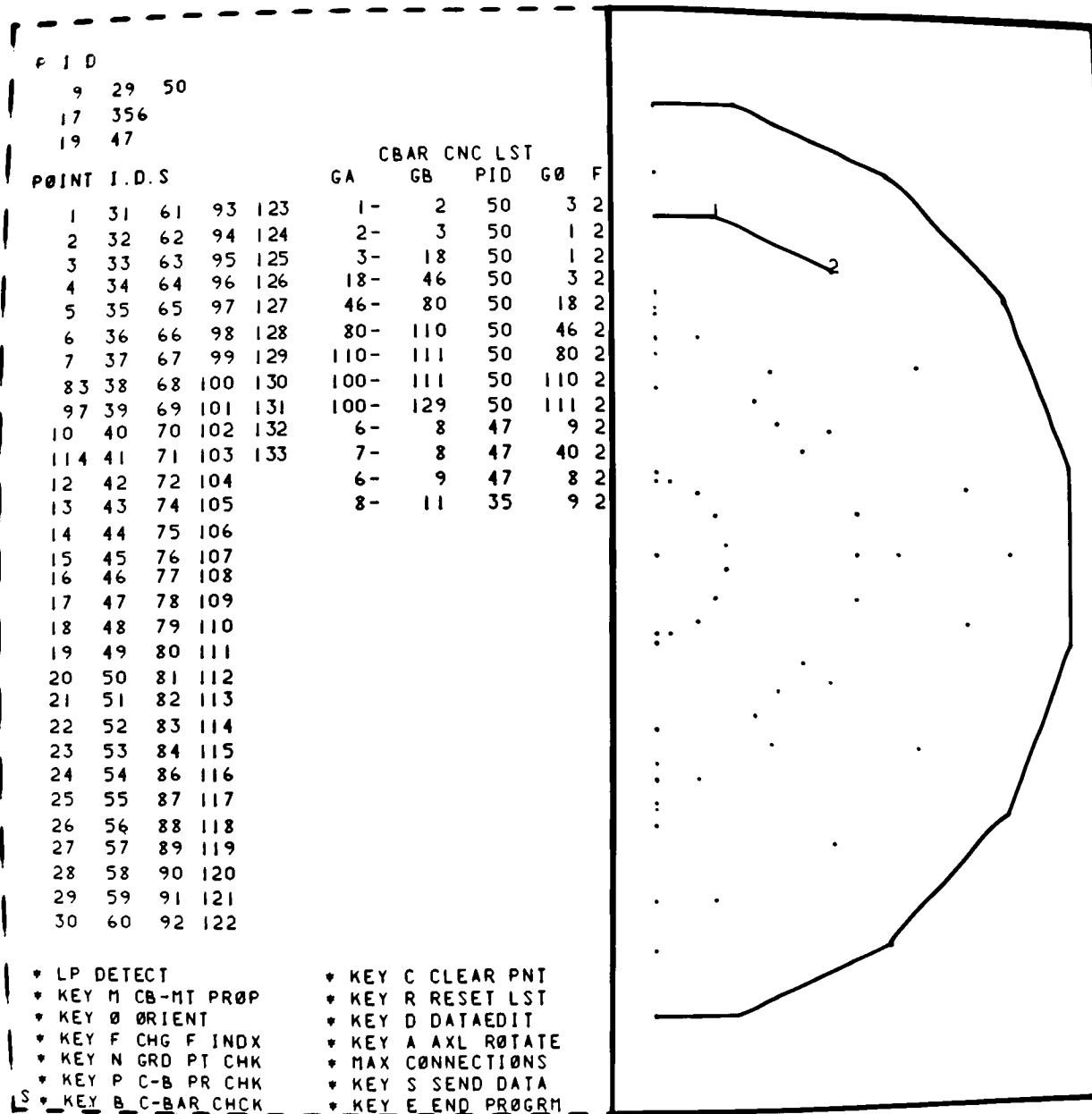


Fig. 1. The XY plane image data development program

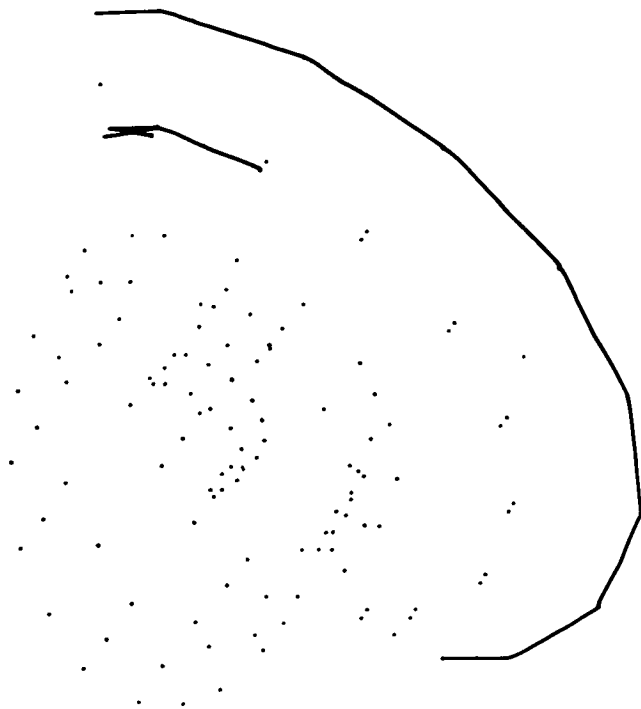


Fig. 2. Rotated partial development, rotation subprogram

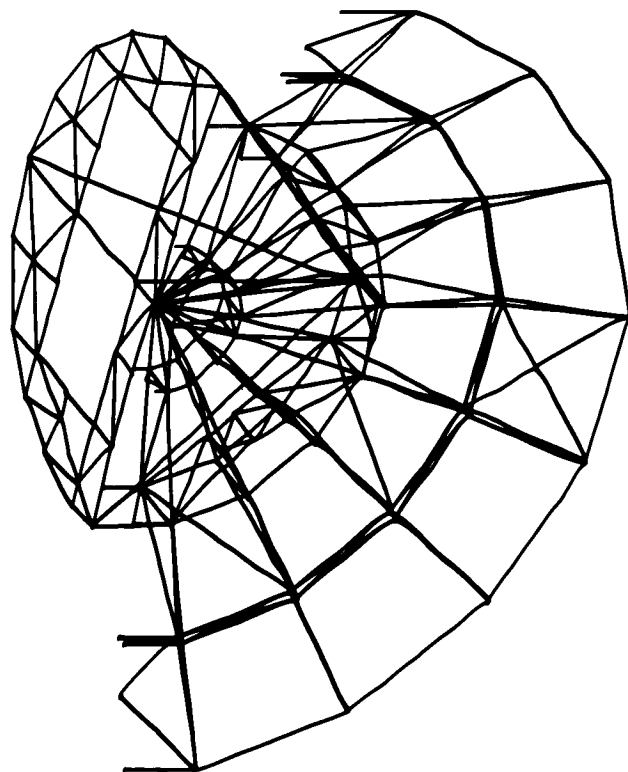


Fig. 3. Rotated full structure, rotation subprogram

CBAR	EID	PID	GA	GB	G0	F
*CBAR	61	35	20	22	19	2
*CBAR	44	35	19	21	22	2
*CBAR	65	35	20	42	33	2
*CBAR	69	35	21	33	42	2
*CBAR	129	35	42	49	33	2
*CBAR	107	35	33	50	42	2
*CBAR	152	35	49	64	77	2
*CBAR	156	35	50	64	76	2
*CBAR	157	35	50	77	76	2
*CBAR	199	35	64	77	76	2
*CBAR	198	35	64	76	77	2
*CBAR	238	35	76	106	77	2
*CBAR	243	35	77	107	76	2
*CBAR	308	35	106	115	116	2
*CBAR	310	35	107	116	115	2
*CBAR	*****					

* OLD PAGE

* LIST

* NEW PAGE

* RETURN

PL

Fig. 4. CBAR listing, data set edit subprogram

Preliminary Analysis of the Microwave Weather Project Data for CY 1971

M. S. Reid and R. W. D. Booth
Communications Elements Research Section

The Weather Project forms part of an overall Radio Systems Development Project which seeks to optimize the spacecraft-to-ground communications link. Statistical correlations of weather and communications capability at X- and K-bands are needed to provide practical predictions of link performance. Thus the objective of the Weather Project is the statistical prediction of the performance of the DSN at X-band and, in the future, at K-band. A previous article discussed the general approach of the Weather Project, the measurements, calibrations, equipment, and methods. Problems encountered were also discussed as well as proposed future work. This article reports on a preliminary analysis of the Weather Project data for calendar year 1971. These results are presented in tabular form. Cumulative frequency distributions of percentages of excess system temperature are tabulated as a function of time (whole year and quarterly periods) and of antenna elevation angle (four elevation ranges and all elevation angles). Averages, standard deviations, and confidence limits are tabulated, and the experimental results are compared with the data from a theoretical study based on estimated and observed cloud cover effects.

I. Introduction

The Weather Project forms part of an overall Radio Systems Development Project which seeks to optimize the spacecraft-to-ground communications link. Statistical correlations of weather and communications capability at X- and K-bands are needed to provide practical predictions of link performance. Thus the objective of the Weather Project is the statistical prediction of the per-

formance of the DSN at X-band and, in the future, at K-band. A previous article (Ref. 1) discussed the general approach of the Weather Project, the measurements, calibrations, equipment, and methods. Problems encountered were also discussed as well as proposed future work. This article reports on a preliminary analysis of the Weather Project data for calendar year 1971. These results are presented in tabular form. Cumulative frequency distributions of percentages of excess system

temperature are tabulated as a function of time (whole year and quarterly periods) and of antenna elevation angle (four elevation ranges and all elevation angles). Averages, standard deviations, and confidence limits are tabulated, and the experimental results are compared with the data from a theoretical study (Ref. 2) based on estimated and observed cloud cover effects.

II. Discussion of the Tables

The results for calendar year 1971 are presented in tabular form. Table 1 is a cumulative frequency distribution of percentages of excess system temperature due to atmospheric conditions and other unknowns as a function of antenna elevation angle. The excess system temperatures have been divided into increments of 10 K. Four antenna elevation angle ranges have been considered: 6 to 14.99, 15 to 24.99, 25 to 44.99, and 45 to 90 deg. The table consists of percentages of time that the excess system temperature was less than the nominal magnitude for the various antenna elevation angles. Thus for 88.4 percent of the time that the antenna's elevation angle was in the range 6 to 15 deg, the excess system temperature was under 10 K. The column on the right lists percentages for all elevation angles.

The frequency distribution shown in Table 1 is for the whole of calendar year 1971. The table lists percentages of time, in each antenna elevation angle range, that the excess system temperature was less than the value given in the left-hand column. Tables 2 through 5 are similar tables for quarterly periods. Table 4, for example, is the frequency distribution for June through August 1971.

The total number of minutes of good data recorded in each category is listed at the bottom of each of the above tables. In Table 1, for example, which refers to the whole of calendar year 1971, the total number of minutes of good data recorded is listed as 172,000 out of a possible 529,000 minutes. This means that good data were obtained for only 33% of the year. The reasons for missing or bad data are several. Data were lost when scheduled X-band radio science experiments were carried out, or when the X-band system was undergoing frequency changes, development or diagnostic work, or when equipment failed. The unusable or "bad" data were recorded when the X-band system suffered from S-band transmitter fourth harmonic interference, noise burst interference, or when calibration was lost due to equipment or operator error, etc.

The usable or "good" data, however, are also subject to some error. The most common sources of error in the good data are inaccuracies in the scale calibrations due to drifts in the equipment and an insufficiently determined fair weather baseline. These sources of error are being investigated.

Table 6 shows averages, standard deviations, and confidence intervals on measured excess system temperatures for the whole year and for the year divided into separate quarters. In each period the data have been divided into the same antenna elevation intervals as in the previous tables. The results have been computed taking one data point per minute of recorded data. The mean values of the excess system noise temperature for the various periods and elevation angles are shown in the second column. The next column lists the standard deviation of the data. This column shows that there is a considerable spread in the data, particularly at low elevation angles and for the winter months. The next two columns list the 95 and 50% confidence intervals, computed from the measured data, on the mean values of the excess system temperatures. These confidence intervals were calculated assuming all errors are random and neglected the effects of any bias in any of the measurements. Bias errors would degrade the calculations by widening the intervals for a fixed confidence. Hence, neglecting bias errors and assuming the same conditions held for next year (same equipment, same weather, etc.), one would expect to obtain a mean excess near 5.6 K with a probability of about 0.95.

The mean value can be calculated with good resolution since one data point per minute is recorded and used in the calculations; hence N , the total number of data points, is large. The sample mean converges fairly rapidly, approximately as σ/\sqrt{N} , where σ is the standard deviation of the data. The sample mean converges as σ/\sqrt{N} if the data are gaussian distributed, which is only approximately true in this case.

Tables 7 and 8 are a comparison between experimental and calculated data for 0.90 and 0.99 probability conditions. The experimental data are the frequency distribution tables of excess system noise temperatures, Tables 1 through 5, and the calculated results are based on a theoretical study of cloud cover (Ref. 2). The agreement is not good at 0.99 probability but is somewhat better at 0.90 probability. There are several possible reasons for this. The theoretical study was based on observed and estimated cloud cover of the Goldstone area for a time period of a few years prior to the start of the Weather

Project. One would expect that as the elevation angle of the antenna is lowered, the probability of a cloud intercepting the beam of the antenna would increase, resulting in a higher expected noise temperature. Hence the calculated results show a steady increase in excess system temperature with decrease in elevation angle.

The statistics from the experimental data are a little more uneven. The experimental results include all elements that affect the system noise temperature such as clouds, rain, snow, and all the effects and errors not related to the atmosphere and described above. Furthermore, the 0.99 probability level is extremely sensitive to the actual data. Roundoff errors, the choice of antenna elevation channel size, and in some cases such as low elevation angles, the relatively few data points all lead to these uneven results. The 0.90 probability level should be more reliable since a fairly large amount of data falls above the 0.90 probability level.

It must be noted that:

- (1) Measured results are based on one year of data only. It is not possible to derive meaningful statistics from one year of recorded data.
- (2) The calculated values are based on cloud cover only, whereas the measured values are for all atmospheric effects.
- (3) For the measured results the underlying data are only approximately gaussian distributed (as indicated by a test for normality), and therefore the use of confidence intervals is suspect.
- (4) More measured data are required before meaningful statistics can be deduced.
- (5) A more accurate baseline must be determined.

References

1. Reid, M. S., "A Description of the Weather Project," in *The Deep Space Network Progress Report*, Technical Report 32-1526, Vol. X, pp. 116-122. Jet Propulsion Laboratory, Pasadena, Calif., Aug. 1972.
2. Smith, T. B., and Chien, C. W., "Cloud Cover Effects on Signal Attenuation at DSN Sites," Subcontract No. 952757, Meteorology Research Inc., Altadena, Calif., April 1970.

Table 1. Cumulative percentage probabilities of excess system temperature for CY 1971

Excess system temperature less than, K	Range of antenna elevation angle, deg				
	6-15	15-25	25-45	45-90	6-90
10	88.4	94.4	95.3	97.1	96.3
20	91.1	96.1	96.6	97.8	97.2
30	93.1	96.4	97.2	98.2	97.7
40	94.8	96.7	97.6	98.4	98.0
50	95.3	96.7	97.8	98.5	98.2
60	96.6	97.0	98.0	98.5	98.3
70	96.6	97.3	98.3	98.6	98.4
80	97.0	97.6	98.4	98.7	98.5
90	97.0	97.9	98.5	98.9	98.7
100	97.0	98.2	98.8	99.2	99.0
110	97.0	98.2	98.8	99.3	99.1
120	97.0	98.7	98.9	99.3	99.2
130	97.8	99.0	99.2	99.4	99.4
140	97.8	99.3	99.4	99.4	99.5
150	98.6	99.6	99.5	99.4	99.6
160	98.6	99.9	99.6	99.4	99.7
170	99.0	99.9	99.6	99.5	99.8
180	99.0	100.0	99.8	99.6	99.9
190	99.4	100.0	100.0	99.7	100.0
200	99.4	100.0	100.0	100.0	100.0
210	99.8	100.0	100.0	100.0	100.0
220	99.8	100.0	100.0	100.0	100.0
270	100.0	100.0	100.0	100.0	100.0

Antenna elevation angle was:

6-15 deg 4.61% of the time.
15-25 deg 6.40% of the time.
25-45 deg 16.75% of the time.
45-90 deg 72.24% of the time.

Total number of minutes of good data recorded was 172,000 out of a possible 529,000 minutes.

Table 2. Cumulative percentage distribution of excess system temperature for CY 1971 (December, January, February)

Excess system tempera- ture less than, K	Range of antenna elevation angles, deg				
	6-15	15-25	25-45	45-90	6-90
10	77.2	92.6	92.7	90.4	89.6
20	82.6	92.6	93.5	91.1	90.8
30	88.0	92.6	94.3	92.9	92.7
40	92.0	92.6	94.3	93.9	93.8
50	93.3	92.6	94.3	94.6	94.4
60	96.0	92.6	94.3	95.0	95.0
70	96.0	92.6	94.3	96.0	95.7
80	97.3	95.1	94.3	96.3	96.1
90	97.3	97.6	94.9	96.5	96.5
100	97.3	100.0	96.6	97.5	97.6
110	97.3	100.0	96.6	97.9	97.9
130	100.0	100.0	96.6	98.1	98.3
150	100.0	100.0	97.1	98.1	98.4
160	100.0	100.0	97.9	98.1	98.5
180	100.0	100.0	99.4	98.1	98.8
190	100.0	100.0	100.0	98.5	99.2
200	100.0	100.0	100.0	99.4	99.8
210	100.0	100.0	100.0	100.0	100.0

Antenna elevation angle was:

6-15 deg 10.25% of the time.

15-25 deg 5.59% of the time.

25-45 deg 17.92% of the time.

45-90 deg 66.24% of the time.

Total number of minutes of good data recorded was 21,830 of a possible 129,750 minutes.

Table 3. Cumulative percentage distribution of excess system temperature for CY 1971 (March, April, May)

Excess system temperature less than, K	Range of antenna elevation angles, deg				
	6-15	15-25	25-45	45-90	6-90
10	98.4	98.2	99.5	99.3	99.3
20	100.0	100.0	100.0	99.8	99.8
30	100.0	100.0	100.0	100.0	100.0
40	100.0	100.0	100.0	100.0	100.0

Antenna angle was:

6-15 deg 2.13% of the time.

15-25 deg 2.71% of the time.

25-45 deg 11.52% of the time.

45-90 deg 83.63% of the time.

Total number of minutes of good data recorded was 43,345 out of a possible 133,400 minutes.

Table 4. Cumulative percentage distribution of excess system temperature for CY 1971 (June, July, August)

Excess system temperature less than, K	Range of antenna elevation angles, deg				
	6-15	15-25	25-45	45-90	6-90
10	80.5	93.1	92.4	92.9	92.3
20	83.9	93.1	92.5	94.9	93.9
30	86.6	93.1	92.5	95.2	94.2
40	86.6	93.1	94.7	95.4	94.7
50	87.2	93.1	95.8	95.6	95.1
60	87.2	93.1	95.8	95.6	95.1
70	87.2	93.1	96.3	95.6	95.2
80	87.2	93.1	96.3	95.8	95.4
90	87.2	93.1	96.3	96.6	96.0
100	87.2	93.1	96.8	97.3	96.6
110	87.2	93.1	96.8	97.5	96.8
120	87.2	95.1	97.3	97.6	97.1
130	87.2	96.1	98.9	97.8	97.6
140	87.2	97.1	100.0	98.0	98.0
150	91.4	98.1	100.0	98.1	98.3
160	91.4	99.1	100.0	98.3	98.6
170	93.5	99.1	100.0	98.9	99.1
180	93.5	100.0	100.0	99.4	99.5
190	95.6	100.0	100.0	99.5	99.7
210	97.7	100.0	100.0	99.5	99.8
220	97.7	100.0	100.0	100.0	99.9
270	100.0	100.0	100.0	100.0	100.0

Antenna elevation angle was:

6-15 deg 4.07% of the time.

15-25 deg 8.69% of the time.

25-45 deg 16.0% of the time.

45-90 deg 71.23% of the time.

Total number of minutes of good data recorded was 34,866 out of a possible 132,900 minutes.

Table 5. Cumulative percentage distribution of excess system temperature for CY 1971 (September, October, November)

Excess system tempera- ture less than, K	Range of antenna elevation angles, deg				
	6-15	15-25	25-45	45-90	6-90
10	96.4	94.9	95.7	99.6	98.2
20	97.3	97.9	98.0	99.7	99.0
30	97.3	98.4	99.0	100.0	99.5
40	98.6	98.9	99.0	100.0	99.6
50	98.6	98.9	99.0	100.0	99.6
60	100.0	99.4	99.4	100.0	99.8
70	100.0	100.0	99.7	100.0	100.0
80	100.0	100.0	100.0	100.0	100.0
90	100.0	100.0	100.0	100.0	100.0
100	100.0	100.0	100.0	100.0	100.0
110	100.0	100.0	100.0	100.0	100.0

Antenna elevation angle was:

6-15 deg 4.65% of the time.

15-25 deg 7.76% of the time.

25-45 deg 19.93% of the time.

45-90 deg 67.66% of the time.

Total number of minutes of good data recorded was 71,904 out of a possible 132,500 minutes.

**Table 6. Averages, standard deviations, and confidence intervals
on excess system temperature for CY 1971**

Period	Range of antenna elevation angles, deg	Excess noise temperature mean value, K	Standard deviation, K	95% confidence level, K	50% confidence level, K
CY 1971	6-15	11.0	32.1	± 0.71	± 0.24
January	15-25	7.9	21.8	± 0.41	± 0.14
through	25-45	6.4	18.3	± 0.21	± 0.07
December	45-90	5.6	17.1	± 0.10	± 0.03
	All angles	6.1	18.6	± 0.09	± 0.03
December	6-15	11.6	26.0	± 1.07	± 0.18
January	15-25	7.2	23.6	± 1.32	± 0.37
February	25-45	9.8	34.7	± 1.09	± 0.46
	45-90	9.0	31.2	± 0.51	± 0.37
	All angles	9.3	31.0	± 0.41	± 0.14
March	6-15	4.0	5.2	± 0.34	± 0.12
April	15-25	3.1	5.0	± 0.29	± 0.10
May	25-45	2.1	4.2	± 0.12	± 0.04
	45-90	3.9	5.2	± 0.05	± 0.02
	All angles	3.7	5.1	± 0.05	± 0.02
June	6-15	30.6	63.0	± 3.30	± 1.13
July	15-25	15.5	35.5	± 1.26	± 0.44
August	25-45	11.6	24.9	± 0.65	± 0.22
	45-90	11.6	27.3	± 0.34	± 0.12
	All angles	12.7	30.3	± 0.32	± 0.11
September	6-15	4.2	9.1	± 0.31	± 0.11
October	15-25	5.0	8.9	± 0.23	± 0.08
November	25-45	4.9	8.6	± 0.14	± 0.05
	45-90	2.7	4.7	± 0.04	± 0.01
	All angles	3.4	6.4	± 0.05	± 0.02

**Table 7. Comparison of cumulative probabilities derived from calculated and measured results for 0.99 probability conditions
(Probability of 0.99 excess noise temperatures will be less than value tabulated)**

Period	Elevation angle, deg	Calculated results, K	Measured results, K
CY 1971	6-15	75	170
January	15-25	40	130
through	25-45	25	123
December	45-90	17	93
December	6-15	110	116
January	15-25	60	96
February	25-45	40	167
	45-90	25	195
September	6-15	45	53
October	15-25	25	52
November	25-45	18	30
	45-90	14	< 10

**Table 8. Comparison of cumulative probabilities derived from calculated and measured results for 0.90 probability conditions
(Probability of 0.90 excess noise temperatures will be less than value tabulated)**

Period	Elevation angle, deg	Calculated results, K	Measured results, K
CY 1971	6-15	35	16
January	15-25	18	< 10
through	25-45	10	< 10
December	45-90	6	< 10
December	6-15	50	35
January	15-25	25	< 10
February	25-45	15	< 10
	45-90	9	< 10
September	6-15	25	< 10
October	15-25	12	< 10
November	25-45	7	< 10
	45-90	4	< 10

High-Reliability Microcircuit Procurement in the DSN

E. F. Zundel

DSIF Digital Systems Development Section

The implementation of microelectronic circuits in the DSN is discussed together with utilization of an equivalent MIL-STD-883 Class B device, screening tests to be used and screening philosophy relative to failure mechanism patterns. The costs to be expected and the advantages of standardization of device types to increase quantity buys are also discussed.

I. Introduction

For the past several years, the JPL DSIF Digital Systems Development Section has utilized a standardized line of digital logic elements in system development and implementation. These modules were manufactured with discrete components which were screened by being subjected to voltage/temperature stresses and specified visual and electrical tests. The component screening process coupled with workmanship controls during module assembly produced a digital module at a reliability level suitable for ground telemetering and control systems.

As systems have become more complex, increased speed requirements and space limitations have necessitated the use of microcircuits in DSIF digital systems. This article discusses the philosophy being used in the procurement of these microcircuits.

II. The Reliability Level

MIL-STD-883, "Test Methods and Procedures for Microelectronics," contains industry-accepted methods and conditions of test that might be selected to achieve a desired level of quality and reliability. Three reliability classes have been defined by this standard as follows:

Class A. Devices intended for use where maintenance and replacement are extremely difficult or impossible and reliability is imperative.

Class B. Devices intended to be used where maintenance and replacement can be performed but are difficult and expensive and where reliability is imperative.

Class C. Devices intended to be used where maintenance and replacement can readily be accomplished and where downtime is not a critical factor.

Various levels of screening tests can be selected from MIL-STD-883 to verify that the device can be properly classified for an intended use as indicated above. The highest levels of screening tests are more restrictive and therefore more costly to perform. To be cost effective, a careful study of screening levels must be made to select only those which contribute significantly to the assurance that the device meets the classification desired.

Class B is considered adequate for DSN systems. Screening test levels have been selected from those recommended in MIL-STD-883 for this device classification.

III. Failure Mechanisms

Experience data which will identify the most frequent failure mechanisms for similar device types are extremely valuable in selecting screening tests. Rome Air Development Center (RADC) Reliability Notebook Vol. II lists the most common failures of microelectronics as:

- (1) Lead bond failures.
- (2) Leakage (nonhermetic).
- (3) Changes in transfer characteristics.

The following are listed by RADC as failure mechanisms which are representative of the industry average:

Failure mechanism	Percent of total failures
1. Wire bond failures	33
2. Metalization failures	26
3. Contact and photolithographic failures	18
4. Others	23

In another survey, less than 50% of total defects can be traced to device complexity while more than 50% of defects are due to lead bonds, photolithography, and contamination.

The Digital Systems Development Section has accumulated failure data on the high-reliability modules referred to in Section I by utilization of a program which requires each failed component to be reported and the failure mechanism determined. The transistor is the only

discrete component which is sufficiently similar to the microcircuit to be of interest. The results on some 275,000 transistors are:

Failure mechanism	Percent of total failures
Contamination due to nonhermeticity	79
Lead bond failures	14
All other	7

A special set of circumstances existed which contributed to the very high contamination failure rate. Since this has been corrected, the leading defects are lead bond failures, with metalization defects next in frequency of occurrence.

IV. Screening and Test Philosophy

The Digital Systems Development Section has published a general specification for integrated microelectronic circuits (ES 506145) which is being used to procure devices for DSN digital systems. This specification has incorporated screening tests which are expected to minimize the probability of that devices with potential defects will be installed in system hardware. Special emphasis is placed in those areas of high failure incidence as shown below:

Failure mechanism	Screening test
Lead bond failures	Pre-cap visual Temperature cycle Centrifuge Burn-in Bond strength
Contamination defects	Pre-cap visual Temperature cycle Hermeticity Burn-in
Metalization defects	Pre-cap visual Temperature cycle Burn-in

It will be noted from the table above that pre-cap visual, burn-in, and hermeticity play prominent roles in detecting potential failures. Electrical tests which are designed to identify changes in parameter and functional characteristics are contained in a detail specification

because of the unique nature of each device type. The detail specification also specifies limits on certain critical parameters and requires that measured values be provided. A lot percent defective allowable (PDA) is defined in the detail specification. This requires the supplier to collect certain test failures for each device in a given screening lot. If the percentage of fails exceeds the allowable limit, the entire lot is rejected. This prevents the acceptance of any lot which encountered a higher than normal rejection rate, with the likely possibility that the remainder passed the test with marginally acceptable characteristics.

The general specification requires that JPL be permitted to monitor any of the manufacturing or screening operations. Failure mechanisms may not be in the same ratio for a particular supplier when compared to the industry average. As this becomes known, it permits a shift in monitoring effort into the area of greatest concern. It has been found that suppliers of this product devote attention to process details in direct proportion to the interest and concern shown by the user. Inherent reliability is a function of process controls, while screens aid in identifying devices where process variations occur.

V. Costs of Screening

Screening costs can be reduced to a practical level by pooling orders to increase quantities and providing a controllable specification to facilitate a competitive bidding environment. Pooling of orders is readily accomplished when devices are standardized for use in multiple systems. In addition to the cost benefit resulting from large-quantity orders, the customer also benefits because the supplier can assign a manager to the program and still make a profit. The supplier can also accommodate process monitoring and benefit from the usual upgrading of his system. Larger quantities attract more suppliers, thus increasing competition. The supplier is willing to

furnish meaningful data which can be used effectively on follow-up procurements, including histograms of population distributions by parameter, which enables the user to adjust his specification limits, increasing the yield and further reducing costs.

An example of unit price reductions resulting from quantity buys is shown below:

Device	Catalog price for 100 units at equivalent Class B, \$	Recent procurement to JPL Class B, \$
Device A (SSI) ^a	6.30 ea.	4.20
Device B (SSI) ^a	11.44 ea	5.90
Device A (MSI) ^b	18.45 ea.	7.90
Device B (MSI) ^b	29.91 ea.	11.45

^aSmall-scale integrated circuit.

^bMedium-scale integrated circuit.

While the unit price reductions are impressive, the real benefit comes from a better managed program which gives added confidence to the user.

VI. Follow-up and Analysis

Persistent follow-up is required in order to continue to realize maximum benefit from procurement dollars. Devices which fail must be analyzed to properly evaluate the screens. Proper data analysis permits the elimination of money spent on screens which detect very few or no failures. Increased processing is of no value if it delays deliveries without producing a more reliable lot. Only by follow-up and analysis can an assessment be made as to whether the objectives are being met.

Ground Communications Facility Functional Design for 1973-1974

J. P. McClure

DSIF Digital Systems Development Section

The Ground Communications Facility (GCF) 1973-74 capability, described herein, will be used to support Pioneer, Mariner Venus-Mercury 1973 (MVM73), and Helios operations, plus the early development and testing associated with the 1975 Viking project. The design includes a full spectrum of GCF capabilities for the overseas 64-m-diameter antenna stations. The wideband data system will be enlarged to cover all 64-m stations, plus CTA 21 and DSS 71. The standard wideband rate will be 28.5 kbps with limited use of 50 and 230 kbps for special purposes. The wideband block length will be increased to 2400 bits after MVM73. The number of teletype circuits will be reduced in keeping with the DSN's policy of eliminating this medium for computer-to-computer data transfer.

I. Introduction

The Ground Communications Facility (GCF) provides the ground communications capability required by the DSN for the conduct of space flight operations. This capability changes in an evolutionary manner to meet the constantly changing (generally increasing) communications requirements of the DSN.

This article discusses the general design of the GCF for the 1973-1974 era. The majority of the implementations required for this new capability will be completed by mid-1973. The capability outlined herein will be used to support the Pioneer 10, Pioneer G, MVM 73, and Helios 1974 operations. This capability will also support early development and testing associated with the 1975 Viking project.

The GCF consists of four systems: voice, high-speed data (HSD), teletype, and wideband (WB). Although each system provides a distinctly different capability, the systems share some terminal equipment and transmission circuits.

II. Transmission Capability

The GCF 1973-74 committable transmission capability is shown in Fig. 1. This capability will provide a basic allocation of one voice, one high-speed data, and two teletype circuits per DSS. Wideband data circuits will interconnect the SFOF with Deep Space Stations 14, 42/43, 61/63, 71, and CTA 21. The specialized MVM 73 project-

oriented requirements of Hangar AO and Boeing are depicted. Except for one teletype, the AO circuits will be activated only in support of launches and prelaunch testing, while the Boeing circuits will be turned up only for testing purposes in early 1973. The NASCOM Madrid Switch Center will be the circuit interface point for data exchange between the Mission Control and Computing Center (MCCC) and the Helios operational facilities in Germany. The circuits necessary for the traffic load will be provided between the Central Communications Terminal and the Network Control System (NCS). The composition of these circuits will vary depending on the NCS location.

Most of the GCF transmission capability is furnished by the NASA Communications Network (NASCOM) from a pool of circuits which it uses to satisfy all of NASA's long-haul tracking network communications requirements. The communications capability of the GCF ebbs and flows as requirements change and is seldom constant from day to day. The capability shown in Fig. 1 represents the circuit quantities used for terminal equipment design purposes. Although circuit quantities may change quickly, the highly specialized terminal equipment is permanently installed and has a relatively lengthy development and implementation cycle. The transmission capability shown in Fig. 1 is not exhaustive. The GCF provides many circuits to other locations too numerous to depict herein.

III. Voice System

The GCF voice system for 1973-74 will be functionally the same as the present system. Voice circuits are shown on Fig. 1 although this figure does not include NASCOM west coast switch circuits.

Tactical intercom assemblies for DSS 43 and DSS 63 will be installed at these new stations, and tactical intercoms will replace the STDN-supplied equipment at Stations 11, 42 and 61. Voice circuits will be installed between the NCS and the Central Communications Terminal, and an internal NCS voice capability will be implemented. During noncritical periods, all overseas Deep Space Stations supporting a particular project will normally be combined on a single net. Independent circuits to each DSS will be provided during critical periods, NASCOM resources permitting.

IV. High-Speed Data System

The general configuration of the GCF 1973-74 high-speed data capability at the Central Communications Ter-

minal (CCT) (JPL Bldg. 230), the 26-m stations, CTA 21, and DSS 71 will be as shown in Fig. 2. In comparison with the present configuration, this configuration has been changed as follows:

- (1) The Central Communications Terminal high-speed capability has been increased to accommodate eight HSD streams instead of the six formerly available. These extra channels are now accommodating the joint MM71/Pioneer needs.
- (2) The three channels of the HSD equipment in the Simulation Center will be relocated to the Central Communications Terminal, thus increasing the CCT capability to 11 channels.
- (3) Two new additional channels may be installed in the CCT to raise its capability to 13 channels total in support of MVM 73, Pioneer F and G, and Helios.
- (4) The simulation conversion assembly/antenna pointing subsystem (SCA/APS) computer transmit channel will be connected to an existing block multiplexer (BMXR) input port at DSSs 11, 42, and 61.

The Central Communications Terminal will be modified to interconnect the Network Control System (NCS) to the Deep Space Stations and Office of Computing and Information Systems (OCIS)/Project locations. The nature of the modifications will be reported later.

The HSD configuration at DSSs 14, 42/43, and 61/63 is shown in Fig. 3. This configuration, which is substantially different from that at the 26-m-diameter antenna stations, provides for two operational HSD circuits, with dual BMXRs, error detection encoder-decoders (EDEDs) and data sets. Dual circuits will connect each location to its area switch. A monitor interface unit will also be provided at all 64-m station locations.

The new BMXR selector will permit any of the Deep Space Station computers to be connected to any of the operational or backup block multiplexers. The BMXRs will continue to provide four input ports; thus not all of the computers may be simultaneously connected to the same HSD line. Barring this limitation, complete switching flexibility will be provided.

The block demultiplexer selector, a new device, will permit any of the block demultiplexer (BDXR) output ports to be connected to any of the DSS computers. Full switching flexibility will be provided. However, this selector will include provisions against accidental connection of two BDXR ports to the same computer input channel.

No provision will be made in this device to permit one BDXR port to drive two computer input channels.

The high-speed data assembly at all Deep Space Stations will be structured so that a conventional audio loop-around will be possible at the line side of the data sets. These loop-around capabilities will aid station prepass checkout.

The high-speed data block size will continue to be 1200 bits long. Circuit speed will remain at 4800 bps. However, all future HSD equipment and interfaces (except data sets) will be designed to operate at rates up to 9600 bps.

The HSD system will have an end-to-end (DSIF-JPL/CCT) long-term uncorrected bit error rate of 6×10^{-5} or lower. On a long-term basis, 98% of all blocks will be delivered error free. (Of the remaining 2%, nominally up to 1% may be delivered with known transmission errors, and up to 1% will either not be delivered or will not be properly identified.)

V. Teletype System

The 1973-74 GCF teletype system will typically provide only two (instead of four) teletype circuits per station (Fig. 1). These 100-wpm circuits will carry very limited traffic: OPS-X (operational teletype) messages, conferences, and administrative messages. The DSS teletype circuits will not be used for telemetry, command, monitor, or simulation data. Tracking data will be phased off teletype during this period. During 1973-74 the GCF will continue to deemphasize teletype for operational traffic with the ultimate aim of reserving teletype as a medium for administrative traffic only. Teletype will not be interfaced to the NCS. The existing Communications Processor will provide the necessary teletype switching and OCIS computer interfacing. Plans will be developed during this period to phase out the Communications Processor.

For teletype west coast switching purposes, the Central Communications Terminal will continue to provide the JPL end of a 32-channel voice-frequency telegraph group (VFTG) configuration, plus interconnections for up to 30 teletype drops in the western area of the U.S.

The teletype interconnections to the DSIF telemetry and command processor assemblies (TCPs) and digital instrumentation subsystem (DIS) will be removed when the third and fourth station teletype circuits are removed. Each control room at the joint 26/64-m stations will be

provided with teletypewriter (TTY) machines which can be connected to any of the SFOF teletype circuits serving the joint station.

VI. Wideband System

The current (1971-72) wideband data capability operates at 50 kbps, interconnecting the CCT with DSS 14 and CTA 21. A terminal in the Simulation Center permits simulated data to be forwarded to DSS 14, CTA 21, or the mission and test computer (MTC). Incoming telemetry data from CTA 21 or DSS 14 are normally routed to the MTC. The present wideband data terminals accept and process standard 1200-bit data blocks, using standard high-speed data error detection encoder/decoder, block multiplexer, and demultiplexer units.

The wideband data capability for 1973-74 will be as shown in Fig. 4. In this interval wideband data will interconnect the SFOF to DSSs 14, 42/43, 61/63, 71, CTA 21, and a single project location at Hangar AO, Boeing, etc. As in the current system, JPL will provide the circuits between the SFOF and CTA 21 and DSS 14. NASCOM will provide the DSS 42/43, 61/63, 71 and project-location circuits. All of the OCIS/Project wideband data interfaces in Building 230 will be at the CCT. The basic wideband data capability will operate at 28.5 kbps in support of MVM 73 and Viking. The DSS 14 regular link will later be upgraded to 50 kbps to meet Viking needs at that location. Additionally, a short-period 230-kbps circuit will be installed from DSS 14 to the JPL CCT to accommodate an MVM 73 Venus encounter data rate of 117 kbps.

A new device, the coded multiplexer, will accomplish the equivalent functions of a block multiplexer, error detection encoder, error detection decoder, and block demultiplexer. This device will be much smaller and less costly than the four individual units and will be capable of operation at 250-kbps or higher rates. The device will include self-test features and the capability of loop-around testing. Separate monitor outputs will denote loss of signal, search, block error, etc. The coded multiplexer will accommodate block lengths of 1200, 2400, and 4800 bits.

The standard wideband data block length will remain 1200 bits long through MVM 73 and will then shift to 2400 bits in preparation for Viking. The DSN Network Control System will interface the wideband system in the JPL CCT. Additionally, wideband circuits may also be used to interconnect NCS elements. Details of such interfaces and usage will be reported at a later date.

The long-term (several-hour) end-to-end (DSIF-CCT) bit error rate will be 5×10^{-5} or lower. Of all of the 1200-bit wideband data (WBD) blocks handed over to the GCF for transmission, 97% will be delivered error free. (Of the remaining 3%, nominally up to 1% will be delivered with errors, and up to 2% will either not be delivered or will not be properly identified.)

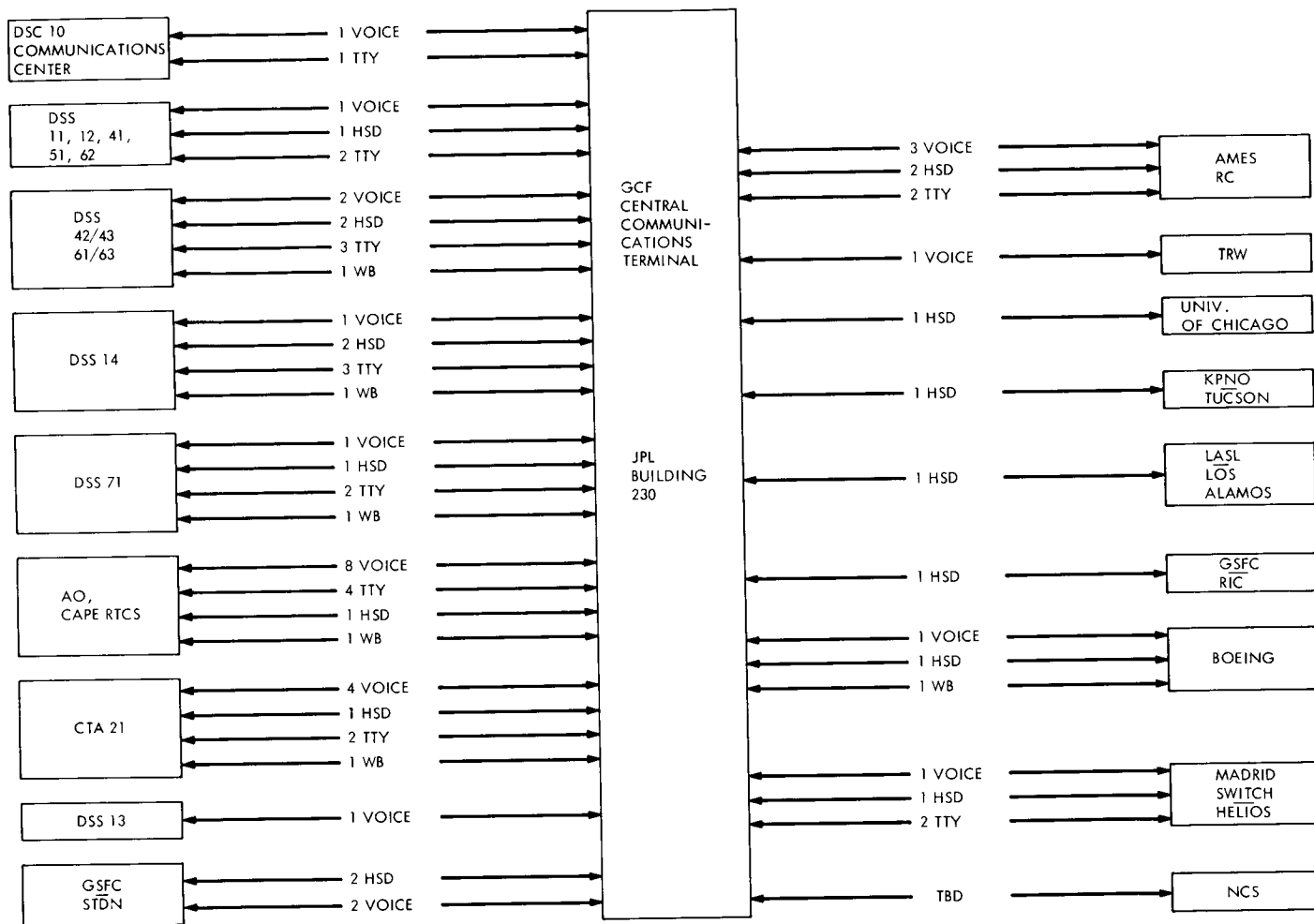
VII. West Coast Switching

In support of NASCOM, the GCF provides and operates the West Coast Switching Center for voice, teletype, and high-speed data circuits. Permanent circuits radiating out from Pasadena to many NASA/contractor locations are switched (on a scheduled basis) to long-haul trunks extending to the NASCOM Central Switch at the Goddard Space Flight Center in Greenbelt, Maryland. This west

coast switch permits a relatively few cross-country trunk circuits to satisfy the needs of numerous individual users in the western U.S. The same GCF equipment is currently used to switch both DSN and west coast traffic, thus providing further economies.

VIII. Reliability

In 1973-74, each traffic path through the end-to-end GCF (except WBD) will have a critical period long-term availability of not less than 0.99 during any scheduled usage period, measured after data flow is established. WBD will have an availability of 0.98 on the same basis as above. The critical-period mean-time-to-restore (MTR) any service except WBD will not exceed 15 min. No MTR is specified at this time for WBD.



ALL STATIONS SUPPORTING A PARTICULAR PROJECT WILL NORMALLY BE CONFERENCED ON A SINGLE SHARED VOICE NET. MULTIPLE VOICE CIRCUITS, AS SHOWN, WILL BE USED ONLY DURING CRITICAL PERIODS.

Fig. 1. GCF 1973-74 transmission capability

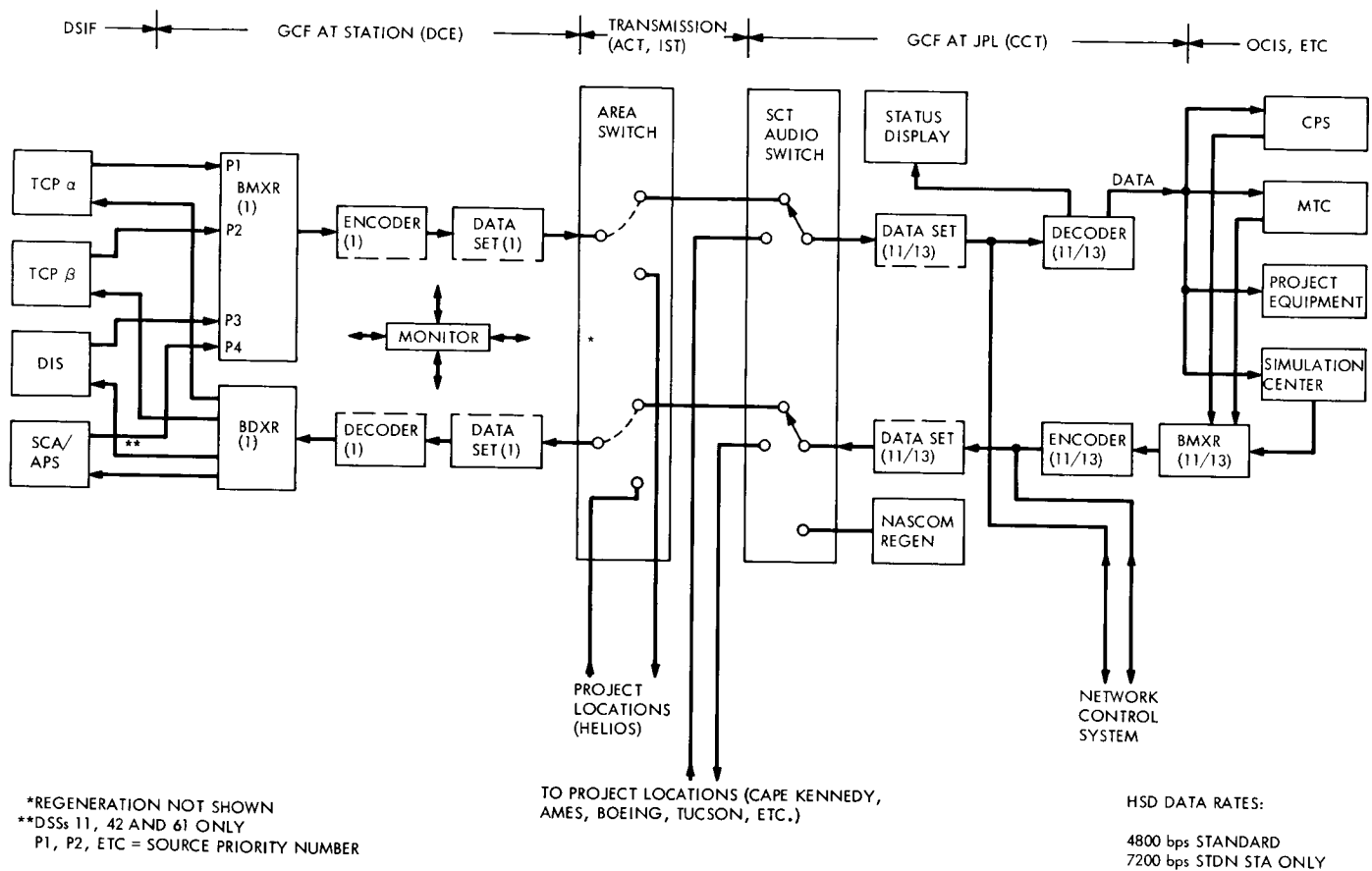


Fig. 2. GCF 1973-74 high-speed data system, 26-m DSS and central capabilities

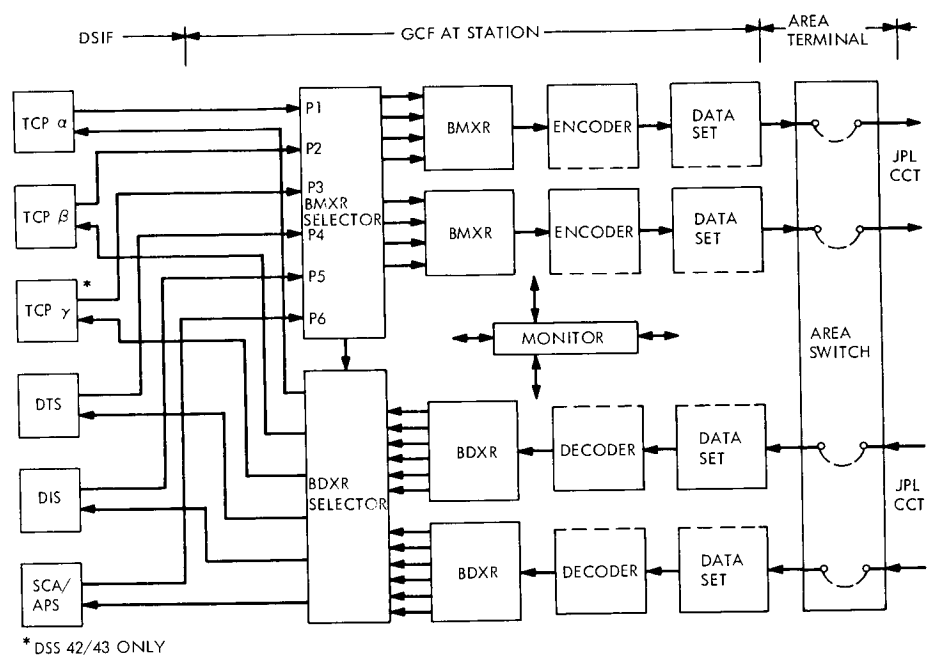
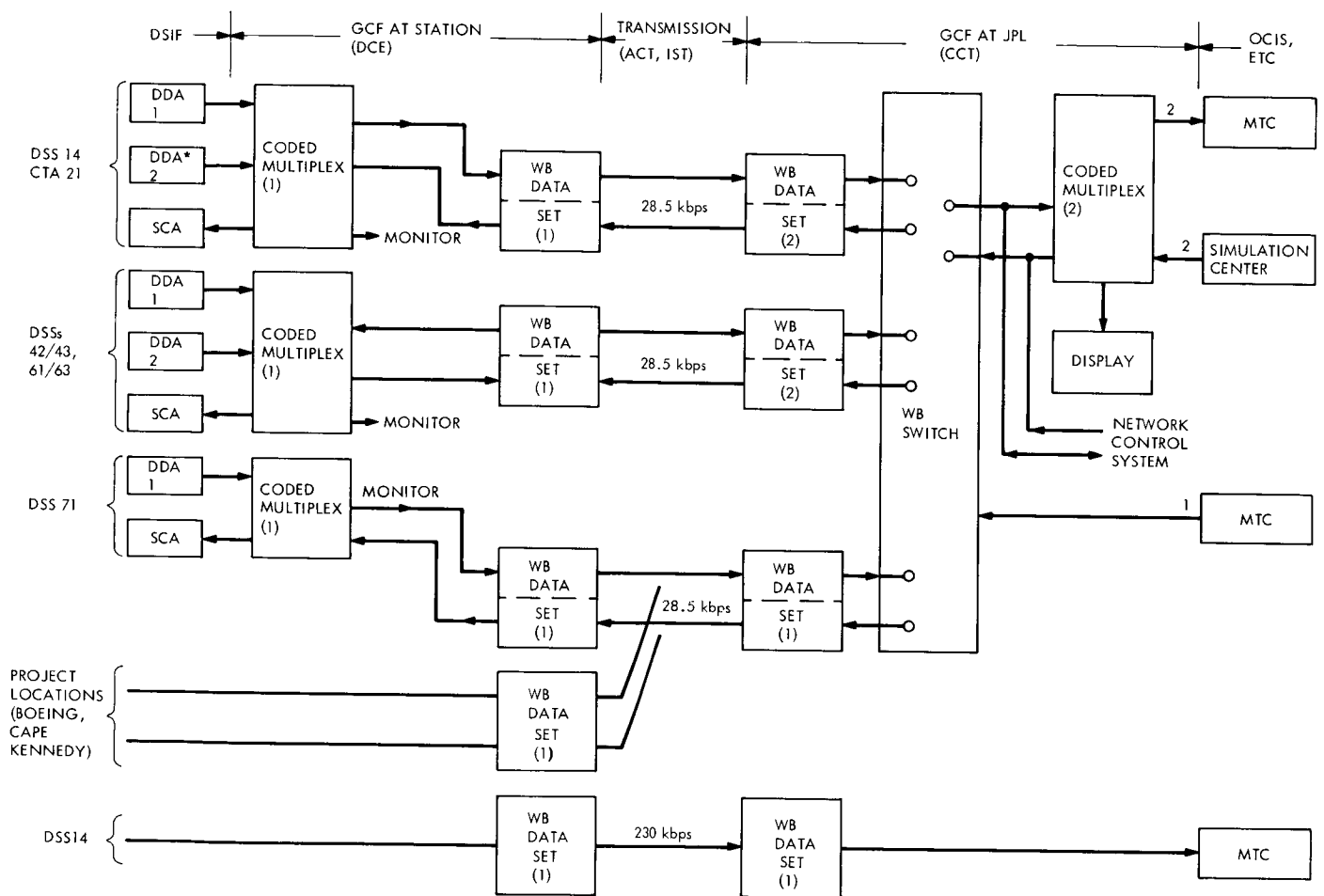


Fig. 3. GCF 1973-74 high-speed data system, colocated (26/64-m) and 64-m DSS capabilities



*NOT EQUIPPED AT CTA 21

Fig. 4. GCF 1973-74 wideband data capability

DSN Research and Technology Support

R. M. Gosline
RF Systems Development Section

The activities of the Development Support Group for the 2-month period ending August 15, 1972, are summarized. The activities are arranged according to whether they were performed at DSS 13 or at the Microwave Test Facility (MTF), and are further subdivided as to the section receiving support. Activities include operational clock synchronization, precision antenna gain measurements, weak source observations, pulsar observations, planetary radar, and DSS 14 400-kW transmitter support.

During the 2 months ending 15 August 1972 the Development Support Group performed the following activities.

I. DSS 13 Activities

A. In Support of Section 331

1. *Pulsars.* Observations of various pulsars continued at the Venus Station (DSS 13) for a 24-hour period once per week.

2. *Planetary radar.* Continuing the support of the MVM 73 spacecraft missions, ranging data were obtained for the planet Venus on 5 different days. As in the past, the transmitting and receiving are done at DSS 14 with the pseudonoise code generation, data processing, and mission control at DSS 13. Ranging experiments were also performed on the Jupiter moon Calisto, the planet Mercury, and the asteroid Toro.

B. In Support of Section 333

1. *Precision antenna gain measurement.* The Apollo Lunar Surface Experiments Package (ALSEP) and various radio stars were used as calibration sources from which data were obtained to calculate the absolute antenna gain and absolute flux density. A total of 89 hours was devoted to ALSEP and 128 hours to the radio stars.

2. *Weak source observations.* Data were obtained on 17 radio sources which are being investigated as suitable calibration sources for the DSN. The automatic boresight and data-taking technique utilized the SDS-930 computer and the DSS 13 Conscan program.

C. In Support of Section 337

1. *Clock synchronization transmissions.* Transmissions resumed in accordance with DSN scheduling as tabulated in Table I.

2. *DSN 400-kW transmitter support (DSS 14).* Continued technical support was provided to DSS 14 in this area.

II. Microwave Test Facility (MTF) Activities

A. In Support of Section 333

1. *Antenna panel noise burst generation.* Testing has continued prior to planning a more extensive investigation at DSS 13.

B. In Support of Section 335

1. *Pocket RF Monitor.* Testing of the pocket RF monitor, described in Ref. 1, has begun.

C. In Support of Section 337

1. *Klystron testing.* Additional klystron tests were performed in support of the DSN transmitters.

Reference

1. Jackson, E. B., "DSN Research and Technology Support," in *The Deep Space Network Progress Report*, Technical Report 32-1526, Vol. X, pp. 149-151. Jet Propulsion Laboratory, Pasadena, Calif., Aug. 15, 1972.

Table 1. Clock synchronization activity from DSS 13

Stations	Number of transmissions
DSS 41	21
DSS 42	9
DSS 51	17
DSS 62	13

Coaxial Switch Evaluation

H. G. Nishimura
R.F. Systems Development Section

Miniature coaxial transfer switches from various manufacturers were tested for the purpose of finding an acceptable replacement for the larger switch now used in the Deep Space Instrumentation Facility (DSIF). The switches, which are planned for use in the S- through X-bands, were tested to determine both their mechanical and electrical properties. Two units were considered acceptable. These switches will reduce the size and cost of future microwave equipment and will also provide the requirements for meeting increasing performance demands.

I. Introduction

The Antenna Microwave Subsystem of the Deep Space Instrumentation Facility (DSIF) has for years been using coaxial transfer switches for configuration control of the receiver and exciter signals. Transfer switches are essentially double-pole, double-throw RF switches. The switches are employed within equipment mounted on the antenna structure and in the control room; most are controlled by push-button switches from equipment in the control room.

The DSIF equipment has been mounting in complexity and, with the advent of X-band equipment as well, there is an urgent need for smaller components. In order to prepare for future hardware requirements, a simulated life test was conducted on a number of newer types of miniature coaxial switches.

Miniature coaxial transfer switches from several different manufacturers were extensively tested for the purpose of selecting one or two units for use in the Deep Space Instrumentation Facility. The switches were submitted to both mechanical and electrical tests. The radio frequency (RF) tests were conducted in the lower S-band only, although most of the switches are rated for use in the X-band as well.

II. Test Description

Prior to testing, the switches were mounted on a test chassis as shown in Fig. 1. Table 1 shows in detail the manufacturer's rating of each switch and serves to point out the differences among the various units. The switches are latching types with indicator contacts and are actuated by 115 Vac. They all employ SMA RF connectors. Tests were conducted as described below.

A. Connector Pin and Dielectric Depth Measurements

The female SMA connectors of the switches consist of an outer shell and center pin with Teflon dielectric between the two segments. The pin and dielectric are pressure-fitted within the outer shell. Because of internal forces during switching, both pin and dielectric can be displaced during the life of a switch. Initially, the pin and dielectric depths below a fixed point were measured to establish a reference for a later measurement to be made at the conclusion of the simulated life test.

B. RF Tests

The switches were tested for voltage standing wave ratio (VSWR), insertion loss, and isolation at 5-MHz intervals between 2000 and 2300 MHz. These readings were made at ambient temperatures of 0, 25, and 50°C. This temperature range is adequate, because of the controlled environment of the DSIF equipment. The switches were sent to a commercial testing firm equipped with automatic microwave testing equipment, resulting in a significant cost reduction.

C. Simulated Life Test

The units were continuously switched from position 1 to position 2 for more than 200,000 complete cycles. A cycling period of 10 s was employed. RF power was not applied during the test.

D. Connector Pin and Dielectric Depth Measurements

The measurements of Subsection A above were repeated after the simulated life test. The two sets of readings provide reasonable data on pin and dielectric displacements as a result of continuous switching.

E. RF Tests

The RF measurements discussed in Subsection B above were repeated, with the exception that the measurements at ambient temperatures of 0 and 50°C were omitted. Because there were only negligible changes at varying ambient temperatures in the previous measurements, little was left to be gained by repeating this portion of the test. Instead, an RF repeatability test was substituted, consisting of three readings at each data point, each reading taken after switching through one complete cycle. The purpose of this test was to ascertain the repeatability of the switch properties for any given position of the switch.

III. Test Results

Table 2 summarizes some of the data from the tests. The figures shown are average values.

As a result of the simulated life test, three of the switch types were considered failures. At 20,000 cycles, the first failure occurred when the switch froze in one of its positions. Another switch developed an intermittent latching problem at 23,000 cycles. A third switch, which had displayed an annoying 60-cycle hum from the outset, had an indicator circuit failure at 80,000 cycles.

The two switches which displayed no mechanical malfunction during the simulated life test revealed data inconsistency during the RF repeatability test. When one of the manufacturers was contacted, it was indicated that a similar problem occurred at the manufacturer's facility after the JPL evaluation switch had been purchased. The gold plating on the RF contacts had worn due to cycling, exposing the beryllium copper contacts, and creating a higher than normal dc contact resistance. The manufacturer assured JPL that corrective action had been taken, and subsequent cycling of his switch had indicated that the steps taken were satisfactory.

The contact resistances of the JPL switches were measured with a Wheatstone Bridge, and there was correlation between the resistance measurements and the contacts that had shown intermittent performance.

The switches were taken apart, including the RF head, for a visual inspection of workmanship and design.

IV. Conclusion

The tests were helpful in two ways: (1) they were invaluable in ascertaining whether the manufacturer's specifications met his claims; (2) they have resulted in the selection of two switches of outstanding characteristics, either of which may be utilized on future design within the DSIF. The selected switches are manufactured by Teledyne Microwave and Transco Products.

Future plans include tests at X-band and additional simulated life tests.

Table 3 shows a comparison of specifications between the presently used switch and one of the miniature switches selected as a result of the tests.

Table 1. Manufacturer's ratings

Characteristic	Switch type				
	RLC Electronics SR-T-R-A-I-L	Wavecom Industries 2921-0500	Microwave Associates MA7531-TMNA	Transco Products 700C70400	Teledyne Microwave CS-37S7C-1
Frequency, GHz	DC-12.4	DC-3	DC-18	0.1 — 12.4	DC-18
VSWR at Frequency, GHz	1.30:1 at DC-7 1.80:1 at 7-12.4	1.20 at DC-3	1.25:1 at DC-4 1.35:1 at 4-8 1.50:1 at 8-12.4 1.70:1 at 12.4-18	1.25 at DC-4 1.35 at 4-8 1.50 at 8-12.4	1.25:1 at DC-6 1.40:1 at 6-12 1.50:1 at 12-18
Isolation, dB Min. at Frequency, GHz	60 at DC-12.4	75 at DC-3	60 at DC-18		70 at DC-6 60 at 6-12 60 at 12-18
Insertion Loss, dB (max.)	0.3 at DC-7 0.6 at 7-12.4	0.25 at DC-3	0.3 at DC-7 0.5 at 7-11 0.7 at 11-12.4 0.9 at 12.4-18	0.25 at DC-4 0.35 at 4-8 0.50 at 8-12.4	0.2 at DC-6 0.3 at 6-12 0.5 at 12-18
RF power handling capability, W	50	Not available	30	20	20
Switching time, ms (max.)	15	25	20	20	10
Operating ambient temperature, °C	Not available	-40 to +85	-55 to +55	-40 to +85	-54 to +100
Dimensions, overall, cm	5.1 × 5.7 × 10.0	4.8 × 6.0 × 7.0	3.5 × 3.8 × 6.2	3.3 × 5.5 × 7.3	3.7 × 5.7 × 4.6
Weight, g	511	312	169	156	85
Connection	Solder lugs	Connector	Solder lugs	Solder lugs	Solder lugs
Life, cycles	1,000,000	200,000	200,000	100,000	1,000,000

Table 2. Performance data summary, before and after life test

Characteristic	Switch type									
	RLC		Wavecom		MA		Transco		Teledyne	
	Before	After	Before	After	Before	After	Before	After	Before	After
Pin depth, 10^{-3} in.	+13.0	+12.0	+10.0	+9.0	-2.0	+2.0	-2.0	+1.0	+14.0	+14.0
Dielectric depth, 10^{-3} in.	-2.0	+3.0	-2.0	+2.0	+3.0	+5.0	-1.0	0	+11.0	+11.0
VSWR	1.06	— ^b	1.11	— ^b	1.12	1.17	1.07	1.07	1.09	1.10
Isolation, dB ^a	>75	— ^b	>75	— ^b	73	75	>75	>75	>75	>75
Insertion loss, dB	0.09	— ^b	0.16	— ^b	0.15	0.10	0.21	0.19	0.16	0.12

^a75 dB is limit of test equipment.

^bNo rf tests were made on these switches.

Table 3. Comparison of switch specification ($f = 2.3$ GHz)

Characteristic	Former switch	New miniature switch
Weight, g	1225	113
Volume, cm ³	1066	164
Cost	\$364	\$234
Delivery, days	90	45
VSWR	1.3:1	1.25:1
Insertion Loss, dB	0.35	0.20
Isolation, dB	60	70
Life, cycles	60,000	200,000

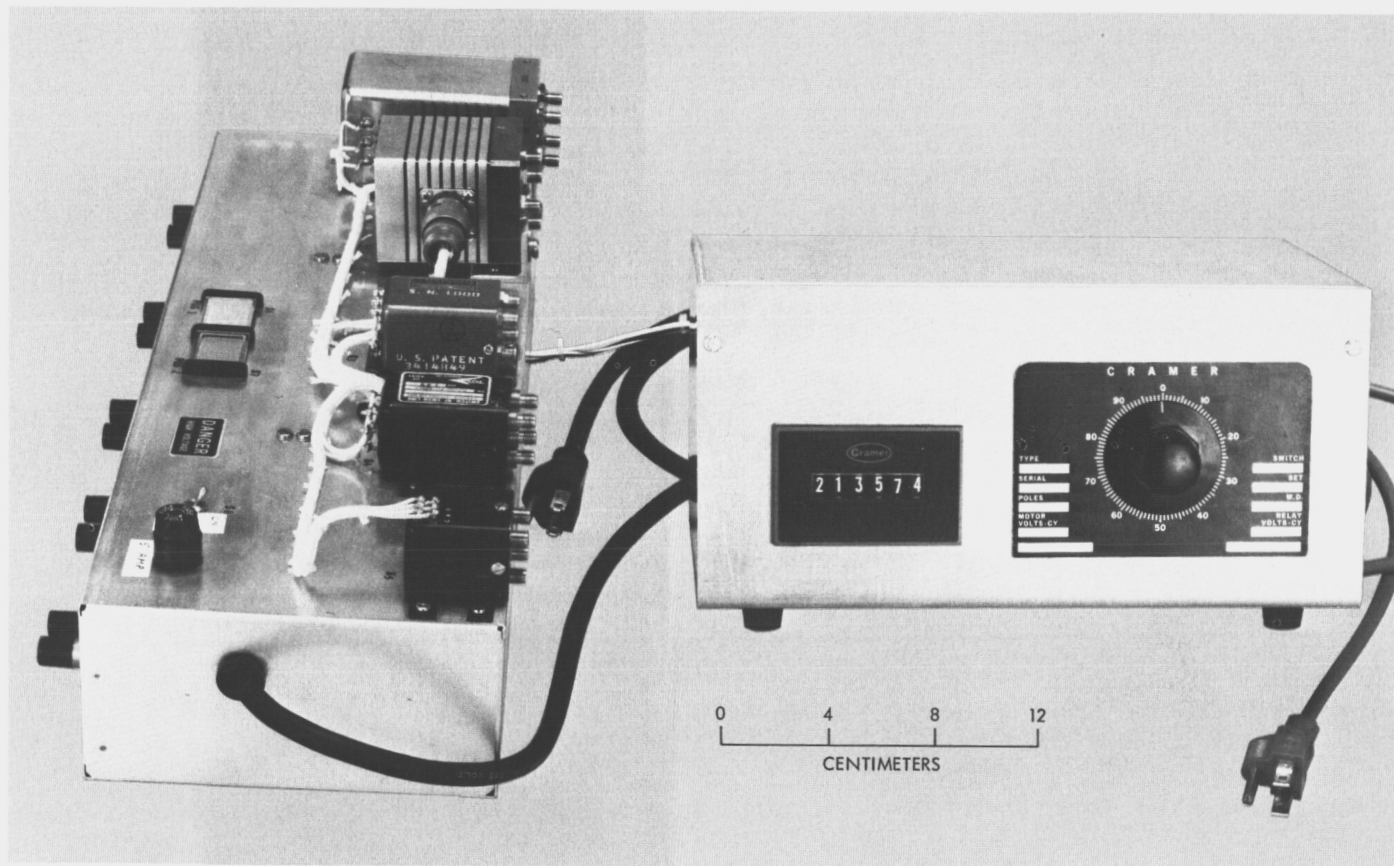


Fig. 1. Switches evaluated, shown with cycling switch and counter

Wideband Distribution Amplifier for Coherent Reference Generator

C. F. Foster

R. F. Systems Development Section

A wideband (0.1 to 100 MHz) frequency distribution module has been designed to have high output-to-output isolation, low phase shift with temperature, no RF tuning, and internal means to detect module performance that can be monitored by a computer.

I. Introduction

The DSN Mark III development plan is placing more stringent specifications on the Deep Space Stations' frequency standard distribution systems to have rigid control over phase shift and output-to-output isolation. The subsystems are further required to provide internal means of monitoring their performance and produce an indication compatible with computer interface.

II. Amplifier Development

A development program was initiated to create such an amplifier module for the coherent reference generator

since no commercial amplifier exists that provides the following: (1) 12 outputs isolated from each other by 70 dB at 100 MHz, (2) a frequency range of 0.1 to 100 MHz, (3) less than 2 deg phase shift over a temperature change of 0 to 50° centigrade, and (4) a computer-level output of module quality.

Figure 1 is a block diagram of the basic amplifier. A wideband power amplifier drives a passive power divider and the 12 output isolation amplifiers. The high output-to-output isolation was achieved by using the 30-dB minimum isolation of the power divider and the reverse isolation of the output isolation amplifiers.

Two mechanical designs were attempted during the development. The first (Fig. 2) used the machined compartment technique and semirigid coax; the second (Fig. 3) used stripline transmission and flexible coax techniques. The difference in isolation measured over frequency range is shown in Table 1.

The final production module will be as shown in Fig. 3. This method meets the original design requirements, provides a high control over reproducibility, and is less costly to produce. The module quality monitor circuit shown in Fig. 1 uses hot carrier diodes to detect the power level at the input and at the 12 outputs, which are sampled by a multiplexer whose output goes to a comparator. The detected input power signal goes to a

separate comparator. The detected input and multiplexer output signals are compared in a gate. If the input is out of its specified limits, the gate is *off* and the module indicates that it is operational. If the input is within its specified limits, and one of the outputs drops out of its preset limits, an external system detector latches until the problem is solved.

III. Planned Production and Installation

The wideband amplifier has passed the prototype stage and a contract has been issued for a production run. These modules will be evaluated for uniformity of performance and will be installed in the engineering prototype of the coherent reference generator.

Table 1. Performance data for wideband distribution amplifier

Parameter	Design goal	Compart- mentized module (Fig. 2)	Printed circuit stripline module (Fig. 3)
Phase stability, < 2 deg, at temperature of 0 to 50° C	<2	<1.5	<1.5
Output-to-output isolation, dB, at			
10 MHz	≥80	103	87
25 MHz	≥80	96	81
50 MHz	≥80	90	79
100 MHz	≥70	80	71
Harmonic distortion, %	≤5	<3	≤3
Nonharmonically related spurious output, dB	-70	-70	-70

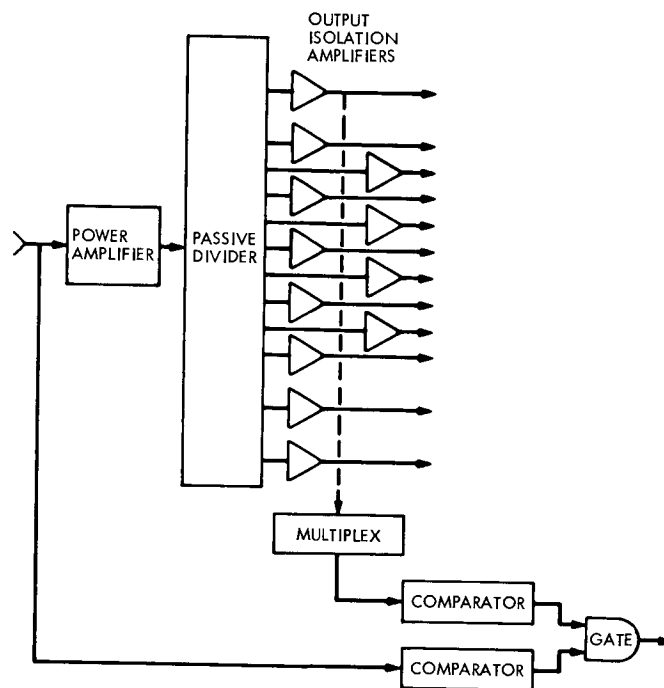


Fig. 1. Coherent reference generator wideband distribution amplifier

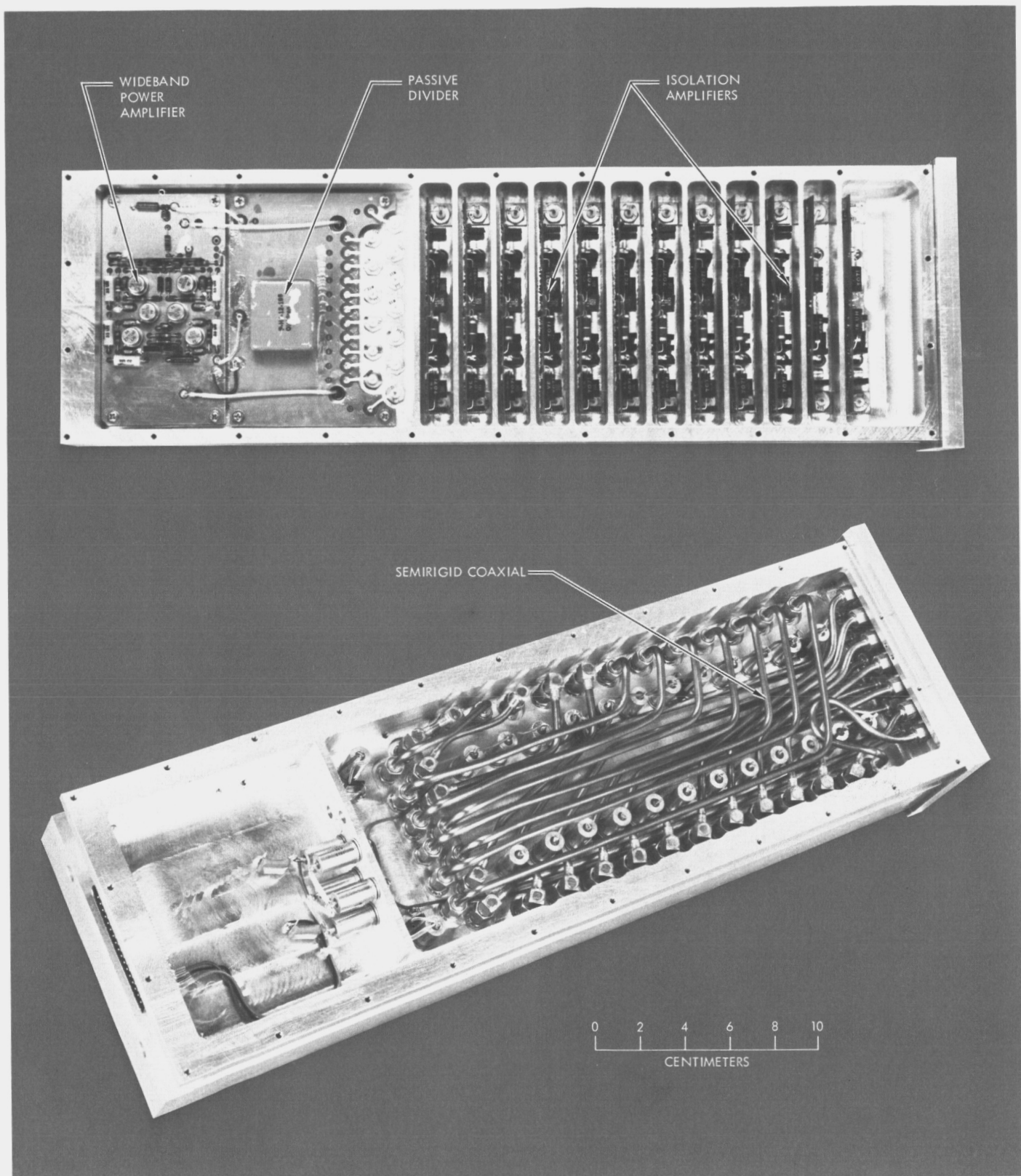


Fig. 2. Mechanical details of machined wideband distribution amplifier

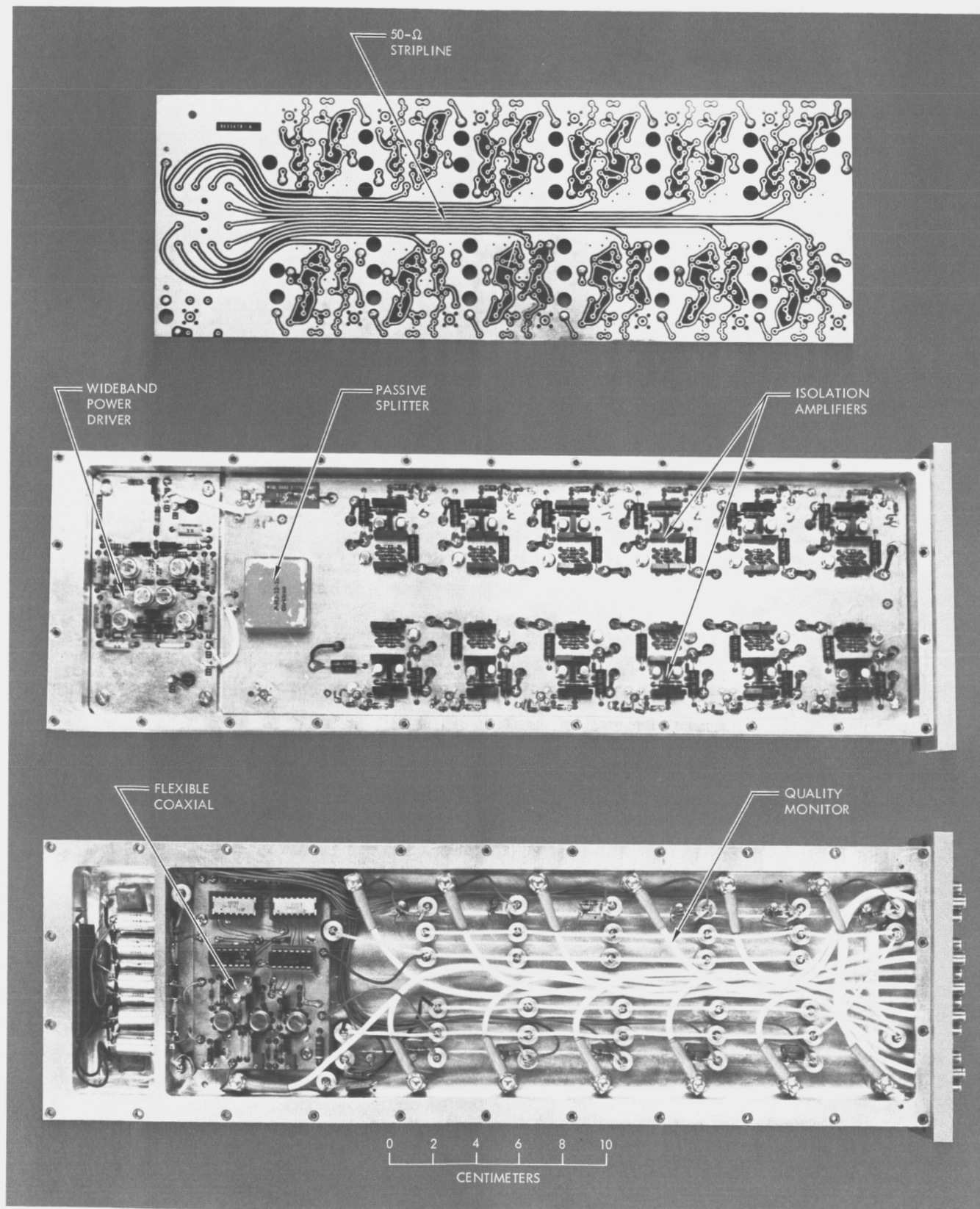


Fig. 3. Mechanical details of stripline wideband distribution amplifier

Dual Carrier Preparations for Viking

D. A. Bathker

Communications Elements Research Section

D. W. Brown

R. F. Systems Development Section

Multiple spacecraft vehicles for the Viking mission require simultaneous transmission of two S-band carriers from a single Deep Space Station. Past experience in high-power diplexing, coupled with dual carriers, has shown that, in addition to controlled uplink intermodulation products, a complex form of receive band interference will be generated within the ground station. Recent efforts to define and minimize these effects are being supplemented with additional resources including reconfiguration of DSS 13 for dual-carrier diplexed operation with the objective of assuring DSN capability in the Viking mode.

I. Introduction

Two simultaneous uplinks and four simultaneous downlinks are to be supported by each Deep Space Station (DSS) of the 64-m-diameter antenna subnet for the Viking 1975 mission to Mars (Ref. 1). A 26-m-diameter antenna subnet will also be utilized during certain mission phases including cruise periods during which the two spacecraft will not lie within a single antenna beam. This 26-m-diameter support will be in the customary single uplink and one or two downlink configuration.

During orbital operations, two additional vehicles (landers) will be in time-shared communications with the DSN, utilizing a common S-band carrier frequency allocation. Three other S-band channels provide for each orbiter and for a spare orbiter radio system. The fourth downlink is at X-band, coherently generated from one of the orbiter S-band uplinks in the so-called S/X band mode.

Early work on dual uplinks from a single DSS includes field investigations in relation to the Apollo Manned

II. Interference Problems

Experience has shown that wherever multiple carriers share a common high-intensity field, mixing or intermodulation products (IMPs) can be expected to be generated (Refs. 2, 3, and 5). As a practical matter, this interaction can and will occur in some degree both within the internal waveguide system (Ref. 6) and in the external incidental nonlinearities encountered in the illuminated portion of the antenna structure as well as in the near field physical environment of the station (Ref. 5). This latter point illustrates the fact that even two independent, but adjacent, stations cannot be presumed to be totally free of this effect.

Within the context of the DSN, these IMPs will, in general, appear within the uplink transmit band and as a self-jamming of the receiving band, regardless of where they may be generated in a given configuration. Whether or not they degrade performance depends, of course, on the frequency and amplitude distribution in either link for the configuration in question.

Another effect, in the DSN context known as "noise bursts," has been encountered in single-carrier duplexed operation in a variety of circumstances (Refs. 7-10). While this is a continuing concern, an intensive program at DSS 14 of waveguide maintenance and the reduction and control of "loose" incidental hardware in the illuminated portion of the antenna has resulted in some improvement of the single high-power carrier performance (Ref. 11). This phenomenon is primarily manifested as an impulse-like random increase in the receiving system temperature. In severe form, it has been known to momentarily disrupt receiver tracking and presumably to degrade the data streams. More work is needed in this area to correlate data quality to observed system temperature, but, as yet, there is no known verified report of loss of operational data quality attributable to noise bursts.

Of particular concern in the dual uplink mode is the evidence that the noise burst phenomenon is greatly intensified under this condition as well as apparently interacting with, and probably contributing to, the IMP effect (Ref. 2).¹

¹Also evidenced in many observations and system temperature recordings taken in the course of recent dual carrier testing at DSS 14.

III. Status for Viking

The current S-band frequency allocations for the Viking mission (channels 9, 13, 16, 20) (Ref. 12) have been selected to preclude uplink IMPs falling "on channel" in addition to the usual single-carrier criteria (Ref. 1). One additional consideration was applied to minimize the level of high order IMPs in the receive band: reduction of channel separation has the effect of drawing higher order (and consequently weaker amplitude) products into the receiving band, some 180 MHz removed from the transmitting band.

Current overall performance at DSS 14 for nominal 40-kW dual carriers provides a minimum carrier-to-adjacent-channel IMP ratio of 20 dB in the uplink and receiving band interference in the form of quasi-monochromatic IMPs ranging from the order of -160 dBmW to a presumed -190 or -200 dBmW level depending upon which pair of the four uplink S-band channels are in use at given time. At this time, it is known that the receiving band IMP has a time-varying (in the spectral range of 1 Hz) amplitude and or phase modulation component and probably has a typical spectral width of more than 10 Hz. Whether or not the similar spectral characteristics of the noise burst phenomenon are causal or coincidental has not yet been determined. In addition to the IMPs, dramatic increases in apparent broadband noise occur (as monitored by the maser instrumentation equipment, including system temperature) and are seemingly time correlated to the instantaneous IMP level.

In addition to the maser instrumentation equipment, the principal instrumentation in use has included conventional spectrum analyzers and the standard DSN phase-locked receiver. Recent attempts at calibration of the amplitudes of the weaker IMPs and of their spectral characteristics by means of digital processing techniques have offered some qualitative confirmation of these phenomena. Further work in this area is expected to provide quantitative data which can be applied to the question of possible degradation of tracking in the presence of this interference.

These conclusions have been developed for Viking over the last two or three years and are based primarily upon the DSS 14 dual-exciter, single 400-kW klystron configuration (Ref. 1). Noise burst investigations have also been conducted at the Goldstone Microwave Test Facility (MTF), and 100-kW klystron uplink data have been obtained in the dual 10-kW mode at DSS 13 (Ref. 13).

Documentation of the DSS 14 work is largely in the form of informal memoranda for the period of late 1969 to date. Alternative methods of dual carrier generation have been considered, notably time sharing (Refs. 14-16), but do not at this time appear promising for the Viking application.

Because two-thirds of the 64-m-diameter antenna subnet is scheduled to be equipped with 100-kW klystrons and because scheduling adequate time at DSS 14 to pursue these concerns of dual carrier interference is

virtually impossible, an effort has been recently undertaken to reconfigure DSS 13 for 100-kW single/dual carrier diplexed test operation (Ref. 13).

This facility, together with continued intermittent usage of DSS 14, will provide the opportunity to quantitatively bound the interference phenomena, to hopefully reduce and control them through microwave and antenna modifications, and, if necessary, to provide the basis of negotiation of operational solutions to the residual interference.

References

1. Mudgway, D. J., "Viking Mission Support," in *The Deep Space Network Progress Report*, Technical Report 32-1526, Vol. II, pp. 28-32. Jet Propulsion Laboratory, Pasadena, Calif., Apr. 15, 1971.
2. Chernoff, R. C., and Hartop, R. W., "Noise and Intermodulation Interference in MSFN Back-Up Tracking Systems During Transmission of Dual Up-Link Carriers," in *The Deep Space Network*, Space Programs Summary 37-57, Vol. II, pp. 138-145. Jet Propulsion Laboratory, Pasadena, Calif., May 31, 1969.
3. Breithaupt, R. C., and Moorehead, R. M., Final Report Phase II, for Spurious Interference Investigation, NASA 5-21377, 123-7301-001. Prepared by the Collins Radio Co., Dallas, Tex., for the National Aeronautics and Space Administration, Nov. 1, 1971.
4. Mudgway, D. J., "Mariner Mars 1971 Missions," in *The Deep Space Network*, Space Programs Summary 37-54, Vol. II, pp. 9-11. Jet Propulsion Laboratory, Pasadena, Calif., Nov. 30, 1968.
5. Eastman, A. V., and Horle, L. C. F., "The Generation of Spurious Signals by Nonlinearity of the Transmission Path," *Proc. IRE*, Vol. 28, No. 10, pp. 438-443, Oct. 1940.
6. Cox, R. D., "Measurements of Waveguide Component and Joint Mixing Products in 6 GHz Frequency Diversity Systems," *IEEE Trans. Comm. Tech.*, Vol. COM-18, No. 1, Feb. 1970.
7. "Low Noise Diplexing at L-Band," in *The Deep Space Network*, Space Programs Summary 37-20, Vol. III, pp. 11-12. Jet Propulsion Laboratory, Pasadena, Calif., Mar. 31, 1963.
8. "S-Band Cassegrain Monopulse Cone Assemblies," in *The Deep Space Network*, Space Programs Summary 37-34, Vol. III, pp. 44-45. Jet Propulsion Laboratory, Pasadena, Calif., July 31, 1965.

References (contd)

9. Kelly, W. A., and Burberry, R. A., "A Review of Helicopter Aerial Problems," in *Proceedings of the IEEE Conference on Aerospace Antennas*, held in London, England, June 8-10, 1971, IEEE Conference Publication 77, pp. 77-82. Institution of Electrical Engineers London, England.
10. Kurtz, L. A., *Noise Burst Study at DSS 14*, Final Report, P.O. GR-538248, July 31, 1971.
11. *Noise Burst Status Report No. 4*, IOM 3331-72-038, Jet Propulsion Laboratory, Pasadena, Calif., May 12, 1972 (JPL internal document).
12. *Frequency Assignments for Viking Project*, IOM 335A-72-413, Jet Propulsion Laboratory, Pasadena, Calif., July 19, 1972 (JPL internal document).
13. Jackson, E. B., "DSN Research and Technology Support," in *The Deep Space Network Progress Report*, Vol. X, pp. 149-151. Jet Propulsion Laboratory, Pasadena, Calif., Aug. 15, 1972.
14. *Efficient Use of DSIF Transmitters*, IOM 3300-69-841, Jet Propulsion Laboratory, Pasadena, Calif., Dec. 2, 1969 (JPL internal document).
15. Kolbly, R. B., "Switched Carrier Experiments," in *The Deep Space Network Progress Report*, Technical Report 32-1526, Vol. III. Jet Propulsion Laboratory, Pasadena, Calif., June 15, 1971.
16. *Switched Carrier Analysis Summary Report*, IOM 3396-72-274, Jet Propulsion Laboratory, Pasadena, Calif., Aug. 11, 1972 (JPL internal document).

Salvaging an Expensive Shaft by Brush Electroplating

H. McGinness
DSIF Engineering Section

An expensive shaft was salvaged by depositing nickel on an undersized bearing journal. The shaft is a component in the Master Equatorial instrument, required for the 64-m-diameter antenna of the Deep Space Network. In special cases, this electroplating process could be considered part of the fabrication method rather than a salvage process.

I. Introduction

The DSN 64-m-diameter antenna employs a precision reference instrument, called the Master Equatorial, which allows the antenna to be directed accurately where desired. Figure 1 shows the fork and polar axle of the Master Equatorial, a mild steel weldment weighing approximately 800 kilograms. Its shaft has journals for the two highly precise (ABEC class 9) angular contact ball bearings.

Several problems are encountered in grinding the journals of a shaft of this size to the required accuracy. If it is turned on dead centers, the process usually assumed to produce the best degree of roundness, the wear on the centers will be excessive because of the high weight loading. The addition of a steady rest support, which might

otherwise seem desirable, negates some of the inherent advantages of turning on dead centers. The fact that the part is not symmetrical about every plane through the longitudinal shaft axis means that gravity loading deflections vary with the angle of rotation. These problems can be eliminated by mounting the part vertically, as, for example, on the turntable of a vertical boring mill or vertical grinder. However, this method introduces another serious problem: the inaccuracies of the machine turntable bearings will be reflected in the journal being ground.

Thus it is always difficult to obtain simultaneously, through grinding, the required degree of roundness and a specified diameter to within a very small tolerance range, and yet these are exactly the requirements that must be met to ensure that the installed bearings will

have their intrinsic accuracies realized. Thin bearings in particular will conform to the shape of the journal when installed with a zero clearance or interference fit.

Hence, the roundness of the inner race will be no better than that of the journal. Obviously a too-small journal would allow the part to move with respect to the bearing, unless an excessively high axial preload were applied in order to expand the inner race. But this higher preload would increase the bearing friction. An increase in bearing friction would also occur if the bearing journal is too large, thus producing more interference fit than desired. From the bearing performance point of view, it is necessary that journal roundness to a specified diameter be maintained.

II. Hand Salvaging of Shafts

Recently two fork and axle units were manufactured for use at DSS 43 and DSS 63. The journals were ground by a tool post grinder mounted on a vertical boring mill. It was determined experimentally that the machine runout was quite small and that the machine-made journals would be near enough round so that a moderate amount of hand work would make them satisfactory. It was agreed to attempt to grind them to a diametral dimension from 0 to 8.0 μm over the upper dimensional limit. The lower dimensional limit is 5.0 μm less.

This process worked out very well for the first shaft. A moderate amount of hand lapping produced a surface

round to within 0.50 μm and within the dimensional limits of the drawing.

However, the large journal of the second shaft came out undersized by approximately 12.0 μm . After hand lapping to achieve roundness, it was undersized by 17.0 μm .

This shaft was then brush electroplated using the proprietary "Dalic Process," which is a method of electroplating localized areas without using immersion tanks. Various metals can be deposited onto conductive surfaces from highly concentrated electrolyte solutions which are held in absorbent materials attached to portable electrodes. Thickness of the deposited metal can be controlled by an ampere-hour meter.

A nickel solution was chosen for electroplating the shaft. The result was not uniformly thick, thus requiring some additional hand lapping to restore roundness. It is believed that the lack of thickness uniformity was caused by the necessity of stopping the turning of the part frequently during plating in order to replenish the solution. A more sophisticated arrangement could have prevented this.

Thus a very expensive part was salvaged through an inexpensive process. It may be that for bearing journals of this size, where roundness and dimension must be met simultaneously, the designer should consider this kind of brush plating as part of the fabrication method, rather than as a strictly salvage process.

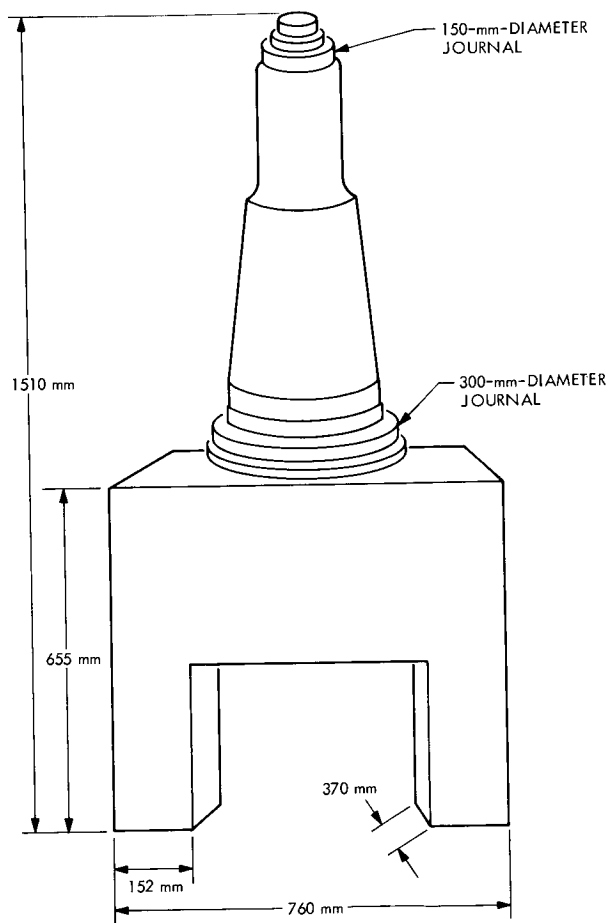


Fig. 1. Sketch of Master Equatorial polar axle and fork

Performance of the 64-meter-diameter Antenna Servo

P. Lipsius
DSIF Engineering Section

A 64-m-diameter antenna has been installed and tested at the Tidbinbilla Deep Space Station in Australia. Part of the final acceptance testing was demonstration of antenna servo performance. This report summarizes the major tests and the resulting data.

The antenna servo as implemented during these tests consisted of three feedback control loops: a current loop, a rate loop, and a manual position loop (Fig. 1).

The testing process started with frequency response tests of the closed current loop on each axis. For the complete response plots, see Figs. 2 and 3. The specification on the current loop was a bandwidth (defined as the frequency at which the response reaches 90 deg) greater than 150 Hz and less than 6 dB of peaking. Review of Figs. 2 and 3 shows that for the azimuth axis the bandwidth is 1100 Hz and the peaking is 4.5 dB; for the elevation axis the bandwidth is 1100 Hz and the peaking is 4.2 dB.

Open rate loop tests were then run to determine the frequency location of various resonances — hydraulic, natural structural, and other structural resonances, some of which are tabulated below:

Location	Azimuth, Hz	Elevation, Hz
Hydraulic	1.1	1.2
Natural (first) structural notch	1.5	2.1
Next	2.5	4.0
Next	3.0	8.0
Resonance	20.0	40.0

From these tests and data a compensation network was developed to close the loop with a bandwidth frequency of 5 Hz, minimum phase shift at the position loop bandwidth frequency, and maximum attenuation of peaking responses above 5 Hz.

The next test was the frequency response of the closed rate loop. For the complete response plots see Figs. 4 and 5. This test was run under two conditions: (1) a steady-state rate of 0.05 deg/s was applied to the antenna; (2) a zero steady-state rate condition. The specification on the rate loop is a nominal bandwidth of 5 Hz. Review of Figs. 6 and 7 shows that the following responses were achieved:

Axis	Zero rate, Hz	0.05-deg/s rate, Hz
Azimuth	5	5
Elevation	4.7	5

The last loop tested was the manual position loop, which corresponds to the closed loop used during normal spacecraft tracking. The position loop has two bandwidths available and was tested in both modes. The specification value for the high bandwidth mode is 0.2 Hz; in the low bandwidth mode the specification is 0.02 Hz. The frequency response plots for azimuth and elevation axes are shown in Figs. 6 and 7. Review of these plots shows that the following bandwidths were obtained:

Axis	High bandwidth, Hz	Low bandwidth, Hz
Azimuth	0.20	0.0135
Elevation	0.205	0.019

A further test was made to verify position loop stability under simulated conditions of wear, aging, and signal degradation by varying the position loop gain by +3 and -3 dB increments. Step responses under these conditions showed that control system stability was maintained.

Other tests of significance to antenna tracking performance are (1) tracking error with the antenna moving at a rate of 0.0015 deg/s, which corresponds approximately to a sidereal rate, (2) pointing jitter under a static position command, and (3) the minimum velocity the antenna is capable of maintaining. These results are tabulated below:

Test	Azimuth	Elevation
Tracking error		
maximum peak-peak	0.00082 deg	0.00101 deg
average	0.00006 deg	0.00005 deg
Pointing jitter	± 0.00012 deg	± 0.00032 deg
Minimum velocity	0.0002 deg/s	0.0005 deg/s

Various other tests were also performed: full speed (0.5 deg/s) tests through the complete travel range; verification of the two sets of electrical travel limit switches as well as the "deadman" emergency hydraulic limit valves; and tests on the control logic circuits involved in turning on (and off) the antenna drive and hydrostatic bearing hydraulic systems, which were performed to ensure satisfactory operation and "fail-safe" shutdown characteristics.

The antenna servo and the associated controls were completely tested and found to be achieving satisfactory specification performance.

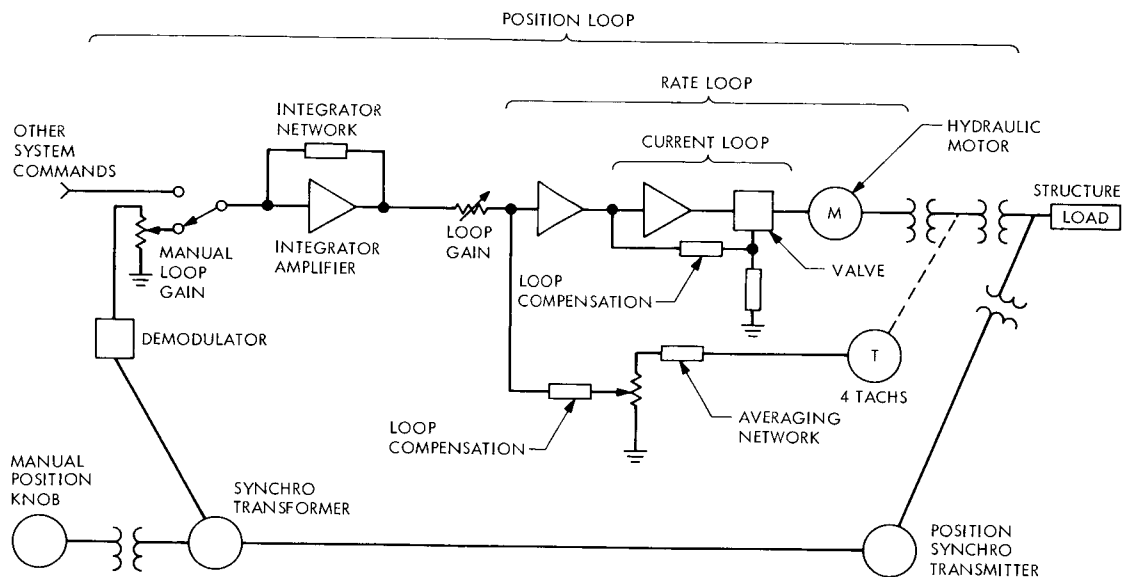


Fig. 1. Manual position loop block diagram

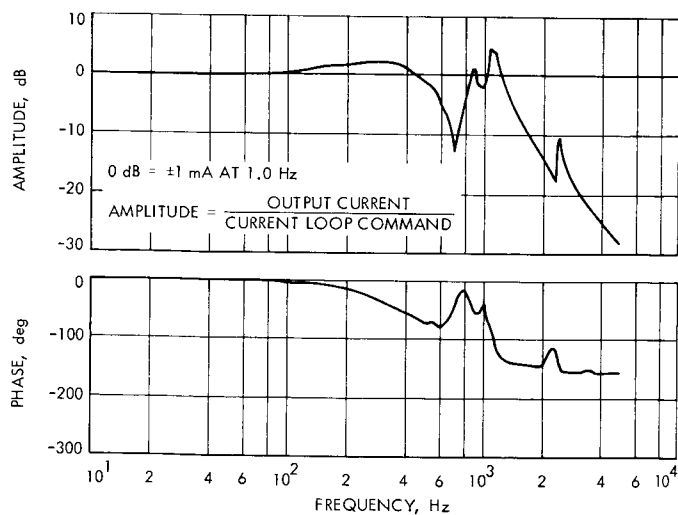


Fig. 2. Azimuth current loop frequency response

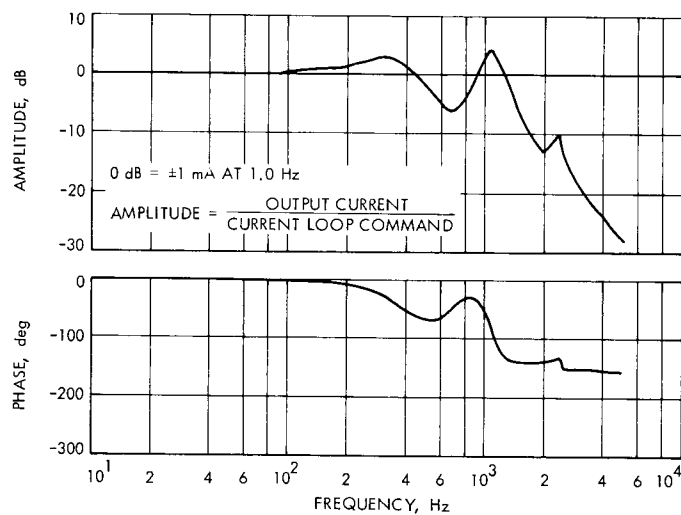


Fig. 3. Elevation current loop frequency response

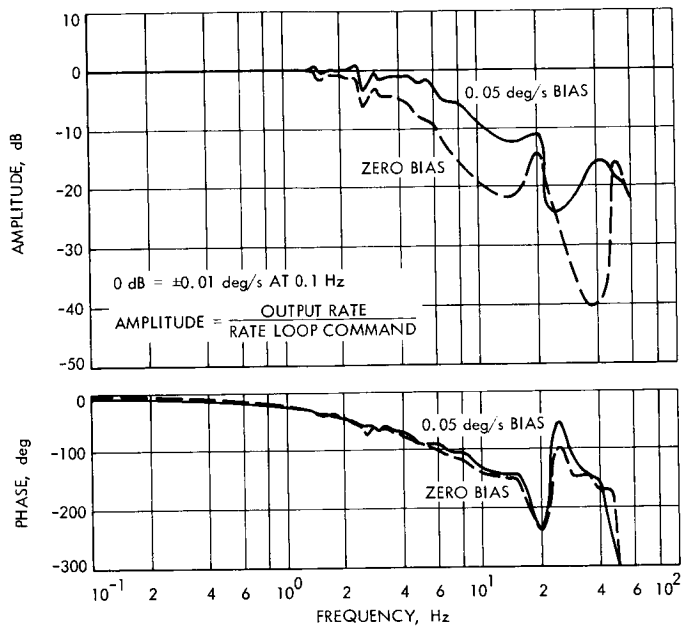


Fig. 4. Azimuth rate loop frequency response

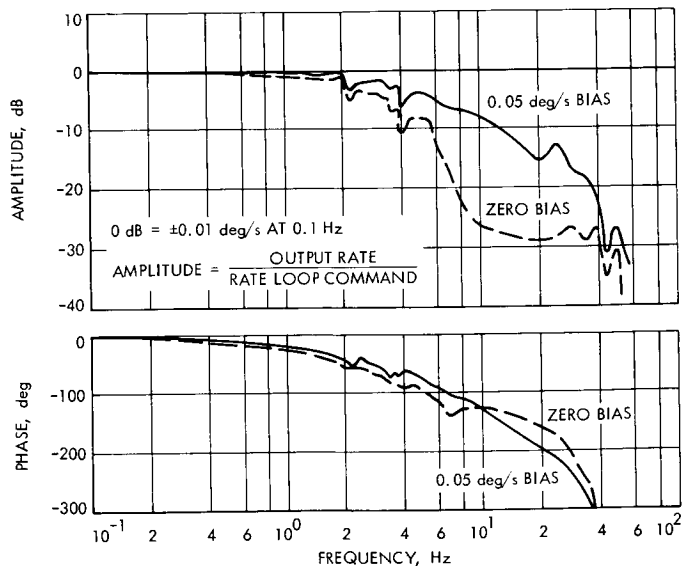


Fig. 5. Elevation rate loop frequency response

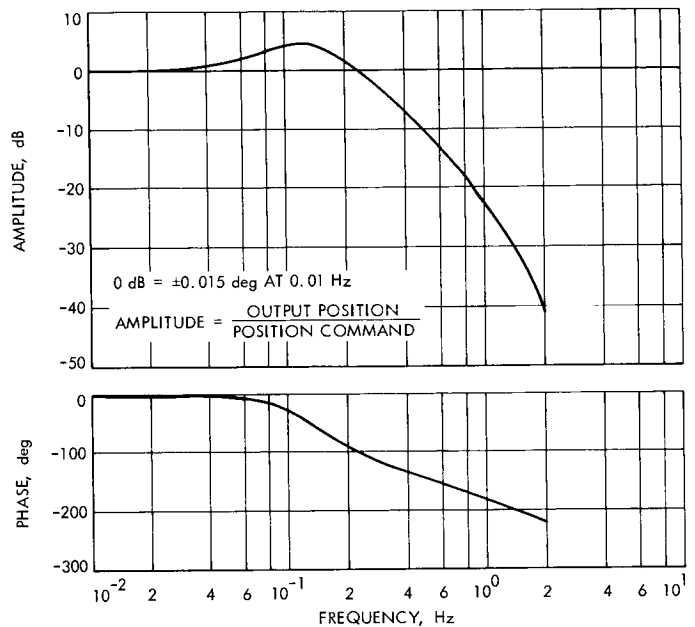


Fig. 6. Azimuth position loop frequency response

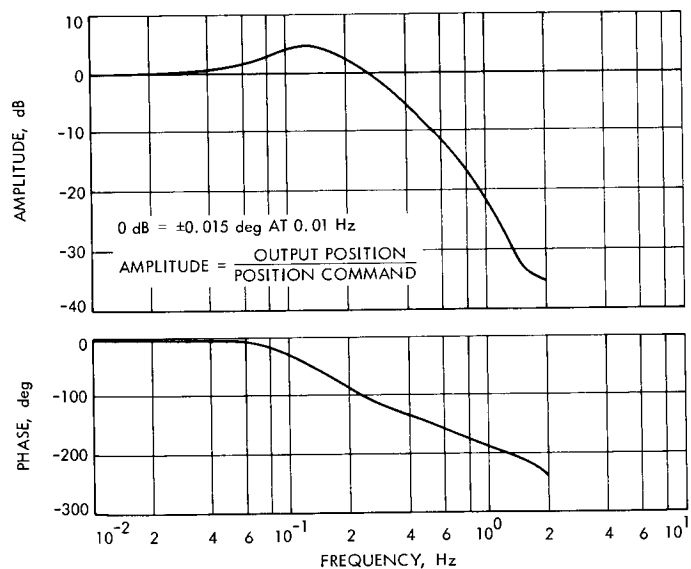


Fig. 7. Elevation position loop frequency response

Network Operations Control

R. J. Amorose
DSN Engineering and Operations

The DSN Operations Control Team controls and operates the DSN in real-time to support Flight Project Operations. DSN Operational Control, a mission-independent organization, is headed by the DSN Operations Chief, who is supported by the DSIF Operations Chief, GCF Operations Chief, Network Operations Analysis Chief, and Network Operations Support Chief. The real-time operation is supported by two non-real-time functions, with liaison provided by: (1) the DSN Operations Representative, who represents the DSN organization to the DSN manager and Flight Project Chief of Mission Operations, (2) the DSN Scheduling Representative, who schedules DSN resources for flight projects.

I. Introduction

The DSN Operations Control Team (OCT), headed by the DSN Operations Chief (OC), controls and operates the DSN in real-time to support Project flight operations. On July 1, 1972, real-time DSN Operations was reorganized as illustrated in Fig. 1. The DSN Operations organization ensures that standardized methods will be used for support of each flight project, while at the same time maintaining the capability for responding in real-time to nonstandard anomalies and emergencies.

II. Responsibilities

DSN operational control is provided by the mission-independent DSN Operations organization. Functional responsibilities of the DSN OCT are as follows:

- (1) Operate the network to meet the requirements of several flight projects simultaneously.
- (2) Operate the DSN Monitor System.
- (3) Operate the DSN in support of project simulation activities.
- (4) Operate the DSN in support of compatibility testing.
- (5) Support maintenance of the operational network.
- (6) Produce the Original Data Records (ODRs).
- (7) Perform real-time (through the 7-day schedule) allocation of resources based on guidelines of the DSN Network Allocation System.
- (8) Respond to the requirements of Tracking Data System (TDS)/flight project interface documentation.
- (9) Perform, in real-time, analyses of telemetry, tracking, and command operations to ensure that the network has met its commitment.

III. DSN Operations Control Team Organization

The operating positions and organizational responsibilities of the key members of the OCT are described in the following paragraphs.

A. DSN Operations Chief

The DSN Operations Chief (OC) is responsible to the DSN Operations Manager for the overall direction of DSN operations and is specifically responsible for proper operation of the DSN resources committed to the Project. The DSN OC directs and coordinates the activities of the Network Operations Analysis Chief, DSIF Operations Chief, GCF Operations Chief, and the Network Operations Support Chief in the real-time operation of committed resources. The DSN OC is the controlling interface for the DSN with the Mission Control and Computing Center (MCCC) Operations Controller (OPSCON). The DSN OC coordinates the isolation of equipment or procedural problems and any required corrective or contingency actions. The DSN OC controls the real-time configuration of the DSN and resolves any conflicts in the use of DSN resources that arise during periods of operational support. He is responsible for the coordination of end-to-end systems data flow. He is also responsible for keeping the flight projects advised of DSN status.

B. DSIF Operations Chief

The DSIF Operations Chief provides real-time direction and control of DSIF operations. He controls committed DSIF resources and the real-time configuration of DSIF equipment and procedures.

C. GCF Operations Chief

The GCF Operations Chief directs and controls the operations of the GCF in real-time. He coordinates circuit requirements with the NASA Communications Network (NASCOM) and controls the real-time configuration of the GCF.

D. Network Operations Analysis Chief

The Network Operations Analysis Chief supervises and coordinates the activities of the real-time Tracking, Telemetry, Command, and Monitor Systems Analysts (described below).

1. Tracking System Analyst. The real-time Tracking System Analyst determines the performance of the Tracking System and recommends corrective action in case of

failure or substandard performance. He is also responsible for the generation of tracking predictions and providing real-time recommendations in support of spacecraft acquisitions and tracking. He provides a real-time technical interface with the Project navigation area and Project telecommunications analyst.

2. Telemetry System Analyst. The real-time Telemetry System Analyst determines the performance of the Telemetry System and recommends corrective action in case of failure or substandard performance. He is also responsible for the generation of DSN telecommunication predictions and provides real-time recommendations to isolate the problem in the case of any nonstandard acquisition. He provides a real-time technical interface with the Project telecommunication analyst.

3. Command System Analyst. The real-time Command System Analyst is responsible for monitoring and analyzing the operation of the DSN Command System. He is responsible to the DSN Operations Chief for defining, isolating, and recommending solutions to problems that occur in the DSN Command System. In addition to this monitoring function, the Command System Analyst generates and transmits the standards and limits, configuration, and test commands utilized at the Deep Space Stations. The Command System Analyst determines the DSN data record outages and coordinates the required playback from the DSS digital ODR. He provides a real-time technical interface with the Project Command Team.

4. Monitor System Analyst. The Monitor System provides the capability for sensing certain characteristics of the various elements of the network and for processing and displaying these data for use by the network operations personnel. Monitor data are used for determining status and configurations, for guidance in directing network operations, for furnishing alarms of nonstandard conditions, and for analysis of quality and quantity of data provided to the Project.

5. Real-Time Monitor Analysis Team. The Real-Time Monitor Analysis Team is responsible for the following tasks:

- (1) Maintain continuous operational control of the Monitor System.
- (2) Monitor and analyze the performance of the Monitor System.
- (3) Gather and validate standards and limits for all network systems.

- (4) Maintain continuous interface with the Operations Control Chief.
- (5) Perform computer I/O functions necessary for the support of system operation.
- (6) Participate in system tests and analyze results.
- (7) Maintain system logs and records.
- (8) Generate pass folder and transfer to ODC.
- (9) Generate postpass reports.
- (10) Maintain status display board.
- (11) Monitor technical information service.

E. Network Operations Support Chief

The Network Operations Support Chief is responsible to the DSN Operations Chief for the direction and coordination of real-time and near-real-time operational support functions that are performed by elements of the DSN Scheduling and Discrepancy Reporting Group and the DSN Operational Data Control Group. These functions include real-time scheduling, sequence of events generation, data traceability and reporting, and discrepancy reporting.

IV. Non-Real-Time Operational Roles

A. DSN Operations Representative

A DSN Operations Representative is appointed for each flight project utilizing the DSN. His function is to represent the mission-independent DSN operations organization to (1) the DSN Manager and his DSN Support Team and (2) the Flight Project Chief of Mission Operations (CMO) and his mission operations team.

Responsibilities are defined for the periods before and after formal transfer of operational responsibility from the DSN Manager to the DSN Operations Chief (OC). This transfer will nominally occur approximately 6 months prior to launch. Responsibilities before operational transfer are as follows:

- (1) Provide liaison between the DSN Manager and the DSN OC.
- (2) Act as operations advisor to the DSN Support Team.
- (3) Flag conflicts between planned activities and DSN operational capabilities; assist in resolving these conflicts.

- (4) Review integration schedules prepared by the support team; ensure that all milestones are in agreement with DSN operational implementation schedules.
- (5) Interpret DSN operational philosophy, capabilities, and requirements to other DSN/TDS elements and to flight project mission operations teams.

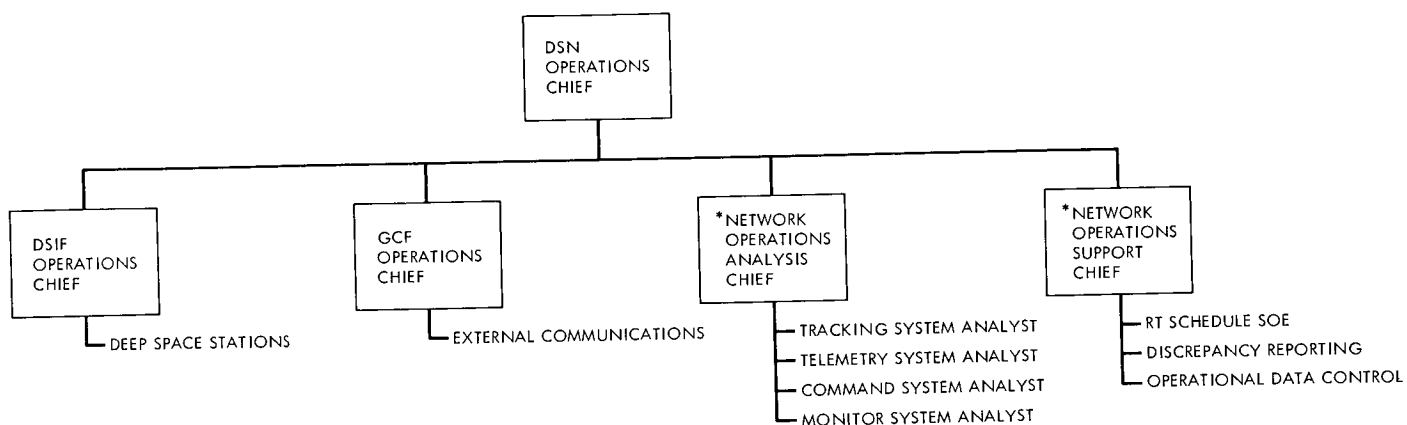
Responsibilities after operational transfer are as follows:

- (1) Act as DSN operations advisor to the flight project mission operations team.
- (2) Participate in mission operations planning meetings; flag conflicts between planned activities and DSN operational commitments; assist in resolving these conflicts.
- (3) Coordinate planned activities with the DSN operations organization; transmit necessary instruction and information to the DSN OC.
- (4) Act as operations advisor to the DSN Manager in planning and developing support for nonstandard operations.
- (5) Provide sequence of events (SOE) inputs, necessary for flight project support, to the DSN Scheduling Group.

B. DSN Scheduling Representative

Each major project that uses the DSN will be assigned a Scheduling Representative by the DSN Scheduling Office. The duties and responsibilities of the Scheduling Representative are as follows:

- (1) Be responsible for scheduling, within the framework of the DSN Network Allocation System, all Project activities and Project-related DSN activities from the establishment of DSN configuration control at (nominally) launch minus 6 months until the end of the operational mission and for the duration of extended mission operations, if any.
- (2) Following the establishment of DSN configuration control, interface with the DSN Operations Representative for all special operational scheduling requirements and for Project-related DSN Operations Control Team scheduling requirements.
- (3) Interface with the Supervisor of DSN scheduling for overall and Project-related ground rules, priorities and constraints.



*THESE GROUPS FUNCTION IN REAL-TIME AND NEAR-REAL-TIME AS ELEMENTS OF THE OCT. THEY ALSO HAVE NON-REAL-TIME OFF-LINE RESPONSIBILITIES.

Fig. 1. DSN operations control team

High-Speed Data Communication: A Description of Software Techniques

R. W. Livermore
Tidbinbilla Deep Space Communications Complex

Some methods are described of using the high-speed data assembly of the Ground Communications Facility operating at 4.8 kbps and the Xerox Data Systems (XDS) 920 computers for keeping the Deep Space Stations supplied with up-to-date programs and documentation. The present method for transmitting this information employs magnetic tapes, punched tapes, and hardcopy documentation transmitted by mail or air freight.

I. Introduction

The present system of keeping stations supplied with up-to-date programs and documentation is to dispatch magnetic tapes, punched tapes, and documentation by mail or air freight. This article describes some methods of using the high-speed data assembly (HSDA) operating at 4.8 kbps and Xerox Data Systems (XDS) 920 computers for this communication.

II. Description of Data Transmission

Blocks of high-speed data (HSD) require codes such as a synchronization code for the start of a block, source, and destination code and a code to route the block to the appropriate computer. During initialization this information is entered on the typewriter connected to the computer in the form of answers to an interrogation (e.g., STATION ID=). After these codes have been allocated space in the HSD block, the programmer is left with 44

full 24-bit words for other information. The method of transmission adopted requires the following extra information to be included in a block of HSD:

- (1) An indication to the remote station that a block has been received with a bad error status and not stored.
- (2) Address information of where to store the message or effective data of the block.
- (3) Whether it is a one-only block.
- (4) Whether it is a first block with more to follow.
- (5) Whether it is a last block.
- (6) Whether it is an intermediate block.
- (7) If it is (3) or (5), an indication of which peripheral device the data are for and how much are to be outputted.
- (8) A serial number for each block.

The desired information for (1) to (6) uses one 24-bit word. An additional three words are used for blocks of type (6) with information for peripheral devices and where programs should commence. The serial number of (8) is accommodated in a $\frac{1}{2}$ word available in word 49. This leaves space for 43 words of data in the first and intermediate blocks. Last blocks have space available for 40 words of data.

III. High-Speed Data Validation Techniques

A simplified flowchart of HSD validation is presented in Fig. 1.

A. Sending

A HSD block is sent with an initial serial number of zero.

B. Receiving

The receive computer examines the GCF error status. If the block is in error the data are not stored and word 4 is made all 1s and the block sent back for verification. If the error status is good, words 5 to 48 are stored in the area indicated by word 4 and sent back for verification. If the block serial number is the same as a previous block received, the data are not stored and the block is sent back for verification.

C. Sending

After sending a block, the sending program waits for a block to be returned for verification. If a block is not returned within 2 s, the block is sent again. If the error status of the returned block is bad, the block is sent again. Word 4 is examined and if it is all 1s (indicating an error at the receive station) the block is sent again. If word 4 is not all 1s, words 4 to 48 are then compared with the original data sent. If they do not compare, the block is sent again. If the data verify correctly, the serial number is incremented by 1 and the next block of data is sent.

IV. Media Validation Techniques

After a program has been received and punched on paper tape or written on magnetic tape, two levels of validation are available:

- (1) A simple check sum is made of all characters with a punched tape. Similarly a check sum is made of all words on a magnetic tape.
- (2) An extremely accurate check can be made by using the Ground Communications Facility (GCF) error detector encoder. The HSD program is initialized to return data to itself while simulating transmission of a program. As each HSD block is returned, the 33-bit polynomial check code is punched onto tape. The resultant tape must be the same every time the check is performed with an identical program.

V. Documentation Preparation

The Editor Program DOI-5250-SP can be used to produce a punched paper tape ready for transmission. Source programs which are stored on punched cards can be transferred to punched paper tape by use of the Media Program DOI-5012-SP-A. Then the program can be assembled locally by use of Monarch DOI-5254-SP-A, and the receiving station can produce as many listings of the program as desired.

Standard forms can be prepared by use of the Editor Program and stored on punched paper tape. The typist can then make the required entries and produce tapes for transmission.

VI. Future Expansion

Very often a computer is not available for document preparation. Preparation on an off-line teletype machine could be performed. A simple conversion program to convert from 5-level TTY code to 7-level XDS code is being considered. An addition to the Editor Program to enable direct writing onto magnetic tape is also being considered.

The program has also included an option which allows programs to be sent to core and operate, e.g., a magnetic tape test. By careful programming it can be arranged to return to the HSD program with results of the test. This portion of the program has not been exercised at the time of writing this article.

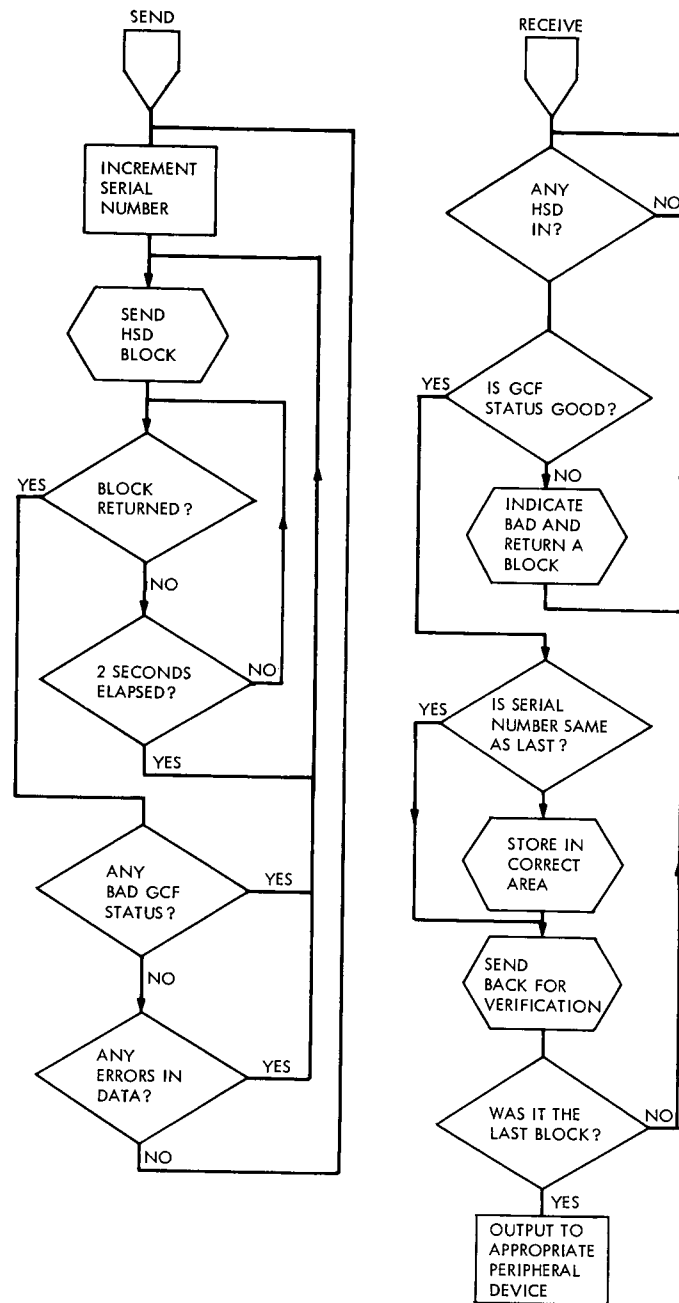


Fig. 1. Simplified flowchart of HSD validation

Accuracy of the Signal-to-Noise Ratio Estimator: A Comment on the Derivation of the Estimator Mean

J. R. Lesh
DSIF Operations Section

The mean of the signal-to-noise ratio estimator used with the symbol synchronizer assembly (SSA) is derived without assuming independence of the sample mean and sample variance errors. The resulting expression is found to differ only slightly from a previous expression determined by assuming independence.

I. Introduction

In Ref. 1, expressions for the mean and variance of the signal-to-noise ratio (SNR) estimator were derived and studied. However, in the derivation of these expressions the assumption was made that the error in the sample mean is independent of the error in the sample variance. This assumption has been the target of some criticism since the errors that produce the error in the sample mean are precisely the same errors that create the error in the sample variance. To answer this criticism, the mean of the SNR estimator was rederived without the assumption of independence of these errors. It was found that the error produced by the independence assumption is negligible for even moderately small sample sizes (in fact, for a sample size of 10, the corresponding error in the estimator mean is bounded by 3.7%).

II. Derivation of the Estimator Mean

We begin by assuming that the reader is familiar with the notation and results of the referenced article. Then the estimated SNR is given by

$$\hat{R} = \frac{\frac{1}{2} \left(\frac{1}{N} \sum_{i=1}^N y_i \right)^2}{\frac{1}{N-1} \sum_{i=1}^N \left(y_i - \frac{1}{N} \sum_{j=1}^N y_j \right)^2} \quad (1)$$

Now assume that $y_i = \mu + \xi_i$ where ξ_i is the error (from the mean μ) of the i th sample. The ξ_i are assumed to be independent, identically distributed, zero-mean random variables having a variance σ^2 . Furthermore, since we desire to apply the Central Limit Theorem (to the sample mean only) we can obtain the same result by assuming

the ξ_i 's are gaussian distributed initially. Thus, the estimated SNR can be expressed as

$$\hat{R} = \frac{\frac{1}{2} \left(\mu + \frac{1}{N} \sum_i \xi_i \right)^2}{\frac{1}{N-1} \sum_i \left(\xi_i - \frac{1}{N} \sum_j \xi_j \right)^2} \quad (2)$$

where the summations are over the N samples. Now by adding and subtracting σ^2 to the denominator and expanding the result in a geometric series we have

$$\hat{R} \approx \frac{1}{2\sigma^2} \left\{ \mu^2(1 - \alpha + \alpha^2) + \frac{2\mu}{N} \sum_i \xi_i (1 - \alpha + \alpha^2) + \frac{1}{N^2} \left(\sum_i \xi_i \right)^2 (1 - \alpha + \alpha^2) \right\} \quad (3)$$

where

$$\alpha = \frac{1}{\sigma^2(N-1)} \sum_i \left(\xi_i - \frac{1}{N} \sum_j \xi_j \right)^2 - 1 \quad (4)$$

Therefore, the mean of the estimator can be expressed as

$$E\{\hat{R}\} \approx \frac{1}{2\sigma^2} [E(T_1) + E(T_2) + E(T_3)] \quad (5)$$

$$E\{T_3\} = E \left\{ \frac{3}{N^2} \left(\sum_i \xi_i \right)^2 - \frac{3}{N^2 \sigma^2 (N-1)} \left(\sum_i \xi_i \right)^2 \sum_j \xi_j^2 + \frac{3}{N^3 \sigma^2 (N-1)} \left(\sum_i \xi_i \right)^4 + \frac{1}{N^2 \sigma^4 (N-1)^2} \left[\left(\sum_i \xi_i \right)^2 \left(\sum_j \xi_j^2 \right)^2 \right] - \frac{2}{N^3 \sigma^4 (N-1)^2} \left(\sum_i \xi_i \right)^4 \sum_j \xi_j^2 + \frac{1}{N^4 \sigma^4 (N-1)^2} \left(\sum_i \xi_i \right)^6 \right\} \quad (10)$$

To evaluate the expected value of these terms is not difficult in theory but does require a very large amount of algebra. For example, the summation in the first term can be expanded to yield

$$\left(\sum_i \xi_i \right)^2 = \sum_i \xi_i^2 + \sum_i \sum_{j \neq i} \xi_i \xi_j \quad (11)$$

and by using the independence of the ξ_i 's we have

$$E \left\{ \left(\sum_i \xi_i \right)^2 \right\} = N\sigma^2 \quad (12)$$

By similarly expanding the remaining terms and taking the expected value,

$$E\{T_3\} = \frac{1}{N^3(N-1)^2} (N^4 - N^2 + 6N + 6)\sigma^2 \quad (13)$$

where T_1 , T_2 and T_3 are the three terms in the bracket of Eq. (3). Now consider the terms separately. For T_1 , we have

$$E(T_1) = \mu^2 - \mu^2 E(\alpha) + \mu^2 E(\alpha^2) \quad (6)$$

But note that α is the error of the sample variance. Thus,

$$E(\alpha) = 0$$

$$E(\alpha^2) = \frac{\sigma_{sv}^2}{\sigma^4} \quad (7)$$

where σ_{sv}^2 is the variance of the sample variance. Therefore

$$E(T_1) = \mu^2 + \frac{\mu^2}{\sigma^4} \sigma_{sv}^2 \quad (8)$$

For T_2 , note that all of its terms involve odd powers of the ξ_i 's. Thus, since the odd moments of a zero-mean gaussian random variable vanish we have

$$E(T_2) = 0 \quad (9)$$

To compute the expectation of T_3 we must first expand the α 's. Using the definition of α we have

Combining the expected values of T_1 , T_2 , and T_3 yields

$$E\{\hat{R}\} \approx \frac{\mu^2}{2\sigma^2} \left[1 + \frac{\sigma_{sv}^2}{\sigma^4} + \frac{\sigma^2}{N\mu^2} + \frac{(N^3 - N^2 + 3N + 3)}{N^2(N-1)} \left(\frac{2}{N-1} \right) \left(\frac{\sigma^2}{N\mu^2} \right) \right] \quad (14)$$

Now, we note that (see Ref. 1)

$$\sigma_M^2 = \frac{1}{N} \sigma^2$$

and from Appendix A of the article we know that for gaussian random variables

$$\sigma_{sv}^2 = \frac{2}{N-1} \sigma^4$$

Thus, Eq. (14) becomes

$$\begin{aligned} E\{\hat{R}\} &\approx \frac{\mu^2}{2N\sigma_M^2} \left[1 + \frac{\sigma_{sv}^2}{\sigma^4} + \frac{\sigma_M^2}{\mu^2} + \frac{N^3 - N^2 + 3N + 3}{N^2(N-1)} \left(\frac{\sigma_{sv}^2}{\sigma^4} \right) \left(\frac{\sigma_M^2}{\mu^2} \right) \right] \\ &= \frac{\mu^2}{2N\sigma_M^2} \left[1 + \frac{\sigma_{sv}^2}{\sigma^4} + \frac{\sigma_M^2}{\mu^2} + k \left(\frac{\sigma_{sv}^2}{\sigma^4} \right) \left(\frac{\sigma_M^2}{\mu^2} \right) \right] \end{aligned} \quad (15)$$

where

$$k = \frac{N^3 - N^2 + 3N + 3}{N^2(N-1)}$$

Returning now to Ref. 1 (Eq. (8)) we found that the expression for the estimator mean was

$$E\{\hat{R}\} = \frac{1}{2NA} [1 + A + B + AB] \quad (16)$$

where

$$A = \frac{\sigma_M^2}{\mu^2} \text{ and } B = \frac{\sigma_{sv}^2}{\sigma^4}$$

Equations (15) and (16) are identical except for the factor k multiplying the AB term of Eq. (15). Thus, if k is close to 1, then the original assumption of independence of the sample mean and variance errors is justified. However, note that

$$k = 1 + \frac{3(N+1)}{N^2(N-1)}$$

Thus, k is indeed close to unity for even moderate N . For example, if $N = 10$, then $K = 1.037$, so that the estimator mean is increased by approximately 3.7% if $AB \gg 1 + A + B$ and is increased by a much smaller percentage otherwise.

Reference

1. Lesh, J. R., "Accuracy of the Signal to Noise Ratio Estimator," in *The Deep Space Network Progress Report*, Technical Report 32-1526, Vol. X, pp. 217-235. Jet Propulsion Laboratory, Pasadena, Calif., Aug. 15, 1972.

Bibliography

- Anderson, J. D., *Determination of the Masses of the Moon and Venus and the Astronomical Unit from Radio Tracking Data of the Mariner II Spacecraft*. Technical Report 32-816. Jet Propulsion Laboratory, Pasadena, Calif., July 1, 1967.
- Anderson, J. D., et al., "The Radius of Venus as Determined by Planetary Radar and Mariner V Radio Tracking Data," *J. Atmos. Sci.*, pp. 1171-1174, Sept. 25, 1968.
- Berman, A. L., *Tracking System Data Analysis Report, Ranger VII Final Report*, Technical Report 32-719, Jet Propulsion Laboratory, Pasadena, Calif., June 1, 1965.
- Berman, A. L., *ABTRAJ—On-Site Tracking Prediction Program for Planetary Spacecraft*, Technical Memorandum 33-391. Jet Propulsion Laboratory, Pasadena, Calif., Aug. 15, 1968.
- Cain, D. L., and Hamilton, T. W., *Determination of Tracking Station Locations by Doppler and Range Measurements to an Earth Satellite*, Technical Report 32-534. Jet Propulsion Laboratory, Pasadena, Calif., Feb. 1, 1964.
- Carey, C. N., and Sjogren, W. L., "Gravitational Inconsistency, in the Lunar Theory: Confirmation by Radio Tracking," *Science*, Vol. 160, pp. 875, 876, Apr.—June 1968.
- Curkendall, D. W., and Stephenson, R. R., "Earthbased Tracking and Orbit Determination—Backbone of the Planetary Navigation System," *Astronaut. Aeronaut.*, Vol. 7, May 1970.
- Curkendall, D. W., "Planetary Navigation: The New Challenges," *Astronaut. Aeronaut.*, Vol. 7, May 1970.
- Efron, L., and Solloway, C. B., *Proceedings of the Conference on Scientific Applications of Radio and Radar Tracking in the Space Program*, Technical Report 32-1475. Jet Propulsion Laboratory, Pasadena, Calif., July 1970.
- Flanagan, F. M., et al., *Deep Space Network Support of the Manned Space Flight Network for Apollo: 1962-1968*, Technical Memorandum 33-452, Vol. I. Jet Propulsion Laboratory, Pasadena, Calif., July 1970.
- Flanagan, F. M., et al., *Deep Space Network Support of the Manned Space Flight Network for Apollo: 1969-1970*, Technical Memorandum 33-452, Vol. II. Jet Propulsion Laboratory, Pasadena, Calif., May 1, 1971.
- Fjeldbo, G., and Eshleman, V. R., "Radio Occultation Measurements and Interpretations," in *The Atmospheres of Venus and Mars*, p. 225. Gordon and Breach, Science Publishers, Inc., New York, N.Y.
- Georgevick, R. M., "Mathematical Model of the Solar Radiation Force and Torques Acting on the Components of a Spacecraft," Technical Memorandum 33-494. Jet Propulsion Laboratory, Pasadena, Calif., Oct. 1, 1971.
- Goldstein, R. M., "Radar Time-of-Flight Measurements to Venus," *Astron. J.*, Vol. 73, No. 9, Aug. 1968.
- Goldstein, R. M., and Rumsey, H., Jr., "A Radar Snapshot of Venus," *Science*, Vol. 169, Sept. 1970.

Bibliography (contd)

- Gordon, H. J., et al., *The Mariner 6 and 7 Flight Paths and Their Determination From Tracking Data*, Technical Memorandum 33-469. Jet Propulsion Laboratory, Pasadena, Calif., Dec. 1, 1970.
- Hamilton, T. W., et al., *The Ranger IV Flight Path and Its Determination From Tracking Data*, Technical Report 32-345. Jet Propulsion Laboratory, Pasadena, Calif., Sept. 15, 1962.
- Kellermann, K. I., et al., "High Resolution Observations of Compact Radio Sources at 13 Centimeters," *Astrophys. J.*, Vol. 161, pp. 803-809, Sept. 1970.
- Kliore, A., "Radio Occultation Measurements of the Atmospheres of Mars and Venus," in *The Atmospheres of Venus and Mars*, p. 205. Gordon and Breach Science Publishers, Inc., New York, N. Y.
- Labrum, R. G., Wong, S. K., and Reynolds, G. W., *The Surveyor V, VI, and VII Flight Paths and Their Determination from Tracking Data*, Technical Report 32-1302. Jet Propulsion Laboratory, Pasadena, Calif., Dec. 1, 1968.
- Lieske, J. H., and Null, G. W., "Icarus and the Determination of Astronomical Constants," *Astron. J.*, Vol. 74, No. 2, Mar. 1969.
- Lorell, J., and Sjogren, W. L., *Lunar Orbiter Data Analysis*, Technical Report 32-1220. Jet Propulsion Laboratory, Pasadena, Calif., Nov. 15, 1967.
- Lorell, J., *Lunar Orbiter Gravity Analysis*, Technical Report 32-1387. Jet Propulsion Laboratory, Pasadena, Calif., June 15, 1969.
- Lorell, J., et al., "Celestial Mechanics Experiment for *Mariner*," *Icarus*, Vol. 12, Jan. 1970.
- McNeal, C. E., *Ranger V Tracking Systems Data Analysis Final Report*, Technical Report 32-702. Jet Propulsion Laboratory, Pasadena, Calif., Apr. 15, 1965.
- Melbourne, W. G., et al., *Constants and Related Information for Astrodynamical Calculations*, Technical Report 32-1306. Jet Propulsion Laboratory, Pasadena, Calif., July 15, 1968.
- Melbourne, W. G., "Planetary Ephemerides," *Astronaut. Aeronaut.*, Vol. 7, May 1970.
- Miller, L., et al., *The Atlas-Centaur VI Flight Path and Its Determination from Tracking Data*, Technical Report 32-911. Jet Propulsion Laboratory, Pasadena, Calif., Apr. 15, 1966.
- Moyer, T. D., "Mathematical Formulation of the Double-Precision Orbit Determination Program (DPODP)," Technical Report 32-1527, Jet Propulsion Laboratory, Pasadena, Calif., May 17, 1971.
- Mulhall, B. D., et al., *Tracking System Analytic Calibration Activities for the Mariner Mars 1969 Mission*, Technical Report 32-1499. Jet Propulsion Laboratory, Pasadena, Calif., Nov. 15, 1970.
- Mulholland, J. D., and Sjogren, W. L., *Lunar Orbiter Ranging Data*, Technical Report 32-1087. Jet Propulsion Laboratory, Pasadena, Calif., Jan. 6, 1967.

Bibliography (contd)

- Mulholland, J. D., *Proceedings of the Symposium on Observation, Analysis, and Space Research Applications of the Lunar Motion*, Technical Report 32-1386. Jet Propulsion Laboratory, Pasadena, Calif., Apr. 1969.
- Muller, P. M., and Sjogren, W. L., *Consistency of Lunar Orbiter Residuals With Trajectory and Local Gravity Effects*, Technical Report 32-1307. Jet Propulsion Laboratory, Pasadena, Calif., Sept. 1, 1968.
- Muller, P. M., and Sjogren, W. L., *Lunar Mass Concentrations*, Technical Report 32-1339. Jet Propulsion Laboratory, Pasadena, Calif., Aug. 16, 1968.
- Null, G. W., Gordon, H. J., and Tito, D. A., *Mariner IV Flight Path and Its Determination From Tracking Data*, Technical Report 32-1108. Jet Propulsion Laboratory, Pasadena, Calif., Aug. 1, 1967.
- O'Neil, W. J., et al., *The Surveyor III and Surveyor IV Flight Paths and Their Determination From Tracking Data*, Technical Report 32-1292. Jet Propulsion Laboratory, Pasadena, Calif., Aug. 15, 1968.
- Pease, G. E., et al., *The Mariner V Flight Path and Its Determination From Tracking Data*, Technical Report 32-1363. Jet Propulsion Laboratory, Pasadena, Calif., July 1, 1969.
- Renzetti, N. A., *Tracking and Data Acquisition for Ranger Missions I-V*, Technical Memorandum 33-174. Jet Propulsion Laboratory, Pasadena, Calif., July 1, 1964.
- Renzetti, N. A., *Tracking and Data Acquisition for Ranger Missions VI-IX*, Technical Memorandum 33-275. Jet Propulsion Laboratory, Pasadena, Calif., Sept. 15, 1966.
- Renzetti, N. A., *Tracking and Data Acquisition Support for the Mariner Venus 1962 Mission*, Technical Memorandum 33-212. Jet Propulsion Laboratory, Pasadena, Calif., July 1, 1965.
- Renzetti, N. A., *Tracking and Data Acquisition Report, Mariner Mars 1964 Mission: Near-Earth Trajectory Phase*, Technical Memorandum 33-239, Vol. I. Jet Propulsion Laboratory, Pasadena, Calif., Jan. 1, 1965.
- Renzetti, N. A., *Tracking and Data Acquisition Report, Mariner Mars 1964 Mission: Cruise to Post-Encounter Phase*, Technical Memorandum 33-239, Vol. II. Jet Propulsion Laboratory, Pasadena, Calif., Oct. 1, 1967.
- Renzetti, N. A., *Tracking and Data Acquisition Report, Mariner Mars 1964 Mission: Extended Mission*, Technical Memorandum 33-239, Vol. III. Jet Propulsion Laboratory, Pasadena, Calif., Dec. 1, 1968.
- Renzetti, N. A., *Tracking and Data System Support for Surveyor: Missions I and II*, Technical Memorandum 33-301, Vol. I. Jet Propulsion Laboratory, Pasadena, Calif., July 15, 1969.
- Renzetti, N. A., *Tracking and Data System Support for Surveyor: Missions III and IV*, Technical Memorandum 33-301, Vol. II. Jet Propulsion Laboratory, Pasadena, Calif., Sept. 1, 1969.
- Renzetti, N. A., *Tracking and Data System Support for Surveyor: Mission V*, Technical Memorandum 33-301, Vol. III. Jet Propulsion Laboratory, Pasadena, Calif., Dec. 1, 1969.

Bibliography (contd)

- Renzetti, N. A., *Tracking and Data System Support for Surveyor: Mission VI*, Technical Memorandum 33-301, Vol. IV. Jet Propulsion Laboratory, Pasadena, Calif., Dec. 1, 1969.
- Renzetti, N. A., *Tracking and Data System Support for Surveyor: Mission VII*, Technical Memorandum 33-301, Vol. V. Jet Propulsion Laboratory, Pasadena, Calif., Dec. 1, 1969.
- Renzetti, N. A., *Tracking and Data System Support for the Mariner Venus 67 Mission: Planning Phase Through Midcourse Maneuver*, Technical Memorandum 33-385, Vol. I. Jet Propulsion Laboratory, Pasadena, Calif., Sept. 1, 1969.
- Renzetti, N. A., *Tracking and Data System Support for the Mariner Venus 67 Mission: Midcourse Maneuver Through End of Mission*, Technical Memorandum 33-385, Vol. II. Jet Propulsion Laboratory, Pasadena, Calif., Sept. 1, 1969.
- Renzetti, N. A., *Tracking and Data System Support for the Pioneer Project. Pioneer VI. Prelaunch to End of Nominal Mission*, Technical Memorandum 33-426, Vol. I. Jet Propulsion Laboratory, Pasadena, Calif., Feb. 1, 1970.
- Renzetti, N. A., *Tracking and Data System Support for the Pioneer Project. Pioneer VII. Prelaunch to End of Nominal Mission*, Technical Memorandum 33-426, Vol. II. Jet Propulsion Laboratory, Pasadena, Calif., Apr. 15, 1970.
- Renzetti, N. A., *Tracking and Data System Support for the Pioneer Project. Pioneer VIII. Prelaunch Through May 1968*, Technical Memorandum 33-426, Vol. III. Jet Propulsion Laboratory, Pasadena, Calif., July 15, 1970.
- Renzetti, N. A., *Tracking and Data System Support for the Pioneer Project. Pioneer IX. Prelaunch Through June 1969*, Technical Memorandum 33-426, Vol. IV. Jet Propulsion Laboratory, Pasadena, Calif., Nov. 15, 1970.
- Renzetti, N. A., *Tracking and Data System Support for the Pioneer Project. Pioneer VI. Extended Mission: July 1, 1966–July 1, 1969*, Technical Memorandum 33-426, Vol. V. Jet Propulsion Laboratory, Pasadena, Calif., Feb. 1, 1971.
- Renzetti, N. A., *Tracking and Data System Support for the Pioneer Project. Pioneer VII. Extended Mission: February 24, 1967–July 1, 1968*, Technical Memorandum 33-426, Vol. VI. Jet Propulsion Laboratory, Pasadena, Calif., Apr. 15, 1971.
- Renzetti, N. A., *Tracking and Data System Support for the Pioneer Project. Pioneer VII. Extended Mission: July 1, 1968–July 1, 1969*, Technical Memorandum 33-426, Vol. VII. Jet Propulsion Laboratory, Pasadena, Calif., Apr. 15, 1971.
- Renzetti, N. A., *Tracking and Data System Support for the Pioneer Project. Pioneer VIII. Extended Mission: June 1, 1968–July 1, 1969*, Technical Memorandum 33-426, Vol. VIII. Jet Propulsion Laboratory, Pasadena, Calif., May 1, 1971.
- Renzetti, N. A., *Tracking and Data System Support for the Pioneer Project. Pioneers VI–IX. Extended Missions: July 1, 1969–July 1, 1970*. Technical Memorandum 33-426, Vol. IX. Jet Propulsion Laboratory, Pasadena, Calif., Aug. 15, 1971.
- Sjogren, W. L., *The Ranger III Flight Path and Its Determination From Tracking Data*, Technical Report 32-563. Jet Propulsion Laboratory, Pasadena, Calif., Sept. 15, 1965.

Bibliography (contd)

- Sjogren, W. L., et al., *The Ranger V Flight Path and Its Determination From Tracking Data*, Technical Report 32-562. Jet Propulsion Laboratory, Pasadena, Calif., Dec. 6, 1963.
- Sjogren, W. L., et al., *The Ranger VI Flight Path and Its Determination From Tracking Data*, Technical Report 32-605. Jet Propulsion Laboratory, Pasadena, Calif., Dec. 15, 1964.
- Sjogren, W. L., et al., *Physical Constants as Determined From Radio Tracking of the Ranger Lunar Probes*, Technical Report 32-1057. Jet Propulsion Laboratory, Pasadena, Calif., Dec. 30, 1966.
- Sjogren, W. L., *Proceedings of the JPL Seminar on Uncertainties in the Lunar Ephemeris*, Technical Report 32-1247. Jet Propulsion Laboratory, Pasadena, Calif., May 1, 1968.
- Sjogren, W. L., "Lunar Gravity Estimate: Independent Confirmation," *J. Geophys. Res.*, Vol. 76, No. 29, Oct. 10, 1971.
- Spier, G. W., "Design and Implementation of Models for the Double Precision Trajectory Program (DPTRAJ)," Technical Memorandum 33-451, Jet Propulsion Laboratory, Pasadena, Calif., Apr. 15, 1971.
- Stelzried, C. T., *A Faraday Rotation Measurement of a 13-cm Signal in the Solar Corona*, Technical Report 32-1401. Jet Propulsion Laboratory, Pasadena, Calif., July 15, 1970.
- Stelzried, C. T., et al., "The Quasi-Stationary Coronal Magnetic Field and Electron Density as Determined From a Faraday Rotation Experiment," *Sol. Phys.*, Vol. 14, No. 2, pp. 440-456, Oct. 1970.
- Thornton, J. H., Jr., *The Surveyor I and Surveyor II Flight Paths and Their Determination From Tracking Data*, Technical Report 32-1285. Jet Propulsion Laboratory, Pasadena, Calif., Aug. 1, 1968.
- Vegos, C. J., et al., *The Ranger IX Flight Path and Its Determination From Tracking Data*, Technical Report 32-767. Jet Propulsion Laboratory, Pasadena, Calif., Nov. 1, 1968.
- Winn, F. B., *Selenographic Location of Surveyor VI, Surveyor VI Mission Report: Part II. Science Results*, Technical Report 32-1262. Jet Propulsion Laboratory, Pasadena, Calif., Jan. 10, 1968.
- Winn, F. B., "Post Landing Tracking Data Analysis," in *Surveyor VII Mission Report: Part II. Science Results*, Technical Report 32-1264. Jet Propulsion Laboratory, Pasadena, Calif., Mar. 15, 1968.
- Winn, F. B., "Post Lunar Touchdown Tracking Data Analysis," in *Surveyor Project Final Report: Part II. Science Results*, Technical Report 32-1265. Jet Propulsion Laboratory, Pasadena, Calif., June 15, 1968.
- Winn, F. B., *Surveyor Posttouchdown Analyses of Tracking Data*, NASA SP-184. National Aeronautics and Space Administration, Washington, D.C., p. 369.
- Wollenhaupt, W. R., et al., *The Ranger VII Flight Path and Its Determination From Tracking Data*, Technical Report 32-694. Jet Propulsion Laboratory, Pasadena, Calif., Dec. 15, 1964.